UNIVERSITY OF SOUTHAMPTON

Faculty of Engineering & Environment
*Computational Engineering & Design Research Group*

# Coronary artery stent design for challenging disease: insights into patient specific modelling

by

GEORGIOS E. RAGKOUSIS

Thesis for the degree of Doctor of Philosophy

Supervisors:
Prof. Neil W. Bressloff
Prof. Nick Curzen

March 1, 2016

*To Olga and Lefteris*

*"...we may never find a universe to fit us all but the beauty lies in the quest."*

---

Hainis D. Apostolakis

UNIVERSITY OF SOUTHAMPTON

## ABSTRACT

FACULTY of ENGINEERING AND THE ENVIRONMENT
Computational Engineering and Design Research Group

Doctor of Philosophy

# CORONARY ARTERY STENT DESIGN FOR CHALLENGING DISEASE: INSIGHTS INTO PATIENT SPECIFIC MODELLING

by Georgios E. Ragkousis

In the last two decades, numerical methods have been a widely recognised tool for investigating stenting procedures. Initially, computer models of stenting were restricted to ideal vessels and in some cases by two dimensional analysis due to limited computational capabilities and resources. Nevertheless, nowadays, the increased computational power along with the development of solid imaging processing techniques, have launched a new category in computational stenting, that of imaged-based computational modelling.

Recent clinical evidence has shown that new generation stents are better in terms of in-stent restenosis and stent thrombosis. However, improving stent performance regarding one factor can impair others and, as a result, a compromised approach is likely to be necessary. This fact seems to be more evident in challenging anatomies where a long and flexible stent has to be implanted. Challenging anatomies can be characterised by long and tortuous geometry, comprising non-focal and highly calcified plaque. Common complications of percutaneous coronary intervention in such anatomies include stent malapposition and stent longitudinal deformation.

The aims of this doctoral work were (i) to reconstruct diseased patient-specific coronary artery segments, (ii) simulate the deployment of state of the art stents into these segments following model validation and verification, (iii) assess the degree of stent malapposition and stent longitudinal deformation, (iv) design stent systems to mitigate the risk of stent malapposition and longitudinal deformation in these segments and (v) analyse optimum stent deployments according to a patient-specific vessel.

Patient-specific cases were reconstructed by combining coronary angiography and ultrasonography to an acceptable accuracy level for the computational purposes of this project. Then, after generating contemporary virtual stent/balloon models, they were validated/calibrated against experimental data. In addition, novel varying diameter balloon models and a modified stent were generated to mitigate the risk of stent malapposition and longitudinal deformation, respectively. After developing an inexpensive numerical methodology for image-based stenting simulations, numerous patient-specific structural simulations were carried out to investigate the effect of i) different stent design in stent malapposition and longitudinal deformation and ii) different dilation system design in stent malapposition. Finally, a multi-objective optimisation framework was presented to investigate the optimum dilation protocol in a patient-specific segment via structural and surrogate modelling.

Results indicate that stent malapposition, for the simulated patient specific cases, is dependent on the so-called “reference diameter”. Remarkably, the proposed balloon models demonstrated superior results of performance especially as far as stent malapposition is concerned. In particular, they led to an approximately 40% reduction in malapposed struts when compared with the baseline models, whilst maintaining a relatively low stressed mechanical environment. As for stent longitudinal deformation, the outcomes indicated that (i) it is significantly different between the stent platforms in a manner consistent with physical testing in a laboratory environment, (ii) there was a smaller range of variation for simulations of *in vivo* performance relative to models of *in vitro* experiments, and (iii) the modified stent design demonstrated considerably higher longitudinal integrity. Interestingly, it was shown that stent longitudinal stability may differ significantly after a localised in vivo force compared to a distributed in vitro force. Lastly, the multi-objective optimisation study demonstrated that given a patient-specific vessel, different optimum dilation strategies could be extracted according to the interventional cardiologist’s preference.

Significantly, this work computationally investigates stent longitudinal deformation and stent malapposition of patient-specific reconstructed vessels. Such numerical models can provide three dimensional qualitative and quantitative information in the investigated clinical problems. Moreover, they may represent a potentially valuable tool for predicting stent malapposition, avoiding stent deformations and, consequently, optimising the interventional protocol according to any patient-specific case.

# Contents

# List of Figures

# List of Tables

# DECLARATION OF AUTHORSHIP

I, Georgios E. Ragkousis, declare that the thesis entitled *Coronary artery stent design for challenging disease* and the work presented in the thesis are both my own, and have been generated by me as the result of my own original research. I confirm that:

- this work was done wholly or mainly while in candidature for a research degree at this University;
- where any part of this thesis has previously been submitted for a degree or any other qualification at this University or any other institution, this has been clearly stated;
- where I have consulted the published work of others, this is always clearly attributed;
- where I have quoted from the work of others, the source is always given. With the exception of such quotations, this thesis is entirely my own work;
- I have acknowledged all main sources of help;
- where the thesis is based on work done by myself jointly with others, I have made clear exactly what was done by others and what I have contributed myself;
- parts of this work have been published as:
    1. Ragkousis GE.,Curzen N., Bressloff NW. (2013) **Patient Specific Stent Malapposition in Challenging Anatomy: An FEA methodology to understand numerically the extend of malapposition of latest generation stents**, In: *ASME 2013 Summer Bioengineering Conference*, pp. V01AT12A004 (DOI:10.1115/SBC2013-14582)
    2. Ragkousis GE.,Curzen N., Bressloff NW. (2014) **Simulation of longitudinal stent deformation in a patient-specific coronary artery**, In: *Medical Engineering & Physics*, 36: 467-476 (DOI:10.1016/j.medengphy.2014.02.004)
    3. Ragkousis GE.,Curzen N., Bressloff NW. (2015) **Computational modeling of multi-folded balloon delivery systems for coronary artery stenting: Insights into patient specific stent malapposition** In: *Annals of Biomedical Engineering*, 43:1786-1802 (DOI:10.1007/s10439-014-1237-8)

4. Bressloff NW., Ragkousis GE., Curzen N. (2015) **Design optimisation of coronary artery stent systems** In: *Annals of Biomedical Engineering* (DOI:10.1007/s10439-015-1373-9)
5. Paulson C., Ragkousis GE. (2015) **pyKriging: A python Kriging Toolkit** *Zenodo* (DOI:http://dx.doi.org/10.5281/zenodo.21389)
6. Ragkousis GE.,Curzen N., Bressloff NW. (2015) **Multi-objective optimisation of stent dilation strategy in a patient-specific coronary artery via computational and surrogate modelling** In: *Biomechanics* (DOI: http://dx.doi.org/10.1016/j.jbiomech.2015.12.013)

Signed:........................................................................................................................

Date:............................................................................................................................

# ACKNOWLEDGEMENTS

Upon the completion of my doctoral work, I would like to thank everyone who supported me during these four productive years: academics, colleagues, family and friends. Particularly, I would like to express my gratitude to Prof. Neil W Bressloff, my supervisor, who opened the door and took me on this long educational journey. He ensured that during my candidature, I was being provided with the best guidance, expertise, resources and facilities. He was always supportive to my ideas and he contributed the most to the design of this thesis. I am also grateful to Prof. Nick Curzen, my second supervisor and a great interventional cardiologist. He has been providing valuable advices during our fruitful meetings throughout these years. His unrivalled dedication to the improvement of patient care, filled me with vision and tenacity.

Best regards to all my friends. Firstly, to those who I am missing most, those who I have left back home. I will do my best to get back to them, as soon as possible. Secondly, to those friends who I have made in London and in Southampton, during my MSc course and my PhD, respectively. Each one has contributed with many ways to the completion of this thesis.

I would like to acknowledge my brother, Mihalis and, my sister, Katerina for their undivided support. They have always been by my side in every step I have made. They were the first to encourage me to accept this research position. Along with my siblings, I would like to thank Evi, my aunt, for her critical role to overcome the most difficult situation in my life. Without them, this work would not have been materialised.

Sincere thanks to Mairina, my other half, my friend and my partner. She has always been next to me during these four difficult years providing love and understanding. I thank her for the endless moments of support and encouragement, especially in stressful periods and in unexpected irritating situations. I will now be spending the maximum time with her and we will keep visiting warm places. Marvin Gaye sings "*...let's get it on..., let's get it on...*". Essentially, we have got it on!

Most of all, I would like to acknowledge my mother, Olga and, my father, Lefteris. The reasons are numerous and most of them are beyond the writing and completion of this thesis. Nikos Kazantzakis, in Report to Greco wrote that "*...true teachers are those who use themselves as bridges over which they invite their students to cross; then, having facilitated their crossing, joyfully collapse, encouraging them to create their own*". Well..., apart from "true" parents, they have always been our "true" teachers!

Georgios E. Ragkousis

January 2016, Southampton,
UK.

# ABBREVIATIONS

**CAD** computer-aided design

**2D** two dimensional

**3D** three dimensional

**BMS** bare-metal stents

**CA** coronary angiography

**CABG** coronary artery by-pass grafting

**CAD** coronary artery disease

**CDF** cumulative distribution function

**CFD** computational fluid mechanics

**CT** computed tomography

**Cx** circumflex

**DES** drug-eluting stent

**DoE** design of experiment

**FEA** finite element analysis

**FSI** fluid-structure interaction

**GA** genetic algorithm

**GP** Gaussian process

**hrMRI** high resolution magnetic resonance imaging

**ISR** in-stent restenosis

**IVUS** intravascular ultrasound

**LAD** left anterior descending

**LAO** left anterior oblique

**LCA** left coronary artery

**LDL** low density lipoprotein

**LHC** Latin hyper-cube

**LMB** left main bifurcation

**LSD** longitudinal stent deformation

**MLA** minimum lumen area

**MRI** magnetic resonance imaging

**NIH** neo-intimal hyperplasia

**NSGA-II** non-sorting genetic algorithm

**NURBS** non-uniform rational B-spline

**OCT** optical coherence tomography

**PA** posteroanterior

**PCI** percutaneous coronary intervention

**PET** positron emission tomography

**PF** pareto front

**PTCA** percutaneous transluminal coronary angioplasty

**RAO** right anterior oblique

**RCA** right coronary artery

**SM** stent malapposition

**ST** stent thrombosis

# LIST OF SYMBOLS

## Units

| | |
|---|---|
| $atm$ | atmosphere |
| $bar$ | bar |
| $g/cm^3$ | grammar per unit cubic centimeter |
| $GPa$ | gigaPascal |
| $g$ | grams |
| $Kg$ | kilogram |
| $KPa$ | kiloPascal |
| $m$ | meter |
| $MHz$ | megahertz |
| $\mu m$ | micrometer |
| $mm$ | millimeter |
| $MPa$ | megaPascal |
| $m/s$ | meter per second |
| $N$ | Newton |
| $N/mm^2$ | Newton per unit square millimeter |
| $sec$ | second |

## Greek symbols

| | |
|---|---|
| $\mathbf{\Gamma}$ | Covariance matrix |
| $\mathbf{\Psi}$ | Correlation matrix |
| $\alpha$ | Phase shift |
| $\alpha_s$ | $\alpha$ weighting factor of snake internal energy |
| $\beta$ | Mean of a random field |
| $\beta_s$ | $\beta$ weighting factor of snake internal energy |
| $\gamma_s$ | $\gamma$ weighting factor of snake external energy |
| $\lambda_i$ | Principal stretches |
| $\mu_0$ | Shear modulus |
| $\omega$ | Angular frequency |
| $\omega_{min}$ | Lowest eigenfrequency |
| $\omega_{max}$ | Highest eigenfrequency |
| $\phi$ | Probability density function |

| | |
|---|---|
| $\mathbf{\Phi}$ | Probability distribution function |
| $\phi$ | Fi angle |
| $\nu$ | Poisson's ratio |
| $\psi$ | Correlation vector between a new point and the points used to build a Gaussian Process model |
| $\sigma^2$ | Variance of a Gaussian process |
| $\sigma_\Box$ | Stress $\Box$ component |
| $\theta_j$ | Hyper-parameter in Gaussian process correlation function |
| $\theta$ | Theta angle |

## Operators

| | |
|---|---|
| $\Delta\Box$ | Incremental value of $\Box$ quantity |
| cos | Cosine |
| $\Box_i \times \Box_j$ | Cross-product of the vector $\Box_i$ and $\Box_j$ |
| $\delta\Box$ | Admissible variation of the quantity $\Box$ |
| $\det(\Box)$ | Determinant of $\Box$ matrix/tensor |
| $\Box_i \cdot \Box_j$ | Dot-product of the vector $\Box_i$ and $\Box_j$ |
| $\Box^{-1}$ | Inverse of matrix $\Box$ |
| $\Box^T$ | Transpose of matrix $\Box$ |
| $\partial\Box_i/\partial\Box_j$ | Partial derivative of function $\Box_i$ with respect to $\Box_j$ quantity |
| sin | Sine |
| $\sum_i^n \Box$ | Sum of quantity $\Box$ from $i$ to $n$ |
| tan | Tangent |
| $\|\|\Box\|\|$ | Norm of matrix/vector $\Box$ |

## Latin symbols

| | |
|---|---|
| $A$ | Area |
| $\mathcal{D}(t)$ | A topological region as a function of an arbitrary parameter $t$ |
| $\mathbf{F}$ | Deformation gradient tensor |
| $\mathbf{F}(\mathbf{t},\mathbf{n},\mathbf{b})$ | Transformation matrix as a function of arbitrary vector parameters $\mathbf{t};\mathbf{n};\mathbf{b}$ |
| $\mathbf{G}(.)$ | Out of balance/residual force |
| $\bar{I}_1$ | First invariant of the Cauchy-Green tensor |
| $\mathbf{I}$ | Identity matrix |
| $\mathcal{J}$ | Total volume ratio |
| $K_0$ | Bulk modulus |
| $L_{ivus}$ | Lenght of the IVUS pull-back |

| | |
|---|---|
| $\mathbf{M}_{global}$ | Global matrix |
| $N_{frames}$ | Number of IVUS frames |
| $\mathcal{O}(t)$ | The osculating Frenet plane as a function of an arbitrary parameter $t$ |
| $\mathcal{P}(t)$ | The normal Frenet plane as a function of an arbitrary parameter $t$ |
| $\mathcal{R}(t)$ | A topological space as a function of an arbitrary parameter $t$ |
| $\mathbf{R}_z(\theta)$ | Rotation matrix as a function of an arbitrary rotation angle parameter $\theta$ |
| $R$ | Correlation function |
| $\mathcal{R}e(t)$ | The rectifying Frenet plane as a function of an arbitrary parameter $t$ |
| $\mathbf{R}(.)$ | Tangent stiffness matrix |
| $S_{pullback}$ | Speed of the IVUS pull-back |
| $\mathbf{T}(\mathbf{p})^{-1}$ | Translation matrix as a function of an arbitrary displacement vector parameter $\mathbf{p}$ |
| $U$ | Strain energy density |
| $V(\mathcal{Q})$ | Volume as a function of an arbitrary topological object parameter $\mathcal{Q}$ |
| $VG$ | Volume gain |
| $AASM$ | Area average stent malapposition |
| $y(.)$ | Observed value as a function of an input vector |
| $S_{\square}$ | Arc length of $\square$ instance |
| $\mathbf{b}$ | Bi-normal unit vector |
| $\mathbf{T}(\mathbf{c_0})_{curve}$ | Translation matrix as a function of an arbitrary position vector parameter $\mathbf{c_0}$ |
| $\mathbf{c}(t)$ | Parametrised space curve as a function of an arbitrary parameter $t$ |
| $C_{\square}$ | Circumferential length of $\square$ instance |
| $\mathbf{cp}(t)$ | Parametrised space curve as a function of an arbitrary parameter $t$ |
| $\mathbf{C}$ | Global damping matrix |
| $D_{\square}$ | Diameter length of $\square$ instance |
| $c$ | Drug concentration |
| $E_{\square}$ | Energy of $\square$ quantity |
| $d$ | Euclidean distance |
| $E\left[I(\mathbf{x})\right]$ | Expected improvement as a function of an input vector $\mathbf{x}$ |
| $\bar{f}_i(\mathbf{x})$ | Normalised objective function value of the $i^{th}$ model as a function of an input vector $\mathbf{x}$ |

| | |
|---|---|
| $f_i(\mathbf{x})$ | Objective function value of the $i^{th}$ model as a function of an input vector $\mathbf{x}$ |
| $\mathbf{f}(t)$ | Time-dependant load vector |
| $f_{acq}$ | Image acquisition frequency |
| $f$ | Frequency |
| $\mathbf{f}$ | Load vector |
| $D_{global}$ | Global deflection |
| $k(t)$ | Curvature as a function of an arbitrary parameter $t$ |
| $d_2(\mathbf{f}, \mathbf{z}, \mathbf{w})$ | $l_2$ metric as a function of $\mathbf{f}$, $\mathbf{z}$ and $\mathbf{w}$ vectors |
| $L_\square$ | Length of instance $\square$ |
| $\mathbf{M}$ | Global mass matrix |
| $MSE$ | Mean square error |
| $n_i^*$ | Maximum objective function value of the $i^{th}$ model |
| $N_{folds}$ | Number of balloon folds |
| $N_{rings}$ | Number of circumferential rings along the stent longitudinal length |
| $N_{struts}$ | Number of struts in a circumferential stent ring |
| $\mathbf{n}$ | Normal unit vector |
| $T$ | Time period |
| $C(.,.)$ | Posterior variance |
| $p_j$ | Exponential hyper-parameter in Gaussian process correlation function |
| $\hat{y}(.)$ | Predicted value as a function of an input vector |
| $p$ | Pressure |
| $r_\square$ | Radius of instance $\square$ |
| $SCVR$ | Standardised cross validated residual |
| $\mathbb{S}$ | The search space |
| $Stent_{Circ}$ | Circumference length of the stent |
| $\mathbf{K}$ | Global stiffness matrix |
| $\tau(t)$ | Torsion as a function of an arbitrary parameter $t$ |
| $TAC$ | Total average curvature |
| $TAT$ | Total average torsion |
| $Th_\square$ | Thickness of $\square$ instance |
| $\mathbf{t}$ | Tangent unit vector |
| $\ddot{\mathbf{u}}$ | Nodal acceleration vector |
| $\dot{\mathbf{u}}$ | Nodal velocity vector |
| $\mathbf{u}$ | Nodal displacement vector |

| | |
|---|---|
| $\mathbf{v}$ | Position vector |
| $VAD$ | Volume average drug |
| $VAS$ | Volume average stress |
| $V_{impact}$ | Impact velocity |
| $w_i$ | Weighting factor of the $i^{th}$ model |
| $W_{\square}$ | Width of instance $\square$ |
| $\mathbf{x}(t)$ | Position vector as a function of an arbitrary parameter $t$ |
| $X_{bridge}$ | Length of a stent connector |
| $X_{strut}$ | Axial length of a circumferential stent ring |
| $\mathbf{x}$ | Unit vector |
| $Y_{bridge}$ | Vertical length of a stent connector |
| $E$ | Young's modulus of elasticity |
| $Y_{strut}$ | Vertical length of a stent strut |
| $\mathbf{y}$ | Unit vector |
| $z_i^*$ | Minimum objective function value/ideal value of the $i^{th}$ model |
| $\mathbf{z}$ | Unit vector |

# PROLOGUE

The human circulatory system consists of the heart, arterial, veinous and micro-circulatory systems. The current study is carried out with respect to a human disease, named atherosclerosis, that affects the arterial system by reducing the flow of blood to distal tissue. Atherosclerosis occurs in almost any artery but appears with greatest frequency in the aorta, iliac, cerebral and coronary arteries. It is primarily an intimal disease of large and medium sized arteries and is characterized by the presence of lipid in the intima, usually in localised form, and accompanied by inflammation, fibrosis, and by hyperplasia in the endothelium (Nichols and O'Rourke 2005). Atherosclerosis is the result of unusual hemodynamic conditions occurring mainly in the arteries that can lead to abnormal biological responses. There are two principal manifestations of atherosclerosis, occlusive ("stenosis") disease and aneurysms. The former is the reference point of this work.

It is well known that, across all populations (based on geographic location, race, ethnicity, age, and sex), coronary artery disease (CAD) is the single most common cause of death. The pathological complications of atherosclerosis remain the leading cause of mortality in the western world. In the UK, in 2010 CAD resulted in about 80,000 deaths and every year over 100,000 percutaneous coronary intervention (PCI) operations are carried out, more than three times the number a decade ago, resulting in a multi-billion pound cost for the UK economy (Townsend et al. 2012).

Coronary arteries carry oxygenated blood from the left ventricle of the heart to the myocardium. In its advanced stages, atherosclerosis can cause serious events such as myocardium infraction (heart attack), angina and stroke. The form of the illness, typically, is accumulation of atheromatic plaque on the walls of the arteries, restricting the flow of the blood, therefore, obstructing the physiologic oxygen supply to the myocardium. Different stages of CAD are now well identified either by using invasive imaging methods such as coronary angiography (CA), and intravascular ultrasound (IVUS) or more rarely non-invasive imaging tools including cardiac computed tomography (CT) and positron emission tomography (PET).

In the past, CAD treatment was focused primarily on fully invasive open heart surgery methods in which coronary artery by-pass grafting (CABG) is used to restore the blood flow in diseased vessels (Richard and Timothy 1995). Such operations could be very traumatic for the patient. However, nowadays catheter based operations (angioplasty and stenting) have been developed. In general, there is a range of choices for treating CAD. These choices are mainly dependent on the stage of the disease, usually determined by visualising the diseased segments with coronary angiography or IVUS (Berry et al. 2007), and secondly on individuality (physician's decision). The conservative approach is taken when the disease is at its early stage (minimal arterial occlusion) and involves the delivery of medications such as beta-blockers, nitrates, and calcium-channel blockers. The interventional approach, which involves percutaneous transluminal coronary angioplasty (PTCA) was introduced in the mid 1960s. It was first applied to the revascularization of the femoral, popliteal and renal arteries, and finally it was adapted in the coronary arteries in the late 1970s (Htay and Liu 2005). Since the first stent implantation in 1987 (Sigwart et al. 1987), PCI or stenting has become the main method for treating coronary artery occlusions.

PCI involves the intra-vascular insertion of a balloon-stent catheter along a guide wire from the femoral artery (or radial artery) to the stenotic region of the coronary artery. The procedure ends up with the inflation of a balloon to deploy a stent which undergoes plastic deformation to maintain an acceptable diameter of the vessel (Grech 2003). There are two main distinct categories of stents, bare-metal stents (BMS) and drug-eluting stent (DES).

The major limitations of PCI success are stent thrombosis (ST) and in-stent restenosis (ISR) a complex and incompletely understood event, in which plaque re-develops within the vessel lumen as a result of the post-stent mechanical conditions. It is strongly believed that ISR pathogenesis depends on three distinct processes and these include: (1) immediate vessel recoil after stretch injury, (2) negative arterial remodeling, and (3) neo-intimal hyperplasia (NIH) (Mudra et al. 1997).

In Rogers and Edelman (1995), it was examined how arterial expansion, stent configuration, and the material in contact with the blood vessel wall each contribute to endovascular stent-induced vascular injury and repair. The outcomes showed that configuration dependent interactions of stent struts with vessel wall elements determine vascular injury and NIH. Stent material in contact with the vessel wall plays a greater role in ST. Although many approaches have been investigated, including antiplatelet pharmacological treatments and anti-proliferative drug coatings (in DES), long term ISR rates are still under research. In one of the most famous studies concerning ISR (Kastrati et al. 2001), 4510 patients were analysed after stent implantation and showed that other than vessel size, stent design is the most important factor influencing restenosis. DES have shown to behave better in terms of ISR although they have been associated with allergic reactions, stent malapposition (SM) and inflammation leading to early and late ST (Cook et al. 2009).

SM is the lack of contact between struts of the stent and the underlying arterial wall and is associated with significantly higher levels of thrombus deposition (Ozaki et al. 2010). Recently, the occurrence of SM has been correlated with axial stent deformations. Hanratty and Walsh (2011) were the first to address the event of longitudinal compression at the proximal and distal end of a stent which has been implanted in segments with challenging disease. This event, if it occurs, may cause very adverse effects.

In the review by Lewis (2008), the outcomes of several studies have been outlined in order to predict potential ISR or ST from coronary artery stent implantation. The author considers two decades of material, fluid dynamics, and solid mechanics aspects of coronary artery stents. It is clear that a lot of effort is being given to design stent-catheter systems which will cause the most minimal adverse effects in short and long term periods after implantation, often resulting from ISR and ST. Most of these studies have outlined some of the following design recommendations: strut width must be less than 100 $\mu m$ for better flow characteristics in the vicinity of the stented vessel; to reduce the number of connectors between the circumferential rings so as to increase flexibility and deliverability; the strut design must be oriented in the same direction with the direction of flow, etc.

However, improving one factor can impair other measures of stent performance. This is more evident in diseased segments with very complex geometry. Coronary arteries run on the surface of the heart, such that they take the curvature of the heart. This complexity, which can include vessel tortuosity may result in very complicated and unwanted post-operation events especially when the disease has spread all along the vessel with highly calcified and diffuse plaques. As expected, the access to a potential diseased site of such complex vessels is favoured by very flexible and deliverable systems. In general, long diseased tortuous vessels with non-focal and highly calcified plaque, which represent the so-called “challenging disease”, often require post-dilation of a second balloon for better stent apposition and/or to achieve uniform and consistent lumen area. As a result of such manoeuvrings, longitudinal stresses may occur following compression or elongation of the two ends of the stents dislocating the stent. This complication is addressed as longitudinal stent deformation (LSD) provoked by SM.

# Aims and objectives

In this work, SM and LSD are the major investigated clinical complications in PCI. The main aim of this work was to investigate the development of stent-system models and deployment techniques to simulate the treatment of patient-specific vessels with challenging disease, while minimising the potential for ISR and ST. For the purposes of this doctoral work, vessel reconstructions were carried out by combining CA with IVUS. Latest generation virtual stent/balloon computer-aided design (**CAD**) models were generated. Thereafter, finite element analysis (FEA) studies quantitatively evaluated the performance of the latest generation stent systems implanted in patient-specific geometries. The FEA was based on model definitions through the application of representative constitutive laws which describe the hyper-elastic behaviour of the arterial walls, and the elastoplastic behaviour of coronary stents.

To summarise, the objectives of this work were:

- develop a method to reconstruct patient-specific models
- design parameterised virtual models of contemporary generation stent systems
- design parameterised virtual models of realistic folded dilation systems
- generate FEA models to investigate numerically the performance of stent deployment in reconstructed segments
- investigate which features of the stent-system influence SM and LSD
- provide recommendations for optimum stent-systems and dilation protocols to minimise SM, and consequently, avoid LSD

# Organisation of the doctoral thesis

The content of the current doctoral work is outlined in each chapter as follows:

- In Chapter 1, the anatomy along with the physiology of human coronary arteries is introduced. Atherosclerosis and its development stages are briefly presented. Different procedures which have been used to treat CAD during the last decades are outlined, with special focus on the evolution of PCI during the last years. Then, the clinical problems of SM and LSD are presented and discussed.
- A literature review of FEA stent studies is carried out in Chapter 2. Firstly, a brief description of the fundamental principles in a FEA package is provided.

Then, the most popular and state-of-the-art computational studies (to the author's judgement) are introduced to indicate the capabilities of FEA simulations to predict, guide and improve the PCI procedure.

- The three dimensional (3D) reconstruction process which has been followed to reconstruct the vessels is presented in Chapter 3. Firstly, a brief overview of CA and IVUS is presented to provide an overall knowledge of these medical imaging modalities. Then, the steps along with the mathematical concepts for vessel reconstruction are presented and discussed. Finally, the limitations of the process are outlined to indicate potential future improvements.

- Chapter 4 describes the design methodology followed to generate stent and balloon virtual models. In the beginning, a brief overview of stent/balloon features is provided following the analytic description of **CAD** construction methods of contemporary coronary artery stents and parametrised dilation catheter systems.

- Chapter 5 presents the developed FEA methods used in this doctoral work along with validation and verification of the (mesh) discretised virtual space comprising the stent system (stent and dilation catheter system) and the reconstructed coronary artery segment. Furthermore, a description of setting up the FEA parameters to run quasi-static simulations is provided. Finally, limitations of the presented FEA models are presented and elaborated upon.

- In Chapter 6, patient-specific simulations of LSD and SM are presented between different contemporary stent devices implanted in a reconstructed patient-specific right coronary artery (RCA). The longitudinal compression behaviour of the investigated stents are validated against compression charts obtained after experimental testing in the respective commercial devices by Ormiston et al. (2011).

- The first computational study investigating non-uniform dilation systems implanted in patient-specific arteries is presented in Chapter 7. In particular, two reconstructed vessels are modelled, one RCA and one left main bifurcation (LMB), representing challenging cases in PCI practice. The performance of the proposed dilation systems is quantitatively measured by different indices characterising i) the induced mechanical environment after stenting, ii) the average malapposed struts after stent expansion and iii) the geometrical configuration of the vessel after balloon inflation.

- Chapter 8 introduces the first multi-objective optimisation study of the stent dilation strategy in a patient-specific RCA. In the work presented in this chapter, the dilation strategy is parametrised by the balloon inflation pressure and the balloon unpressurised diameter. The objectives functions; or figures of merit, are characterised by three indices which stand for i) the mechanical induced environment during the maximum balloon inflation, ii) the average malapposition and iii) the average drug diffusion in the vessel walls after stent implantation. Gaussian process (GP) models were implemented to construct response surfaces, model uncertainty and improvement. Then, the non-sorting genetic algorithm (NSGA-II) was implemented to search for potential updates and objective function improvement.

- Finally, Chapter 9 is the epilogue of this doctoral work. Specifically, in this content, an outline is provided with the contributions and conclusions made from this work, concerning: i) patient-specific modelling and new simulation design methodologies, ii) stent system design regarding the investigated clinical complications of SM and LSD, and iii) multi-objective optimisation of stent dilation strategy in patient-specific vessels via surrogate and structural modelling.

# Chapter 1

# INTRODUCTION

CAD, caused by atherosclerosis is one of the main causes of death in the Western World. The coronary arteries that surround the heart carry oxygenated blood and other nutrients to the heart muscle for normal function. CAD occurs when the inner walls of the coronary arteries thicken due to a buildup of cholesterol, fatty deposits, calcium, and other elements. This substance is known as plaque. As plaque develops, the vessel narrows, blood flow through the vessel is reduced and less oxygen and other nutrients reach the heart muscle. Obstruction of a coronary artery can result in a heart attack. This chapter provides a basic description of the anatomy and physiology of coronary arteries, the mechanisms behind the development of CAD, different treatments during recent decades and the PCI evolution. At the end, the investigated clinical problems of SM and LSD are introduced and illustrated via clinical studies and cartoon images to enable the reader to obtain a clear view of these complications.

## 1.1 Coronary arteries

The adult human heart, which has a mass of 250 to 350 $g$, has three main arteries: the RCA, the left anterior descending (LAD) and the circumflex (Cx) (Smith and Kampine 1990). The latter two represents the left coronary artery (LCA).

The RCA and LCA take their origin from the aorta at the base of the sinuses of Valsalva behind the cups of the aortic valve. Figure 1.1 illustrates how the RCA runs in the coronary sulcus along the diaphragmatic surface of the heart before descending toward the apex. It gives off branches to the right atrium, to the free wall of the right ventricle, and to a variable extent to the posterior third of the ventricular septum and posterior wall of the left ventricle. In about 70% of hearts, these latter structures receive most of their blood supply from the RCA (Robert 1981). In $50-60\%$ the first branch of the RCA is the small conus branch, that supplies the right ventricle outflow tract. In $20-30\%$ the conus branch arises directly from the aorta. In 60% a sinus node artery arises as second branch of the RCA, that runs posteriorly to the sinoatrial node node (in 40% it originates from the Cx) (Smithuis and Willems 2008).

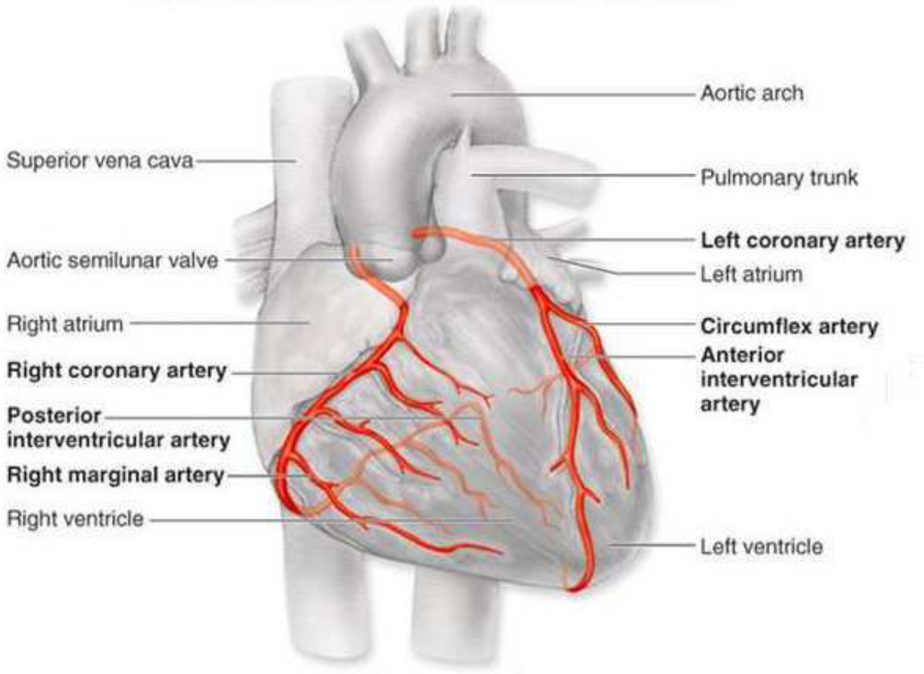

Figure 1.1: Coronary arteries (Medchrome 2012)

The LCA divides soon after it leaves the aorta and forms the left Cx artery and the LAD. It supplies the left atrium and the lateral wall of the left ventricle. In addition, it shares with the RCA the provision of blood to the posterior wall of the left ventricle. In about 10% of human hearts, the LCA becomes the dominant vessel and supplies all or nearly all of this part of the heart. The LAD continues as an extension of the main vessel before turning down in the interventricular groove toward the apex. It supplies the free wall of the left ventricle, the ventricular septum, and, to a limited extent, the anterior wall of the right ventricle (Rushmer 1976, Smithuis and Willems 2008).

## 1.2 Physiology of coronary arteries

In general, the arteries of the human body depending on the composition of the constituents, the relative diameter and the distance from the heart are divided into two types: elastic and muscular arteries (Mazumdar 1998). The macroscopic structure of elastic and muscular arterial walls is composed of three different layers (c.f. Figure 1.2). The innermost layer is the tunica *intima*. The middle layer is the tunica *media* and the outermost layer is the tunica *adventitia*. Elastic arteries have relatively larger diameter than muscular arteries, and are located close to the heart (for instance, the aorta, carotid, and illiac). In contrast, muscular arteries are located more peripherally (except in the case of coronary arteries) (Holzapfel et al. 2000). Elastic arteries experience the greatest pressure as the heart forces blood into them. Moreover, in elastic arteries the elastin is abundant in tunica *media*, enabling them to expand to larger diameters. On the other hand, in muscular arteries, the tunica *media* comprises mainly of smooth muscle cells. This enables them to actively constrict and relax.

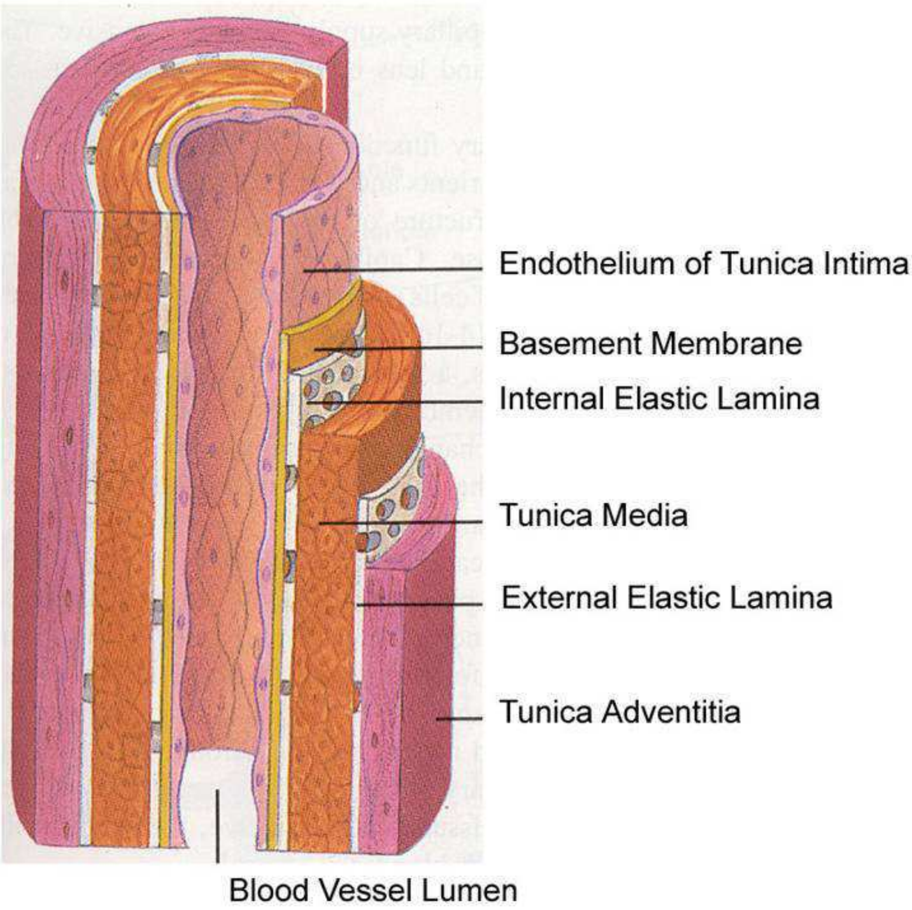

Figure 1.2: Schematic view of medium muscular artery (Fishbein 2014)

*Intima*, the innermost layer, consists of endothelium, the basement membrane, the sub-endothelial layer and the internal elastic lamina. The internal elastic lamina joins the media and a thin layer of epithelial cells that lie adjacent to the blood. This provides a smooth and slippery inner surface for the vessel and as long as it remains intact, and prevents blood clotting (Mazumdar 1998). *Media*, the middle layer, is constituted principally of smooth muscle cells, elastin, and collagen fibres, supplying mechanical strength to the intimal layer. As stated above, according to the relative composition of these cells and fibers, arteries are classified either as elastic or muscular. *Adventitia*, the outermost layer, is constituted of connective tissue, fibroblasts, collagen and elastic fibers (Bernard and Alain 1999), forming a protective layer around the vessel. The walls of elastic arteries are generally thinner than those of smaller muscular arteries and the walls of some large thick-walled arteries have their own blood supply (Mazumdar 1998).

## 1.3 Atherosclerosis

Atherosclerosis is an arterial inflammatory disease which is widespread in the Western world and shows increasing prevalence in developing nations (Townsend et al. 2012). It is the most common cardiovascular cause of death and commonly resulting in serious events, including heart attack (myocardial infraction), angina and stroke. Atherosclerosis is primarily an intimal disease of large and medium-sized elastic and muscular arteries (e.g. coronary arteries, carotid arteries) and is characterised by the presence of lipid in the intima accompanied by inflammation, fibrosis and by hyperplasia of the endothelium (Figure 1.3). In most cases the disease extends into the arterial lumen obstructing the physiologic rheology of blood flow. The latter process, is referred to as stenosis (rightmost panel of Figure 1.3).

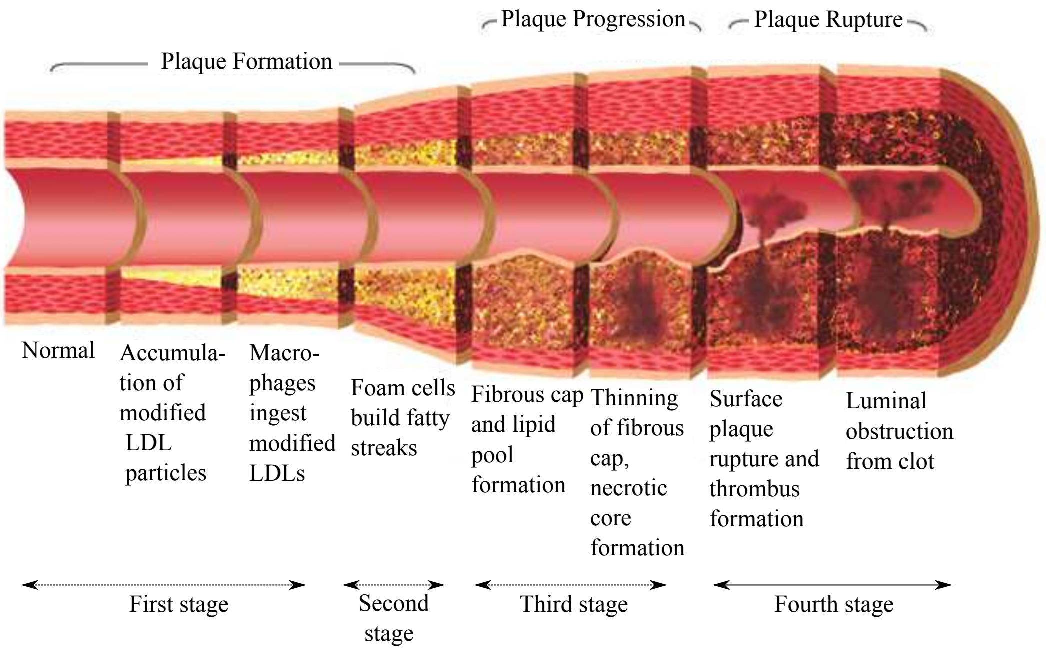

Figure 1.3: Progression of atherosclerosis in coronary arteries: from normal artery (left panel) to severe atherosclerosis (rightmost panel) (Berkeley-Heart-Lab 2015)

The inflammatory nature of atherosclerosis plays the main role in CAD pathogenesis. Its immune mechanisms interact with metabolic risk factors to initiate, propagate, and activate lesions in the arterial tree. Inflammatory immune activation initiates acute coronary syndromes in which the circulating levels of inflammatory markers are used to evaluate the clinical outcome of the condition. In Hansson (2005), it is stated that there are several different inflammatory markers, with different biologic activities contributing to CAD. This fact makes the clarification and contribution of these molecules in CAD very difficult to define. However, in this section, the basic idea of atherosclerosis development and its role in CAD pathogenesis is outlined.

Possible causes of endothelial dysfunction which leads to atherosclerosis include elevated and modified low density lipoprotein (LDL), genetic alterations, age and male sex, hypertension, cigarrete smoking, diabetes mellitus, elevated plasma homocysteine concentrations, infectious microorganisms such as herpesviruses or *Chlamydia pneumoniae*, physical inactivity, adiposity and race (Ross 1999). Additionally, there have been outlined some other more specific risk factors, including reduced high density lipoprotein cholesterol, excess oxidative stress, elevated C-reactive protein and elevated homocystine level (Nichols and O'Rourke 2005).

Three circulatory components (monocytes, platelets, T-lymphocytes) together with two arterial wall cells (endothelial, smooth muscle cells) and LDL-cholesterol interact in multiple ways in generating atherosclerotic lesions (Osterud and Bjorklid 2003). In Ross (1999), atherosclerosis development is defined by four stages: (i) endothelial dysfunction, (ii) fatty-streak formation, (iii) formation of an advanced and complicated lesion, and (iv) unstable fibrous plaque. As shown in Figure 1.3, the earliest event in atherosclerosis takes place in the endothelium where its permeability to lipoproteins and other plasma constituents changes. The second stage, fatty-streak formation, include smooth-muscle migration, foam cell formation (which is mediated by oxidized LDL, T-cell activation, and the adherence and migration of leukocytes because of the permeability of the endothelium. As fatty streaks progress to intermediate and advanced lesions, they tend to form a fibrous cap that walls off the lesion from the lumen. Finally, the last stage involves the rupture of the fibrous cap or ulceration of the fibrous plaque which can lead to thrombosis and usually occurs at sites of thinning of the fibrous cap that covers advanced lesions.

Mechanical factors such as flow oscillations and low shear stress in parallel to increased risk factors as hypertension, smoking, increased cholesterol levels in a specific arterial site can potentially lead to atherogenesis. Atherogenesis develops into atherothrombosis which results in vascular remodelling. This vascular remodelling is either outward or inward. Here, only inward remodelling or "stenosis" is being considered.

## 1.4 Interventional Cardiology

Depending on the stage of disease, coronary artery stenosis is treated by CABG, PTCA, or PCI. A brief description of each procedure is provided in the following sections.

### 1.4.1 Coronary artery by-pass grafting

The first CABG operation was successfully performed by Robert H. Goetz at the Albert Einstein College of Medicine-Bronx Municipal Hospital Center (Konstantinov 2000). CABG operations are performed in order to relieve angina and heart disease in cases where medical therapy has failed and PCI and PTCA are not appropriate. CABG is ideal for patients with multiple narrowings in different coronary artery branches, a phenomenon mostly observed in patients with diabetes. With bypass surgery the flow over a stenosed segment is restored by the transplantation of a healthy blood vessel, as shown in Figure 1.4. Bypass surgery, improves blood supply to the heart muscle directly by the aorta, going around the obstruction of the vessels. In almost all cases, CABG access is achieved by a sternotomy. Operation of CABG has been shown to improve long-term survival of patients with severe and multiple blockages. Such operations take about three to four hours to complete.

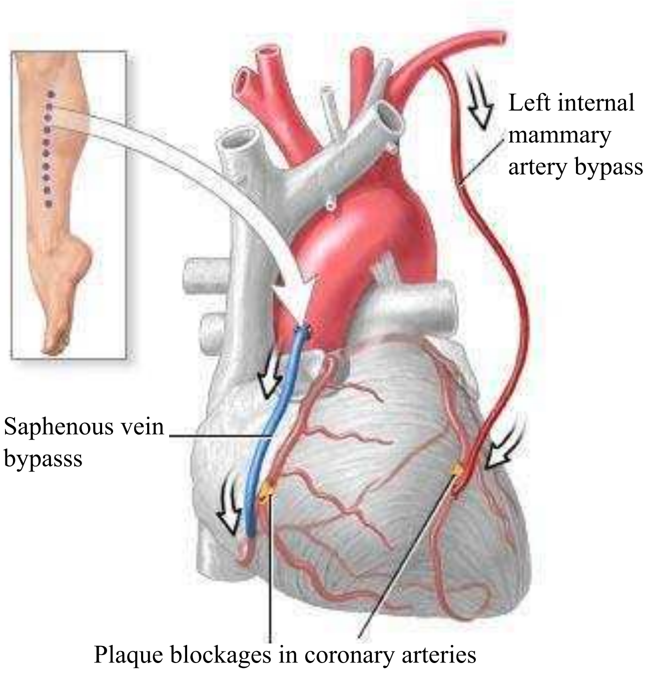

Figure 1.4: Coronary artery bypass grafting (Sharecare 2012)

### 1.4.2 Percutaneous transluminal coronary angioplasty

PTCA (c.f. Figure 1.5) is a minimally invasive technique in which a balloon is inserted in a diseased site through a catheter and then is dilated to unblock the narrowing of the vessel in order to recover physiological blood flow to the heart muscle. The very first PTCA was performed in 1977 at St. Mary's Hospital in San Francisco by Richard and Timothy (1995). Since then, the use of this technique has been developed and used broadly throughout those years. Relative to bypass surgery, minimal invasive techniques such as PTCA can reduce the risks, costs, hospital accommodation and patient recovery time always depending on the severity of the disease. In brief, the catheter-balloon system is driven through a guide wire to the plaque site inserted usually from the radial, femoral and in some cases from the brachial artery. The procedure is visualised by fluoroscopic means enabling the desired position of the balloon into the blockage. Although improved blood flow can be restored, PTCA has been shown to result in vessel recoil, arterial dissections and high restenosis rates (Schwartz et al. 1990). Vessel recoil is noticed when the balloon is removed due to the energy released by the elastic fibers in the vessel wall. Dissections have been reported in regions where shear forces from dilation are high (Redwood et al. 2010). Restenosis occurs in long term basis (1-12 months), and three of its major contributors have been identified as the vessel recoil, plaque persistence and dissections. Restenosis occurs in about one out of three successful angioplasty operations (Hamon et al. 1995). Nowadays, PTCA has been replaced by PCI where a stent is implanted in order to avoid the elastic recoil of the artery.

### 1.4.3 Percutaneous coronary intervention and stents

PCI or "stenting" is the most mildly invasive procedure undertaken in order to unblock narrowings or blockages in diseased coronary arteries. This operation has now become the main method of treating coronary occlusions. It involves the intra-vascular insertion (typically, through the groin or the femoral artery) and deployment of a stent on a balloon-catheter-guidewire system (c.f. Figure 1.5). Before "stenting", CA is undertaken to estimate how many vessels have been affected, and subsequently, the degree of the blockage. In cases where the physician is not able to evaluate the condition and make a decision on how the case will be treated, IVUS can be used. IVUS is usually used pre-operationally and in cases of uncertain stent apposition, it can be performed post-operationally to evaluate potential suboptimal stent delivery and assist in further procedural planing.

The characteristic element of PCI is the so-called stent. Stents are small cylindrically metal mesh shape devices that scaffold the artery walls and restore the physiologic

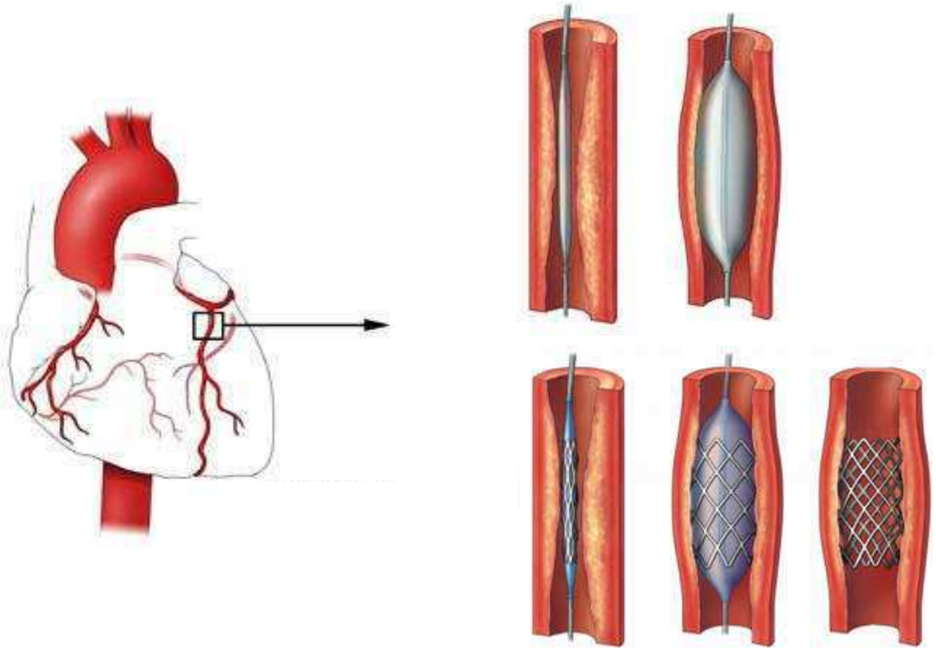

Figure 1.5: Schematic diagrams of PTCA (upper panel) and PCI (lower panel) (NMA 2008)

blood flow through vessels. In PCI, a stent system consists of a stent that has been crimped on the outer surface of a balloon which in turn is attached at the end of a catheter shaft, Figure 1.5. When the system is placed at the correct position then, with a specific pressure, the balloon is inflated to expand the stent to a diameter which for most stent systems is in proportion to the dilation pressure. The balloon then is deflated and removed leaving the stent in place permanently (c.f. Figure 1.5). Within several weeks, the artery wall heals around the stent.

In general, stents can be classified as BMS, DES, and bioabsorbable stents. BMS consist of a metallic platform. On the other hand, DES consist of a metallic alloy serving as the system's substrate and a drug coating which is normally bounded to the substrate with a polymer. Bioabsorbable stents are made from biodegradable materials, and they can be coated with drug such as Poly-L-lactic-acid or without drug as magnesium or iron alloys. Stents are also categorised according to their expansion mechanism, geometrical shape, materials, and manufacturing process. Concerning their expansion mechanism, stents can be divided into two main categories, that of self-expanding stents and balloon expanded stents (c.f. Figure 1.6). Self-expanding stents are manufactured mainly from Nickel-Titanium or Nitinol, a material that can undergo large deformations and recover back to its manufactured shape. Their implantation process involves a restraining catheter shaft which, when removed, the stent expands to the required diameter. Balloon expanded stents are those that undergo large plastic deformations. Initially, nearly all balloon expandable stents were made of 316L stainless steel. However, most of the contemporary devices are made of cobalt-chromium (CoCr) alloys to allow relatively thinner struts without downgrading the radial stiffness of the stent. Recently, platinum-chromium (PtCr) alloy has been used to manufacture more radiopaque devices (O'Brien et al. 2010). The majority of stents implanted in PCI are balloon expandable and crimped on folded balloons to obtain low crossing profiles for increased deliverability. In Konig et al. (2002), a self-expanding stent and a balloon expandable stent were compared and it was shown that, depending on the expansion mechanism, NIH and late stent expansion results differ. Specifically, the neo-intima formation was significantly higher in self-expanding segments (4.23 +/- 2.07 vs. 2.22 +/- 2.22 mm) resulted by the exaggerated stent expansion in the medial segment.

Secondly, in terms of geometrical design, stents can be classified into the following classes: coil designs, modular open-cell designs, and multi-cell closed-cell designs. As far as the process of stent manufacture is concerned, stents can be divided into wound coils, woven mesh designs, and laser cut designs. More information on stent characterisation can be found in Lally et al. (2006) and Butany et al. (2005).

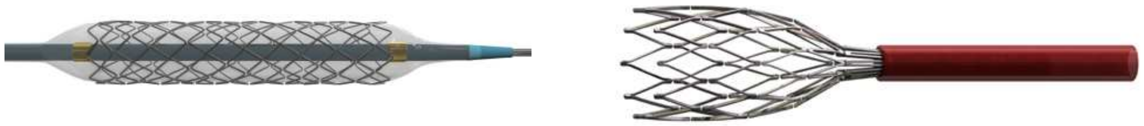

(a) Balloon expandable stent system (Medtronic-Inc 2014)

(b) Self expanding stent system (Blockwise-Engineering 2015)

Figure 1.6: Expansion Mechanisms

The vessel response to stent implantation can be characterised as a wound healing process and consists of four stages: thrombosis, inflammation, cellular proliferation and vessel remodeling (Edelman and Rogers 1998). Excessive cellular proliferation results in NIH, a remodelling process that occurs due to changes in the biomechanical environment to which the intervened vessels adapts (Keller et al. 2014, Timmins et al. 2011). In particular, studies have revealed that there is a strong correlation between the stent induced biomechanical environment and the NIH formation (Keller et al. 2014, Li et al. 2002, Moore and Berry 2002, Rachev et al. 2000, Timmins et al. 2011). In a recent IVUS study (Hoffmann et al. 2001) a six-month post-stenting follow up in 131 patients was conducted in order to examine the impact of the stent design on NIH and ISR. The outcomes showed that NIH and as a result ISR depend on stent design, surface material, and vessel damage related to the implantation procedure (Hoffmann et al. 2002, Rogers and Edelman 1995). Collectively, *in-vivo* (Hoffmann et al. 2001, Kastrati et al. 2001, Keller et al. 2014, Li et al. 2002, Timmins et al. 2011) and *in-silico*

(Berry et al. 2002, Conway et al. 2012, Keller et al. 2014, Lally et al. 2005, Martin and Boyle 2015, Timmins et al. 2011) data reveal that stents systems that result in minimal biomechanical vessel state alteration to the homeostatic, will have greater long-term success. Moreover, alloys with enhanced material properties have led to increasingly thinner struts and, hence, greater possibility to SM (Mortier et al. 2011a).

Although stents reduce restenosis rates compared to PTCA, ISR remains a drawback when BMS are implanted in patients with CAD (Kastrati et al. 2001, Serruys et al. 2006). In response to NIH and ISR, manufacturers have been producing DES from the early 2000s. DES can reduce ISR and subsequently, repeated revascularisation by delivering an anti-proliferative and anti-inflammatory drug exactly at the site of vessel injury (Serruys et al. 2006). DES have a drug coating, often sirolimus or placlitaxel which inhibits potential NIH formation by preventing the progression of smooth muscle cell proliferation which is the main cellular process in ISR (Lally et al. 2006). The drug is released by most DES within 30 days and involves the use of a polymer matrix. Although DES have shown to behave better in terms of ISR, those devices are correlated with allergic reactions, SM, and inflammation leading to early and late ST (Joner et al. 2006). In an IVUS study (Takebayashi et al. 2004) it was found that ISR pathogenesis after sirolimus stents can be partially related to the non-uniform strut distribution.

Ideally, a stent should have enhanced radial stiffness, great flexibility and at the same time minimise arterial injury, elute uniform drug distribution and minimise hemodynamic alteration. The radial stiffness provides a solid substrate to the vessel and minimises the vessel recoil. The flexibility enables the stent to be advanced to complex regions characterised by tortuous and long geometry containing diffuse, non-focal plaques. A stent should minimise arterial injury and hemodynamic alteration and maximise the drug distribution to eliminate ISR.

## 1.5 PCI evolution, SM and LSD

In the early days of PCI, stainless steel alloys were used as the stent platform for BMS differing in the manufacture process, stent cell geometry, and strut dimensions. Over the years, researchers have focused on different areas of stent development in order to improve both clinical outcomes and physicians convenience. As a result, simultaneously to stent development, PCI as a whole procedure has been improved considerably.

Nowadays, physicians prefer to implant longer stents. As a result, longer and more challenging (in terms of both vessel geometry and decease) segments can be accessed. Therefore, the current engineering design trends in PCI are characterised by longer, thinner, and more flexible stent platforms which can be implanted into the most challenging diseased vessel segments.

Engineers face a lot of difficulties when trying to optimise the stent design. By altering one stent parameter other stent characteristics can be affected resulting in unwanted clinical outcomes. For instance, while thinner struts and in general a lower profile can lead to good results in terms of ISR, such alteration could downgrade the radial strength. Likewise, reducing the number of connectors between the circumferential rings and increasing the area between the struts, the risk of ISR can be reduced significantly, although, this has been shown to affect the longitudinal stent strength. This is a reason why a current design trend concerns the way connectors are distributed along the longitudinal stent length. For instance, longitudinal stent integrity is a new concern about stent performance in interventional cardiology and occurring most times as a result of SM.

Late ST has been proven clinically to be linked to SM (Cook et al. 2007, Ozaki et al. 2010). When a stent is malapposed (see left panel of Figure 1.7), an event observed primarily in eccentric plaques and developed mainly on the disease-free side of vessel wall (Redwood et al. 2010), additional practices need to be carried out such as balloon post-dilation and/or another stent implantation. These methods, requiring additional manoeuvrings by the physician, can result in stent distortion. This unwanted event occurs more frequently at the proximal edge of the stent resulting in longitudinal compression and/or elongation stresses. These stresses are usually imposed by balloon and/or IVUS guide catheters, multiple balloon post-dilations, aggressive guide catheter manipulations, bifurcation stent techniques, and rotational atherectomy (Hanratty and Walsh 2011). In Figure 1.8, a cartoon image demonstrates the event of proximal stent edge deformation by the contact of a dilation catheter with the malapposed struts. An IVUS image is also attached to demonstrate how the clinical problem can be diagnosed.

## 1.6 Clinical studies reporting SM and LSD

*Stent malapposition*

In Shah et al. (2002), 206 patients who were implanted with BMS, were studied after the first 6 ± 3 month post-operative period and in nine (4.4%) of them, late malapposition was found. In this study, SM was defined as the separation of at least one stent strut from the arterial wall (intima) and by observing a speckling behind the malapposed strut. Interestingly, in 8 of 9 patients, the location of late SM was the stent edge. Four years later, Hong et al. (2006), investigated the incidence, predictors, and long term prognosis of stent malapposition after DES implantation in 557 patients. They found that SM occurs in 12% of cases after DES implantation, and one of the

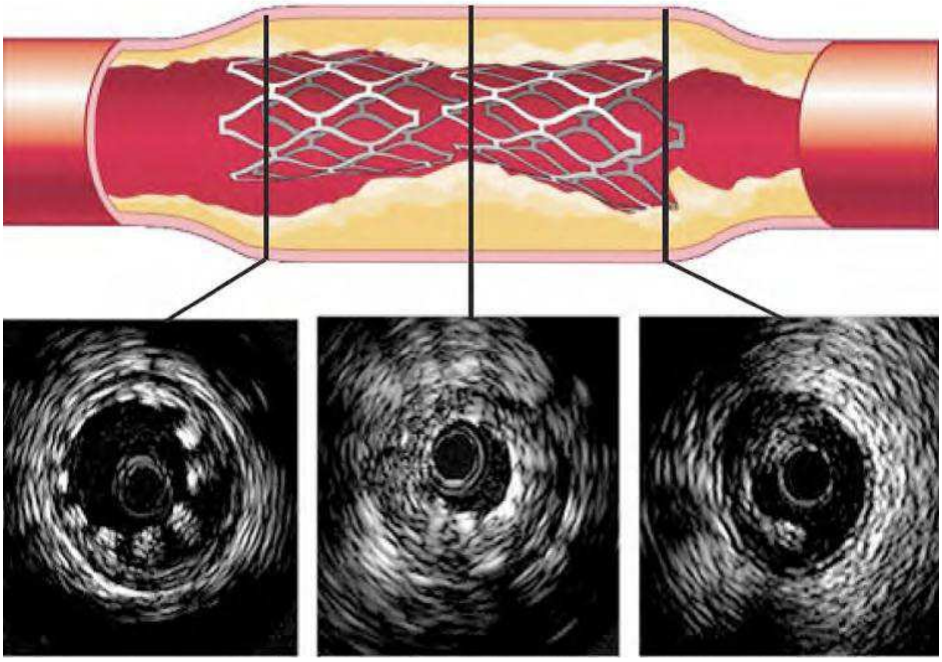

Figure 1.7: Stent-related complications after stent deployment. Reused from (Yoon and Hur 2012), with permission from Korean Association of Internal Medicine.

predictors was the total stent length.

In Cook et al. (2007), 13 patients with late ST ($> 1 year$), after DES implantation underwent IVUS, and their results were compared with a control group of patients with no late ST within a period of more than two years after DES implantation. The comparative study showed that late ST occurred in patients with longer lesions, longer stents, more stents, and stent overlap. SM was more frequent-77% versus 12%-in patients with late ST compared with controls.

Using IVUS, van der Hoeven et al. (2008b) studied the incidence of acute SM and late SM after implanting sirolimus eluting stents and BMS in patients with heart attack. Acute SM occurred in 38% of sirolimus eluting stent patients and 33.8% of BMS patients while late SM occurred in 37.5% of sirolimus eluting stent patients and 12.5% of BMS patients. The predictors of acute SM were the reference diameter and the balloon pressure, while for late SM they were the diabetes, reference diameter and the maximum balloon pressure. The results show that acute SM is not dependent on the type of the stent in comparison to late SM where it seems to occur more frequently when a sirolimus eluting stent is implanted. Finally, Guo et al. (2010) studied the incidence and mechanics after paclitaxel-eluting and BMS implantation in 241 patients and found that post-intervention acute SM occurred in 34.3% in paclitaxel-eluting stents, and 40.3% in BMS. Late SM occurred in higher frequency for paclitaxel-eluting stents (46.8%) than BMS (30.8%).

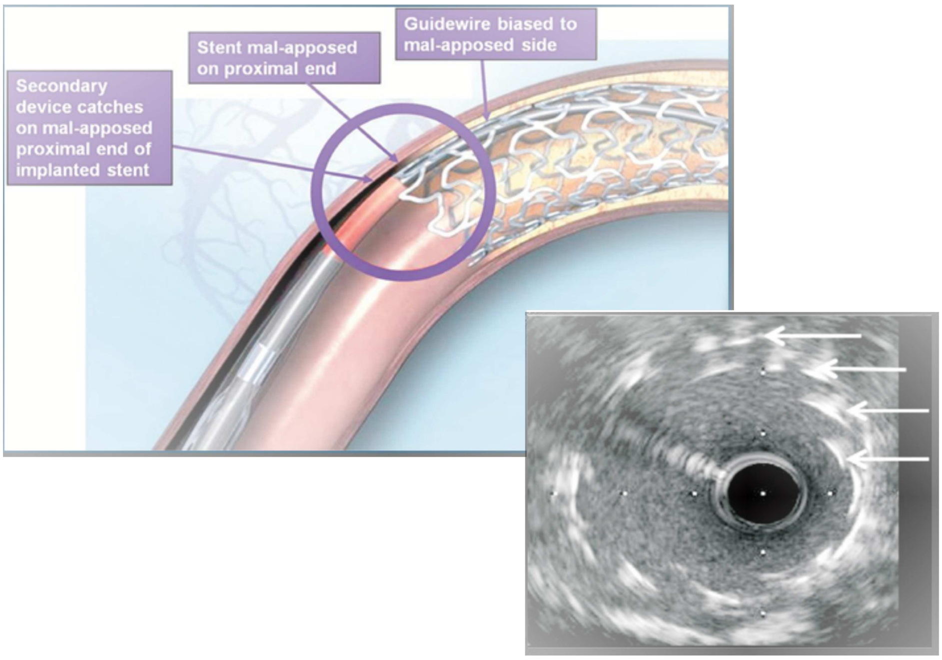

Figure 1.8: Longitudianl stent deformation as a result of contact interaction between balloon catheter tip and malapposed struts (Boston-Scientific 2011). The IVUS image on the bottom right panel depicts clearly the clinical complication (strut protrusion in the vessel lumen)

*Longitudinal Stent Deformation*

Thirteen real cases where stent deformation occurred as a result of SM have been reported in three recent studies (Hanratty and Walsh 2011, Robinson et al. 2011, Williams et al. 2012). Eleven cases concerned proximal stent crush, only one distal crush, and one both distal and proximal. Eight cases were caused by guide catheter, guide catheter extension, or proximal embolic protection catheter, and five cases were caused by the contact between post-dilation balloons and proximal malapposed stent struts. Five different stent platforms were involved in those cases with an average length of $30.7mm$. Longitudinal deformation was identified by angiography in all cases except one case where distorted struts were identified by IVUS (Hanratty and Walsh 2011). This is due to the increased radio-opacity of the implanted stents (in last generation stents, alloys with increased atomic number -Z- are used so as to be easily visible by angiographic means). Most cases (seven out of twelve) involved a stent platform with very thin struts ($81\mu m$) and open cell design, characteristics that may result in device deformations (Promus Element stent, Boston Scientific, MA, USA., c.f. section 4.2.1). Decreasing strut thickness and increasing the area which is surrounded by struts (open cell stent), improves deliverability, flexibility, and conformability. However, even though the radial strength is maintained, the longitudinal integrity may not be efficient to resist compression and/or elongation stresses. The authors believe that those kind of deformations have more potential to occur either during vein graft interventions (after CABG operation) where the vessel wall does not provide a good substrate for deployed stents or when the proximal and distal stent struts are malapposed. Therefore, attention should be given when the interventional cardiologist feels resistance during catheter withdrawals or post-dilation balloon catheter insertion. As a consequence, longitudinal deformation must be identified as soon as possible in order to avoid undesired results potentially leading to ST.

It is observed that LSD was addressed for the first time in 2004 and Hanratty and Walsh (2011) were not the first to state this complication. Mamas and Williams (2012), searched the FDA MAUDE database (from 2004 to 2011) in order to investigate cases that resulted in such complications and investigate further its mechanistic reasons. A total of 57 unique cases of longitudinal deformation were found (first in 2004), 90% reported from 2010 to 2011. LSD were experienced with six different platforms. LSD occurred due to the attempt of passing or withdrawing of secondary devices as undeployed post-dilation balloons, IVUS catheters, undeployed stents or protection devices through a previously deployed stent. LSD was shown to be connected with mortality results in eight cases. In most cases, the treatment involved the use of a second stent or balloon post-dilation. Two cases could not be treated because it was impossible to withdraw the distorted devices, and so, CABG was performed to revascularise the vessel. In general, adverse clinical outcomes including emergent cardiac surgery and acute and sub-acute ST occurred in eight cases. All 57 cases were experienced in long lesions with highly calcified and tortuous geometry, representing challenging disease.

## 1.7 Experimental studies investigating SM & LSD

*Stent malapposition*

Mortier et al. (2011b) investigated SM of two contemporary stent devices in two idealised coronary bifurcations. Rapid prototyping techniques were used to build the silicone models in which the two investigated devices were implanted. Two stent samples of each stent were deployed at room temperature in the silicone bifurcation models which were submerged in a “Ringer’s lactate solution”. Then, optical coherence tomography (OCT) was used to measure and identify malapposed struts. OCT was performed pre-stenting, post-stenting and after post-dilating the proximal main vessel. The results showed different average values of SM between the stents and, for both platforms, increased malapposition occurred in the proximal part of the stent. For

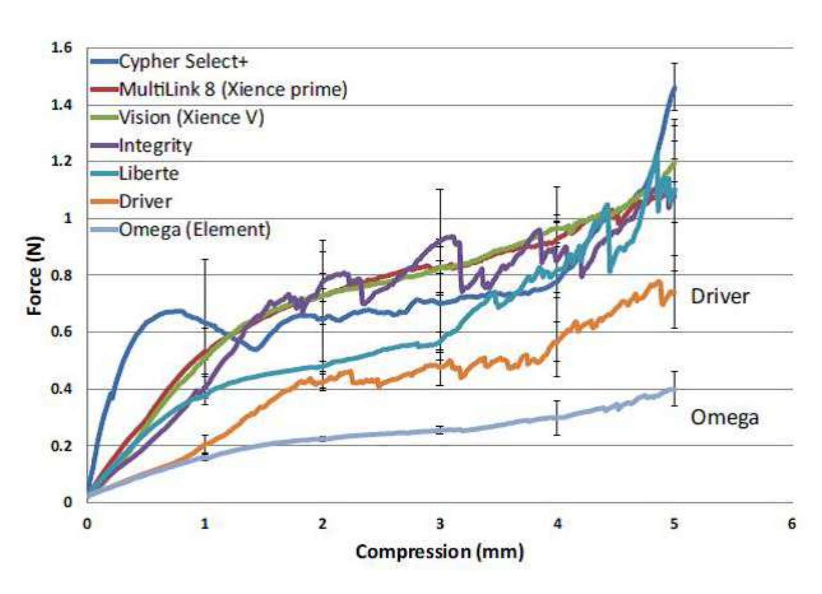

(a) Stent shortening (millimeters) against force (Newtons) for 3 examples of the 7 stent designs. Compression graphs are not smooth but are complicated because of strut collision and over-ride

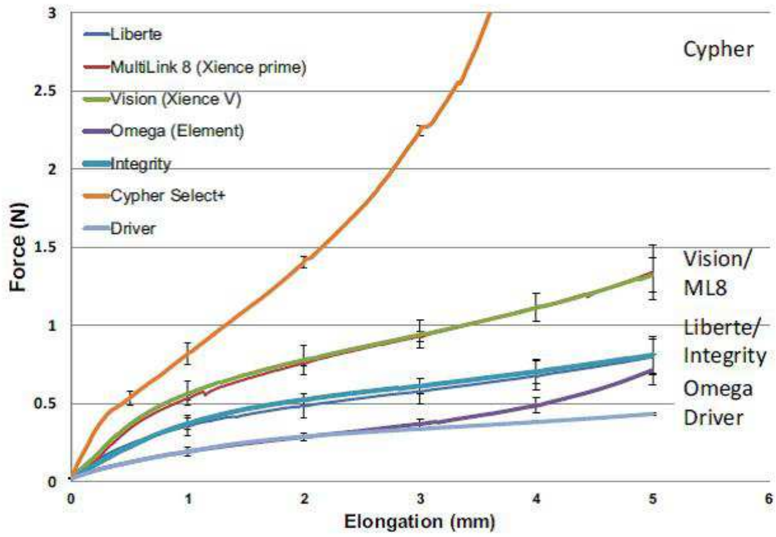

(b) The most easily deformed stents were the Omega and Driver. The force in Newtons to elongate stents by 1 $mm$ was least for the Omega ($0.19 \pm 0.01$ $N$) and Driver ($0.20 \pm 0.03$ $mm$, $p = NS$). That to elongate Liberte ($0.36 \pm 0.07$ $N$) was not different from the Integrity ($0.37 \pm 0.04$ $N$) but significantly more than for the Driver ($p = 0.023$). Force to elongate the MultiLink 8 ($0.54 \pm 0.02$ $N$) by 1 $mm$ was not different from the Vision ($0.56 \pm 0.08$ $N$), but significantly more than for Integrity ($p = 0.02$) and significantly less than the Cypher Select ($0.8 \pm 0.08$ $N$, $p < 0.001$). For elongation of 5 $mm$, the force required did not differ between Driver ($0.43 \pm 0.01$ N), Omega ($0.72 \pm 0.01$ $N$), Liberte ($0.80 \pm 0.1$ $N$), Integrity ($0.81 \pm 0.11$ $N$), Vision ($1.32 \pm 0.11$ $N$), and Multilink 8 ($1.34 \pm 0.12$ $N$). However, the force for the Cypher Select ($5.7 \pm 3.46$ $N$) was significantly more that for the other stents (p values ranged between 0.015 and 0.006).

Figure 1.9: Experimental results on longitudinal integrity of contemporary stent platforms. Images reused from Ormiston et al. (2011), with permission from Elsevier.

both stents, the extent of malapposition was significantly decreased after post-dilating the proximal vessel with a second balloon. Interestingly, the authors constructed computational models in correspondence with the experimental ones to compare the results from both methods. They highlighted the fact that the computational models can predict equivalent values of malapposition and, more importantly, malapposed struts can be visualised in full model dimensionality.

*Longitudinal Stent Deformation*

Two recent experimental studies (Ormiston et al. 2011, Prabhu et al. 2012) shed light on the increasingly recognised clinical problem of LSD arising from malapposed stent struts. In particular, the longitudinal integrity of the latest generation stent platforms that were examined in those two studies seems to correlate with the number of the connectors between the circumferential rings of each device. The device with two connectors between two sequential circumferential rings (Omega/Promus Element in Figure 1.9a, 1.9b), has a poor behaviour, always in terms of longitudinal integrity and, in general, it is connected with possible stent distortion. In contrast, devices with more than two connectors demonstrate lower longitudinal deformation. Moreover, it is assumed that in addition to the number of connectors, an important role is played by the angulation of connectors according to the long axis of the platform. Connectors with perfect alignment to the stent longitudinal axis seem to provide integrity to the device in order to resist compression and elongation stresses (e.g Multilink 8, and Vision Xience V on Figure 1.9a, 1.9b). Noteworthy, in Ormiston et al. (2011), the test experiments suggested that device deformations are often accompanied by protrusion of struts into the lumen and, as a result, this event complicates the passage of any secondary device (e.g post-dilation balloon) through the deployed stent.

## 1.8 Summary

An introduction to coronary artery disease, its PCI treatment procedures and further complications has been provided. As discussed, poor procedural outcomes leading to suboptimal minimum lumen area (MLA) often include SM that can lead to ST. ISR is a more complex multi-factorial problem that has been lessened with second generation DES. However, the endothelialisation is compromised by DES increasing the likelihood of ST. Moreover, biomechanical factors affecting the disease localisation and growth along with factors influencing the post-stenting outcome were reported and discussed. It was shown that investigating the structural factors resulting in unwanted clinical events is of importance for both device and procedure optimisation.

Following SM and LSD description, clinical studies reporting these complications were presented and elaborated. It can be noted that in most cases, SM and stent deformations occurred in anatomies with challenging disease (tortuous, long, and non-focal disease). This can be explained by the fact that in such segments, the diseased regions are not easily accessible, therefore, additional manoeuvrings from the interventional cardiologist have to be conducted to treat the site effectively. New generation stents have been designed in a way to provide high flexibility and deliverability in order to be implanted in such complex vessel lesions and cover the whole length of the disease. As a result, these devices can easily result in SM and experience possible deformations leading to unwanted events and suboptimal stent delivery.

Interestingly, SM and LSD are typically diagnosed and visualised using IVUS (Hanratty and Walsh 2011, Redwood et al. 2010), CA (Hanratty and Walsh 2011, Robinson et al. 2011, Williams et al. 2012), and OCT (Mortier et al. 2011b). Although these imaging modalities have been considered as golden standards in guiding the PCI procedure, a more sophisticated tool is needed. This tool ideally could fuse information from contemporary imaging modalities and provide full 3D computer models to assist in the diagnosis, treatment and procedure planning.

# Chapter 2

# STENTS STRUCTURAL MODELING: A REVIEW

Modelling! During the last decade, computer modelling of PCI have become very popular due to advantages in terms of cost, high flexibility of changing problem parameters and visualisation. Firstly, the virtual models concerned the stent itself, in particular, the researchers developed structural models to investigate the expansion mechanics of stent in terms of deformations, stresses, recoil, and flexibility. However, with the increase of computer power and resources, nowadays, numerical simulations include the complex interactions of the stent with the dilation system and the coronary artery walls investigating the induced biomechanical environment of a vessel after stent deployment. In parallel, computational fluid mechanics (CFD) models have been developed to analyse the flow characteristics after stent implantation and its effect on the flow patterns in terms of wall shear stresses and recirculation zones (believed to be major contributors in the development of ISR). These models have also been used to investigate the drug elution characteristics of different coronary artery stent platforms. Recently, fluid-structure interaction (FSI) models have been developed to couple the principles of structural models to that of fluid models and investigate the interaction between these two types of phenomena. The capabilities of the above methods are hardly achievable by experimental or clinical studies. Therefore, such models are now required by official organisations (e.g. FDA) to approve the production of cardiovascular devices. In this chapter, since in the current work only structural models are concerned, a literature review of FEA studies is provided to describe the recent advances in this field and highlight areas of further research (especially with respect to patient-specific vessels with challenging disease).

## 2.1 FEA modelling

A finite element model is characterised by the definition of its geometry, material properties, loads, and boundary conditions. Three distinct steps can be categorised, pre-processing, analysis, and post-processing. In pre-processing, the continuum is divided into a finite number of discrete regions (elements), connected by nodes. The partitioning of the continuum, the definition of loads and boundary conditions are initially attained by a graphical user interface.

In the analysis step, the data defined by the pre-processing step are used as input to automated finite element codes which construct and solve a system of linear or non-linear equations. The general equation of a static analysis problem is

$$\mathbf{K}\mathbf{u} = \mathbf{f} \tag{2.1.1}$$

where $\mathbf{u}$ and $\mathbf{f}$ are the nodal displacement vector and external forces vector, respectively, and $\mathbf{K}$ is a stiffness matrix dependent on the given problem (e.g. linear or non-linear analysis). An approximate solution is obtained by the collection of the behaviours of the individual elements. Each element behaviour is characterised in turn by its nodal behaviour. Usually, in static problems, the nodal displacements are obtained at the first stage, and then the stresses can be described by means of the material constitutive law. For smooth non-linear static, quasi-static and dynamic problems an implicit iterative solver can be used. Usually the iterative process for static or quasi-static regards a Newton-Raphson method where the initial displacement value is approximated to iterate until convergence criteria are fully met. Eq. 2.1.1 can be rearranged as (Harewood and McHugh 2007)

$$G(\mathbf{u}^{t+\Delta t}) = \mathbf{K}\mathbf{u}^{t+\Delta t} - \mathbf{f} = 0 \tag{2.1.2}$$

where $G$ is the out of balance residual force. Then, the Newton-Raphson method for the $i^{th}$ iteration and for the $t + \Delta t$ increment expressed as

$$\mathbf{u}_{i+1}^{t+\Delta t} = \mathbf{u}_i^{t+\Delta t} - \left[\frac{\partial G(\mathbf{u}_i^{t+\Delta t})}{\partial \mathbf{u}}\right]^{-1} G(\mathbf{u}_i^{t+\Delta t}) \tag{2.1.3}$$

and after rearranging

$$\delta\mathbf{u}_{i+1} = \mathbf{u}_{i+1}^{t+\Delta t} - \mathbf{u}_i^{t+\Delta t} = -\left[\frac{\partial G(\mathbf{u}_i^{t+\Delta t})}{\partial \mathbf{u}}\right]^{-1} G(\mathbf{u}_i^{t+\Delta t}) \tag{2.1.4}$$

with

$$\mathbf{R}(\mathbf{u}_i^{t+\Delta t})^{-1} = \left[\frac{\partial G(\mathbf{u}_i^{t+\Delta t})}{\partial \mathbf{u}}\right]^{-1} \tag{2.1.5}$$

where $\mathbf{R}$ is the tangent stiffness matrix or the Jacobian matrix of the governing equations. Therefore, the equation to be solved for each iteration for change in incremental displacements is

$$\mathbf{R}(\mathbf{u}_i^{t+\Delta t})\delta\mathbf{u}_{i+1} = -G(\mathbf{u}_i^{t+\Delta t}) \tag{2.1.6}$$

In Eq. 2.1.6, $\mathbf{R}$ and $G$ must be solved for each iteration. In order to solve for $\delta\mathbf{u}_{i+1}$, the tangent stiffness matrix must be inverted. This is why the implicit method can be computationally expensive. However, through the iteration process a large increment size can be used while maintaining accuracy of the results. After the $i^{th}$ iteration, $\delta\mathbf{u}_{i+1}$ is calculated which in turn results in a better approximation of the solution, $\mathbf{u}_{i+1}^{t+\Delta t}$ (Eq. 2.1.4). This becomes the current approximation of the solution in the subsequent iterative step $i+1$.

In the case of dynamic problems, the nodal displacements with their second time derivatives (accelerations), are considered. Then, the nodal forces are obtained by integrating the stresses over the volume of elements (weak formulation) satisfying the balance of momentum. Very often, in stent modelling, a non-linear analysis explicit solver is used. The general equation of a viscously damped multi-degree of freedom dynamical system is

$$\mathbf{M}\ddot{\mathbf{u}} + \mathbf{C}\dot{\mathbf{u}} + \mathbf{K}\mathbf{u} = \mathbf{f}(t) \tag{2.1.7}$$

where $\mathbf{M}$ is the global mass matrix, $\mathbf{C}$ is the global damping matrix, $\mathbf{f}(t)$ is the time-dependant load vector, and $\mathbf{u}$, $\dot{\mathbf{u}}$, and $\ddot{\mathbf{u}}$ are the nodal displacement, velocity and acceleration vectors, respectively. In an explicit analysis, the load is applied in different time increments and the solution is obtained by a central difference rule which is implemented to integrate the equations of motion through time. Thus, the solution marches through time. If Eq. 2.1.7 is rearranged as

$$\ddot{\mathbf{u}}_i = \mathbf{M}^{-1}[\mathbf{f}(t)_i - \mathbf{C}\dot{\mathbf{u}}_{i-\frac{1}{2}} - \mathbf{K}\mathbf{u}_i] \tag{2.1.8}$$

then, the central differentiation scheme (half-step implementation) can be expressed as

$$\dot{\mathbf{u}}_{i+\frac{1}{2}} = \dot{\mathbf{u}}_{i-\frac{1}{2}} + \frac{\Delta t_{i+1} + \Delta t_i}{2}\ddot{\mathbf{u}}_i \tag{2.1.9}$$

$$\mathbf{u}_{i+1} = \mathbf{u}_i + \Delta t_{i+1}\dot{\mathbf{u}}_{i+\frac{1}{2}} \tag{2.1.10}$$

The local truncation error of this method is $\mathcal{O}(\Delta t^2)$. In this method, a very important consideration is that the time increment $\Delta t$ should be smaller than a critical value,

$\Delta t_{critical}$, which is limited by the highest frequency of the discrete system $\omega_{max}$, where

$$\Delta t \leq \Delta t_{critical} \leq \frac{2}{\omega_{max}} \tag{2.1.11}$$

If the time step is larger than the critical increment, then, the solution is unstable, resulting in round off error by the integration scheme and making the dynamic response calculation questionable.

To model structural problems which are considered as quasi-static (e.g. metal forming, stent deployment), both implicit and explicit solvers can be used. However, depending on the complexity of each problem, careful consideration should be made regarding the solver choice. As seen above, both solvers provide the solution response incrementally. However, where with the implicit method the solution of finite element equations is obtained by iterating within an increment $\Delta t$ (until a convergence criterion is fully met), in the explicit solver, the solution is advanced from the previous to the next increment without iterating, by formulating the finite element equations in dynamic state. Therefore, the implicit method is effective when the analysis can be performed in relatively few time increments. Moreover, while for the explicit solver the cost of one increment is approximately proportional to the model size, for the implicit approach the cost increases more steeply. Different studies have been published comparing implicit to explicit approach and discussing the advantages and disadvantages of each method (Choi et al. 2002, Harewood and McHugh 2007, Sun et al. 2000). These studies concerned the performance of each solver in metal forming processes and in crystal plasticity. It has been shown that the implicit solver performs well for simpler loading conditions and smaller models. When the loading conditions involve contact and large deformations, then, explicit solver is more efficient. Further, due to the emergence of highly vectorised finite element software, the explicit methods have become more attractive. The latter was evident from the Harewood and McHugh (2007) study, in which the explicit method demonstrated constantly high levels of parallelisation efficiency compared to the implicit method using multiple processors. Contemporary sophisticated FEA software (e.g. ABAQUS, Simulia, Dassault Systemes, Waltham, MA, USA) can automatically decompose the model into a number of topological domains and assign each domain to a processor. Thus, the problem is solved in different blocks (domains) by multiple processors operating simultaneously.

Finally, the post-processing step consists of the visualisation of the results which usually are represented in graphical form. A typical commercially available FEA post-processor has the ability to display the deformed shape of the continuum with the displacement, stress, strain and force field in colour contours or vectors.

## 2.2 Balloon expandable stent FEA studies

The reliability of a numerical study on PCI by using FEA depends on the virtual representation of the stent system (its geometry), and the definition of its material properties. Moreover, the structural representation of the "stenotic" vessel in which the stent is implanted and that of the plaque should be defined with material constitutive models that describe realistic material behaviour.

The basic principles of stent FEA models are well described by Perry et al. (2002). It is stated that a stent FEA model should be subjected to loads and boundary conditions that represent the actual loading of the stent. In other words, the real life loading on an implanted stent has to be simulated incorporating the crimping, recoil, positioning and, finally, the deployment process in which the final recoil should be considered as well. Ideally, the cyclic real life loading of the stent should also be simulated to investigate its fatigue.

In the following sections, some of the most pioneering studies with high impact on stent modelling are described and elaborated. To the author's judgement, these studies (when published) represented the state-of-the-art and their outcomes provided significant contributions for further research. Furthermore, some of the presented methodologies that have been used in these studies were adopted in the current doctoral work to model stenting procedures in patient-specific vessels with challenging disease.

### 2.2.1 Structural studies of stent free expansion

*Studies without considering the presence of a balloon model*

The first structural study was carried out by Dumoulin and Cochelin (2000), investigating the free expansion along with the long-term mechanical behaviour of a tubular peripheral P308 (Palmaz, 1998) stainless steel stent. In particular, the authors presented a methodology to evaluate and characterise numerically different mechanical properties of the investigated stent. These properties concerned the expansion behaviour (shortening percentage of the device during deployment), the elastic recoil (degrees of radial and longitudinal recoil after deployment), the resistance to deformation under external pressure (the pressure beyond which the stent can experience buckling) and at last, the life endurance of the device (fatigue analysis). An internal uniform radial pressure was used to expand the different size stents. The authors validated their method against experimental data provided by the manufacturers demonstrating very satisfactory correspondence (discrepancy $< 0.5\%$ on the lengths of the stent after deployment). Therefore, the authors demonstrated that certain mechanical properties of balloon expandable stents can be investigated by FEA studies.

One year later, Etave et al. (2001) introduced a finite element methodology to compare two stents, one tubular Palmaz-Schatz stent (Johnson & Johnson, NJ, USA) and one coil Freedom stent (Global Therapeutics Inc., CO, USA). The choice for the investigated stents was justified by the argument that in that period these devices were demonstrating the most extreme mechanical properties of the respective types. Moreover, except for the stent type comparison, each stent was modified along the geometric characteristic which, according to authors, had the greatest impact on the stent's mechanical properties. The modelling strategy consisted of three different phases (free expansion of the stent, stent compression, and stent conformability) resulting in seven different mechanical metrics (pressure necessary for stent deployment, elastic recoil, stent resistance to stent compression, etc.). Stent free deployment was driven by controlled incremental radial displacements (0.5 $mm$). It was demonstrated that the coil stent had an overall better mechanical performance with respect to the investigated figures of merit. The numerical findings were not validated against experimental results. Interestingly, at the end of the paper, the authors state that the presented numerical results contributed to the design and manufacture of a new stent, underlying the finite element potential to stent evolution.

The next pioneering study was published by Migliavacca et al. (2002). The authors presented an analytical study which implemented FEA to optimise the design of coronary artery stents. The objectives of this study were i) to understand the effects of different geometrical stent parameters (metal-to-artery ratio[1], strut length, free metal strut length) on the device mechanical performance (radial and longitudinal recoil, foreshortening and dogboning), ii) to compare the response of different actual stent models when loaded by internal pressure and iii) propose suggestions of optimised shape and performance. The results demonstrated that i) the metal-to-artery ratio is directly proportional to dogboning and inversely proportional to radial and longitudinal recoil and ii) the thickness influences foreshortening, longitudinal recoil and dogboning. The stent virtual model expansion was carried out by uniform internal pressure and for different metal-to-artery ratios the functional relationship between the applied pressure and the deployment diameter was reported. This was the first study which reported numerical stent compliance charts. Such compliance charts are used to calibrate/validate the virtual balloon-stent models simulated in the current doctoral work (see section 5.2.3).

Two years later, McGarry et al. (2004) published the first computational study considering the micro-mechanical behaviour of a balloon expandable coronary artery

---

[1] metal-to-stent ratio is the fraction between the metallic circumferential length of a single stent strut and the circumferential length of the gap between two sequential stent struts.

stent (NIR stent, Medicon/Boston Scientific, MA, USA). A two-dimensional unit cell model extracted from the stent was expanded by prescribed boundary conditions. The authors implemented a crystal plasticity theory to describe the plastic deformation of the stent material and they made numerical comparisons of stent performance (stent recoil, foreshortening, fatigue) against results obtained by the classical continuum plasticity theory, the $J2$ flow theory. In particular, the study consisted of three steps: i) deployment of the stent, ii) recoil of the stent, and iii) cyclic loading of the stent. The former step was carried out by applying localised and concentrated loads to the outer ends of the struts representing the load applied by a pressure cardiac pulse. The results obtained by the cardiac cycle load were used as the basis of an elementary fatigue analysis and were presented by Goodman diagrams[2]. Interestingly, the Goodman diagrams demonstrated higher factors of safety for the crystal plasticity comparing to that of the $J2$ flow theory postulating that this could inhibit any stent "over-design" that might result from simpler constitute descriptions. The outcomes indicate that when investigating stent performance (especially for stent recoil) by computational models, the micro-mechanical behaviour of stent material should be taken into account, and by implementing the crystal plasticity theory, more accurate results can be obtained. Moreover, the study highlighted the existence of non-uniform and localised stress and strain fields in the material micro-structure described by the crystal plasticity theory as opposed to the uniform and smooth fields predicted by the continuum approach. Nevertheless, the authors state that in order to improve the presented models, three-dimensional modelling should be performed to enhance the accuracy of predicting the stent recoil, foreshortening and fatigue.

The next novel study was presented by Migliavacca et al. (2005). They published a structural computer model investigating the mechanical behaviour of the "Cordis BX Velocity" stent (Johnson & Johnson, NJ, USA). The stent was modelled in its complete 3D geometry and the deployment to its nominal diameter was carried out by applying a uniform internal pressure on the inner surface of the stent. After the expansion, different quantities were calculated to evaluate its mechanical performance. Noteworthy, this study was the first to compare the virtual stent compliance with corresponding experimental and manufacturer's test data (c.f. Figure 2.1). Via this validation test, it was shown that there is a big difference between the numerical transient stent expansion behaviour with that occurring in reality. The authors stated that this discrepancy was due to the absence of a balloon model suggesting that accurate prediction of transient stent deployment should include a model of the balloon. Thus, in the current doctoral work, sophisticated folded balloons were used to deploy the stents at certain

---

[2] Goodman diagrams are commonly used to quantify the combined effect of mean and alternating stresses on the fatigue life of the material.

diameters after calibrating/validating their numerical compliance charts against the respective commercial ones (see section 5.2.3).

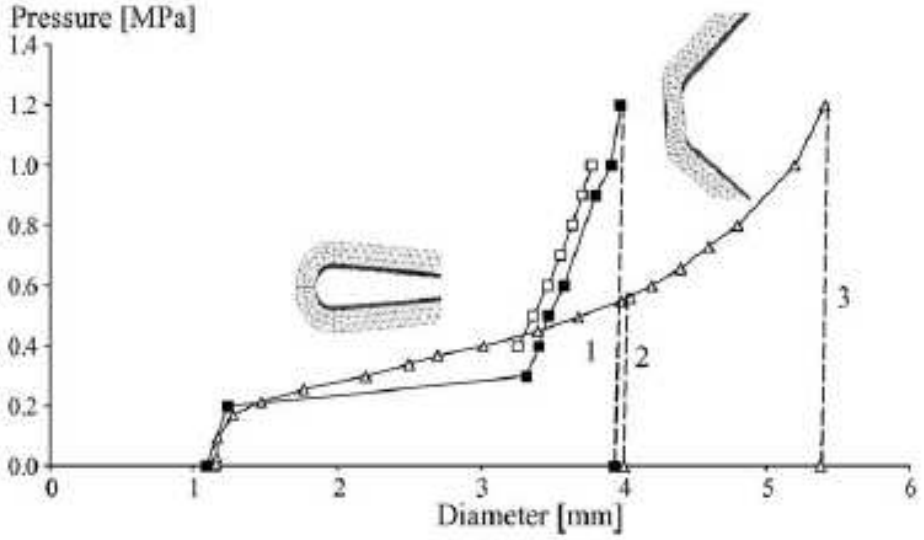

Figure 2.1: Results from the FEM analysis (empty triangle), from the experimental test (solid squares) and data provided by the company (empty squares). The dotted lines represent the unload history at different values of inflating pressures both for the FEM and the experimental analyses. It should be noted that at 0.5 MPa the diameter reached by the stent is similar in the FEM simulation and the experimental test. Image reused from Migliavacca et al. (2005), with permission from Elsevier.

*Studies considering the presence of a balloon model*

In Wang et al. (2006), six different balloon stent models were simulated to eliminate the dog-boning effect during stent expansion. The balloon was modelled as an idealised cylinder characterised by a linear isotropic behaviour. The simulation outcomes demonstrated that the dog-boning effect was highly correlated to the proximal and distal stent strut width and the length of the balloon. In particular, it was shown that dog-boning can be reduced by increasing the stiffness of the stent both proximally and distally (e.g. increase the strut width) and decreasing the length of the balloon. The authors provided qualitatively validation of the virtual transient stent expansions by recording the corresponding actual deployment process and measuring the outer stent diameter along with the stent length at different inflation pressures.

The work by De Beule et al. (2008) represented a ground-breaking development in modelling realistic balloon-stent deployments. In this study, the transient expansion behaviour of the balloon expandable Cypher stent (Johnson & Johnson, NJ, USA) was investigated by three different loading scenarios. The different approaches to deploy the stent to its nominal diameter were by applying: i) an internal uniform pressure to the inner surface of the stent, ii) controlled radial displacements to the nodes of a deformable cylindrical surface and iii) a uniform pressure to the inner surface of a tri-folded sophisticated balloon. In Figure 2.2, the initial, intermediate and final state of the transient stent expansion by the three different approaches are illustrated. As can be observed, only the third sophisticated approach can capture the actual transient deployment behaviour of the investigated platform. Thus, it was further confirmed that when investigating the transient behaviour of balloon expandable stents, realistic balloon models should be included in the expansion simulations. The limitation of the sophisticated model was the fact that the tapered ends of the balloon were not taken into account. Instead, appropriate boundary conditions were applied to represent the axial stretching imposed by the balloon ends. The results extracted by the numerical simulations for the tri-folded balloon were validated against an actual compliance chart provided by the manufacturers. It was noted that the predicted numerical results accomplished an extremely close agreement with the actual pressure-diameter measurements. Since then, this validation methodology has been used in many recent studies (Conway et al. 2012, Foin et al. 2012, Grogan et al. 2011, 2013, Martin and Boyle 2013, Mortier et al. 2014, Pant et al. 2011) to model realistic balloon models. Following this, the same group (Mortier et al. 2008), presented another study investigating the effects of different balloon parameters on the transient stent expansion behaviour. It was demonstrated that changing the folding configuration, balloon length and the relative position of the stent on the catheter have a considerable influence on the uniformity, symmetry and transient behaviour of stent deployment. In this doctoral thesis, a similar balloon technology (see section 4.3) was developed to construct parameterised multi-folded balloon models for realistic stenting simulation in vessels with challenging anatomy.

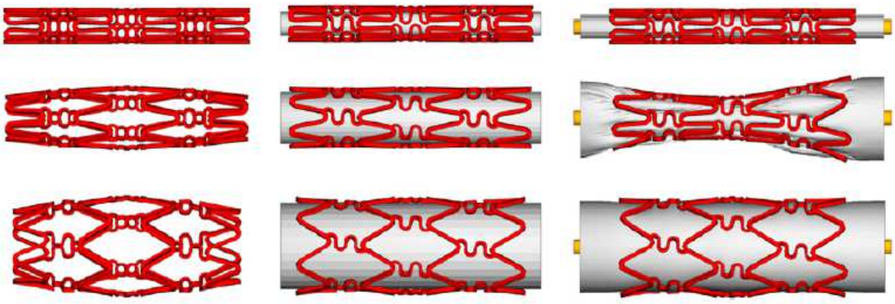

Figure 2.2: Stent deployment patterns resulting from (i) "no balloon" scenario (left), (ii) "cylindrical balloon" scenario (middle) and (iii) "trifolded balloon" scenario (right) prior to (top), during (centre) and after (bottom) the transient expansion. Image reused from De Beule et al. (2008), with permission from Elsevier.

In the same period, Gervaso et al. (2008), carried out a very similar study investigating the effects from different simulation strategies for balloon-expandable stents. The half part of this study concerned the free expansion of a small segment of the Cordis Bx-Velocity stent (Johnson & Johnson, NJ, USA) by an internal pressure, a deformable surface and an idealised-folded balloon system. From the numerical simulations it was demonstrated that all three means of virtual deployment result in the same outcomes regarding the foreshortening, maximum von Mises stresses and stress localisation regions. However, the final deformed stent shape was not the same between the different scenarios. Only the idealised-folded balloon captured the effect of dog-boning.

A year later, Kiousis et al. (2009) presented a novel study investigating the transient inflation behaviour of interventional peripheral balloon and stent models by experimental and numerical analyses. The authors were supplied with six stent systems from three stent manufacturers (two systems from each) for mechanical *in vitro* bench testing. After studying the transient compliance behaviour with respect to pressure and diameter diagrams, they developed a computational model to mimic the actual inflation behaviour of stent systems. Moreover, mechanical properties of the investigated stents (dog-boning, foreshortening, radial recoil) were recorded experimentally in different phases of deployment. In the numerical model, the stent was described by an elasto-plastic material model whereas the balloon was characterised by a cylindrically orthotropic material. The numerical results showed an overall satisfactory agreement with the experimental results (c.f. Figure 2.3). However, it was noted that some phases of the transient stent expansion could not be captured (see c and d regions in Figure 2.3).

Martin and Boyle (2013) carried out a study looking at the effects of three different balloon configurations on the deployment of a stent. This study consisted of two parts. One part was carried out without the vessel presence and the other with an idealised vessel. Both the stent free-deployment (c.f. Figure 2.4) and its deployment within the vessel were investigated using: i) an idealised non-folded balloon, ii) an idealised-folded model and iii) a state-of-the-art folded model. As with the free expansion results, it was shown that balloon folding configuration has no impact on the final stent shape but does have a significant impact on the transient behaviour of a coronary artery stent during its expansion.

### 2.2.2 Structural studies of stent expansion in vessels

*Studies without considering the presence of a balloon model*

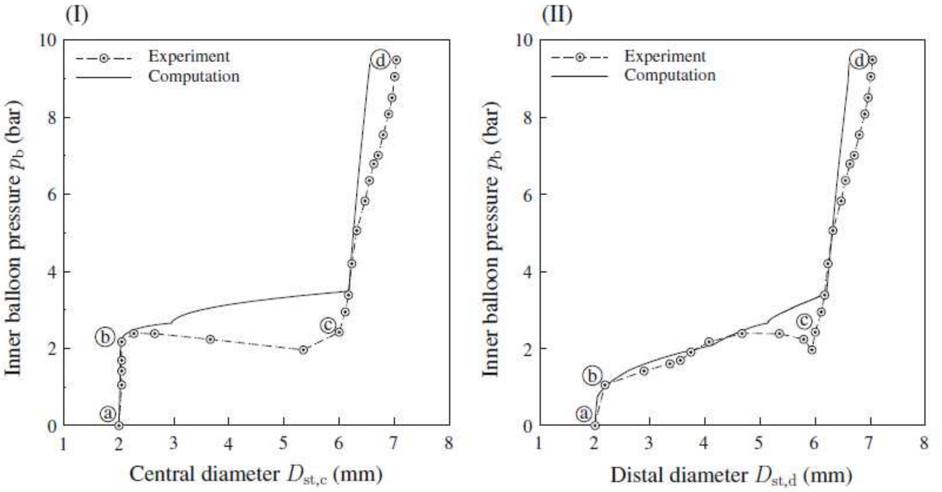

Figure 2.3: Comparison of the experimental and the numerical results for the dilation of the Bridge Assurant balloon-stent system; change of the inner balloon pressure $p_b$ vs. the central diameter $D_{st,c}$ (I), and the distal diameter $D_{st,d}$ (II). Overall, the numerical results (solid curves) are in satisfactory agreement with the experimental data. Image reused from Kiousis et al. (2009), with permission of Springer.

Auricchio et al. (2001), published the first pioneering study of a balloon-expandable stent implanted in an idealised stenotic artery. The mechanical behaviour of the slotted tube Palmaz-Schatz stent (Johnson & Johnson, NJ, USA) was studied both after free expansion and after its deployment in the idealised vessel. Then, a modified device was examined seeking to improve the uniform stent deployment. In addition, typical mechanical properties were assessed (elastic recoil, foreshortening, residual stenosis, etc.). It is noteworthy that for the baseline stent, elastic recoil, foreshortening and metal-to-artery surface ratio agreed with previously published experimental data. The constitutive behaviour of the idealised vessel was assumed to be hyperelastic isotropic described by a reduced polynomial strain energy function after validating the model against published experimental (*ex-vivo*) results.

A novel study regarding the parametric modelling of balloon expandable stents virtually implanted in patient-specific segments was presented by Holzapfel et al. (2005b). The stenotic arterial segment which was used in this study concerned an iliac artery comprising eight different arterial tissues. The constitutive model parameters of each layer were derived after *in-vitro* mechanical testing. Three stent models were parametrised and compared, i) the Multi-Link Tetra (Guidant, IN, USA), ii) NIROYAL-Elite stent (Boston-Scientific, MA, USA) and iii) InFlow-Gold-Flex stent (InFlow Dynamics, Munich, Germany). In this work, the authors presented the first computational framework to i) investigate the three-dimensional interaction between modern stent designs and patient-specific wall models by considering image data and

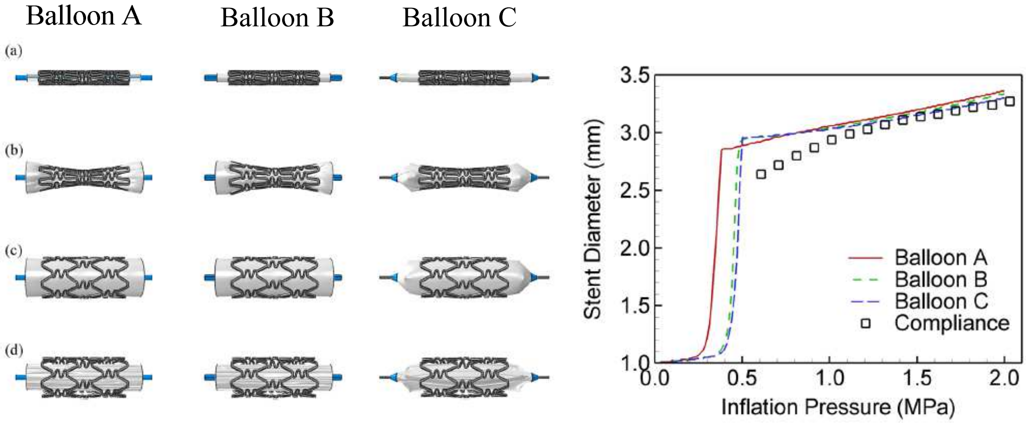

Figure 2.4: Stent transient expansion behaviour by balloon models with different folding configurations. Left panel, configuration of the stent (a) prior to loading, (b) during loading, (c) at maximum loading and (d) at unloading of (left) balloon A, (middle) balloon B and (right) balloon C during the free-deployment analyses. Right panel, pressure-diameter response of the stent during the free-deployment analyses compared with manufacturer's compliance data for the BX-Velocity stent. Images reused from Martin and Boyle (2013), with permission from John Wiley and Sons.

mechanical tests, ii) derive and use novel scalar indicators and quantify the mechanical performance of parametrised stent models, and iii) compare the effects of different parameters and identify optimal stent designs. To simplify the deployment process, the stents were deployed by applying a pressure load directly on the stent struts. It was demonstrated that scalar indicators can guide parametric studies towards optimal stent designs aiming to eliminate ISR rates. Where possible, the authors compared their findings against clinical studies to support their principal arguments that for a given lumen gain, an optimal stent design should result in a relatively low induced mechanical environment (regarding the wall circumferential stresses and lumen-strut contact pressure).

In the same period, Lally et al. (2005) conducted a structural study to compare two balloon expandable stents, the S7 platform (Medtronic, MN, USA) and the NIR platform (Boston Scientific, MA, USA). In their study, a straight idealised arterial segment with a stenosis in its middle part was used to record the wall stresses imposed by the stent-artery contact. The stents were modeled in their expanded state and the stent-artery contact was established in two steps: i) the vessel was inflated by an internal pressure and ii) the vessel internal pressure was reduced gradually to 13.3 $kPa$ (mean blood pressure of 100 $mmHg$). As a result, the vessel contracted around the stent which in turn behaved as a scaffold within the vessel. The authors reported higher stresses for the NIR stent and they referred to published clinical studies reporting that NIR stent results in higher restenosis rates. Thus, they claimed that such numerical models could predict the wall stresses imposed by different stent designs and correlate them to the potential of ISR.

The first patient-specific coronary artery computational model was presented by Gijsen et al. (2008). A RCA patient-specific segment was reconstructed by fusing CA and IVUS images. Within the virtual vessel, a stent with varying strut thickness was deployed by a uniform pressure applied to the inner surface of the device. The vessel wall stresses along with the von Mises stresses in the stent struts were recorded after each deployment. It was shown that the arterial damage was correlated with the thickness of the stent. In particular, by decreasing the strut thickness, the arterial damage was reduced while the von Mises stresses in the stent did not change significantly. It is noteworthy that the vessel reconstruction method presented by the authors, have been implemented in the current doctoral work to model stenting in three patient-specific cases with challenging disease (see Chapter 3).

Three years later, Timmins et al. (2011) published a work in which outcomes from *in vivo* analysis were correlated to results revealed from computational models of stenting. In particular, the authors' main objective was to provide a rationale for the observed clinical differences in restenosis rates between two different stent designs implanted in porcine arteries. Firstly, the arterial response of two different stent designs *in vivo* in terms of 28-day NIH formation were investigated. Then, respective computer models were generated to investigate numerically the mechanical environment induced by these stents. The results indicated that the stress values had a strong correlation with the observed data of neointimal thickening. As expected, the stent which induced higher stresses provoke a more aggressive pathobiological environment. Thus, in the current doctoral work, stent-systems which resulted in relatively higher stresses were evaluated as non-desirable when implanted in patient-specific challenging vessels (see Chapters 7 and 8).

### *Studies considering the presence of a balloon model*

The first structural study which considered the balloon interaction with the vessel wall was the work by Rogers et al. (1999). In this work, the authors presented a two-dimensional FEA model to study the balloon-vessel interaction during stent deployment. In particular, they investigated how different stent-strut geometries, balloon compliance and inflation pressure result in higher contact stresses between stent-struts, and subsequently, in vessel injury. It was shown that higher inflation pressures, wider stent-strut opening and more compliant balloons impose significantly higher stresses on the vessel wall, increasing the risk of ISR.

In the innovative study by Holzapfel et al. (2002), both balloon angioplasty and balloon expandable stenting were modelled in an eight-layer patient-specific iliac artery reconstructed by high resolution magnetic resonance imaging (hrMRI) *in vitro*. The balloon was modelled as a rigid cylinder with the justification that interventional dilation systems inflated at their nominal diameters behave as non-compliant tubular structures. The reconstructed arterial segment was modelled as in Holzapfel et al. (2005b). The authors demonstrated that via such studies, optimal procedural protocols could be defined for certain disease morphologies to minimise the medial overstretch and vessel injury while maximising the luminal gain. In Figure 2.5, a cross-section of the virtually intervened iliac segment is illustrated and the differences in circumferential stresses between the pre- and post-operation configurations are mapped to the different tissue components of the walls. As expected, the average stress is elevated as a result of the luminal gain. Thus, by investigating the impact of different interventional protocols in such models, optimal approaches could be derived to avoid re-narrowing of the lumen due to NIH formation. The latter was one of the motivations for the study presented in Chapter 8 where the optimum dilation strategy in a patient-specific artery was studied via mathematical multi-objective optimisation.

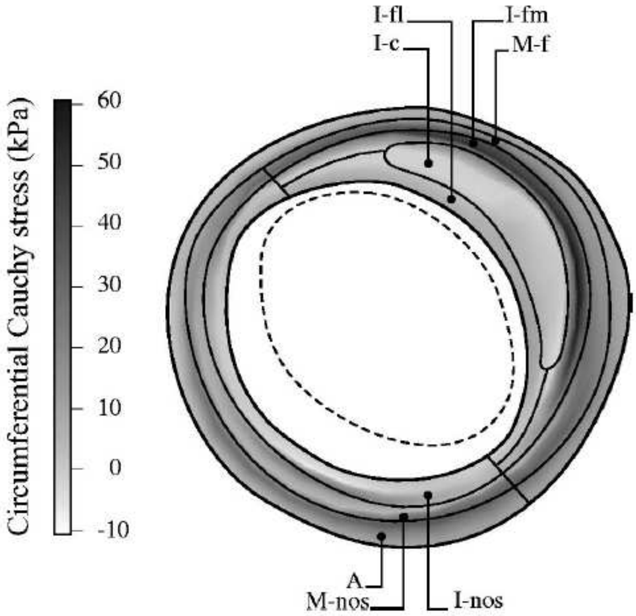

Figure 2.5: Differences in circumferential stresses (postangioplasty stresses minus preangioplasty stresses at 13.3 $kPa$) for a cross section ($z = 6.0\ mm$) after a full expansion of the angioplasty balloon with a diameter of $d = 10.0\ mm$. Stresses are plotted onto the postangioplasty configuration at 13.3 $kPa$. The shape before angioplasty at 13.3 $kPa$ is indicated by a dashed curve. Image reused from Holzapfel et al. (2002), with permission of Springer.

Later, the work by Kiousis et al. (2007) was published, investigating the interaction of vascular stents with a human atherosclerotic reconstructed iliac artery segment. The arterial segment used in the simulations was 1.4 *mm* long, an adequate length to host a whole circumferential stent ring. It consisted of four different layers, the intima, the media, the adventitia and the lipid pool. The authors also introduced initial tears to model dissection during the deployment. Four different simulations run in this study, one with balloon inflation only and three with stent deployment by a balloon model. In the last three simulations, the baseline model of the investigated stent along with two modified designs (one with thinner struts and one with fewer struts) were modelled. The performance of each model was evaluated quantitatively by three scalars representing contact pressure and circumferential wall stresses imposed on the vessel by each device deployment and the lumen gain after each intervention (the scalar index for the circumferential wall stresses quantification was adapted in the studies presented in Chapters 7 and 8). The outcomes showed a strong correlation between the lumen gain and the induced stress level. Thus, the most appropriate approach strongly depends on the optimisation criterion.

Mortier et al. (2010) presented a novel simulation strategy to model stent insertion and deployment in a patient-specific reconstructed coronary bifurcation. The authors presented a detailed simulation methodology to capture the whole PCI procedure, from stent crimping to stent deployment and catheter removal. They compared three different second generation DES designs, the Cypher stent (Johnson & Johnson, NJ, USA), the Endeavor stent (Medtronic, MN, USA) and the Taxus Liberte stent (Boston Scientific, MA, USA). For the stent deployment, sophisticated tri-folded balloon models were used, as proposed by Laroche et al. (2006). The virtual bench test predicted different circumferential wall stress distributions, especially, at the edges of the expanded platforms (c.f. Figure 2.6). Moreover, in order to improve the outcomes, the authors presented simulations of two modified models of the Cypher stent. One design had thinner struts and one had narrowed struts at both stent edges. The results from these simulations showed that especially for the proximal stented region, the stress peaks reduced considerably. Interestingly, in this doctoral work, their proposed detailed simulation strategy was compared with a new less expensive simulation method in which the stent system was geometrically translated to the reconstructed IVUS line (see Appendix C). It was shown that outcomes with respect to final stent deformation and, consequently, the resultant SM were in close agreement for both investigated methods. Hence, the second less expensive approach was implemented to model stenting in patient-specific challenging cases. This was very important for the multi-objective optimisation study presented in Chapter 8, in which numerous simulations were run to extract optimum stent expansion in a subject-specific RCA vessel.

In 2010, Gastaldi et al. (2010) presented a study investigating i) the effects of stent

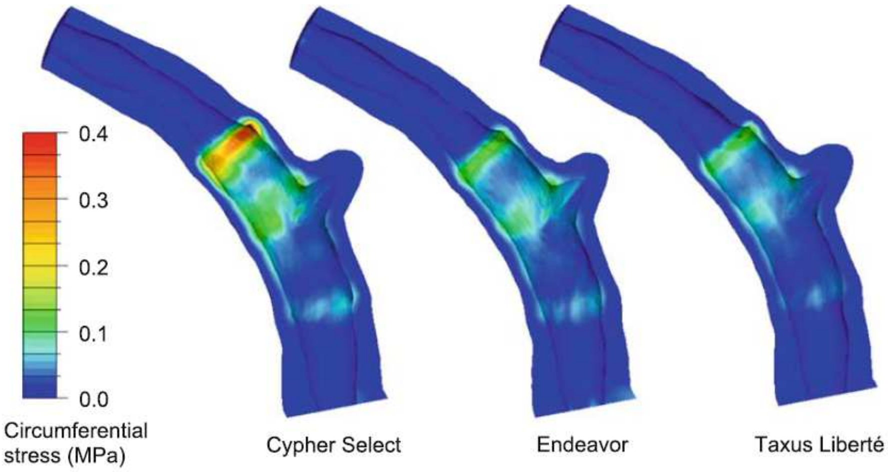

Figure 2.6: Comparison of the circumferential (Cauchy) stress distribution after implantation of the Cypher Select, the Endeavor and the Taxus Liberte stents, with maximal stresses of 0.38, 0.15, and 0.15 $MPa$ from left to right. Image reused from Mortier et al. (2010), with permission of Elsevier.

positioning on provisional bifurcation stenting, and ii) two different post-provisional stenting procedures, the final kissing balloon and the re-dilation of the main branch. The computer models comprised an idealised bifurcation, idealised folded balloon models and a vitual model of a Cordis BX Velocity stent (Johnson & Johnson, NJ, USA), see Figure 2.7. Noteworthy, the authors validated their results qualitatively against experimental results. The outcomes revealed significant differences between the investigated scenarios. Thus, they proposed that their model can be used for further numerical studies to allow stent designers to optimise devices or techniques in treating bifurcations. Subsequently, the same group (Morlacchi et al. 2011) implemented these structural models to create fluid domains to analyse further the induced biomechanical environment of different post-provisional bifurcation techniques.

A ground-breaking study in design optimisation of coronary artery stents was presented by Pant et al. (2011). In this study, advanced mathematical optimisation concepts were implemented to investigate the mechanical performance of a parameterised Cypher stent (Johnson & Johnson) implanted in a stenosed idealised vessel. A three variable geometry parameterisation of the investigated platform was used to explore the performance of each design in terms of six different figures of merit (representing the objective functions) extracted from structural and fluid dynamics simulations. For this multi-objective problem, GP models were constructed for each objective at four different stages: an initial design of experiment (DoE) followed by three update stages. The update points were defined after searching the surrogate models using a dedicated population genetic algorithm. The results demonstrated the existence of a

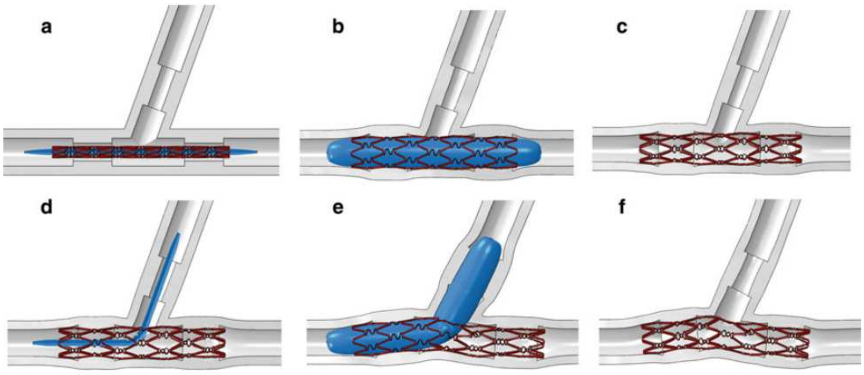

Figure 2.7: Provisional side-branch-stenting simulation steps. Initial position (a) balloon expansion (b) and recoil (c) of the system in the MB. Insertion of a balloon in the SB through a cell of the stent (d), balloon expansion (e) and elastic recoil of the system (f). Image reused from Gastaldi et al. (2010), with permission of Springer.

complex interplay between stent design and stent performance (always with respect to the investigated objective functions, see Fifure 2.8). Similar surrogate models and multi-objective optimisation techniques were implemented in the study presented in Chapter 8 to optimise the stent deployment in a patient-specific vessel with challenging disease.

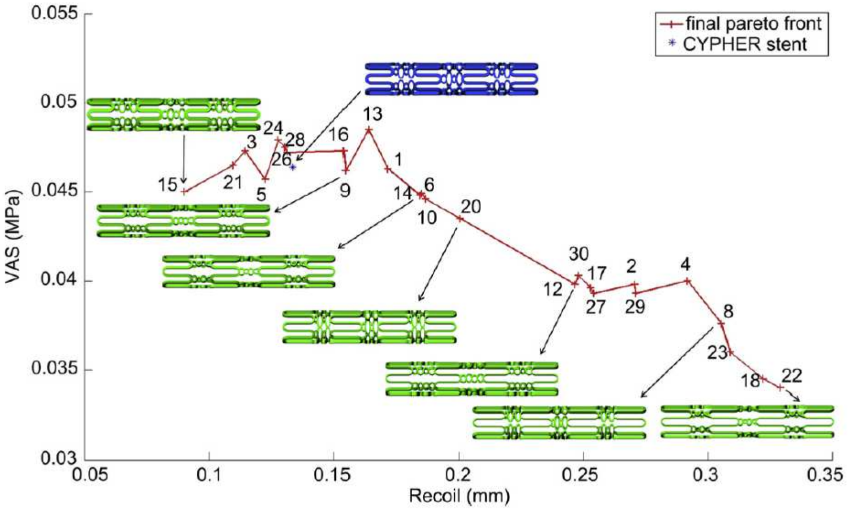

Figure 2.8: Final Pareto front (non-dominated solutions) slice showing the trade-off between volume average stress (VAS) and acute recoil (Recoil). Image reused from Pant et al. (2011), with permission from Elsevier.

Foin et al. (2012) presented sophisticated computer models to investigate post-provisional bifurcation stenting techniques. In this work, apart from numerical simulations, experimental testing was also carried out to investigate *in vitro* bifurcation procedures. After provisional stenting in idealised vessels, two different strategies were compared both computationally and experimentally. Firstly, a final kissing balloon strategy was modelled and, secondly, a more conservative approach was simulated in which a post dilation balloon was inflated only in the main branch to further expand regions of malapposed struts. The results demonstrated that the second approach resulted in better overall outcomes. Especially for the final kissing balloon scenario, the structural models demonstrated a much higher induced mechanical environment increasing the risk of vessel injury (c.f. Figure 2.9). The latter is very important especially in vessels with challenging disease, where if possible, complex stenting techniques should be avoided and PCI should be limited in a single-operational procedure (see Chapter 7).

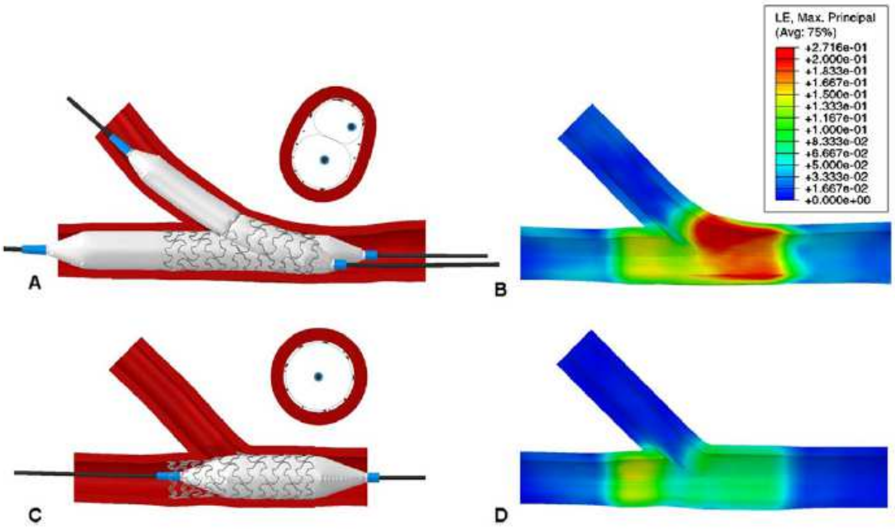

Figure 2.9: Simulation of post-dilation with kissing balloon (A) showing the resulting high strains proximal to the SB created by the 2 overlapping balloons simultaneously inflated (B). Sequential SB-MV post-dilation (C) results in the circular expansion of the stent and significantly more homogeneous strain distribution proximal to the SB (D). Image reused from Foin et al. (2012), with permission from Elsevier.

Recently, a state-of-the-art numerical study was published by Morlacchi et al. (2014) to investigate three different bifurcation stenting techniques. The authors used structural, fluid dynamics and drug elution analyses to compare the different stenting scenarios. The results from this virtual numerical study showed substantially different patterns of wall and stent deformations, shear stress and drug elution among the simulated techniques. Thus, such models can serve as a complementary tool to traditional *in vitro* approaches to study stenting procedures and guide engineers towards optimised devices and procedure protocols. In the same year, state-of-the-art computational structural models were published by Mortier et al. (2014) to: i) study the effects of stent design, and ii) compare two different kissing balloon inflation strategies in three different idealised bifurcation vessels. The authors demonstrated with clarity that the proposed modified final kissing balloon strategy reduced the elliptical stent deformation and optimised side branch access. Interestingly, the number of malapposed struts was not influenced by the kissing balloon strategy. As it will be shown in Chapter 7, SM can be eliminated by single-step procedural approaches in which novel varying diameter dilation systems are used to deploy the stent in a patient-specific challenging bifurcation segment.

### 2.2.3 Numerical Studies of Stent Malapposition

Mortier et al. (2011a), conducted a numerical study comparing six common coronary artery stents in terms of incomplete stent apposition and stent induced vessel wall stresses. In order to evaluate each platform concerning incomplete stent apposition, a criterion was used which was based on a threshold value of 10 μm representing the distance between the centre of the outer strut surface and the inner surface of the vessel wall. In Figure 2.10, the outcomes of this study concerning strut malapposition are illustrated. The red colour represents those areas with high strut malapposition, while the blue colour signifies struts perfectly apposed to the vessel walls. The device with two connectors showed the higher amount of SM (resulting in 43%) for wall-to-strut distance larger than 0.01 mm. Interestingly, the higher amount of malapposed struts were observed at the shoulders of the plaque (in healthy vessel wall surfaces), suggesting that segments with luminal variations (highly calcified, non-focal plaque) are more prone to incomplete strut apposition. In the same year, the same group publised a similar study investigating SM of two contemporary stents implanted in an idealised coronary bifurcation (Mortier et al. 2011b). The authors showed increased SM in the proximal end of the devices due to the diameter mismatch along the length of the vessel. Noteworthy, proximal malapposition was also evident after the computer simulations of stenting in patient-specific vessels with challenging disease, presented in Chapters 6, 7 and 8. Therefore, lessening the malapposed struts in the proximal end of stent device was one of the main objectives of the studies presented in 7 and 8.

## 2.3 Summary

In this chapter, a brief description of the fundamental principles governing the formulation of FEA stent modelling was carried out followed by a literature review that highlighted numerical studies of balloon expandable stents. The review progressed gradually from early structural studies to the most recent sophisticated numerical models.

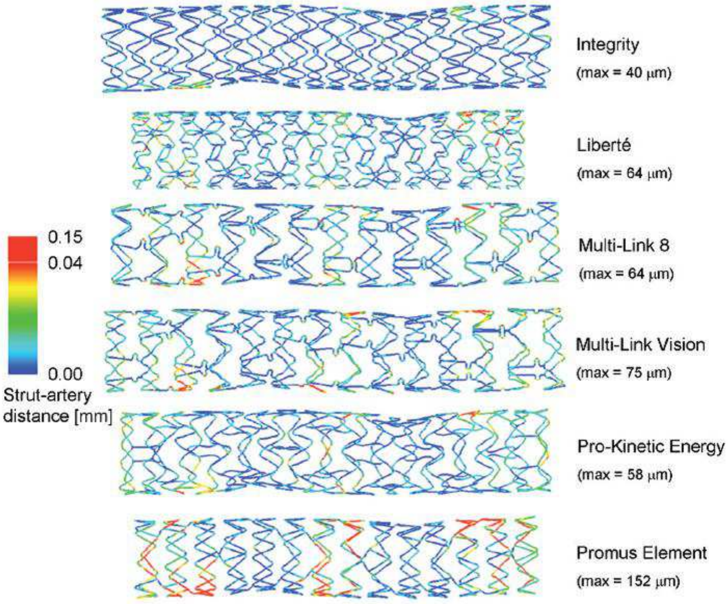

Figure 2.10: Contour plot of the strut apposition of the different stent designs. The plots show the distance between the centreline on the outer strut surface and the inner surface of the arterial wall. A nonlinear colour scale has been used, with red reflecting values between 0.04 and 0.15 *mm*, in order to obtain a better differentiation at lower values. Image reprinted from Mortier et al. (2011a), with permission from Europa Digital & Publishing.

According to the author's judgement, every computational study reported, represented state-of-the-art work in the period which was published. From each study, the methodology along with the most valuable results was outlined and, where appropriate, special references were provided with respect to the current thesis. In particular, the rationale was to outline (where possible) how a certain computational study contributed to the current doctoral work especially in the attempt to optimise stent implantation in patient-specific vessels with challenging disease. Moreover, the presented studies highlight the need for further computational research on a subject-specific basis with models directly derived from real clinical cases. As presented in the following chapters, the latter provides more realistic computational models when trying to eliminate certain clinical complications (e.g. SM and LSD).

Numerical studies can provide quantitative outcomes on the mechanical behaviour of stent platforms when implanted in very complicated geometries and they can give not only numerical outcomes as far as SM is concerned but they can provide 3D information in contrast to the two dimensional IVUS and OCT images. Stent-to-artery wall distance can be calculated and visualised over the complete stent length easily in contrast to common methods where IVUS cross section images can only measure and visualise the particular area. This method could be used to investigate and quantify not only stent performance but it can facilitate numerical studies of different procedural strategies. Prior to the current work, only two numerical studies (Mortier et al. 2011a,b) have been carried out investigating the impact of last generation stent platforms to SM. Furthermore, no computational study investigating the longitudinal integrity of coronary artery stents has been reported. Thus, this thesis has focused on sophisticated computational studies investigating the mechanical behaviour of contemporary coronary artery stent systems regarding SM and LSD in patient-specific vessels with challenging disease. Such numerical studies can shed light both on optimisation of stent design and the improvement of interventional procedures.

# Chapter 3

# 3D PATIENT-SPECIFIC VESSEL RECONSTRUCTION

Reconstructions! There has been much effort over the last decade to develop methods for the reconstruction of coronary arteries to be modelled in computational studies. Such reconstructions are difficult since these segments are small (2-4 *mm* in diameter), tortuous, complex, and continuously in motion. Moreover, coronary artery geometries are characterised by non-planarity in 3D space. For coronary imaging, CA is the golden-standard in PCI practice. More recently, other tomographic and imaging systems such as CT angiography, magnetic resonance imaging (MRI), IVUS and OCT have been developed and used for coronary imaging. This chapter focuses on CA and IVUS imaging, which when fused, 3D vessel models can be obtained. In particular, after a brief overview of CA and IVUS image modalities, the methodology which was developed to reconstruct vessels with challenging disease is presented. These challenging vessels are to be simulated in the following chapters to investigate methods for minimising the risk of SM and, consequently, LSD.

## 3.1 Coronary Angiography

### 3.1.1 Fundamentals of coronary angiography

CA uses x-rays to view coronary vessels. In Figure 3.1, a cartoon image of a typical C-arm machine is depicted. According to the examined vessel the machine is rotating around the patient at certain angles to optimise the vessel visualisation. In CA, a long, flexible tube (catheter) is inserted through either the femoral or radial artery and administers a contrast agent (clear dye) into the area which is under examination (c.f. Figure 3.2). In this way, the morphology and anatomy of coronary arteries can be monitored and, as a result, potential pathogenic events can be diagnosed. Complete blockages, significant narrowing, mild irregularities or no disease at all are the range of possible findings from this test. However, angiography lacks the capability of providing a more analytical description of vessel wall structure. As a result, it can misguide intervention cardiologists in the procedure. Despite this drawback, it is considered to be the most robust and convenient method for monitoring PCI.

Figure 3.1: Cartoon image of CA procedure: patient centrally positioned on the table of a C-arm machine. The C-arm machine rotates at certain angles around the patient to visualise specific coronary arteries (Berkeley-Heart-Lab 2015)

#### 3.1.1.1 Coronary angiographic views

As stated above, in coronary angiography, different fluoroscopic views are used in order to visualise certain coronary vessels. The angiogram image intensifier rotates according to the operator's preferable angle around the patient so as to visualise different vessels and either the distal or proximal parts of each vessel. The main categories of image intensifier rotation is the left anterior oblique (LAO) and the right anterior oblique (RAO). In these three categories an additional rotation according to either caudal or cranial angulation might be operated.

During CA, each examined vessel can be evaluated from different angles (usually two orthogonal views) in order to avoid possible artifacts from spine, diaphragm, and vessel overlap and visualise clearer all important side branches (Askari et al. 2011). In Figure 3.3, image intensifier LAO and RAO directions are illustrated. In the LAO projection, the image intensifier is to the left of the patient while in the RAO projection it is to the right as viewed from above. In the LAO image, the spine is always to the

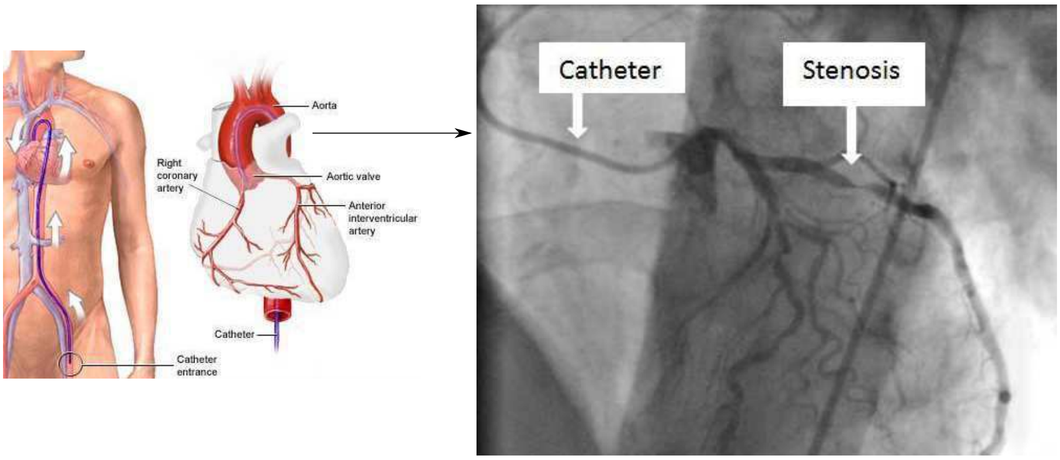

Figure 3.2: CA: schematic representation of cardiac catheterisation (NMA 2008) (left panel) and CA image of left coronary artery (right panel)

right while in the RAO image it is always to the left. In general, cranial angulation is ideal for distal vessel portions while caudal views are ideal for proximal portions.

Figure 3.4 illustrates four commonly used angiographic views. In Figure 3.4a, the 3D diagram (left side) and angiogram (right side) of the 45° LAO-20° cranial view of the left coronary artery is illustrated. As can be seen, the LAD and its diagonal branches can be evaluated easily from this view. The catheter and the spine are to the right side of the heart. Figure 3.4b shows the 20° RAO-20° caudal view of the LCA. The left main and the Cx are visualised by this view. As can be observed, the caudal angulation projects the proximal portions of these vessels. As in all RAO projections, the spine and the catheter are to the left side of the heart. Similarly, Figures 3.4c and 3.4d illustrate the corresponding 3D diagrams (left side) and angiograms (right side) of the right coronary artery. The 35° LAO view is ideal for the visualisation of the proximal and mid right coronary artery and the acute marginal branch and 30° RAO view for the proximal and mid right coronary artery and the posterior descending artery.

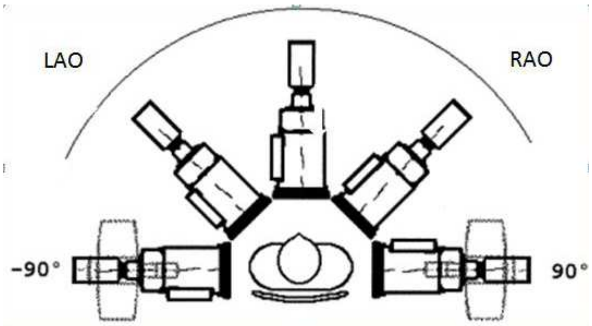

Figure 3.3: Angiographic image intensifier rotation around the patient

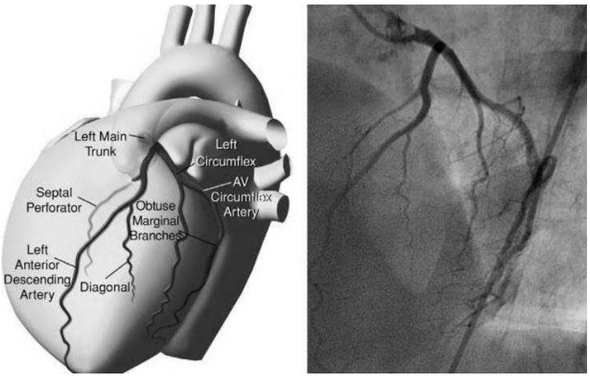

(a) 45°LAO-20° cranial view of the left coronary artery

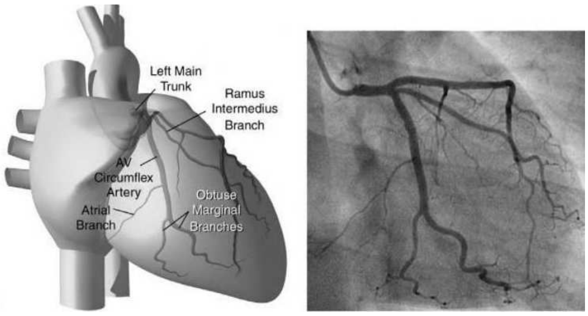

(b) 20°RAO-20° caudal view of left coronary artery

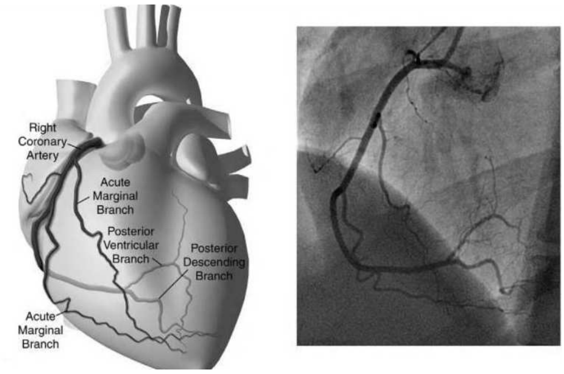

(c) 35°LAO view of the right coronary artery

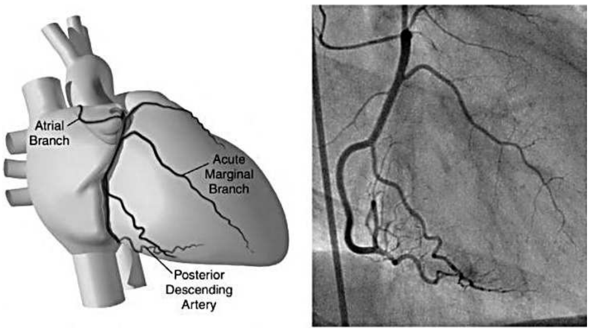

(d) 30°RAO of the right coronary artery

Figure 3.4: Orthogonal angiographic views of LCA & RCA. Image reused with permission from (Askari et al. 2011).

## 3.2 Intravascular ultrasonography

As stated before, despite the fact that angiography represents a very robust monitoring tool for interventional cardiologists it lacks the ability to provide adequate information as far as vessel wall structure is concerned and can give a misleading representation of human area. In contrast, IVUS has been used so far as the only tool to directly visualise atherosclerosis and other pathologic conditions within the vessel wall. Its ability to monitor in real time the entire cross section area of the examined vessels provide a better understanding of possible pathologic events and their distribution within the vessel wall. IVUS also provides a better information concerning arterial morphometry (for instance, lumen and wall area calculation) and morphology.

IVUS imaging systems emit ultrasound waves with centre frequencies ranging from 20 to 45 $MH$ and use the reflected sound waves to visualise the vessel wall in a two dimensional, tomographic format, analogous to a histologic cross-section. The IVUS catheter is approximately 1 mm in diameter and its design is either mechanical or solid-state, both generating 360° cross sectional plane images at 30 frames per second perpendicular to the catheter tip, Figure 3.5. The mechanical catheter uses a higher frequency ultrasound transducer (up to 45 $MH$) while the solid-state device uses a lower ultrasound transducer (up to 20 $MH$). More detailed information on IVUS can be found in Chapter 10 of Redwood et al. (2010).

As can be noted in Figure 3.5, the visualisation of the three different wall layers in an IVUS image can be characterised by a bright-dark-bright appearance. The media which contains less echo-reflective material (e.g. collagen and elastin) is represented as a thin dark layer in contrast to the intima and adventitia which are represented as the two bright areas.

## 3.3 3D Vessel Reconstructions

For the purposes of the current doctoral work, “challenging” geometry segments have been reconstructed by fusing CA and IVUS. The reconstruction of the vessel is based on the analysis of CA and IVUS images through accurate vessel wall segmentation and IVUS catheter (pull-back path) detection. The data was provided by Prof Nick Curzen and were acquired at the University Hospital Southampton. In particular, three coronary arteries, two RCA segments and one left main bifurcation (LMB), were reconstructed. Each of the reconstructed cases represents “challenging diseased vessels”, which during the PCI, were assessed multiple times by the interventional cardiologist to optimise the stent delivery. Therefore, these challenging cases were modelled in Chapters 6, 7 and 8 to investigate novel stent-system designs and/or optimum dilation

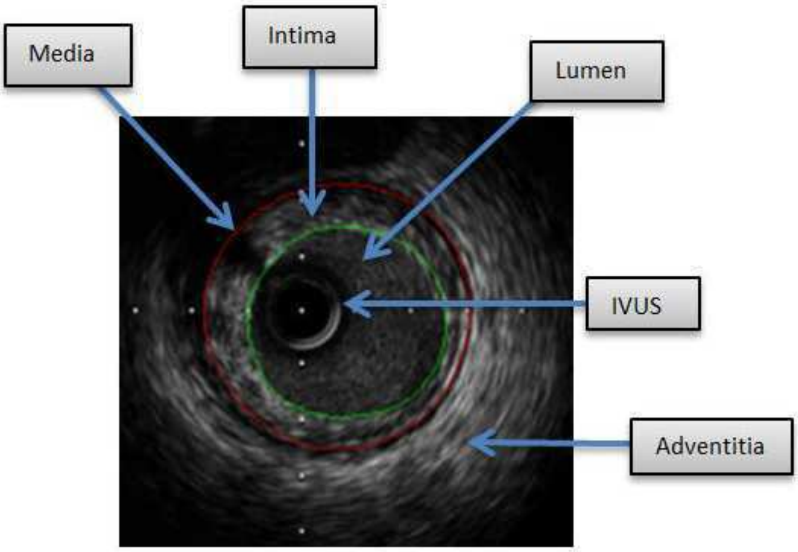

Figure 3.5: Real IVUS cross-sectional histologic plane

protocols according to patient-specificity. The rationale was to propose technology for single-operational PCI procedures to mitigate the risk of SM and LSD in the presented challenging reconstructed segments[1].

### 3.3.1 Introduction

3D vessel reconstruction has been used so far in order to capture morphologic areas and volumes (either lumen or wall layers) and for simulating the endo-coronary blood flow in order to predict hemodynamic factors (g.e. wall shear stresses) (Chatzizisis et al. 2007). While rigid wall assumption in CFD studies require only the lumen volume of the vessel, more complex studies such as imaged based structural simulations require more spatial information, like arterial wall thickness, the presence of atherosclerotic plaques and tissue characterisation. This data cannot be obtained by an individual imaging technique, therefore, methods which combine different techniques have been developed (Doulaverakis et al. 2013, Wahle et al. 1999).

Many previous studies (Foin et al. 2012, Morlacchi et al. 2014, Mortier et al. 2011a, 2014, Pant et al. 2011, Zunino et al. 2009) regarding stent deployment, ideal vessel tubes have been used for stent expansions. In contrast, this project aims to conduct numerical

---

[1] A part of the content of this section was presented in the 1st UK National Conference on Patient-Specific Modelling & Translational Research: **3D Challenging Disease Reconstruction**, G. Ragkousis, N. Curzen, N. Bressloff., 9 & 10 January 2013, Cardiff, UK

studies by modelling realistic stent expansions in 3D reconstructed coronary arteries with challenging disease. This can provide insights in how the clinical problems of SM and LSD can be lessened in such challenging anatomies via patient-specific modelling.

As stated in the preceding sections, the reconstruction has been managed by the fusion of CA with IVUS cross sectional plane images. The reconstructing process has been undertaken in IVUS Angio-Tool 2.1, an open source software (Doulaverakis et al. 2013) and in Rhinoceros 5.0 (Robert McNeel, Seattle, WA, USA), a commercial non-uniform rational B-spline (NURBS) package. The main steps required for the reconstruction of an image-based coronary vessel with challenging disease to be modelled in structural simulations are:

- the selection of two bi-plane CA images
- the selection of several IVUS frames
- the bi-planar IVUS catheter path definition
- the extraction of the vessel center-line
- the vessel lumen and wall extraction via IVUS image segmentation
- the geometrical correct placement and orientation of the extracted IVUS contours onto the 3D catheter path
- the generation of the internal/external surfaces from NURBS curves
- the discretisation of the reconstructed model into a computational mesh

### 3.3.2 Material & Methods

In total, three patient-specific segments with challenging disease were supplied for the purposes of this doctoral thesis. In the first case, a RCA was blocked along the second segment of its length. PCI was undertaken and one 3.5 × 16 *mm* stent was implanted along the stenosed length followed by post-balloon dilation to further expand malapposed struts in the proximal end of the stent. In the second case, a more complex and longer RCA segment was provided and the disease along its length had been spread more widely on its wall. The patient underwent PCI which involved three implanted stents, one 4 × 20 *mm* distal, one 4.5 × 32 *mm* in the middle, and one 4.5 × 16 *mm* proximal segment of RCA. The third case concerns a LMB with a stenosis in the proximal part of the LAD after balloon pre-dilation. The patient underwent PCI and both segments were stented. This case represents one of the most challenging situations that an interventional cardiologist might encounter. The major difficulty of such a case is the size discrepancy between the left main and the LAD.

For each vessel reconstruction, several IVUS frames and two bi-plane CA images were collected and imported into the IVUS Angio-Tool where the catheter path definition and the lumen with the vessel wall segmentation were defined. The catheter path was defined by both LAO and RAO angiographic images which differ by approximately 90°; the LAO and RAO are shown in Figure 3.6a & b. The segmentation of lumen and media-adventitia border contours was carried out by active contours models (Giannoglou et al. 2007), see Appendix A and Figure 3.6c. The contours information was then written as a point-cloud which was imported into Rhinoceros 5.0 for further processing. In Rhinoceros 5.0, the realistic 3D IVUS pull-back path was reconstructed as the intersection of the two bi-plane orthogonal curve extrusions. The resultant curve was scaled to its real dimensions according to[2]

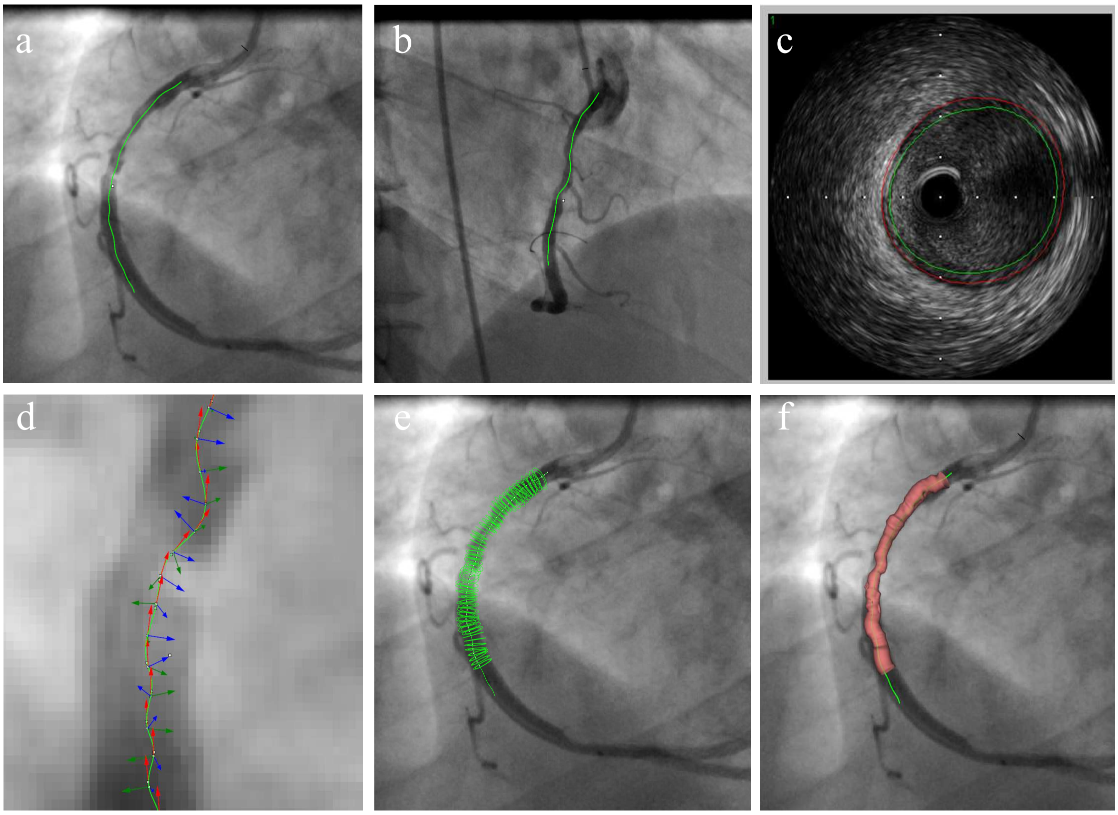

Figure 3.6: Framework for 3D vessel reconstruction: a) catheter path definition in LAO, b) catheter path definition in RAO, c) extraction of lumen and intima-media boundaries, d) Frenet trihedron calculation at finite locations on the IVUS catheter curve, e) orientation of the contour sets (each one comprised of lumen and intima-media border contours) on the catheter line, and f) interpolation of NURBS surfaces to the oriented contour sets.

---

[2] By selecting one frame every sixty frames, 1 mm of the IVUS length is covered.

$$L_{ivus} = \left[\frac{N_{frames}}{f_{acq}}\right] S_{pullback} \tag{3.1}$$

where, $f_{acq} = 30\ frames/sec$, $S_{pullback} = 0.5\,\text{mm}/sec$ and $N_{frames}$ denotes the number of frames.

This curve comprises the backbone on which the lumen and the wall contours are positioned after being converted into real dimensions calculated from the IVUS-Angio Tool. At each location point on the curve, the Frenet trihedron is calculated, Figure 3.6d.

#### 3.3.2.1 Frenet frame

The reconstructed IVUS pull-back is a line in space which can be geometrically characterised using classical differential geometry of curves. Let $\mathbf{c}(t) \in [0, L] \rightarrow \mathbb{R}^3$ and $\mathbf{c}(t) = [x(t), y(t), z(t)]$ be the pull-back path of the IVUS transducer as a function of an arbitrary parameter $t$. The local behaviour of the curve $C$ can be described by the *moving frame* or *Frenet frame* (Millman and Parker 1977), a right handed trihedron of three orthonormal vectors $\mathbf{t}$, $\mathbf{n}$, and $\mathbf{b}$ representing the tangential, the normal and the bi-normal unit vector, respectively, at each location on the curve. The Frenet orthonormal vectors are defined as:

$$\mathbf{t} = \frac{\mathbf{c}'(t)}{\|\mathbf{c}'(t)\|} \tag{3.2}$$

$$\mathbf{n} = \frac{(\mathbf{c}'(t) \times \mathbf{c}''(t)) \times \mathbf{c}'(t)}{\|\mathbf{c}'(t) \times \mathbf{c}''(t)\| \cdot \|\mathbf{c}'(t)\|} \tag{3.3}$$

$$\mathbf{b} = \frac{\mathbf{c}'(t) \times \mathbf{c}''(t)}{\|(\mathbf{c}'(t) \times \mathbf{c}''(t)\|} \tag{3.4}$$

where $\mathbf{c}'(t)$ is the derivative of $\mathbf{c}(t)$ with respect to an arbitrary parameter $t$.

Along with the orthonormal Frenet unit vectors, two scalar quantities, the curvature and the torsion are used to characterise the local behaviour of a 3D curve. Curvature, $k(t)$, measures the deviation of the curve from a straight line and it is always positive whereas torsion, $\tau(t)$, measures how much the curve declines from being planar. Assuming an arbitrary parametrisation, these scalar quantities are calculated from

$$k(t) = \frac{\|\mathbf{c}'(t) \times \mathbf{c}''(t)\|}{\|\mathbf{c}'(t)\|^3} \tag{3.5}$$

$$\tau(t) = \frac{(\mathbf{c}'(t) \times \mathbf{c}''(t)) \cdot \mathbf{c}'''(t)}{\|\mathbf{c}'(t) \times \mathbf{c}''(t)\|^2} \tag{3.6}$$

$$\begin{bmatrix}\mathbf{t}'\\ \mathbf{n}'\\ \mathbf{b}'\end{bmatrix} = \begin{bmatrix}0 & k(t) & 0\\ -k(t) & 0 & \tau(t)\\ 0 & -\tau(t) & 0\end{bmatrix}\begin{bmatrix}\mathbf{t}\\ \mathbf{n}\\ \mathbf{b}\end{bmatrix} \tag{3.7}$$

The precise position of the IVUS contours on the catheter line is formulated by orientating the contours at each location point with geometrical transformations which map three units vectors $[\mathbf{x}, \mathbf{y}, \mathbf{z}]$ (defined on each cross section contour) to the Frenet trihedron $[\mathbf{t}, \mathbf{n}, \mathbf{b}]$ (at each location point).

#### 3.3.2.2 Position and Orientation according to the Frenet trihedron

As discussed in the preceding section, the segmented contours representing the lumen and the walls, need to be positioned onto the catheter path curve according to the Frenet trihedron. This was accomplished by homogeneous matrix transformations (Theoharis et al. 2008). A local orthonormal coordinate system $[\mathbf{x}, \mathbf{y}, \mathbf{z}]$ was defined at each cross section on a control point which represented the centre of the IVUS transducer. Then, each cross section was transformed by a geometrical mapping of its local coordinate system $[\mathbf{x}, \mathbf{y}, \mathbf{z}]$ to the corresponding local Frenet orthonormal coordinate system $[\mathbf{t}, \mathbf{n}, \mathbf{b}]$ at each location point on the curve. When an object was to be transformed, individual homogeneous matrices were created for each step of transformation (e.g. translation, rotation, shearing, etc.). The steps used here were as follows:

1. The contours were first translated to the global origin $[0, 0, 0]^T$ according to

$$\mathbf{T}(\mathbf{p})^{-1} = \begin{bmatrix}1 & 0 & 0 & -p_x\\ 0 & 1 & 0 & -p_y\\ 0 & 0 & 1 & -p_z\\ 0 & 0 & 0 & 1\end{bmatrix} \tag{3.8}$$

   or $\mathbf{T}(\mathbf{p})^{-1} = \mathbf{I}(-\mathbf{p})$, where $-\mathbf{p}$ is the translational vector $-\mathbf{p} = [-p_x, -p_y, -p_z]^T$ which translates the cross sections to the origin and $\mathbf{I}$ is the identity matrix.

2. Then, the contour cross sections were rotated around z axis[3]. The rotation matrix was

$$\mathbf{R}_z(\theta) = \begin{bmatrix}\cos\theta & -\sin\theta & 0 & 0\\ \sin\theta & \cos\theta & 0 & 0\\ 0 & 0 & 1 & 0\\ 0 & 0 & 0 & 1\end{bmatrix} \tag{3.9}$$

---

[3] the z axis will be mapped to the tangential axis t of the Frenet system

with $\theta$ being the clockwise angle of rotation of x and y axis around z

3. The rotated contours were transformed to the $[\mathbf{t}, \mathbf{n}, \mathbf{b}]$ orthonormal system with the corresponding matrix being

$$\mathbf{F}(\mathbf{t}, \mathbf{n}, \mathbf{b}) = \begin{bmatrix} n_x & b_x & t_x & 0 \\ n_y & b_y & t_y & 0 \\ n_z & b_z & t_z & 0 \\ 0 & 0 & 0 & 1 \end{bmatrix} \tag{3.10}$$

   or $\mathbf{F}(\mathbf{t}, \mathbf{n}, \mathbf{b}) = [\mathbf{n}, \mathbf{b}, \mathbf{t}, \mathbf{1}]$. The transformation matrix $\mathbf{F}(\mathbf{t}, \mathbf{n}, \mathbf{b})$ maps the $\mathbf{x}$ with $\mathbf{n}$, $\mathbf{y}$ with $\mathbf{b}$, and $\mathbf{z}$ with $\mathbf{t}$.

4. Within the Frenet system, the contours have to be displaced to the location points on the curve. For each contour, the displacement vector corresponded to the position vector of each location point on the curve. Thus, the translational matrix was

$$\mathbf{T}(\mathbf{c_0})_{curve} = \begin{bmatrix} 1 & 0 & 0 & c_{0x} \\ 0 & 1 & 0 & c_{0y} \\ 0 & 0 & 1 & c_{0z} \\ 0 & 0 & 0 & 1 \end{bmatrix} \tag{3.11}$$

   or $\mathbf{T}(\mathbf{c_0})_{curve} = \mathbf{I}(\mathbf{c_0})$ with $\mathbf{c_0} = [c_{0x}, c_{0y}, c_{0z}]^T$ being the position vector of each location point on the curve.

5. Finally, the above transformation and rotation matrices could be combined into single matrix equivalent to

$$\mathbf{M}_{global} = (\mathbf{T}(\mathbf{c_0})_{curve})(\mathbf{F}(\mathbf{t}, \mathbf{n}, \mathbf{b}))(\mathbf{R}_z(\theta))(\mathbf{T}(\mathbf{p})^{-1}) \tag{3.12}$$

   or

$$\mathbf{M}_{global} = \begin{bmatrix} A_x & B_x & t_x & -p_x(a_x) + p_y(b_x) - p_z(t_x) + c_{0x} \\ A_y & B_y & t_y & -p_x(a_y) + p_y(b_y) - p_z(t_y) + c_{0y} \\ A_z & B_z & t_z & -p_x(a_z) + p_y(b_z) - p_z(t_z) + c_{0z} \\ 0 & 0 & 0 & 1 \end{bmatrix} \tag{3.13}$$

   with $A_i = n_i \cos\theta + b_i \sin\theta$ and $B_i = -n_i \sin\theta + b_i \cos\theta$ with $i = x, y, z$.

The final step comprised the definition of a certain angle which the contours were rotated around $\mathbf{t}$ such that when re-projecting the reconstructed vessel onto either the

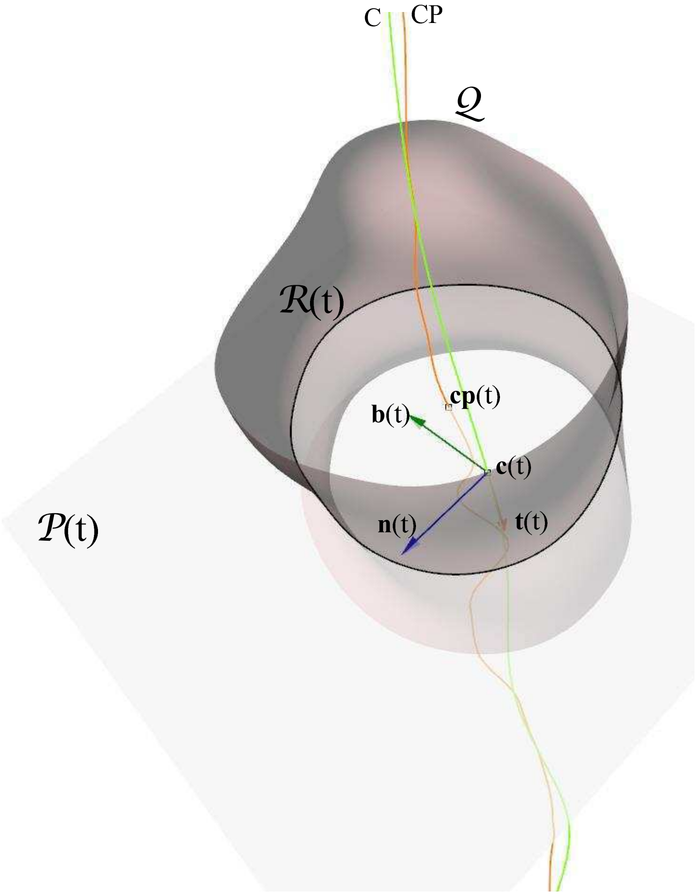

Figure 3.7: Lumen and normal plane intersection along a point $t$ in the parametrised IVUS pull-back curve: **t**, **n**, and **b** is the tangential, the normal and the bi-normal vector at any $\mathbf{c}(t)$ point of the arbitrary parametrised curve $C$, respectively. $\mathbf{cp}(t)$ is the centre of area of each $\mathcal{R}(t)$ created by the intersection of the normal plane $\mathcal{P}(t)$ and the volume $\mathcal{Q}$. $CP$ is the interpolated curve passing through all the $\mathbf{cp}(t)$ points.

RAO or LAO view, a satisfactory match was accomplished (c.f. Figures 3.6e & f). The process of reconstruction was completed by interpolating internal (for the lumen borders) and external (for the media borders) NURBS surfaces through the oriented IVUS contours.

#### 3.3.2.3 Centreline calculation

As the vessel was reconstructed, the IVUS pull-back line was used as a reference to calculate the vessel centre line. In particular, the IVUS pull-back line was sampled across its length and at each sampling point the Frenet frame was re-calculated. Then, the *Frenet frame* of the IVUS parametrised curve was used to segment the vessel according to the *normal moving plane*, expressed as

$$(\mathbf{x}(t) - \mathbf{c}(t)) \cdot \mathbf{t} = 0 \tag{3.14}$$

with $\mathbf{x}(t)$ a position vector of a point $x$ on the normal plane. At each location point $\mathbf{c}(t)$ a planar closed curve (cross section) $\mathcal{R}(t)$ is defined as the intersection of the normal plane $\mathcal{P}(t)$ with the volume of the lumen, $V(\mathcal{Q})$ (c.f Figure 3.7), expressed by

$$\mathcal{R}(t) = V(\mathcal{Q}) \cap \mathcal{P}(t) \tag{3.15}$$

Alternatively, the cross section $\mathcal{R}(t)$ of $V(\mathcal{Q})$ at a point $t$ on curve $C$ is the region lying in $\mathcal{P}(t)$, or

$$\mathcal{R}(t) = r\mathbf{n}(t) + p\mathbf{b}(t) \tag{3.16}$$

with $r$ and $p$ real numbers lying in a region $\mathcal{D}(t)$ of the $r$-$p$ plane (England and Miller 2001). Then, providing that, for any set of points $\mathbf{c}(t)$ and $\mathbf{c}(t+dt)$, the cross sections $\mathcal{R}(t)$ and $\mathcal{R}(t+dt)$ do not intersect, the centre of area of each cross section , $\mathbf{cp}(t)$, is calculated. A smooth curve at least $\mathcal{C}^2$ differentiable has been interpolated through all the calculated $\mathbf{cp}(t)$ points, see Figure 3.7 and 3.8.

The centre line was served to partition the reconstructed vessels and enable solid hexahedral structured mesh discretisation of the volume comprising the vessel walls. By this method, uniform small segments were created along the entire length of each model enabling fast and accurate mesh discretisation. Specifically, each vessel was partitioned along its length by the Frenet planes defined on the centre line of each lumen. The Frenet planes are as follows:

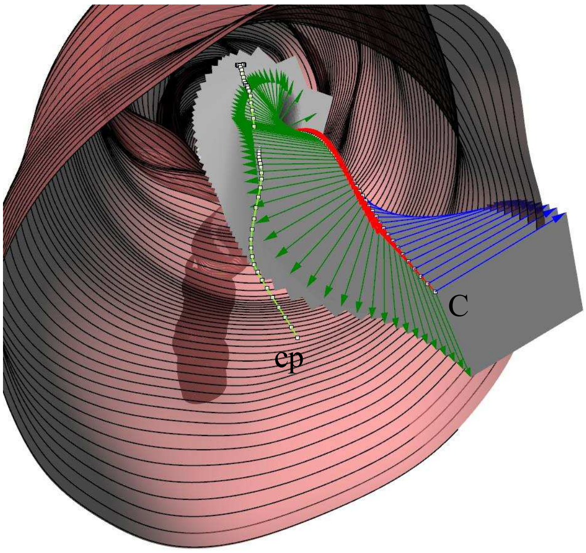

Figure 3.8: Normal cross sectioning of the RCA segment from the $C$ IVUS line to compute the $CP$ centre line of the lumen

- the osculating plane, $\mathcal{O}(t)$, expressed as

  $$(\mathbf{x}(t) - \mathbf{c}(t)) \cdot \mathbf{b} = 0 \tag{3.17}$$

  with $\mathbf{x}(t)$ a position vector of a point $x$ on the osculating plane.

- the rectifying plane, $\mathcal{R}e(t)$, expressed as

  $$(\mathbf{x}(t) - \mathbf{c}(t)) \cdot \mathbf{n} = 0 \tag{3.18}$$

  with $\mathbf{x}(t)$ a position vector of a point $x$ on the rectifying plane.

- and, finally, the normal plane, $\mathcal{P}(t)$, defined by Eq. 3.14

The Frenet planes in local point of a parameterised curve are illustrated in Figure 3.9.

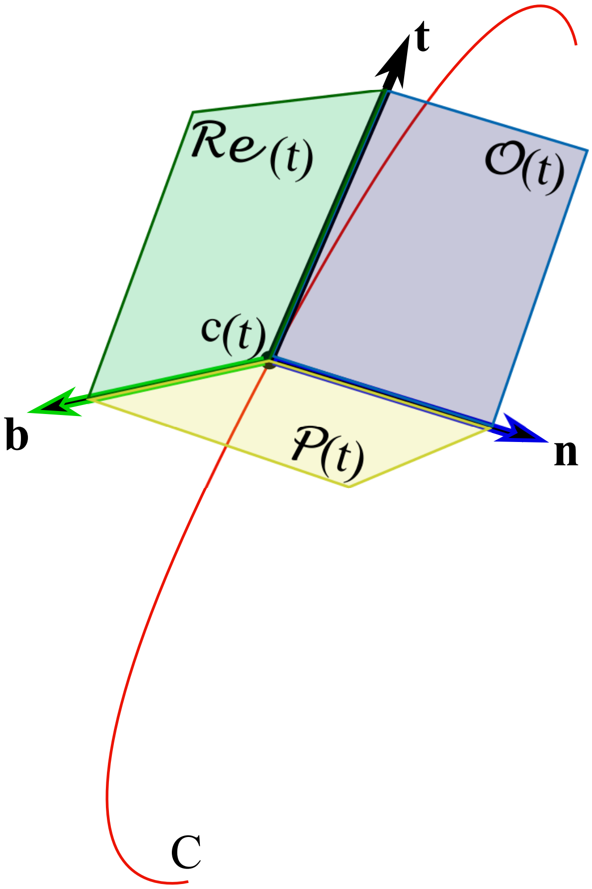

Figure 3.9: Frenet planes calculated on a local point, $\mathbf{c}(t)$, of a parametrised curve: $\mathcal{P}(t)$ is the normal plane, $\mathcal{R}e(t)$ is the rectifying plane and $\mathcal{O}(t)$ is the osculating plane.

Furthermore, as presented in Chapter 7 (see section 7.2.1.3), the geometrical local properties of the centre line were used to derive scalar indices to geometrically

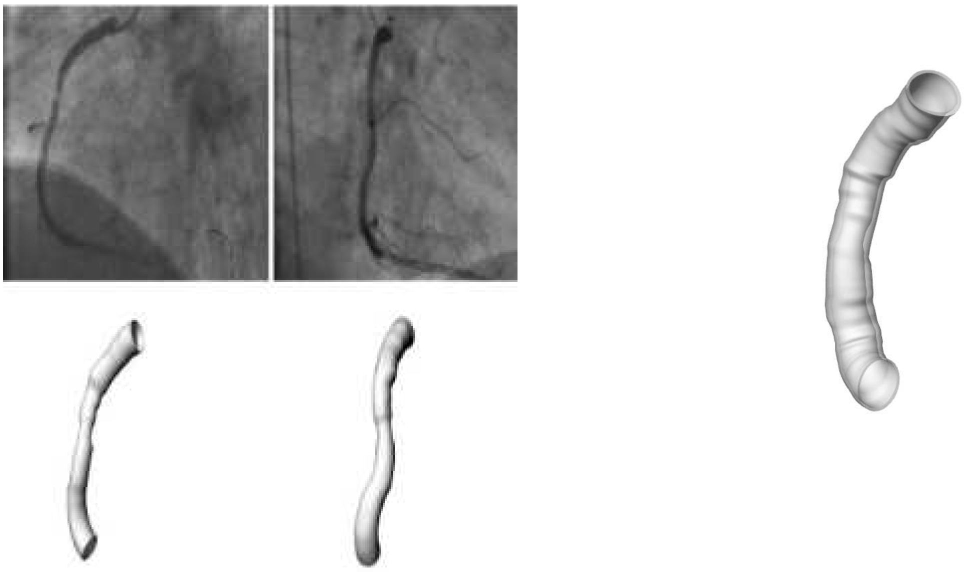

(a) Final reconstructed lumen surface from LAO and RAO

(b) Resultant RCA reconstructed vessel including the arterial walls

(c) Structured hexahedral element mesh for the first RCA case

Figure 3.10: 3D reconstruction and computational mesh generation of the first RCA segment

characterise the reconstructed vessels and quantify pre and post-stenting outcomes.

### 3.3.3 Results

For the first case, Figure 3.10a shows the 3D realistic representations of the reconstructed lumen from LAO and RAO projections. In Figure 3.10b, the solid model of the reconstructed RCA is illustrated including the arterial walls (extracted from the IVUS image segmentation, see Figure 3.6c). The NURBS surfaces were smoothed to enable a better mesh discretisation quality, Figure 3.10c. This was accomplished by decreasing the number of control points of the NURBS curves which were used to make up (loft) the lumen and the wall surfaces.

For the second case, Figure 3.11a illustrates the resultant lumen surface back-projected to the corresponding bi-plane CA view. For our computational purposes, there was a satisfactory fit between the bi-plane lumen and the reconstructed surface in this case. Figure 3.11b and 3.11c depict the reconstructed smoothed RCA solid model including the arterial walls and the generated computational mesh of the model, respectively.

Finally, the reconstruction results of the third case are illustrated in Figure 3.12. In particular, two IVUS sequences were used to reconstruct the bifurcated vessel. One sequence was the IVUS pull-back run from the Cx to the proximal part of the left main and the second was the pull-back run carried out in the LAD after pre-dilating the ostium. Therefore, two different segments were reconstructed by each run and then they were merged to comprise the bifurcated vessel. At the end of the process, this model was extended to 5 *mm* along its edges for the purposes of the work presented in Chapter 7 (to host the entire stent-system in vessel wall vicinity). In Figure 3.12a, the lumen of the reconstructed bifurcated model is back-projected onto the RAO image. The wall composition of the segment and the volumetric mesh discretisation of the model are illustrated in Figure 3.12b and 3.12c, respectively.

### 3.3.4 Discussion

In this chapter, a framework has been presented for the geometrically correct 3D reconstruction of three human coronary arteries by fusion of IVUS and biplane CA. The CA images, as shown, provide the spatial trajectory of the IVUS catheter, representing the backbone on which the IVUS segments contours are placed and oriented in space. Orthogonal projections are desirable, due to a higher amount of spatial information as compared to low inclination angles, but are not required (Wahle et al. 1999). The lumen and the walls were segmented with active contours which are implemented in IVUS Angio-Tool. The algorithms of this open source software were developed to auto-

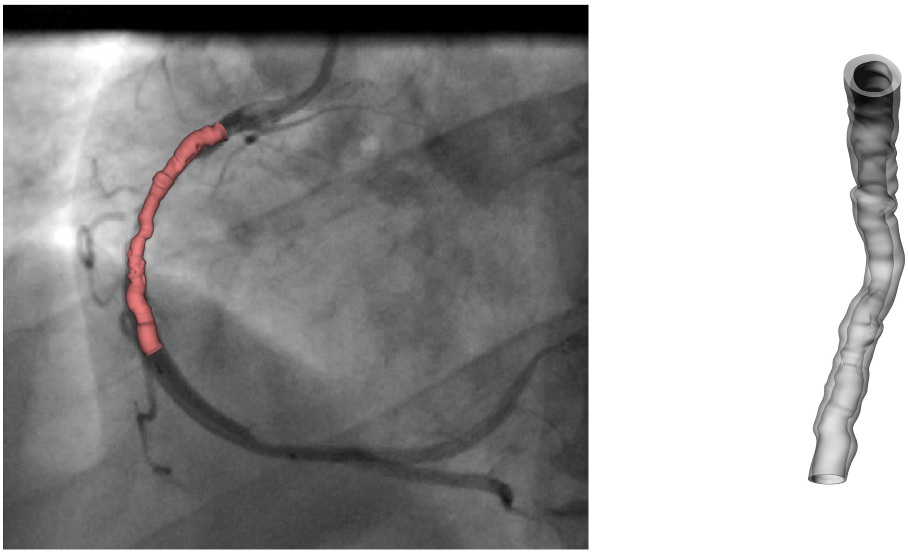

(a) Lumen and border surface superimposed on the LAO image

(b) Solid virtual model of the RCA reconstructed segment

(c) Structured hexahedral element mesh for the second RCA case

Figure 3.11: 3D reconstruction and computational mesh generation of the second RCA segment

mate the segmentation process (Giannoglou et al. 2007), although, it seems that their accuracy is limited. Thus, the frames were manually segmented to improve the final outcomes.

For the qualitative validation of the reconstructed models, the reconstructed lumen were back-projected onto the angiographic images. Ideally, the back-projected luminal surfaces should be in perfect agreement with the actual angiographic ones. However, this was not the case for all the three segments. The discrepancy might occur due to vessel foreshortening, the continuous motion of the vessels, and the difficulty in detecting the IVUS catheter and the luminal edges in angiograms with absolute accuracy. Nonetheless, it has been shown (Chatzizisis et al. 2006), that the method exhibits slightly less accuracy in reconstruction of RCA than LCA. Additionally, since the IVUS transducer is not electrocardiogram gated, it was impossible to filter the IVUS frames according to the R wave[4]. However, for the imaged-based computation purposes of this project, the reconstruction results are considered to be satisfactory.

#### 3.3.4.1 Limitations

The major drawback of the proposed methodology is that it requires time to reconstruct a whole vessel. The segmentation of IVUS images was performed manually, which is a time consuming procedure with results affected by the user. Furthermore, in order to reduce the reconstruction time, the IVUS contours were positioned equidistantly onto the catheter line, although it would be more accurate to position each one on the pull-back path according to their specific location, calculated from its known identical number, pull-back velocity and frame rate (Wahle et al. 1999) given by Eq. 3.1. Finally, it was assumed that the speed of the pull-back is constant. However, in reality, the catheter sometimes might be delayed during the pull-back (Chatzizisis et al. 2006) due to vessel complexity (e.g. increased tortuosity, curvature, plaque morphology, etc.).

### 3.3.5 Summary

The fusion of CA bi-plane images and several IVUS frames can be used for 3D vessel reconstruction of patient-specific arteries. From this method, planarity, curvature, torsion and wall constitution can be obtained with relatively accurate spatial representation, suitable for simulations of PCI procedure especially in vessels with challenging disease. Such reconstructed models can provide 3D information along the entire model length, and in addition, different cross sections and volumes (regions of interest) can be extracted from the virtual space. This can assist the physician to plan the procedure more effectively; and as a result, optimise the stent delivery.

---

[4] R wave corresponds to the end diastolic phase of the cardiac cycle

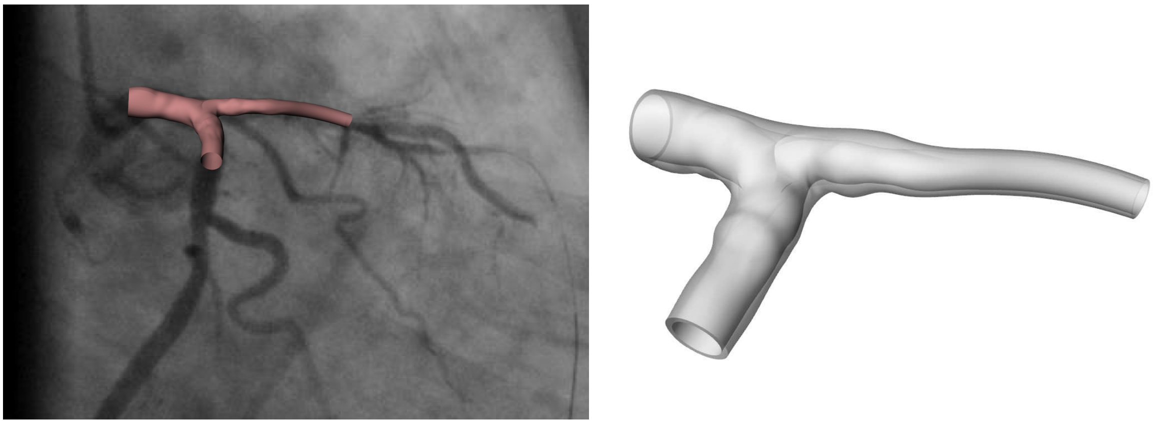

(a) Reconstructed lumen surface of the LMB vessel superimposed on the RAO image

(b) Solid virtual model of the bifurcated reconstructed model

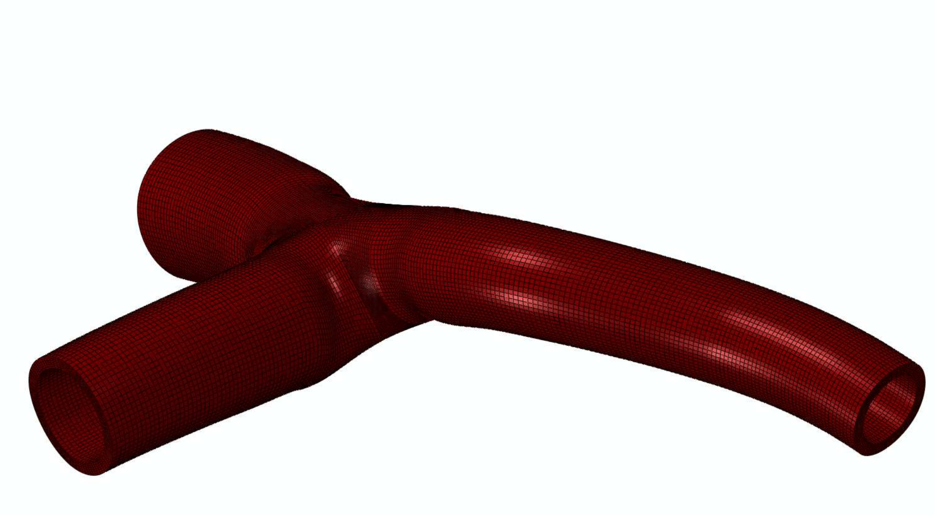

(c) Structured hexahedral element mesh for the LMB case

Figure 3.12: 3D reconstruction and computational mesh generation of the LMB model

The reconstructed vessels presented in this chapter were simulated in Chapters 6, 7, and 8. All models are characterised by diameter discrepancy along their length, tortuous geometry and, finally different degree of stenosis. Therefore, each patient-specific vessel represents different degree of challenging disease. In particular, the first case constitutes the least challenging case characterised by tortuous geometry with a focal plaque in the middle part of its length. It was modelled in the work presented in Chapter 6 to investigate the mechanical performance of different contemporary coronary artery stents with respect to SM and LSD. The second case represents greater clinical challenge due to the increased geometrical complexity (longer segment, higher tortuosity and curvature) and the non-focal state of the disease. This vessel was modelled in the work presented i) in Chapter 7 to investigate the mechanical performance of tapered delivery systems with respect to SM and the imposed stress environment and ii) in Chapter 8 to search for several optimum dilation protocols (via mathematical optimisation) with respect to SM, drug deliverability and tissue stress according to the interventional cardiologist's preference. Finally, the reconstructed bifurcated vessel represents the most challenging case characterised by a sharp change of lumen diameter ($\sim 50\%$) along the length of the intervened vessel. This vessel was modelled in the work presented in Chapter 7 to investigate the mechanical performance of a novel stepped delivery system with respect to SM and tissue stresses.

## Chapter 4

# 3D STENT & BALLOON DESIGN

COMPUTER AIDED DESIGN! Virtual models of different latest generation balloon expandable stents have been constructed for the purposes of the current doctoral thesis. The stents represent commercial devices which have been used broadly in PCI procedure during the last few years. This chapter provides a description concerning the methodology used for the 3D virtual design of the stent systems which were modelled in this thesis. Then, a description is provided regarding the computer aided design generation of realistic multi-folded balloons used for stent deployment. All the virtual models presented in the following content were modelled in the studies presented in Chapters 6, 7 and 8 to investigate their mechanical performance (with respect to SM, LSD and tissue stresses) when implanted in reconstructed vessels with challenging disease (presented in Chapter 3).

## 4.1 Introduction

Commercially available stents come in a variety of shapes and sizes depending on the application and the target site in which they are to be implanted. In reality, laser-cut tubular stent platforms are designed in tube dimensions. Lacking the analytical dimensions of the tube from which stents are cut, an ideal representation of the real stent is compromised. However, being aware of the analytical dimensions of a crimped stent in accordance with the knowledge of stent features (number of struts along a circumferential ring, number of connectors, and number of circumferential rings along stent length), the prediction of stent dimensions of the tube diameter have to be approximated.

Figure 4.1 depicts a typical two dimensional (2D) drawing of a stent platform designed in its minimum diameter (semi-crimped dimensions). $L_s$ is the length of the stent, $L_c$ (or $X_{bridge}$) is the length of a connector, $W_s$ is the width of the stent struts, $L_r$ (or $X_{strut}$) is the axial length of a circumferential ring, and finally, $W_{appex}$ is the width

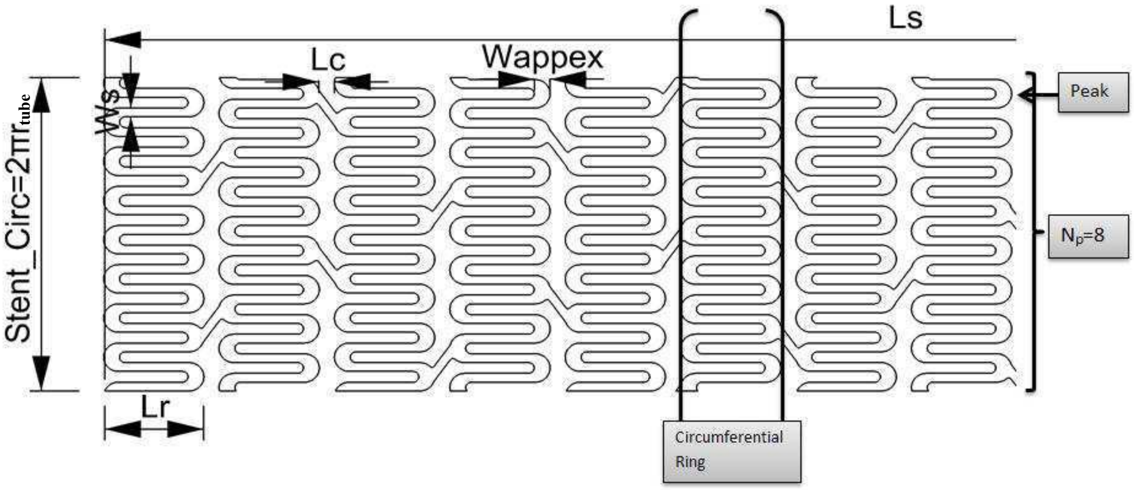

Figure 4.1: A 2D unrolled stent with its characteristic platform dimensions: $L_s$ is the length of the stent, $L_c$ is the length of a connector, $W_s$ is the width of the stent struts, $L_r$ is the axial length of a circumferential ring, and finally, $W_{appex}$ is the width of a peak.

of a peak. $Stent_{Circ}$ is equal to the circumference of the tube that the stent is wrapped around in order to represent a 3D tubular model. $r_{tube}$ denotes the outer radius of the tube. Therefore, being aware of the diameter of a stent-system profile, $r_{tube}$, the number of the struts in a circumferential ring, $N_{struts}$, and the width of the struts, $W_s$, a reliable representation of the stent along its circumference can be obtained by

$$Stent_{Circ} = 2\pi r_{tube} = N_{struts}(W_s + W_{space}) \tag{4.1}$$

where $W_{space}$, the vertical distance between two sequential struts.

The longitudinal length of a stent can be expressed as

$$L_s = N_{rings}L_r + (N_{rings} - 1)L_c \tag{4.2}$$

where $N_{rings}$, the number of circumferential strut rings along the stent length. Since $L_c$ and $L_r$ are not always known, they can be derived by their fraction estimated by a commercially available image. Specifically, being aware of $L_c/L_r$ along with Eq. 4.2, a linear system with two unknowns can be easily solved.

## 4.2 Stent Computer Aided Design

### 4.2.1 Stent A: Promus Element (Boston Scientific, Boston, MA, USA)

The Promus Element stent incorporates a uniform pattern of serpentine segments, each with two offset connectors, that reverse the direction of alternate rows. The connectors are placed helically around the longitudinal axis of the stent. Moreover, it has short ring segments and the peaks are wider than the general width of the struts. Each two sequential circumferential rings differ slightly in phase allowing the device to bend without allowing its rings to overlap. This platform comes in different sizes ranging from 2.25 $mm$ to 4.0 $mm$ in deployed diameter, and 8 $mm$ to 32 $mm$ in length. Stent thickness is 81 µm and the strut width is 91 µm. More information about different commercially available sizes of the Promus platform and its manufacturing process can be found in O'Brien et al. (2010).

In the current work, a 3D design of the Promus platform in its tube dimensions is worked out. Since its analytical dimensional data are not available, the computer aided design of this platform is based on some assumptions. However, as already mentioned above, in case some general features of the stent are known, a reliable design of a stent platform can be carried out. In O'Brien et al. (2010), the manufacturing process is described and the outer diameter of the tube (which the stent is cut from) is given as 1.83 $mm$ and its wall thickness as 107 µm. In parallel, given the strut thickness, it is possible to easily predict the inner and the outer diameter of the stent in its tubular state.

According to the given information and having provided the web released picture (BostonScientific 2009) on the left panel of Figure 4.2, the 2D drawing of Promus Element was created as illustrated in the right picture of Figure 4.2. In particular, the assumptions of dimensional details for this 3.5 × 16 $mm$ stent are as follows:

- $D^{tube}_{inner} = D^{tube}_{outer} - 2(Th_{tube})$, where $D^{tube}_{inner}$ is the inner diameter of the tube, $D^{tube}_{outer}$ is the outer diameter of the tube, and $Th_{tube}$ is the wall thickness of the tube
- $D_s = D^{tube}_{inner} + Th_{struts}$, where $D_s$ is the diameter of the stent and $Th_{struts}$, the thickness of the stent struts
- $Stent_{Circ} = \pi D_s$, where $Stent_{Circ}$ is the circumference of the 2D stent drawing, Figure 4.2
- $Y_{strut} = \frac{Stent_{Circ}}{N_{struts}}$, with $Y_{strut}$ the vertical length of one strut along the circumferential axis

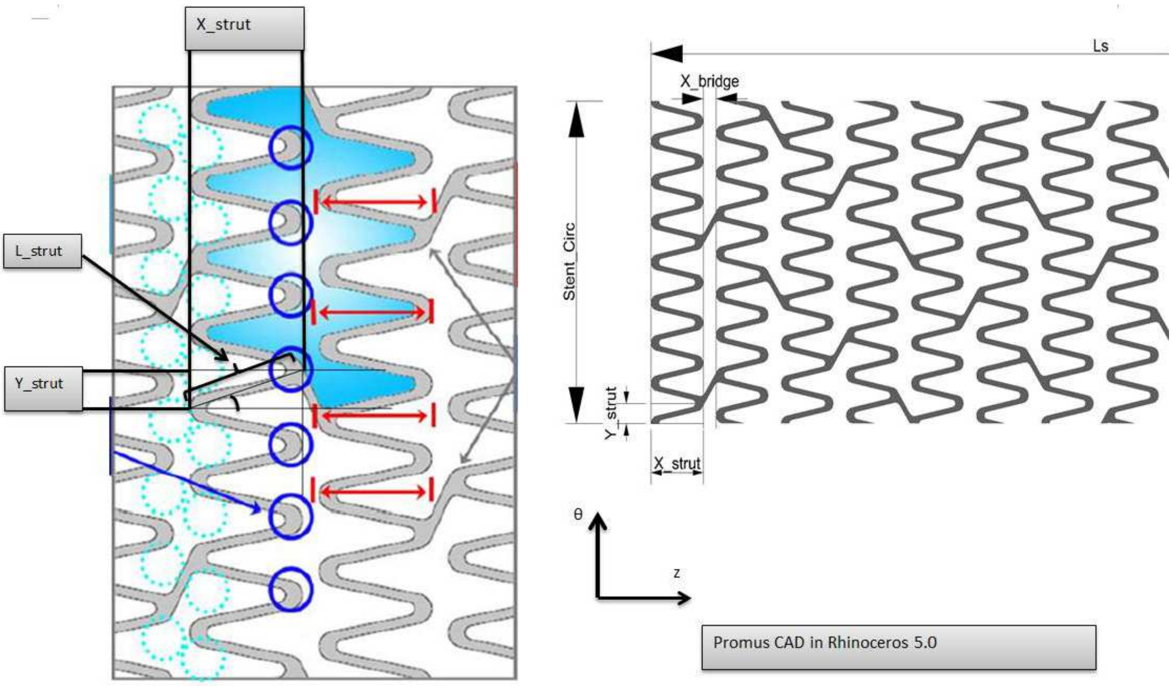

Figure 4.2: 2D drawing of Promus Element: On the left panel, Promus Element as depicted in a commercial leaflet (BostonScientific 2009) and, on the right panel, Promus Element as generated in Rhinoceros.

- according to equation 4.2 along with the ratio $X_{strut}/X_{bridge}$ (estimated in a commercial image of the stent), a linear system with two unknowns is generated. Solving the linear system, the two unknowns $X_{strut}$ and $X_{bridge}$ are given
- $L_{strut} = \sqrt{(X_{strut})^2 + (Y_{strut})^2}$, where $L_{strut}$ is the diagonal length of a unit strut, Figure 4.2
- finally, the diagonal $L_{strut}$ is offset by $W_s$ to build the unit strut, Figure 4.3

Thereupon the unit strut formation, a mirror function is used with respect to the circumferential axis, $\theta$, so as to form a pair of struts. Then, copying the pair object along the circumferential axis, $\theta$, according to $N_{peaks}$, a unit circumferential ring is created which in turn is copied along the z axis and offset along the $\theta$ axis to represent the pair of two sequential ring as depicted on the top right of Figure 4.3. Then, the circumferential pair is copied according to $(N_{rings})/2$, and each copied object is placed at a $X_{bridge}$ distance from the other. The connectors are designed by straight lines between the peak and the tangent points of two opposite appexes/peaks and are smoothed by a blend arc function. The final 2D drawing of the Promus Element is illustrated in the bottom part of Figure 4.3. At the end, the planar design is joined and extruded in both sides along the R axis by $(Th_{struts})/2$ and wrapped into a tubular surface with circumference equal to $Stent_{Circ}$. The final 3D tubular virtual model of

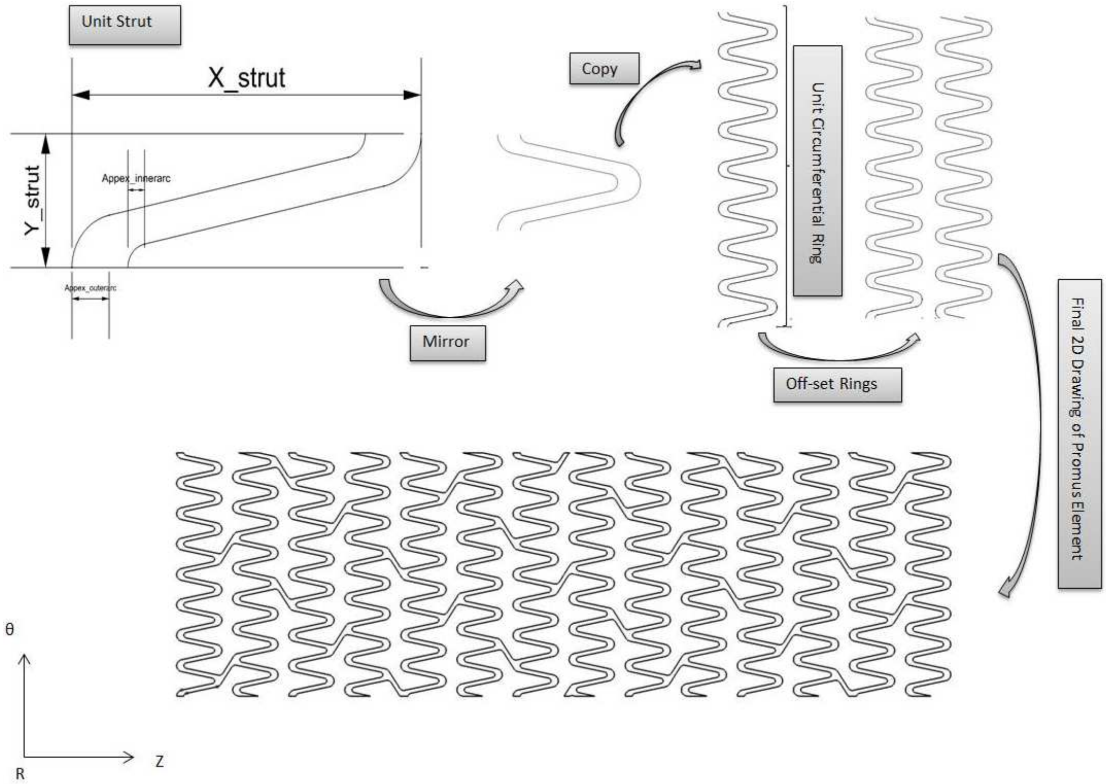

Figure 4.3: 2D design methodology followed for Promus Element **CAD** generation.

Promus Element is depicted in Figure 4.4a. The stent was designed with an outer diameter of 1.77835 $mm$, strut thickness ($Th_{struts}$) of 81 $\mu m$ and a strut width ($W_s$) of 91 $\mu m$. The respective commercial stent system (actual) is illustrated in Figure 4.4b.

### 4.2.2 Stent B: XIENCE (Abbott Vascular, Chicago, IL, USA)

XIENCE is laser-cut from a cobalt chromium alloy (L605). This stent features alternating crown heights and wavy struts. The device consists of three connectors between adjacent circumferential rings. This platform comes in different sizes ranging from 2.75 $mm$ to 4.0 $mm$ in diameter, and 8 $mm$ to 28 $mm$ in length. Stent thickness is 81 µm and the strut width is 91 µm (AbbotVascular 2008). The procedure followed for the overall stent configuration is exactly the same as that of the Promus Element (see section 4.2.1). However, in order to capture the wavy characteristics of the device, the stent struts were generated by NURBS curves. In particular, after deriving $X_{strut}$, $Y_{strut}$, $X_{bridge}$, and $Y_{bridge}$, the construction of the unit cell with degree 5 NURBS[1] was carried out. The curve representing the unit cell has to occupy the $X_{strut} \times Y_{strut}$ rectangle,

---

[1] Degree 5 NURBS was chosen to enhance the local control of the curve in the design phase. This means that the curve could be modified locally without changing its entire shape (global shape of the curve).

(a) 3D virtual model of Promus Element

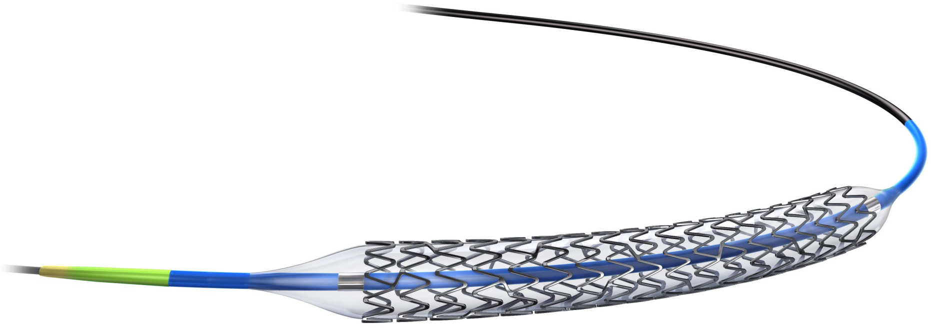

(b) Commercial device of Promus Element stent system (BostonScientific 2009)

Figure 4.4: Promus Element stent platform

whereas the curve representing the unit connector has to occupy the $X_{bridge} \times Y_{bridge}$ rectangle. Then, the control points of the curves were displaced appropriately in order to capture the wavy features of the struts (according to commercial images), Figure 4.5.

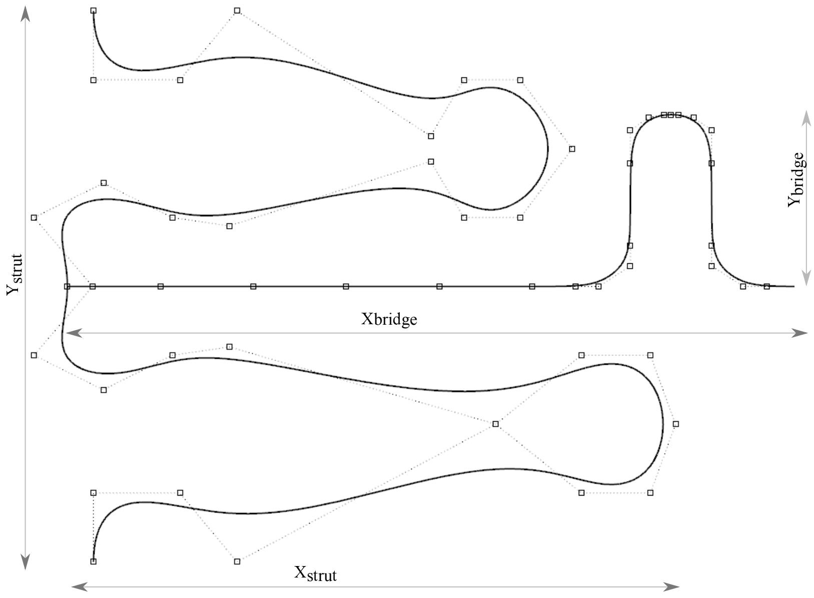

Figure 4.5: Unit cell and connector generation by degree 5 NURBS curves

Thereafter, the 3D stent generation was performed by the same methodology as that described for the Promus stent. The final solid **CAD** model of the Multi-Link coronary stent is depicted in figure 4.6a. The respective commercial stent system (actual) is illustrated in Figure 4.6b.

### 4.2.3 Stent C: Modified Stent

In order to improve the longitudinal integrity of Promus Element (see section 1.6), a variant of the Promus platform was constructed with two additional connectors in each of the first two proximal hoops. The planar sketch of the modified design is depicted in Figure 4.7. The circles illustrate the four additional connectors proximally on the device.

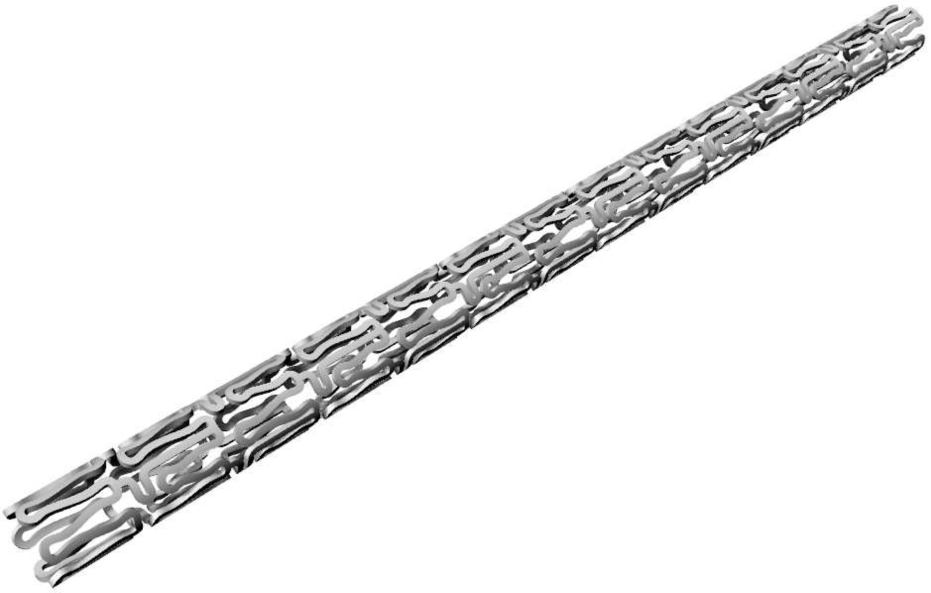

(a) 3D virtual model of Xience

(b) Commercial device of Xience stent system (AbbotVascular 2008)

Figure 4.6: XIENCE stent platform

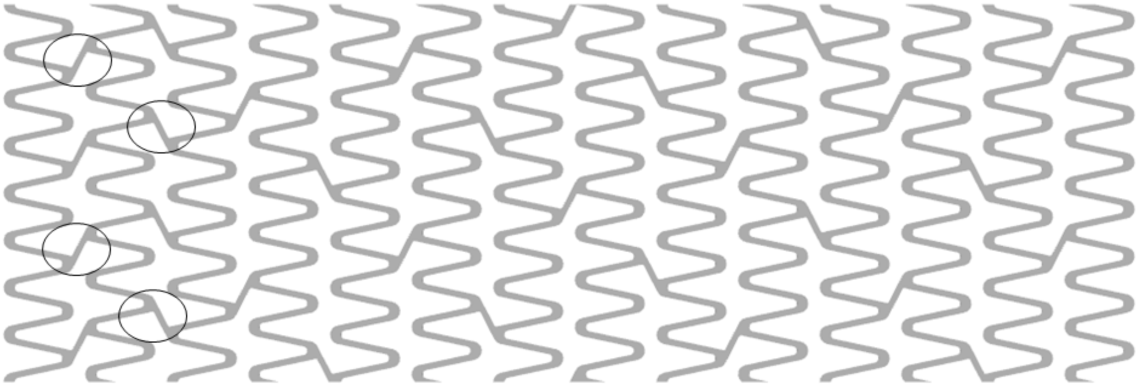

Figure 4.7: Planar sketch of the modified Promus Element (Stent C in Chapter 6). In total, four additional connectors were constructed at the proximal end of the device.

### 4.2.4 Stent D: CYPHER (Johnson & Johnson co., New Brunswick, NJ, USA)

For the purposes of the work presented in Chapter 6, the CYPHER stent was constructed. This closed-cell type stent represents an old "workhorse" device in PCI. It was characterised by very thick struts (140 $\mu m$) and its platform was manufactured by stainless steel (SS) (316L alloy). To generate the virtual model of the CYPHER stent the algorithm developed in Pant et al. (2011) was implemented. The solid **CAD** model of the CYPHER coronary stent is depicted in figure 4.8a. The respective commercial stent system (actual) is illustrated in Figure 4.8b.

## 4.3 Multi-folded balloon models

Multi-folded balloon models were developed in order to conduct realistic stent deployment simulations. As discussed in section 2.2.1, such balloon models were first used by De Beule (2008) (where the folding patterns of an interventional balloon model were considered) followed by Mortier et al. (2008) in which it was revealed that changing balloon's geometrical characteristics (number of folds, balloon length and the relative position of the stent on the balloon) had a great impact on certain outcomes of stent deployment (uniformity, symmetry and transient behaviour). However, in these studies, the tapered ends of these models were neglected by applying appropriate boundary conditions at the proximal and distal nodes. Thus, the methodology was lacking a technique to develop multi-folded balloons with tapered ends along with information on how to control the initial diameter of the balloon[2]. In Grogan et al. (2013), a 3.00

---

[2] As will be shown in section 5.2.3, the initial diameter is the diameter of the un-folded balloon configuration at zero pressure

(a) 3D virtual model of CYPHER stent

(b) Commercial device of CYPHER stent system (Lesiak 2004)

Figure 4.8: CYPHER stent platform

*mm* diameter balloon model with tapered ends was presented. The tapered ends were created by using the loft function of Abaqus/CAE. However, there was no information on how such a balloon can be parameterised with respect to different design variables.

For the purposes of this doctoral work, an algorithm was developed which can parameterise multiple balloon geometrical characteristics along with its tapered ends. This was very important when trying to optimise the dilation protocol (or optimising the balloon profile) in patient-specific vessels with challenging disease (see Chapter 8) where multiple different balloon models had to be generated and simulated. Furthermore, as presented in Chapter 7, novel varying diameter balloon models were generated by this algorithm to mitigate the risk of SM in vessels with diameter discrepancy along the intervened lesion length (cases 2 & 3 in Chapter 3).

### 4.3.1 Methodology

Figure 4.9 illustrates the crossing profile of a virtual five-folded balloon before a stent has been crimped onto it. Such a model can be designed by using five concentric circles. Each circle differs from the next by $D_0+2C_0$, where $D_0$ is the diameter of the first circle (slightly larger than the diameter of the catheter shaft), and $C_0$ is the constant distance between two sequential circles. In order to control the final diameter of any multi-folded balloon, an algorithm was developed which can parameterise the number/configuration of the folds and the unpressurised diameter of the balloon (see appendix D). The balloon models have been generated in Rhinoceros 5.0 (Robert McNeel & Associates, Seattle, WA, USA). Since the balloon was designed as a NURBS surface, a clearance (i.e. $C_0$) greater than the balloon thickness should always be ensured between the folds.

The basic steps of the trigonometric algorithm are as follows:

- the sum of the circumferences of the five circles is calculated in terms of $C_0$ as

$$C_t = 5\pi(D_0 + 4C_0) \tag{4.1}$$

- the total length of the three arcs, $S_{t123}$, subtracted by the angle $\theta$ (to be subtracted from the final profile) is

$$S_{t123} = 1.5\theta(D_0 + 2C_0) \tag{4.2}$$

- similarly, for the total arc length $S_{t45}$, from angle $\phi$, the corresponding relationship in terms of $C_0$ is

$$S_{t45} = \phi(D_0 + 7C_0) \tag{4.3}$$

- the lengths $L_1, L_2, L_3$ are derived as

$$L_1 = \sqrt{[0.5(D_0 + 4C_0) - 0.5D_0 \cos\theta]^2 + (0.5D_0 \sin\theta)^2} \tag{4.4}$$

$$L_2 = \sqrt{[0.5(D_0 + 6C_0) - 0.5(D_0 + 2C_0)\cos\theta]^2 + [0.5(D_0 + 2C_0)\sin\theta]^2} \tag{4.5}$$

$$L_3 = \sqrt{[0.5(D_0 + 8C_0) - 0.5(D_0 + 4C_0)\cos\theta]^2 + [0.5(D_0 + 4C_0)\sin\theta]^2} \tag{4.6}$$

- the general relation between the concentric circles and the profile of the multi-folded balloon in terms of $C_0$, is expressed by

$$C_t + 2N_{folds}C_0 + N_{folds}(L_1 + L_2 + L_3) - N_{folds}S_{t123} - N_{folds}S_{t45} - C_b = 0 \tag{4.7}$$

  where $C_t$ is the desired unpressurised balloon circumference, $C_t = \pi D_{b0}$, and $D_{b0}$ denotes the diameter of the unpressurised balloon and $N_{folds}$ specifies the number of balloon folds

- substitute eq. 4.1 –4.6 the eq. 4.7

- specify $D_0$, $\theta$, and $\phi$, and calculate $C_0$

The final step of a virtual multi-folded balloon construction was to create the tapered ends. Therefore, the balloons' tapered ends were generated by gradually reducing the size of the balloon wings from the initial profile (c.f Figure 4.9) to circular profiles with diameter equal to that of the catheter tip. This was accomplished by the loft command implemented in Rhinoceros.

As it will be shown in Chapter 7, balloon models with varying diameter along their length were constructed to optimise stent expansion in tapering vessels. To construct such balloons, different sized balloon profiles (c.f. Figure 4.9) were generated along the balloon length. As for the tapered ends, the Rhinoceros loft command was implemented to interpolate NURBS surfaces between the different profiles.

### 4.3.2 Results

As can be observed in Figure 4.9, an idealised profile is generated first with the desired clearance $C_0$. Then, the profile is modified by decreasing the control points of the

the interpolated five degree NURBS curve. The final NURBS close curve has the same length with the idealised profile. In Figure 4.10, for the same catheter shaft size and initial diameter, $D_{b0}$, balloon models with different number of folds, $N_{folds}$, are depicted.

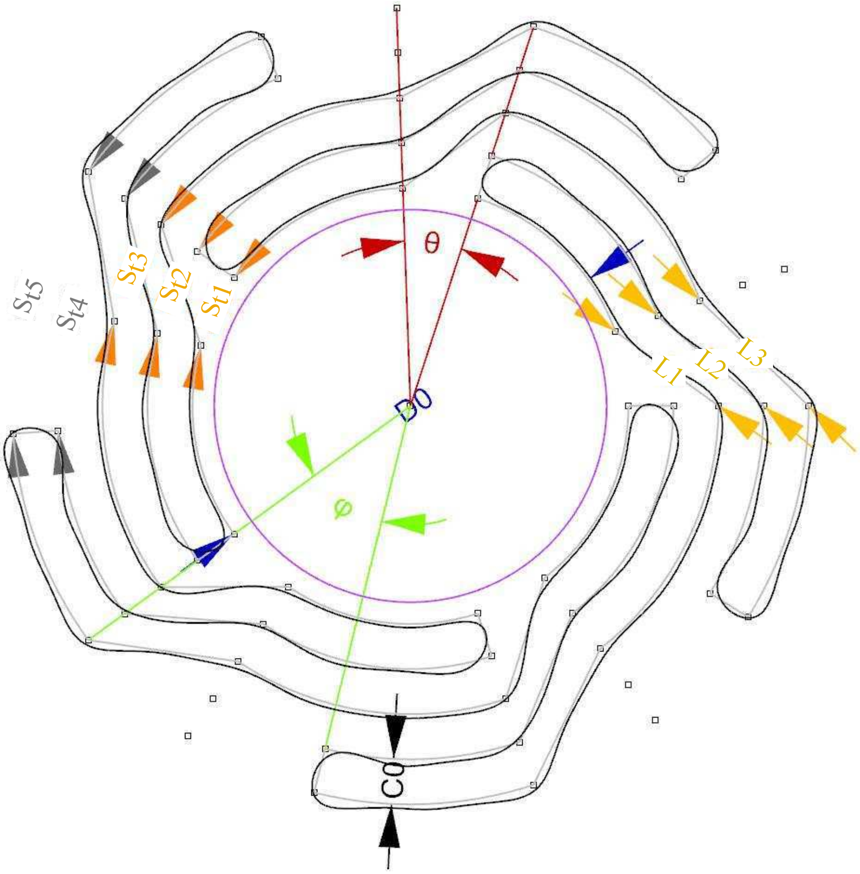

Figure 4.9: A sample **CAD** sketch of a five-folded balloon model: constant distance between two sequential circles, $C_0$, lengths connecting different balloon layers, $L_1$, $L_2$ and $L_3$, the three arc lengths (comprising $S_{t123}$), $S_{t1}$, $S_{t2}$ and $S_{t3}$ subtracted from angle $\theta$ and the two arc lengths (comprising $S_{t45}$), $S_{t4}$ and $S_{t5}$ subtracted by the angle $\phi$.

In Figure 4.11, a **CAD** model of a multi-folded stepped balloon is illustrated. As for the uniform balloon models, NURBS surfaces were interpolated through the different sized balloon profiles.

### 4.3.3 Discussion

A methodology was developed for the accurate and fast design of multi-folded balloon models. Being aware of the catheter shaft diameter, multi-folded balloon models with different numbers of folds, and folding angles can be easily generated. The choice of the folding angles is dependent on the designer and, as shown in Figure 4.10, the angles

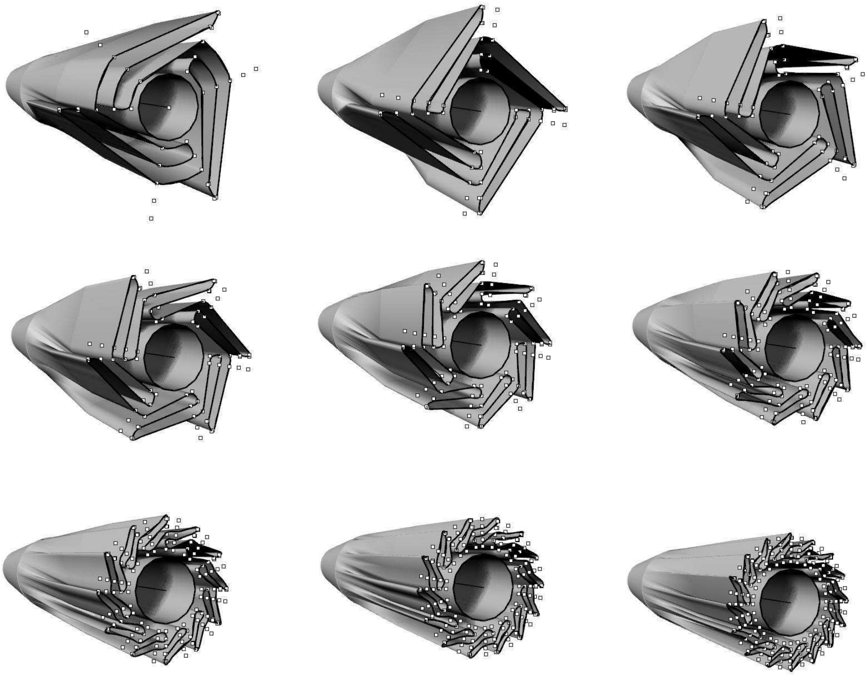

Figure 4.10: Multi-folded balloon models

of the folds directly affects the outer folding diameter (crossing profile of the balloon). Such models, are used in the next chapter, to simulate realistic stent deployments. Interestingly, this algorithm can significantly reduce the cross sectional folded profile when the number of the folds is to be increased.

Figure 4.11: A **CAD** design of a stepped multi-folded balloon model

## 4.4 Summary

In this chapter, the methodology followed to design and generate virtual contemporary stent systems was presented. All the models were parameterised and their generation was accomplished by the execution of python numerical scripts to ensure fast and accurate model construction. Especially for the generation of virtual multi-folded dilation systems, a trigonometric algorithm was developed to control the unpressurised diameter, the folding configuration and the number of the folds. This is essential when: i) investigating non-uniform dilation systems (see chapter 7) with varying diameter along their length, and ii) running optimisation studies (see chapter 8) in which many different models have to be generated to derive the optimum dilation strategy.

# Chapter 5

# FEA METHODS

FEA! The stenting simulation methods used in this thesis are presented in this chapter. Up-to-date of structural computational models of coronary stenting along with the description of the simulation parameters are presented in the following content. Where possible, verification and validation of the FEA models is also presented. At the end of this chapter, potential limitations arising from the material properties assigned to the presented FEA models are outlined and elaborated upon.

## 5.1 Introduction

In this doctoral thesis, the first step to simulate the stenting procedure in patient-specific vessels with challenging disease was the construction of the virtual space. This comprised the reconstructed arterial segments, as presented in Chapter 3 and the generated stent systems presented in Chapter 4. Then, different structural simulations were carried out to i) evaluate the longitudinal integrity of contemporary coronary artery stents, ii) calibrate/validate the balloon-stent expansion behaviour for different sizes of balloon models, iii) investigate the mechanical performance of novel stent-systems when implanted in patient-specific cases with challenging disease and iv) to optimise the stent expansion according to subject-specificity. Therefore, different FEA models and simulation parameters were used in each kind of simulation.

In the following content, the FEA methods used for the structural simulations carried out in this thesis are presented. Furthermore, where possible, the validation and the verification of FEA models is presented. Finally, the method of defining appropriate simulation parameters to run stable and reliable numerical simulations are analytically described.

## 5.2 FEA models

### 5.2.1 Reconstructed vessel models

#### 5.2.1.1 Vessel material properties

For the reconstructed patient-specific vessels presented in Chapter 3, the walls comprise: i) the intima-media layer extracted from the IVUS images for the first RCA case and ii) the intima-media layer (extracted from the IVUS images) along with the adventitia which was generated by assuming a scaling factor of 1.6 to non-diseased lumen areas (Holzapfel et al. 2005a, Mortier et al. 2010) for the second RCA and the third LMB case. Many constitutive models have been used to characterise arteries with the most representative being that reported by Holzapfel et al. (2005a). Clinical and experimental studies (Cook et al. 2009, van der Hoeven et al. 2008b, Hong et al. 2006, Ormiston et al. 2011) showed high correlation of SM and LSD with the stent system, the vessel size and the vessel complexity (tortuosity and plaque composition). Therefore, in order to simplify numerical analyses of patient-specific simulations, the wall of the vessel were modelled as follows:

- **a hyperelastic, neo-Hookean strain energy function for the intima-media layer**: the assumption was based on the fact that the average material of the vessel wall is plaque and the difficulty to extract the plaque composition from the IVUS images; therefore, constitutive parameters for a relatively soft plaque were selected. The latter is proposed by Wong et al. (2009) and its parameters were used within this group previously (Pant et al. 2012). Thus, the strain energy per unit of reference volume is:

  $$U = C_{10}(\bar{I}_1 - 3) + \frac{1}{D_1}(\mathcal{J} - 1)^2 \tag{5.1}$$

  where $\mathcal{J}$ is the total volume ratio, $C_{10}$ and $D_1$ are material parameters related to the shear and bulk moduli ($\mu_0 = 2C_{10}$ and $K_0 = \frac{2}{D_1}$), and $\bar{I}_1$ is the first invariant of the deviatoric Cauchy-Green deformation tensor, defined as

  $$\bar{I}_1 = \bar{\lambda}_1^{\,2} + \bar{\lambda}_2^{\,2} + \bar{\lambda}_3^{\,2} \tag{5.2}$$

  with the deviatoric stretches $\bar{\lambda}_i$ defined as

  $$\bar{\lambda}_i = \mathcal{J}^{-1/3}\lambda_i \tag{5.3}$$

and $\lambda_i$ are the principal stretches, and $\mathcal{J}$ is the total volume ratio, expressed as

$$\mathcal{J} = \det(\mathbf{F}) \tag{5.4}$$

with **F** being the deformation gradient.

- **an isotropic hyperelastic constitutive model described by a sixth-order reduced polynomial strain energy function for the adventitia layer**: the material parameters were defined by Holzapfel et al. (2005a) and they have been used within our group previously (Pant et al. 2011). The sixth order reduced polynomial strain energy function is expressed as

$$\begin{aligned} U = {} & C_{10}(\bar{I}_1 - 3) + C_{20}(\bar{I}_1 - 3)^2 + C_{30}(\bar{I}_1 - 3)^3 + C_{40}(\bar{I}_1 - 3)^4 \\ & + C_{50}(\bar{I}_1 - 3)^5 + C_{60}(\bar{I}_1 - 3)^6 + \frac{1}{D_1}(\mathcal{J} - 1)^2 \end{aligned} \tag{5.5}$$

  In Holzapfel et al. (2005a), the deformation behaviour of 13 non-stenotic human left anterior descending arteries were studied and a constitutive model for each of the three layers was proposed. Their results were implemented for the sixth order reduced polynomial strain energy density function, equation 5.5, by Gervaso et al. (2008), Zunino et al. (2009), and recently by Pant et al. (2011). The six material parameters that were used to define the adventitia layer, are depicted in table 5.1.

Table 5.1: Constitutive material parameters of the adventitia layer (Gervaso et al. 2008, Zunino et al. 2009)

| Layer | $C_{10}$(MPa) | $C_{20}$(MPa) | $C_{30}$(MPa) | $C_{40}$(MPa) | $C_{50}$(MPa) | $C_{60}$(MPa) |
|---|---|---|---|---|---|---|
| Adventitia | $8.27 \times 10^{-3}$ | $1.20 \times 10^{-1}$ | $5.20 \times 10^{-1}$ | $-5.63$ | 21.44 | 0.00 |

The hyperelastic materials were modelled as nearly incompressible with Poisson's ratio, $\nu = 0.495016$. As recommended in ABAQUS User's manual (SIMULIA 2013), for Explicit analyses, an upper ratio limit of 100 was used between the bulk modulus, $K_0$ and the shear modulus, $\mu_0$. The theoretical material behaviour of the intima-media and the adventitia layer as evaluated in ABAQUS is depicted in Figure 5.1a and 5.1b, respectively. To validate the accuracy of the hyperelastic models (with respect to incompressibility), preliminary computational analyses of a single-continuum element (C3D8R) uniaxial tension test were performed. As shown in Figure 5.1, the theoretical response of the fitted hyperelastic material models were in good agreement with the respective numerical behaviour.

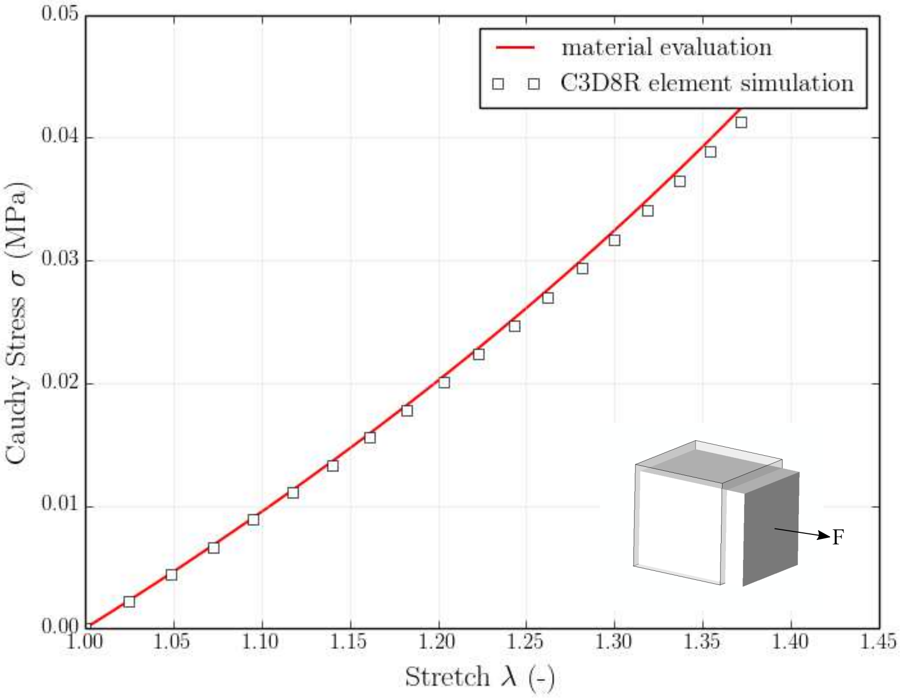

(a) Intima-media layer (Neo-Hookean model)

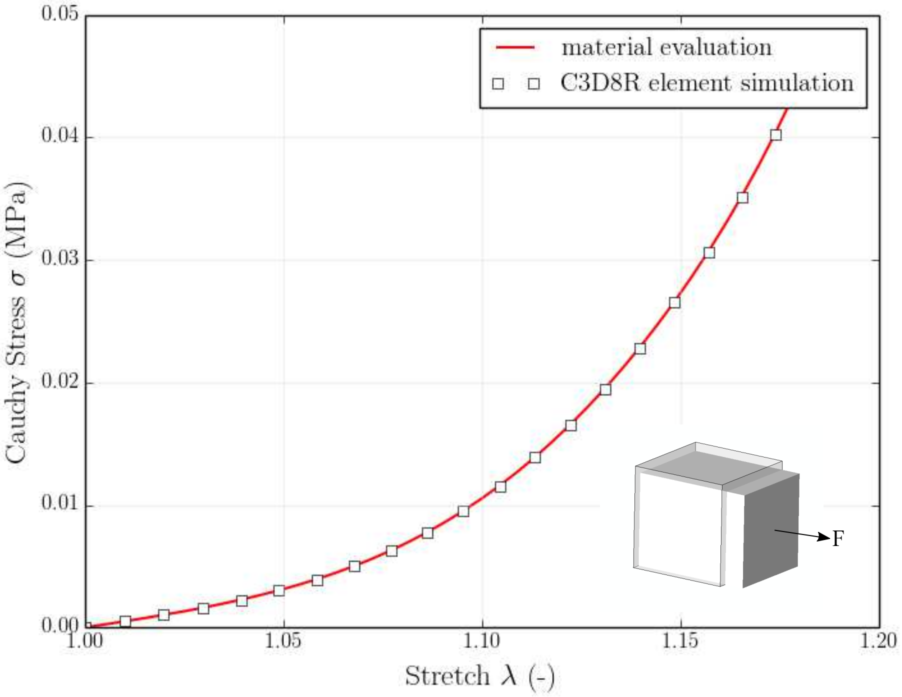

(b) Adventitia layer (Six order reduced polynomial model)

Figure 5.1: Uniaxial tensile stress-stretch theoretical response for vessel wall layers (solid red lines) compared against the respective numerical response of a single-element ($C3D8R$) uniaxial tension test (squared data points)

#### 5.2.1.2 Mesh convergence test

The vessels were meshed with solid hexahedral structured mesh (see section 3.3.3) by using eight node linear brick elements with hourglass control (ABAQUS element type C3D8R). To test the quality of the mesh resolution which was used to discretise the vessels, a mesh verification test was carried out for the first RCA vessel. The mesh size was selected after simulating stent deployment in the RCA segment and by comparing a baseline seed-sized mesh (based on previous studies of this group) against a finer mesh. Differences less than 0.5% were recorded in the mesh-independence test (c.f. Figure 5.2). Therefore, based on this test, the total number of elements which were used for the first, the second and the third reconstructed case was $21,214$, $110,200$ and $196,052$, respectively.

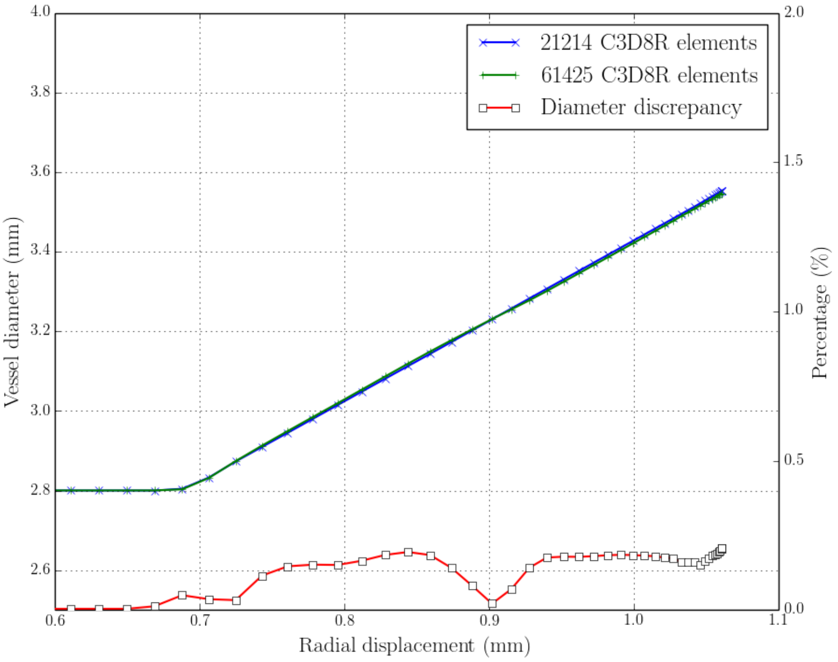

Figure 5.2: Mesh independence test for the first reconstructed vessel: differences less than 0.5% were recorded in a cross-section in the middle of the segment.

### 5.2.2 Stent models

#### 5.2.2.1 Stent material properties

The stents were modelled as rate-independent isotropic elastic-plastic materials with isotropic hardening. Their material properties have been adopted by O'Brien et al. (2010) (c.f. Table 5.2). Bilinear functions were implemented to describe the material behaviour of the Pt-Cr, CoCr and SS alloy as depicted in Figure 5.3a, 5.3b and 5.3c, respectively.

Table 5.2: Material properties of the investigated stents adopted by O'Brien et al. (2010)

| Stent Alloy | Elastic modulus (GPa) | 0.2% Yield Strength (MPa) | Tensile Strength (MPa) | Elongation (%) | Density ($g/cm^3$) |
|---|---|---|---|---|---|
| Pt-Cr | 203 | 480 | 834 | 45 | 9.9 |
| Co-Cr L605 | 243 | 500 | 1000 | 50 | 9.1 |
| 316L SS | 193 | 275 | 595 | 60 | 8.0 |

#### 5.2.2.2 Mesh convergence test

To create a reliable stent FEA model, the initial prerequisite is to discretise it with a high quality mesh. Therefore, after generating the computer aided design instances representing the stent platforms, solid hexahedral elements were used for meshing (ABAQUS element type C3D8R). In order to verify the mesh quality, different numbers of elements were assigned to the Promus Element model through its strut thickness and width increasing the total mesh density. The mesh convergence test was carried out after crimping and expanding the device (Promus Element) by deformable cylindrical surfaces (c.f. Figure 5.4).

Thereafter, a quantitative comparison was carried out between the different meshes by monitoring the displacement values in a cross section segment in the central part of its length. In Figure 5.5, bar plots of the displacement values within this cross section are depicted. The discrepancy produced by the Mesh 1 and Mesh 2 and 3, is in the acceptable range of 2.5%. Therefore, the coarser mesh comprising $36,944$ elements was picked for the numerical analysis. This mesh was generated by assigning two elements along the stent strut thickness and three elements along the stent strut width. According to this mesh size (element dimensions), respective mesh discretisation of the other stent models was carried out. In particular, the XIENCE, and the modified Promus Element stent were discretised by assigning two elements along the strut thickness and three elements along the strut width resulting in $46,216$ and $37,286$ elements, respectively. The CYPHER stent was discretised by assigning four elements along the strut thickness (due to the increased thickness of its platform) and three elements along the strut width resulting in $76,352$ elements. The mesh resolution of the CYPHER stent was in agreement with that used in Pant et al. (2011).

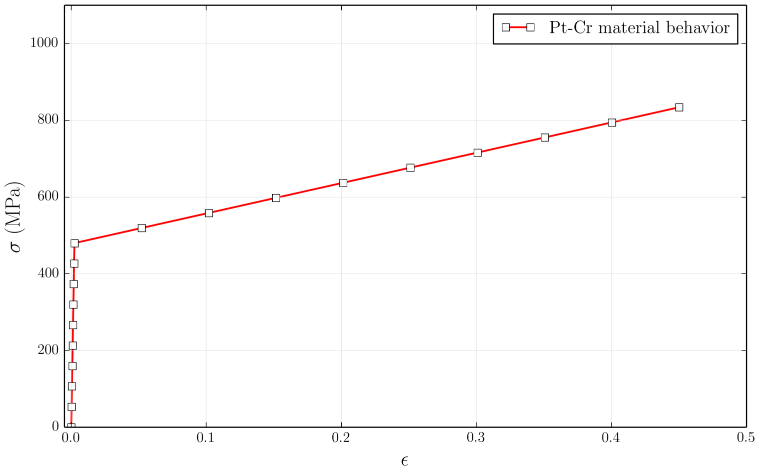

(a) Elastic-plastic stress strain response of the Pt-Cr alloy

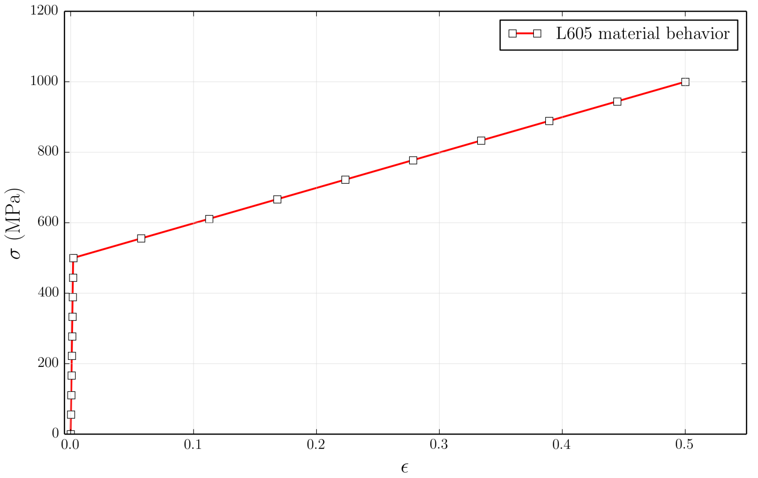

(b) Elastic-plastic stress strain response of the Co-Cr alloy

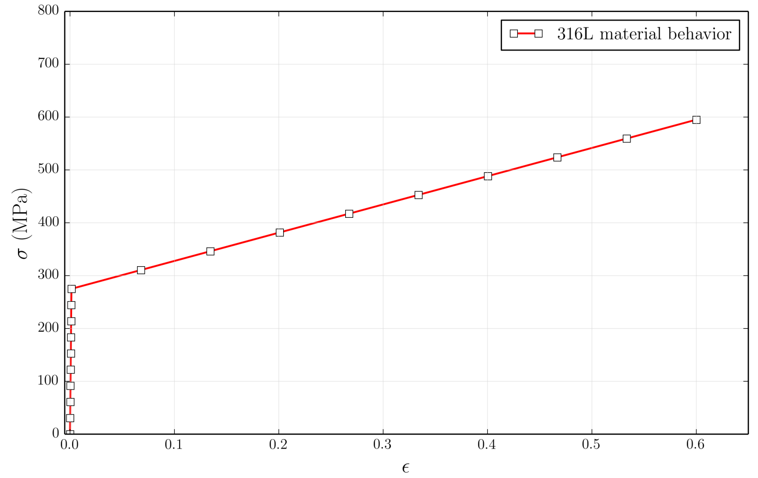

(c) Elastic-plastic stress strain response of the SS alloy

Figure 5.3: Constitutive behaviour of the investigated stents

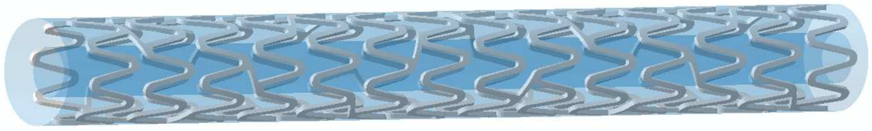

Figure 5.4: Initial assembly of the mesh convergence simulation test. An external surface is controlled by pre-defined displacement to crimp the stent onto the internal surface. Then, the internal surface expands the stent to its nominal diameter

### 5.2.3 Delivery system models

#### 5.2.3.1 Balloon material properties derivation

In this work, after developing a design framework for the realistic balloon construction (see section 4.3), appropriate balloon material properties were defined. In particular, the balloon material properties were derived from the compliance chart (provided by the manufacturer), the thickness of the balloon, and the diameter of the catheter shaft as described by De Beule (2008) and is based on thin shell membrane theory (Timoshenko 1955). Under this theory a balloon can be modelled as thin-walled pressure vessel having a wall thickness less than 0.1 of its inner radius. The balloon material is to be assumed linear elastic, isotropic and homogeneous and is in a state of plane stress. Since the relationship between the pressure and the diameter is not linear (i.e balloon inflation in large diameters, the presence of a stent and friction during the transient unfolding of the balloon), different values of the initial diameter $D_{b0}$ (see section 4.3 for $D_{b0}$ definition) were tested to obtain the best fit (between the actual and the virtual compliance charts). For all the virtual balloons modelled in this work, a Young's modulus $E = 888.52\ MPa$ and a Poisson ratio $\nu = 0.4$ was defined to describe their constitutive material behaviour.

The catheter shaft and tips were modelled as elastic isotropic material manufactured from high density polyethylene. The guide wire was considered to be elastic isotropic, manufactured from nitinol. The superelastic properties of nitinol were neglected because the guide wire deformations were negligible. The material properties of catheter shaft/tips and guide wire are depicted in table 5.3.

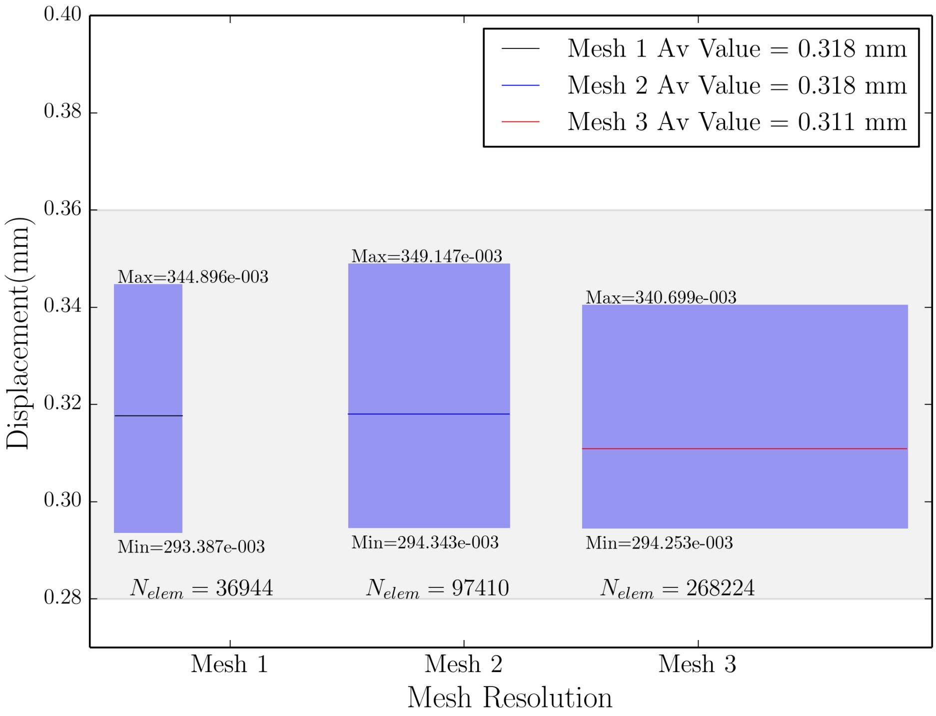

Figure 5.5: Mesh quality verification test: displacement values

Table 5.3: Material properties of catheter system

| | Material | Elastic Modulus(MPa) | Poisson's Ratio | Density ($tonne/mm^3$) |
|---|---|---|---|---|
| Guide Wire | Nitinol | 62E+003 | 0.3 | 6.5E-009 |
| Catheter shaft/tips | PEHD | 1000 | 0.4 | 9.7E-010 |

#### 5.2.3.2 Numerical aspects and mesh convergence test

The mesh discretisation was carried out in ABAQUS CAE. The catheter shaft has been meshed by four node linear quadrilateral shell elements of type S4R. The catheter tips and the guide wire have been modelled by three-dimensional 8-node brick "reduced-integration" elements of type C3D8R. The folded balloon models were discretised by four node quadrilateral membrane elements of type M3D4R. The number of elements varies depending on the balloon length and the folding configuration. However, for each instance, the seed size on the edges was selected according to a mesh independence test. This was carried out for a virtual balloon by simulating free stent balloon expansions.

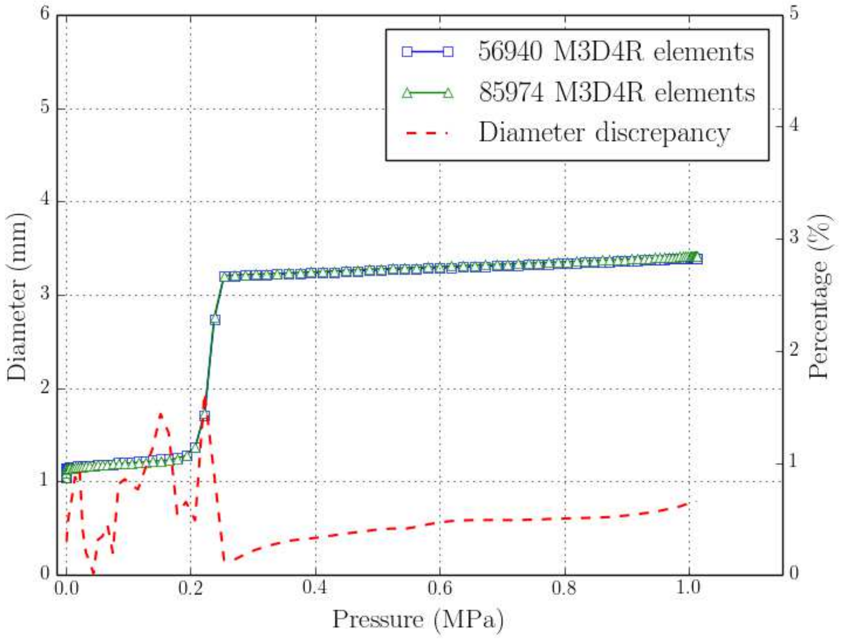

Figure 5.6: Mesh independence test for a balloon model: differences less than 2% in the transient expansion diameter were recorded in the middle part of the model

Specifically, a baseline size-mesh (based on previous study of this group) was tested against a finer mesh and differences between expansion diameter remained less than 2% throughout the transient analysis (c.f. Figure 5.6).

The balloon's fixation to the catheter was modelled by tie constraints. The catheter tips along with the catheter shaft were fully constrained proximally and distally. The free stent-balloon expansion simulations were carried out in ABAQUS/Explicit. Contacts between the balloon internal surface and the catheter shaft were implemented with the general contact algorithm, imposing a hard frictionless contact. The balloon was inflated by a smooth pressure applied incrementally to its inner surface. During the inflation step, the central ring's nodal coordinates were monitored to calculate the radial displacements. For both the stent and balloon models, a self contact was defined by the general contact algorithm. A surface-to-surface contact was defined for the balloon-stent pair. The tangential contact behaviour was characterised by a 0.2 friction coefficient as suggested elsewhere (De Beule et al. 2008).

#### 5.2.3.3 Balloon calibration/validation

Figure 5.7 depicts a compliance chart for a 3.5 *mm* balloon model (with/without mounted stent) with 0.02 *mm* wall thickness and 3.383 *mm* initial diameter. Figure 5.8 depicts the transient unfolding of a six-folded balloon during its free expansion

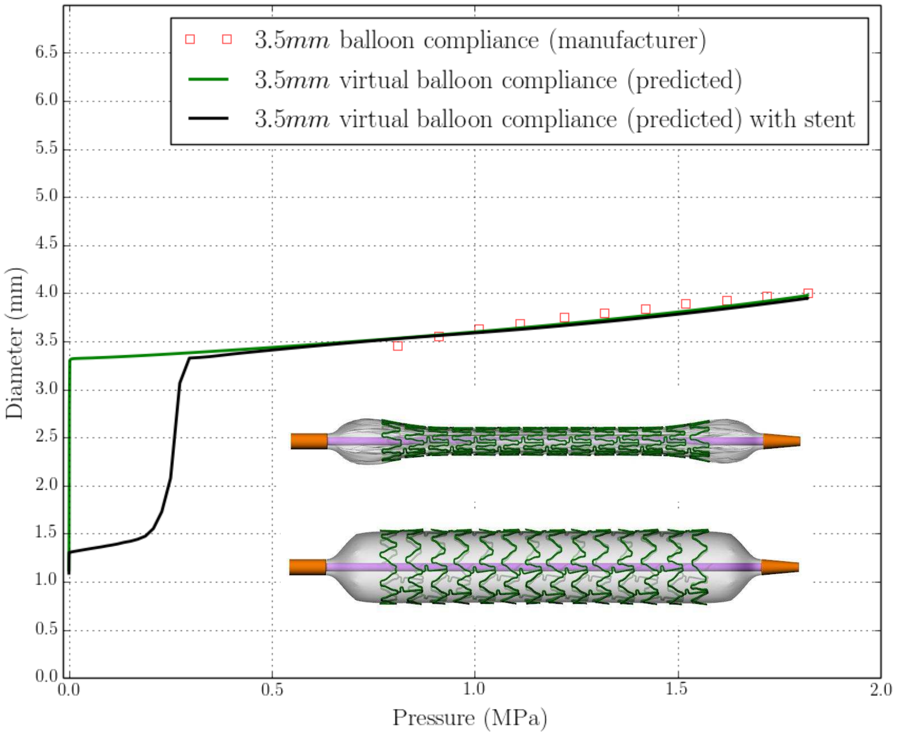

Figure 5.7: Calibration of the virtual behaviour of a 3.5 $mm$ balloon model: Simulation balloon compliance charts for a 6-folded balloon configuration superimposed on the manufacturer's data (AbbotVascular 2008)

simulation. By way of calibration/validation, the virtual balloon is pressurised at a range of pressures and shown to closely follow the expansion behaviour of the actual interventional balloon especially at nominal pressures ($0.8 - 1.2\ MPa$). For each balloon model which was used in this doctoral work, respective calibration/validation tests were carried out to ensure that under a certain pressure the model would be deployed at the desired diameter.

## 5.3 Definition of the parameters of FEA simulations

For the numerical simulations, the commercially available FEA solver, ABAQUS (Simulia, Dassault Systemes, Waltham, MA, USA) was used. The ABAQUS FEA package provides two different tools to solve structural problems; ABAQUS/Standard (solves for static and dynamic equilibrium) and ABAQUS/Explicit (solves for dynamic equilibrium). Each of the solvers has its own advantages and disadvantages and several

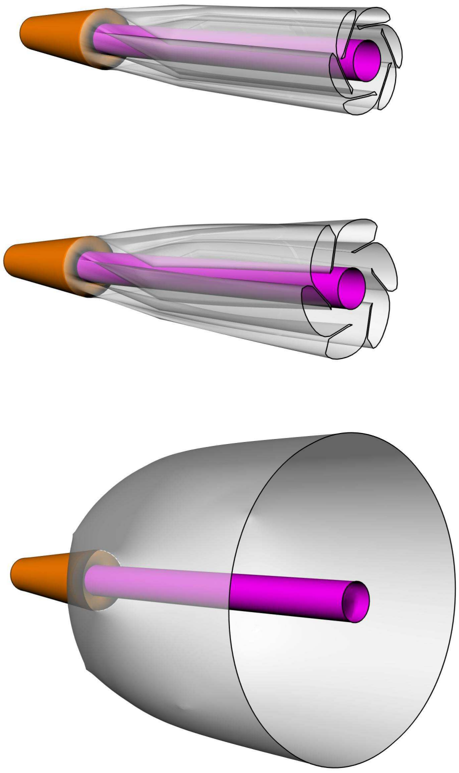

Figure 5.8: Cross sections of a six-folded balloon model: transient unfolding during the free expansion simulation

studies have been recently published to compare the two strategies (Harewood and McHugh 2007, Sun et al. 2000) (see also section 2.1). For the purposes of this thesis, three different problems were simulated: i) stent longitudinal compressions, ii) free balloon-stent expansions and iii) balloon-stent expansions in the reconstructed vessels. All of these kinds of simulations were characterised by a large number of degrees of freedom, self-contact and multiple contact conditions between the simulated instances and, finally, large and highly nonlinear deformations. Thus, the extremely robust contact algorithms available in ABAQUS/Explicit provide a clear advantage over the Standard method.

### 5.3.1 Stability of the solution scheme

ABAQUS/Explicit solver uses a central difference rule to integrate the equations of motion explicity through time. As discussed in section 2.1, the time increment $\Delta t$ which drives the analysis duration must be small enough to provide a stable solution. This $\Delta t$ depends on the characteristic element length, $L_e$, density, $\rho$, and the material properties (Young's modulus, $E$) of the simulated structure. An estimate of the stable time increment size is given by the formula

$$\Delta t_{stable} = \frac{L_e}{c_d} \tag{5.1}$$

where $c_d$ is the dilation wave speed of the material. For a linear elastic material, the dilation wave speed is given by

$$c_d = \sqrt{\frac{E}{\rho}} \tag{5.2}$$

Essentially, $\Delta t_{stable}$ changes when i) different mesh size is used to discretise the models and/or ii) different material properties are defined for the structure which is to be modelled. In this doctoral work, since the simulations comprised different models (e.g. stent, balloon, artery, etc.) the $\Delta t_{stable}$ was dependent on the stent structure which had the most "critical" elements (having the minimum $\Delta t_{stable}$).

### 5.3.2 Time scale definition of the simulations

Quasi-static conditions were ensured by implementing all the appropriate actions in order to eliminate the inertial forces to that of the deformation of the structure only. Throughout the whole period of each step, the kinetic and internal energies of deforming materials were monitored so as to keep their ratio less than 5%, as recommended for a quasi-static event (SIMULIA 2013). Since it is computationally impractical to model the process in its natural time period (literally millions of time increments would be required), the speed of the process in the simulation was artificially increased to obtain an economical solution. The goal was to model the process in the shortest time period in which inertia forces are still insignificant. This was achieved by increasing the loading rate. The time scale of the analyses was based on the extraction of the fundamental frequency (first structural mode) of the stent models by running frequency analysis in ABAQUS/Standard (SIMULIA 2013). As an example, in Figure 5.9, the fundamental frequency extraction of the Promus Element stent is depicted.

Thereafter, the frequency of this mode was used to estimate the impact velocity using the following steps:

- calculate the corresponding time period ($T$) using the first natural frequency by

$$T = \frac{1}{f} \tag{5.3}$$

- estimate the global deflection (target displacement required in the compression simulations), $D_{global}$, in the impact direction of the model.

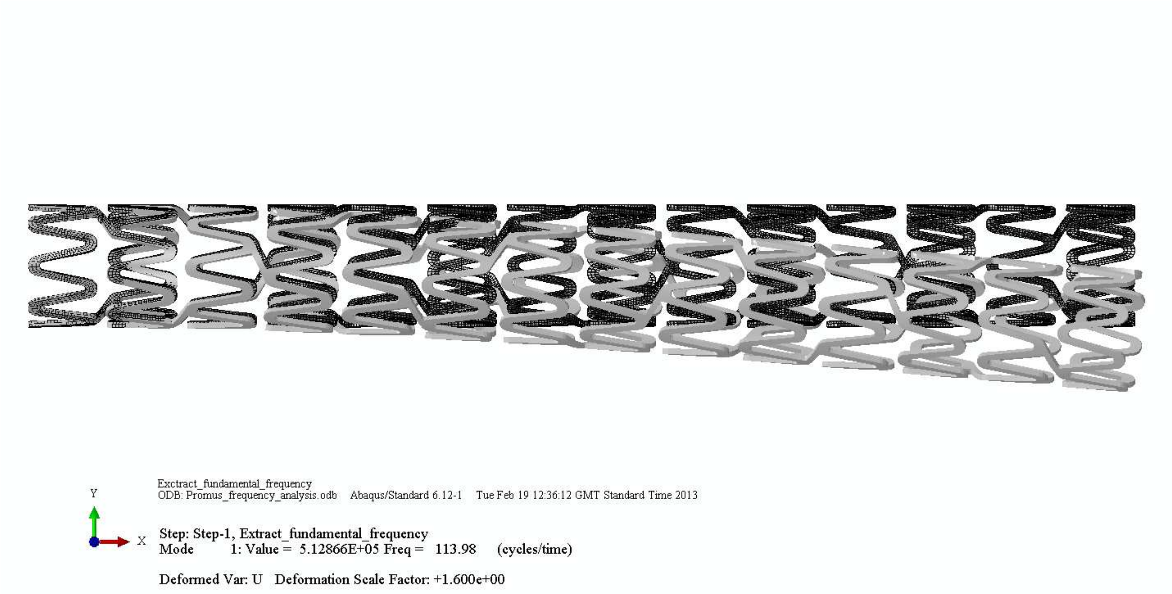

```
Exctract_fundamental_frequency
ODB: Promus_frequency_analysis.odb    Abaqus/Standard 6.12-1    Tue Feb 19 12:36:12 GMT Standard Time 2013

Step: Step-1, Extract_fundamental_frequency
Mode        1: Value =  5.12866E+05 Freq =   113.98     (cycles/time)

Deformed Var: U   Deformation Scale Factor: +1.600e+00
```

Figure 5.9: Fundamental frequency extraction of the Promus stent design

- calculate the impact velocity ($V_{impact}$) from

$$V_{impact} = \frac{D_{global}}{T} \tag{5.4}$$

A general recommendation is to limit the impact velocity to less than 1% of the wave speed of the material (typically, the wave speed in metals is usually close to 5000 $m/s$) and it is recommended that the load to be applied over a period calculated from the fundamental frequency, has to be ten to fifty times longer than the lowest frequency[1] (SIMULIA 2013).

Finally, the chosen loading rate was based on a period sensitivity test. Figures 5.10a and 5.10b depict the maximum values of kinetic energy and displacement during stent deformation. The time periods chosen ranged from 0.04 to 0.24 $sec$[2]. It was observed that after 0.16 $sec$, the differences of the kinetic energy and the displacement values are converged.

Figure 5.11 illustrates the kinetic and the internal energy of the stent during the crimping, expansion and deformation phase. The ratio of internal to kinetic energy is also depicted. As seen, a steep initial high ratio occurs in the first increments of the simulation. This is mainly due to the fact that inertial effects cause increased (non-structural) resistance to initial deformation.

---

[1] Attention should be paid to how the loading is applied. Instantaneous loading may induce the propagation of a stress wave through the model, producing undesired results. Again, it is recommended to ramp up the loading gradually from zero so as to minimise these adverse effects

[2] Note that the time scale in x-axis of the figures includes the two additional steps of crimping and expansion of the stent to its nominal diameter

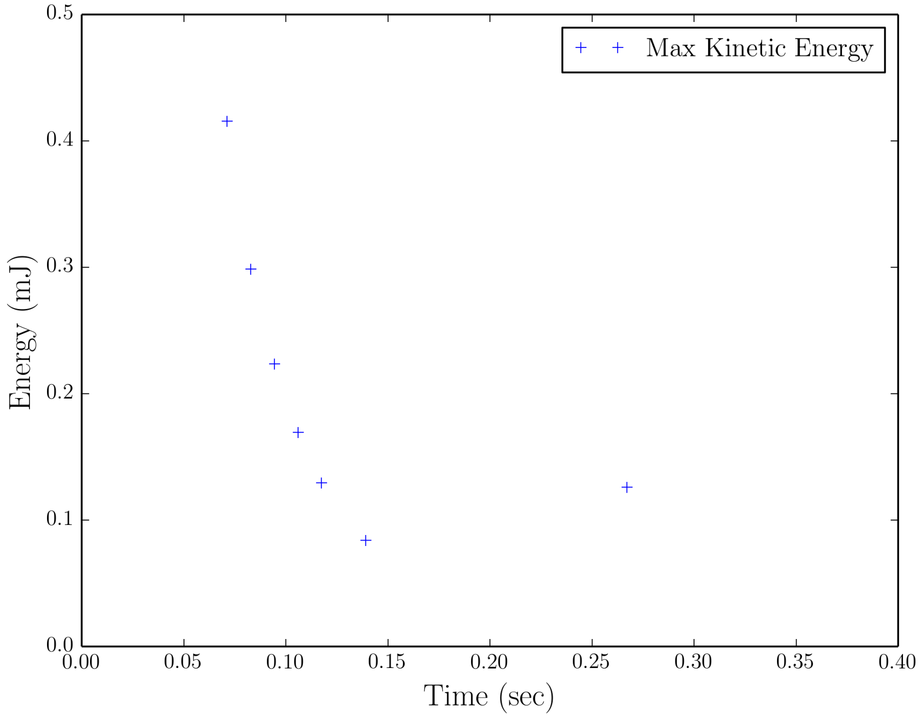

(a) Maximum Kinetic Energy during the stent deformation for $T$: 0.04, 0.06, 0.08, 0.10, 0.12, 0.16, and 0.24 *sec*

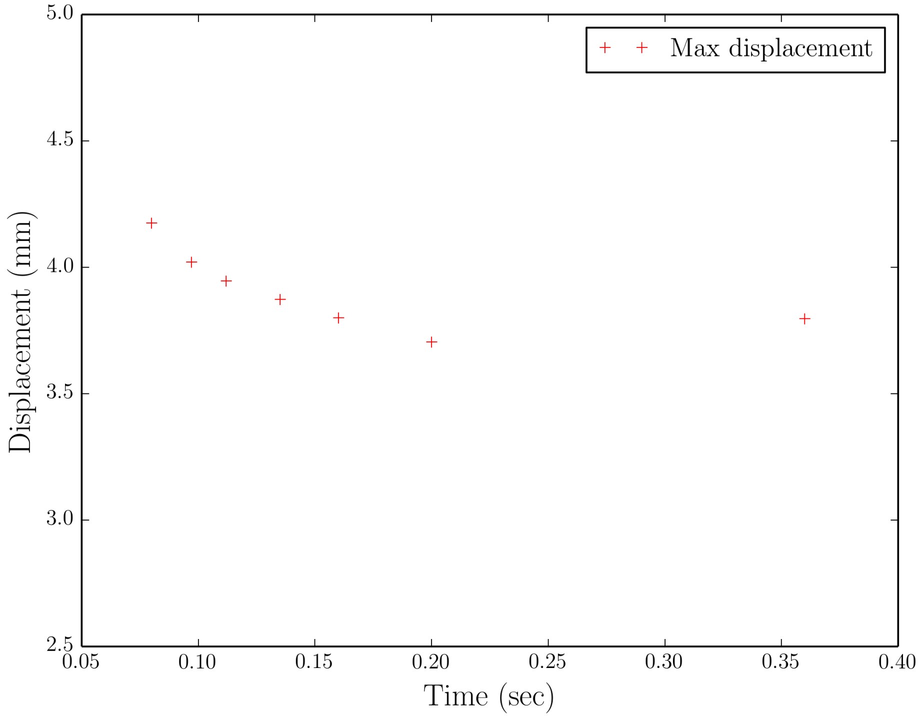

(b) Maximum displacement during the stent deformation for $T_f$: 0.04, 0.06, 0.08, 0.10, 0.12, 0.16, and 0.24 *sec*

Figure 5.10: Period sensitivity test

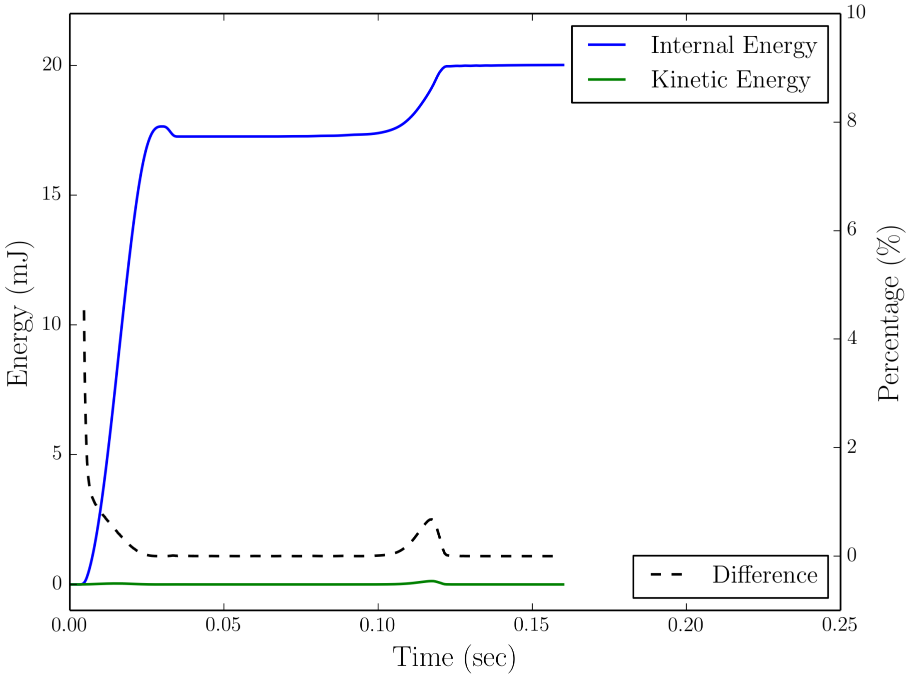

Figure 5.11: Internal and Kinetic Energy for a total simulation time period of 0.16 *sec*. The ratio of kinetic to the internal energy is also depicted

## 5.4 Limitations of the FEA models

The major limitation of the presented FEA models is the constitutive laws characterising the material behaviour of the vessel walls. More advanced constitutive models have been used in the literature with the most representative being the one implemented in Mortier et al. (2010) and Conway et al. (2012). In this hyperelastic anisotropic model introduced in Holzapfel et al. (2005a), the fibre orientation and dispersion are taken into account with respect to a reference orthonormal coordinate system defined in each element of the mesh. For each layer, different scalar parameters are defined, derived by experimental testing. However, in order to implement advanced constitutive models, the calibration of the parameters is essential. Moreover, the fibre orientation and dispersion in a severely diseased vessel and in a bifurcation would be really difficult to obtain, especially by using available clinical data. In addition, the vessel description lacks a constitutive model for the plaque composition. This is due to the fact that our reconstruction method is based on IVUS and CA from which the plaque composition is difficult to accurately define and orientate. A multilayer model would definitely have some influence on the stress values and the overall deformations of the walls. However, due to the comparative nature of the studies which are presented in the following chapters, simpler models can still provide valuable results especially for indicating the non-physiological stress state in regions interacting with the stent system. For this reason, other aspects regarding the arterial wall conditions were also neglected such as tissue pre-stretch and arterial blood pressure.

An additional limitation of this work is that the balloon material behaviour is characterised by an isotropic and linear elastic model with the thickness of the balloon being constant. In reality, modern balloon models are dual layer composites. Therefore, balloons can be characterised by different anisotropic and hyperelastic models (Holzapfel 2000). Moreover, in clinical practice, the balloon is expanded via a hydraulic pressure resulting from inserting a certain volume of liquid into the balloon. Thus, the actual problem of a balloon expansion can only be modelled as a complex FSI problem. However, since the balloon models have been compared to real compliance charts, the virtual expansion behaviour should closely match that which occurs in clinical practice, especially at nominal pressures.

Finally, the material properties assigned to the stent models were taken from O'Brien et al. (2010) and bilinear functions were implemented to describe their elasto-plastic behaviour. Therefore, they might not fully reflect the mechanical behaviour of the respective commercial devices (especially for the plastic region in the stress-strain curves of the alloys).

## 5.5 Summary

In this chapter, a description of the FEA models which have been used in the current doctoral work was provided. This description was with respect to the material constitutive laws used to carry out stenting simulations along with the mesh resolution that discretised the virtual spaces. Further, a general overview of the methods used to set appropriate simulation parameters for the explicit solver was supplied.

Several FEA models were simulated for the purposes of this doctoral work. The mesh resolution of each numerical model differed according to its size. However, each instance was meshed with a specific mesh resolution (element dimensions) extracted after running mesh verification tests. Similarly, the simulation parameters for each kind of simulation (g.e. balloon-stent expansion, stenting in the reconstructed vessels, etc.) were based on appropriate tests to avoid numerical instability and ensure quasi-staticity.

The content of the preceding sections considered the implemented FEA methodology. Additionally, multiple methods were used to carry out the studies presented in the following three chapters. Each of the following three chapters begins with a brief introduction of the investigated clinical problems along with the description of the objectives. Then, different implemented methods to carry out the simulations and to extract quantitatively and qualitatively information are reported. Finally, the results followed by a discussion are presented.

# Chapter 6

# SIMULATIONS OF LSD AND STENT MALAPPOSITION IN A PATIENT SPECIFIC CORONARY ARTERY

PCI MODELLING! The aim of the work presented in this chapter was to assess the longitudinal integrity of first and second generation drug eluting stents in a patient specific coronary artery segment and to compare the range of variation of applied loads with those reported elsewhere. Computational models of three drug-eluting stent designs (described in sections 4.2.1, 4.2.2 and 4.2.4) when assessed for longitudinal deformation were successfully validated. Then, the first reconstructed patient-specific stenosed right coronary artery segment, described in section 3.3, was used for the simulations. Within this model the mechanical behaviour of the same stents along with a modified device (see section 4.2.3) was compared. Specifically, after the deployment of each device, a compressive point load of 0.3 $N$ was applied on the most malapposed strut proximally to the models. Results indicate that predicted stent longitudinal strength (i) is significantly different between the stent platforms in a manner consistent with physical testing in a laboratory environment, (ii) shows a smaller range of variation for simulations of *in vivo* performance relative to models of *in vitro* experiments, and (iii) the modified stent design demonstrated considerably higher longitudinal integrity. Interestingly, stent longitudinal stability may differ drastically after a localised *in vivo* force compared to a distributed *in vitro* force[1], [2].

---

[1] A part of the content of this chapter was presented in the ASME Summer Bioengineering Conference:**Patient-Specific Stent Malapposition in Challenging Anatomy: An FEA methodology to understand numerically the extend of malapposition of latest generation stents**, G. Ragkousis, N. Curzen, N. Bressloff., 26-29 June 2013, Oregon, USA

[2] The content of this chapter has been published in the Journal of Medical Engineering & Physics: **Simulation of longitudinal stent deformation in a patient-specific coronary artery**, G.Ragkousis, N. Curzen, N. Bressloff., Vol.36, 2014 (pp 467-476)

## 6.1 Introduction

As discussed in chapter 1, PCI is now the dominant method of revascularisation, with proven symptomatic and prognostic efficacy. Since the introduction of DES, there has been a marked reduction in events associated with stent failure, in particular ISR. However, DES have been associated with allergic reactions, stent malapposition and inflammation leading to early and late ST (Cook et al. 2009). Furthermore, there are on-going concerns about the attritional nature of the potential sources of failure of PCI, including ISR, ST and, more recently, LSD.

Clinical studies (Cook et al. 2007, van der Hoeven et al. 2008b, Hong et al. 2006), have shown that malapposition is connected with several factors, such as reference diameter, balloon pressure, longer lesions, longer stents, more than one stent or stent overlap. In those studies stent malapposition was investigated by intravascular means such as IVUS or OCT. When malapposition is observed clinically, post stent deployment with a non-compliant balloon dilation is used to further reshape the stent. Such post-deployment techniques, including also re-wiring or IVUS, can potentially contribute to stent distortion. Studies indicate that those deformations are more likely to occur when the proximal struts are incompletely apposed (Hanratty and Walsh 2011, Robinson et al. 2011, Williams et al. 2012).

It is apparent that the iterative process of design in DES has led to reduced ISR (along with anti-inflammatory stent coatings) with reduction in strut thickness, but that an increased reporting of LSD may be a consequence of this evolution (Hanratty and Walsh 2011, Mortier and De Beule 2011, Robinson et al. 2011, Williams et al. 2012). It is therefore important that new stent designs are tested as thoroughly as possible to detect potential flaws.

As discussed in section 1.7, to date, there have been two experimental (engineering) studies shedding light on LSD (Ormiston et al. 2011, Prabhu et al. 2012). However, no patient-specific computational studies have been reported. It is likely that sophisticated computer modelling will play an increasing role in this process of validation and testing.

In the work presented in this chapter, the first reconstructed RCA segment presented in Chapter 3 was simulated; a computer model was developed for the deployment in this segment of different coronary stent architectures based upon one first generation and two second generation DES; post-deployment malapposition was assessed; and the effect of stent malapposition and stent architecture on the response of the devices to a compressive longitudinal force was modelled. The proposed approach allows quantification and 3D visualisation of LSD along the entire length of the model, in contrast to the currently used LSD measurement techniques based on IVUS cross sectional images. It was shown to validate this model as a potential tool for assessment of stent design behaviour and to test it using previously reported physical bench testing data.

## 6.2 Materials and Methods

### 6.2.1 Geometry, meshes and constitutive models

The vessel reconstruction procedure has been presented in detail in section 3.3. For the stents, firstly two balloon expandable stent models were generated whose architecture is closely based upon contemporary stent designs used in the clinical arena (see sections 4.2.1 and 4.2.2). Of the stents studies here, Stent A, that resembles the Promus Element (Boston Scientific, Boston, MA, USA), is an “offset peak to peak stent” and stent B, that resembles XIENCE (Abbott Lab., Chicago, IL, USA), is an “in-phase, peak to valley stent design” as categorised in Prabhu et al. (2012). Also, Stent A was modified by constructing two additional connectors between the first two proximal hoops (see section 4.2.3) and an old out-of-phase, peak-to-peak device was modelled which resembles the CYPHER platform (Johnson & Johnson co., New Brunswick, NJ, USA), used by this group previously (Pant et al. 2011) (see section 4.2.4).

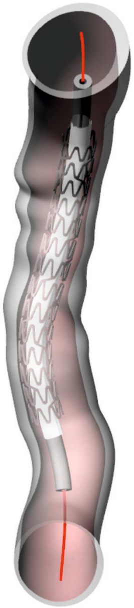

Figure 6.1: Stent A translated onto the 3D reconstructed IVUS pull-back catheter path (red line)

The simulation design approach used in this work was to geometrically transform the stents on to the reconstructed catheter line so as to avoid the additional numerical analysis step of stent implantation and positioning. This method showed that there was no significant difference in the stresses and the final deformed configuration of the expanded stent when compared with the method in which the stent has to be positioned by FEA analysis (see Appendix B). In Figure 6.1, the entire virtual space for Stent A is illustrated. Table 6.1 provides information about the stent designs, alloys and number of links which were assumed for the investigated devices.

Table 6.1: Stent length, stent alloy and the number of connectors between the circumferential rings of the four investigated devices are outlined. Stent family as categorised in Prabhu et al. (2012) is also reported in the second column of the table.

| BMS | Stent Family | Nominal Length/ Uncrimped external diameter (mm) | Strut thickness/ width | Alloy | Number of links |
|---|---|---|---|---|---|
| Stent A (based on Promus) | offset peak-to-peak | 16/1.78 | 81/91 | Platinum Chromium | 2 |
| Stent B (based on XIENCE) | In-phase, peak-to-valley | 18/1.78 | 81/91 | Cobalt Chromium | 3 |
| Stent C (Modified Promus) | offset peak-to-peak | 16/1.78 | 81/91 | Platinum Chromium | 4-proximally/2-along its length |
| Stent D (based on CYPHER) | out-of-phase, peak-to-peak | 16/1.78 | 140/130 | Stainless Steel | 6 |

The constitutive material models along with the mesh resolution information of the reconstructed challenging RCA vessel and the stents was provided in section 5.2.1 and 5.2.2, respectively. No balloon model was used for the purposes of the current work after comparing two expansion techniques in order to simplify the deployment step (see Appendix C). Thus, the deployment of the stents was carried out by a cylindrical deformable surface discretised by 248 linear quadrilateral elements of type SFM3D4R.

## 6.2.2 FEA Simulations

Appropriate simulation parameters were set according to section 5.3 to avoid numerical instabilities and ensure that for all the presented simulations, the inertia forces arise only from the deformation of structure and are not dominating in the analysis (condition for quasi-static events).

### 6.2.2.1 Simulated bench test validation

In order to validate the ability of the model to detect and/or reproduce longitudinal compression, previously published (Ormiston et al. 2011) physical bench testing was simulated in which a compressive force was applied as a distributed longitudinal load.

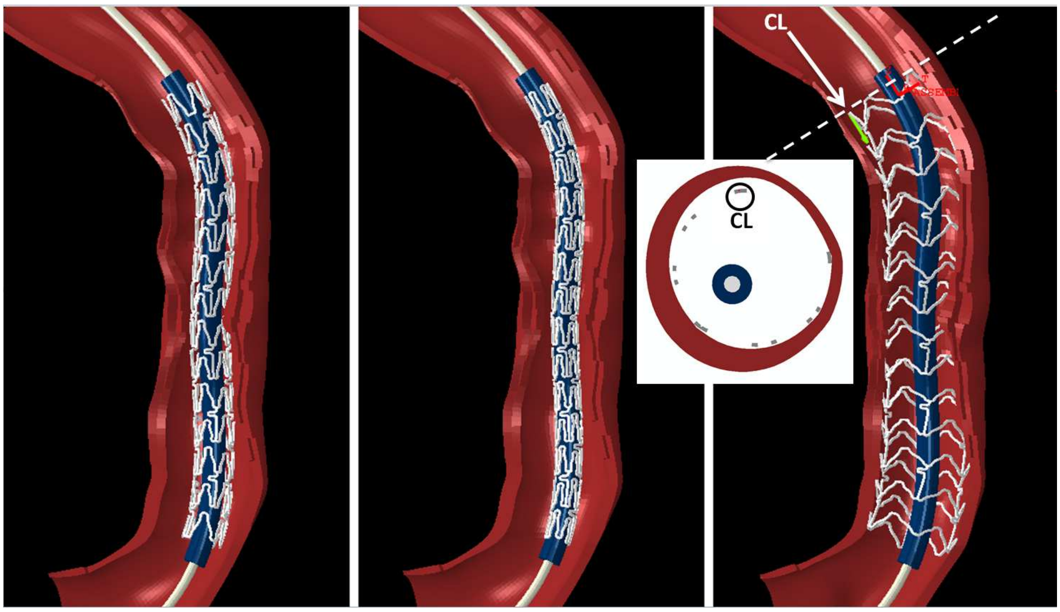

Figure 6.2: Stent pre-flown on the catheter shaft (left), stent crimped on the catheter shaft (centre) and stent expanded from the 3D reconstructed catheter line (right). The imposed compressive load, CL (white arrow), proximally to the model with respect to a reference coordinate system and the cross-sectional image at the proximal edge of the stent are depicted (right)

In order to mimic the experimental method, the devices were constrained distally during the compression test and only 10 $mm$ of their length was exposed to the compressive load. The load was imposed proximally to the devices and distributed on the edges of the circumferential crowns. The stents were first crimped and then expanded to their nominal diameter with deformable surfaces. The LSD was calculated from the displacements of the nodes on which the distributed load was imposed.

#### 6.2.2.2 Virtual stent expansion in the reconstructed vessel

Stents were implanted in the reconstructed vessel at the same location, aligned at the proximal ends. Then, the devices were crimped and expanded by deformable surfaces with controlled predefined displacement, and shown in Figure 6.2. The vessel ends were constrained in the circumferential along with the longitudinal directions of cylindrical coordinate systems defined on planes parallel to their faces. Surface-to-surface contact definition was used for the contact pair of catheter shaft-guide wire, with contact properties defined as tangential and frictionless. A surface-to-surface contact algorithm was used for the stent-vessel pair, and a friction coefficient of 0.05 was defined for the tangential contact property (Auricchio et al. 2011, Dunn et al. 2007). All other contacts (including self-contacts) were modelled with 0.2 friction coefficient for the tangential contact behaviour (De Beule et al. 2008, Mortier et al. 2010). At the end of the expansion step, the relative stent malapposition was evaluated by measuring the minimum distance between the upper nodes of the stent and the inner nodes of the vessel.

#### 6.2.2.3 Virtual longitudinal deformation of stents

To undertake the virtual assessment of longitudinal integrity of the stents, following deployment, a compressive load of 0.3 $N$ (a value close to the clinically relevant longitudinal compression force which a deployed stent may be subjected to as measured in Prabhu et al. (2012)) was imposed on the stent strut that was most malapposed, labelled as CL in Figure 6.2. This strut was chosen because it represents the area most likely to come into contact with the leading edge of a post stent device moving forwards on the coronary line. The direction of the compressive load is represented by the white arrow in Figure 6.2. The LSD was calculated from the displacement of the node to which the localised load was imposed.

## 6.3 Results

### 6.3.1 Validation of the stent longitudinal behavior

Figure 6.3 depicts images of the investigated stents expanded to a diameter of 3.00 $mm$ and deformed by a compressive load applied proximally to each device. The stent compression (millimeters) against the compressive force (Newton) for the investigated devices is depicted in Figure 6.4. Stent A was compressed with 0.4 $N$ and Stent B was compressed with 1.2 $N$ resulting in displacements of 4.75 $mm$ and 5.14 $mm$, respectively.

This numerical bench test shows that the modelled stents, A & B, demonstrated similar longitudinal deformation to that presented by Ormiston et al. (2011), and their experimental results for corresponding devices are superimposed on the same figure (c.f. Figure 6.4). Therefore, one can observe that the numerical bench test is well matched with the experimental results within the acceptable range of 2.8% to 5% of the final displacement. Stents C and D were compressed with 1 $N$ and 3 $N$ resulting in displacements of 4.80 $mm$ and 1.16 $mm$, respectively.

### 6.3.2 Stent Malapposition

The contour plots of the 3D stent malapposition along with cross sectional images proximal, middle and distal to the devices (broken lines) are depicted in Figure 6.5. All the devices show similar results in this regard: specifically, stent malapposition

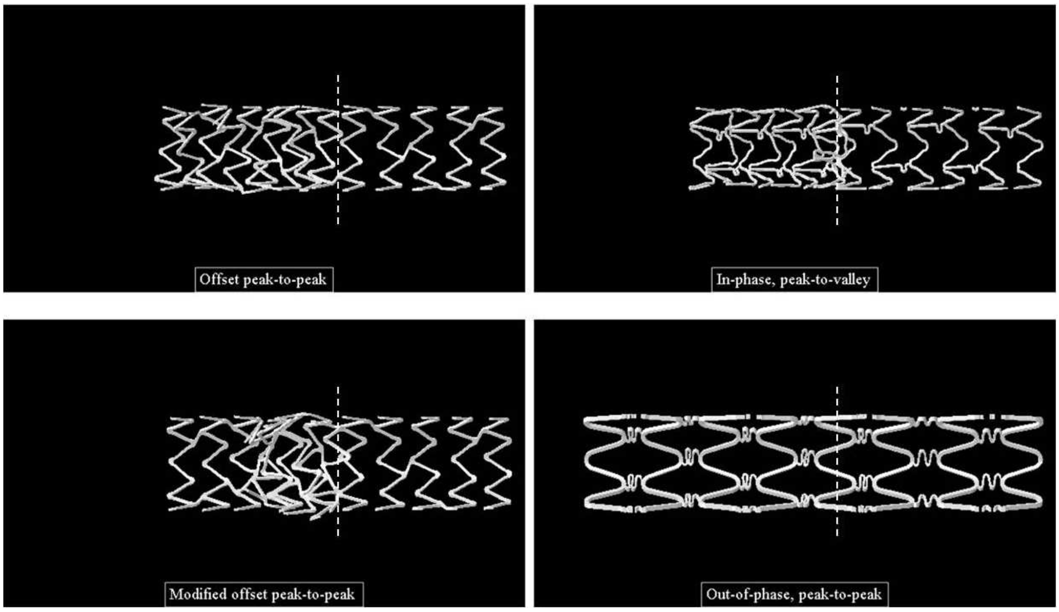

Figure 6.3: Virtual bench test validating the longitudinal integrity of the investigated stents. The devices were expanded to a nominal diameter of 3 *mm* and were constrained along their length so that 10 *mm* of the stents were exposed to the distributed load (broken lines)

occurs predominantly towards the proximal ends of the stents. The maximum distance between a stent node and a vessel wall node is 0.3775 *mm*, 0.3483 *mm*, 0.3329 *mm*, and 0.3325 *mm* for Stents A, B, C, and D, respectively.

### 6.3.3 LSD within the reconstructed coronary segment

Relative performance between the stents can be assessed by considering the force needed to displace by 0.5 *mm* the node at which the load is applied. This displacement also coincides with the onset of noticeable protrusion of struts in the lumen as depicted in the insets of Figure 6.6 (cross-sectional images are depicted proximally to the model-broken lines-where significant strut protrusion for Stents A and B occurs due to the LSD). In Figure 6.7 the longitudinal deformation is depicted with respect to the compressive load. Forces of 0.19 $N$ and 0.29 $N$, respectively, are needed for stents A and B. In contrast, Stent C does not deform significantly in terms of strut protrusion (Figure 6.5) in the lumen although the node at which the load is applied almost reaches a displacement of 0.5 *mm* at the peak load of 0.3 $N$ (Figure 6.6). Stent D shows negligible compression both in terms of strut protrusion or displacement (c.f. Figures 6.6 and 6.7).

## 6.4 Discussion

In Mortier et al. (2011a), a new methodology was developed to study stent malapposition numerically with finite element analysis. In the work presented in this chapter, a similar technique was used to calculate stent malapposition numerically. The technique was based on calculating the shortest distance between the nodes that lie on the outer surface of the stent and the nodes that lie on the inner surface of the reconstructed vessel (relative malapposition). The results showed that, for this patient-specific case, stent malapposition is similar for all the investigated devices. This suggests that the proximal malapposition is primarily dependent on the variation in vessel diameter and the associated diameter mismatch that occurs when sizing the stent on the distal diameter.

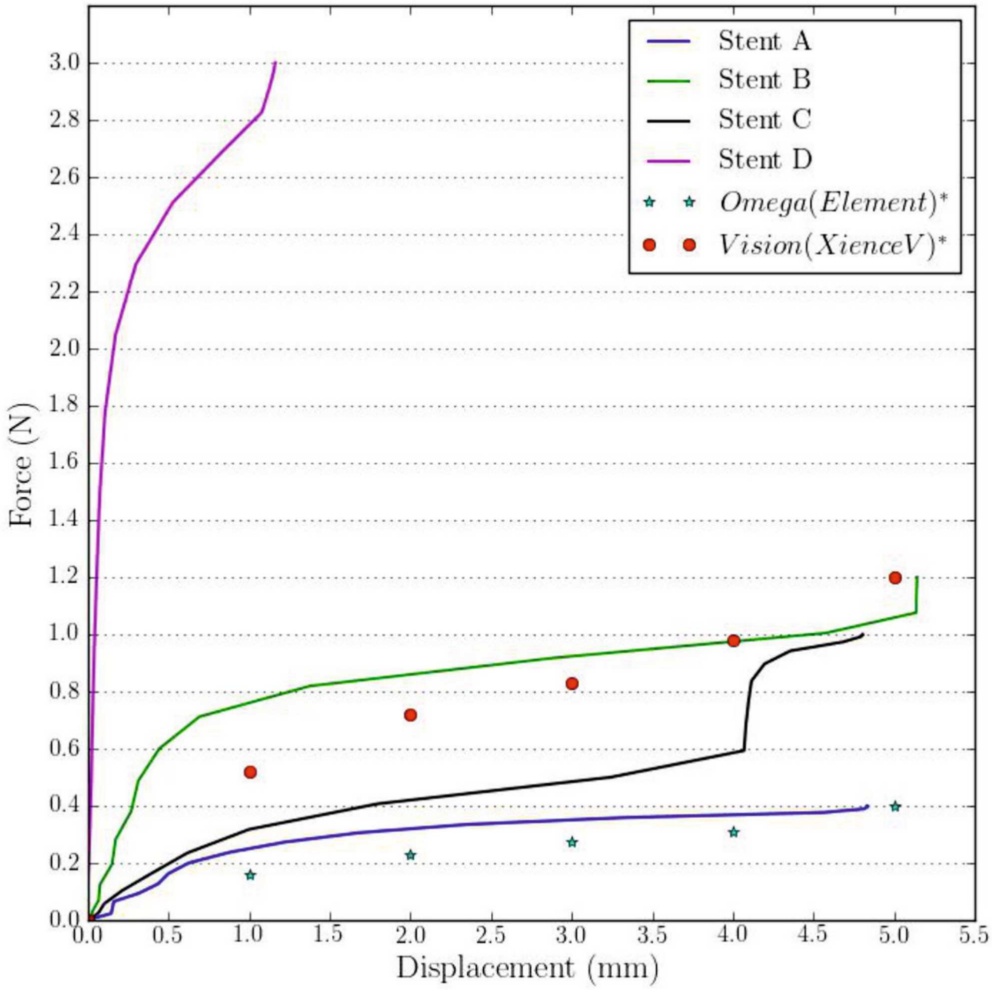

Figure 6.4: Compressive force and stent longitudinal deformation after numerical bench test. Superimposed experimental results (*) published by Ormiston et al. (2011) showing LSD in good agreement with the numerical results.

Longitudinal deformation results in protrusion of stent struts in the lumen (c.f. Figure 6.6) hence potentially obstructing further manipulation(Mortier and De Beule 2011). Most reported cases of LSD involve very thin device platforms with open cell designs (offset peak to peak). Whilst reducing strut thickness and increasing the area between the struts improve the stent flexibility, stent deliverability and stent conformability, the subsequent compromise of stent longitudinal integrity may produce reduced resistance to potential compression loads. Two recent experimental studies (Ormiston et al. 2011, Prabhu et al. 2012) that have investigated current generation stents have reported similar results and have emphasised the importance of the number and the angulation of the connectors between the hoops to resist compression. Specifically, the offset peak to peak device with the open cell design had the poorest behaviour in longitudinal integrity. In contrast, devices with more than two connectors were relatively resistant to compressive loads.

In this computational modelling work, from the compression simulations, it was observed that Stent A with two connectors (with 45° connector angulation) showed significantly less longitudinal strength than Stent B with three connectors (aligned with the longitudinal axis of the device). This is consistent with the concept that stents with two connectors are more susceptible to LSD than devices with three connectors. At the other end of the spectrum, considerable resistance to LSD was observed in a closed cell stent with six connectors (Stent D) in which a force of 3 $N$ compresses the stent only 1 $mm$. From the LSD-graph (c.f. Figure 6.4) Stent A seems to have a more linear behaviour than stent B which demonstrates an initial "hardening" to the first 2 $mm$. This behaviour is consistent with the experimental laboratory-derived results taken from Ormiston et al. (2011) and the virtual LSD simulations extracted from the present work, shown in Figure 6.7. Stent C demonstrated a significantly stiffer response than Stent A to compressive loads but inferior to Stent B. Modifying Stent A by constructing additional connectors proximally, the longitudinal integrity increases significantly (more than double the force was required for a 5 $mm$ compression, see Figure 6.4). Also, it is observed that the proximal end of the modified stent is not distorted by the compression (c.f. Figure 6.3), a fact that can explain the “hardening” of the stent’s response between 4 $mm$ and 4.5 $mm$ in Figure 6.4.

Interestingly, the computer simulations of deformation in the RCA segment (c.f. Figure 6.7) indicate that devices A, B and C do not oppose the load in the same manner with the bench tests (c.f. Figure 6.7). Only Stent D shows similar stiff behaviour in both cases. The virtual compressive simulations indicate that Stent C opposes the compressive force successfully and no significant distortion of the device was observed (c.f. Figures 6.6 and 6.7). Also, in contrast to the bench test, Stent C demonstrates higher resistance than Stent B (c.f. Figures 6.4 and 6.7). This indicates that in contrast

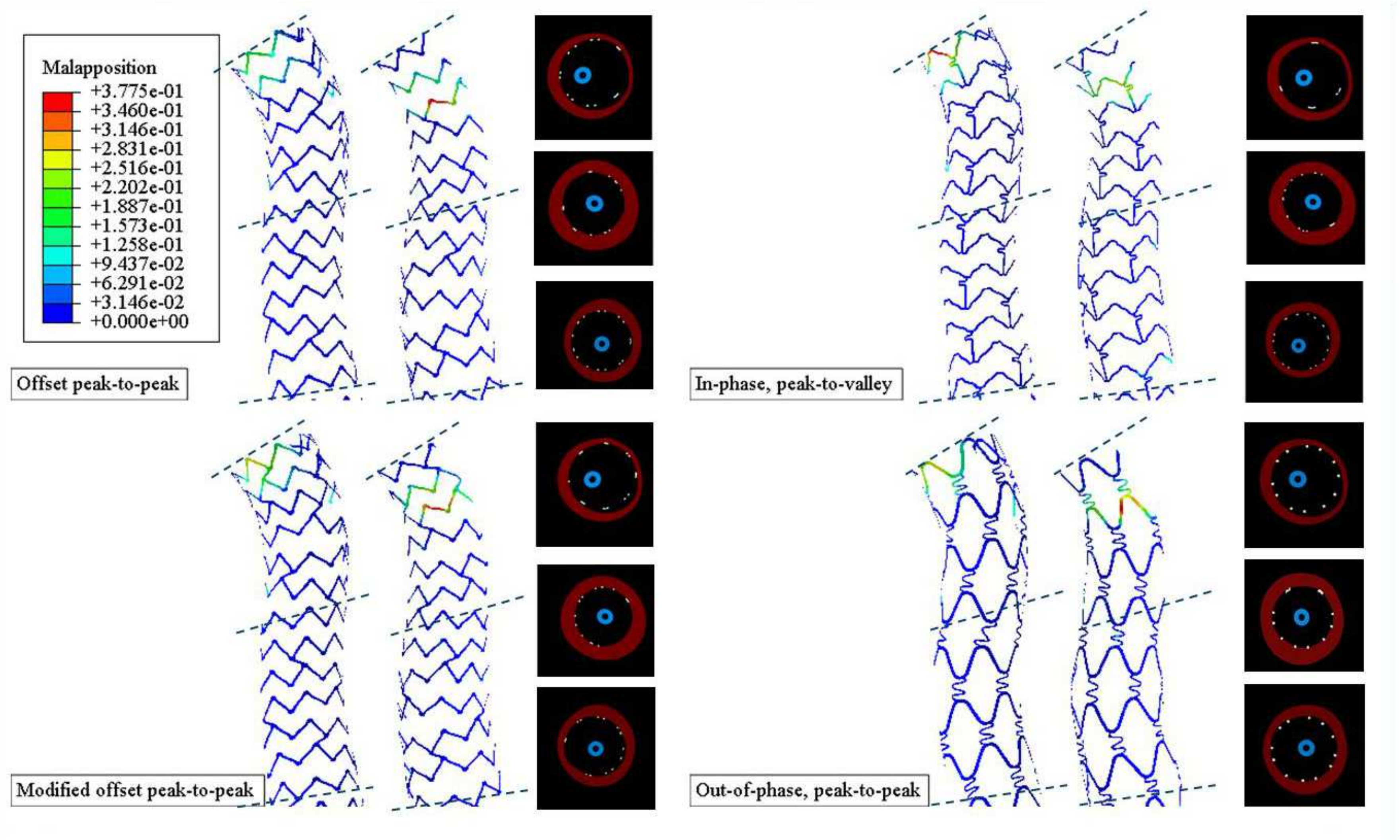

Figure 6.5: Stent malapposition (mm) after the expansion of the investigated devices. For each device, cross sectional images were taken at the proximal, middle and distal area (broken lines) of the model

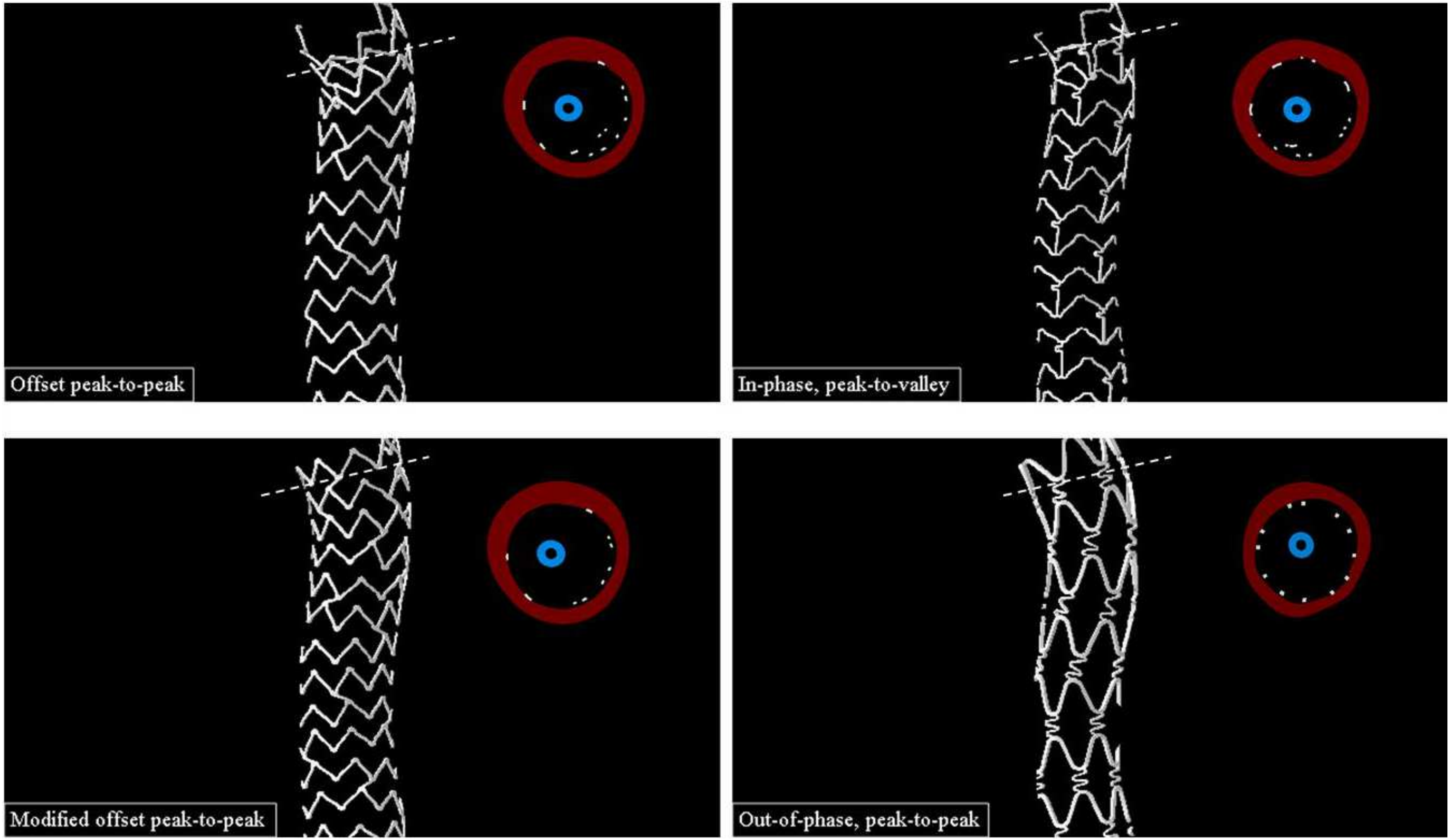

Figure 6.6: Stent computer models cut longitudinally after they had been compressed by a 0.3 $N$ localised load at the most malapposed strut proximally to the device. For each model, a cross sectional image was taken proximally (broken lines) so as to identify potential strut protrusion due to stent deformation

to bench tests, *in vivo* failure of different stent devices may not occur at such drastically different localised loads.

From the compression simulations (both bench test and deployment stent simulations), it is clear that LSD is dependent on the number of the stent connectors and their angulation with the stent longitudinal axis. Apart from the number of the connectors, considerations should be made on the phase angle between stents' sequential hoops. Out-of-phase devices seem to resist more under compressive loads. Further research is needed to investigate variations in the proximal phase angle of the circumferential rings in the offset peak-to-peak device.

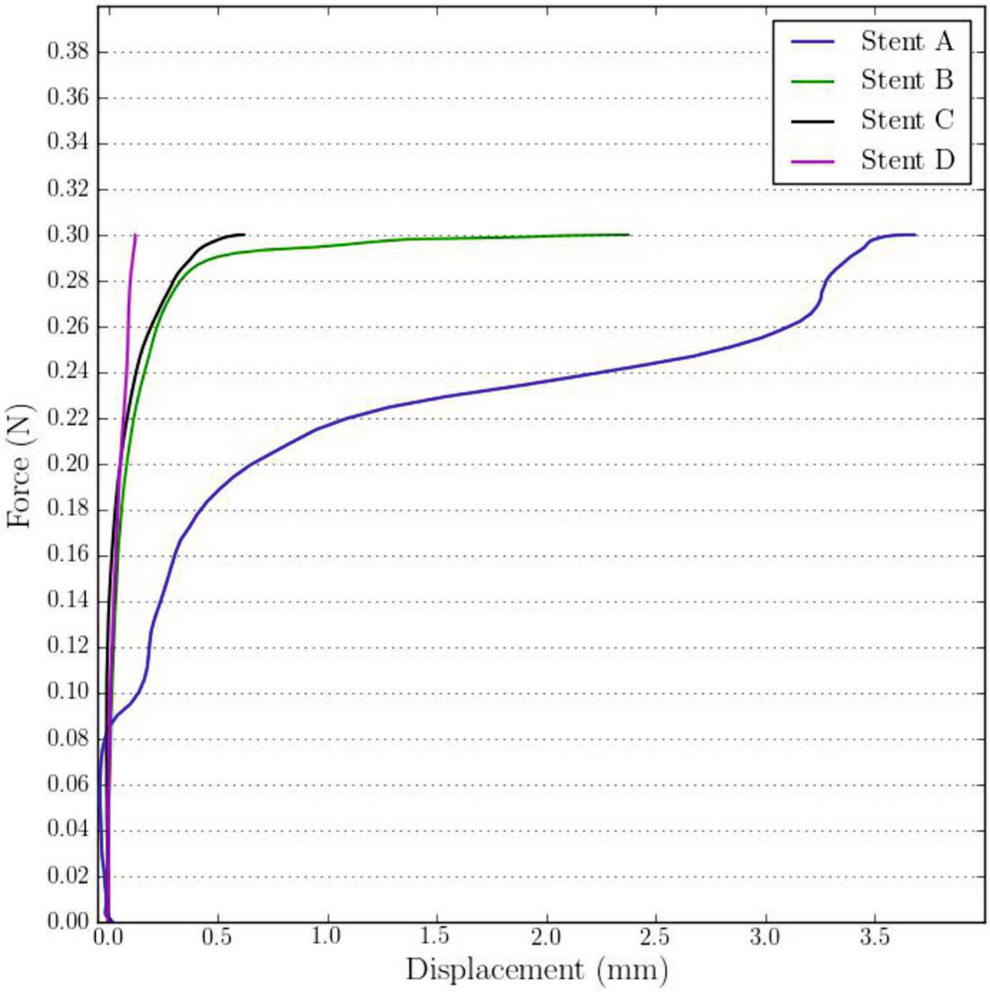

Figure 6.7: Stent compression ($mm$) against a compressive point load. For all devices, a 0.3 $N$ load was applied smoothly so as to evaluate longitudinal resistance.

As far as is known, the work presented in this chapter is the first to investigate longitudinal deformation and stent malapposition virtually in a patient-specific reconstructed vessel. Such numerical studies for research purposes can provide useful information in 3D along the entire length of the models. Figures 6.5 and 6.6 illustrate very clearly the investigated clinical problems and it is strongly believed that such quantitative information can predict and further improve the associated complications by optimising the implanted device in any given challenging geometry.

### 6.4.1 Limitations

The work presented in this chapter has some limitations. First, only one patient-specific case was used and therefore the results cannot necessarily be generalised to other lesions (especially for SM quantification). Second, the vessel wall is assumed to be hyperelastic and isotropic comprising a single layer. This is due to the fact that the reconstruction method is based on IVUS images from which the plaque composition is difficult to extract. Deformable surfaces were used to expand the stents instead of a balloon model. However, for this patient-specific model, the stent malapposition was compared after the surface expansion with a realistic five folded balloon expansion and similar results were obtained in terms of stent malapposition (see Appendix C). This method also generated similar computational results (final stent shape) with a balloon expansion strategy as shown in previous studies (De Beule et al. 2008, Grogan et al. 2012).

## 6.5 Conclusions

A computational engineering model of a coronary lesion has been used to simulate stent malapposition and LSD for three stent designs and a modified device that are based upon one first generation and two second generation DESs. The results are consistent with previous laboratory based experiments of LSD. Also, the simulations suggest that the threshold at which the stent loses its longitudinal resistance may differ *in vivo* compared to *in vitro*, particularly with respect to the range of variation in loads needed to deform second generation drug eluting coronary stents. Therefore, after this study, better *in vitro* tests could be carried out for testing actual stents' behaviour under potential loads during PCI procedures. Finally, it is speculated that such a model may provide a useful tool for testing the integrity and validation of new stent designs.

# Chapter 7

# COMPUTATIONAL MODELLING OF NOVEL MULTI-FOLDED BALLOON DELIVERY SYSTEMS FOR CORONARY ARTERY STENTING: INSIGHTS INTO PATIENT-SPECIFIC STENT MALAPPOSITION

Balloons! This chapter presents how virtual multi-folded balloon models have been developed for simulated deployment in both constant and varying diameter challenging vessels under uniform pressure. The virtual balloons have been compared to available compliance charts to ensure realistic inflation pressure at nominal pressures, as shown in section 5.2.3. Thereafter, patient-specific simulations of stenting in the second and the third reconstructed challenging cases (described in Chapter 3) have been conducted aiming to reduce SM. Different scalar indicators, which allow a more global quantitative judgement of the mechanical performance of each delivery system, have been implemented. The results indicate that at constant pressure, the proposed balloon models can increase the minimum stent lumen area and thereby significantly decrease SM[1],[2].

---

[1] A part of the content of this chapter was presented in the 12th International Symposium in Computer Methods in Biomechanics and Biomedical Engineering: **Patient-specific simulations to improve coronary artery stent malapposition**, G. Ragkousis, N. Curzen, N. Bressloff., 13-15 October 2014, Amsterdam, Netherlands

[2] The content of this chapter has been published in the Annals of Biomedical Engineering Journal: **Computational modelling of multi-folded balloon delivery systems for coronary artery stenting: Insights into patient-specific stent malapposition**, G.Ragkousis, N. Curzen, N. Bressloff., 2015

## 7.1 Introduction

In “virtual” studies, qualitative and quantitative information can be easily accessed in full model dimensionality that would be hardly detectable in *in vitro* and *in vivo* studies. Recently, novel stent designs and stenting techniques (especially for bifurcated vessels) have been investigated and proposed through very elegant virtual bench testing studies (Foin et al. 2012, Morlacchi et al. 2014, Mortier et al. 2014).

FEA is one of the dominant tools for numerical studies, shedding light on the structural response of the arterial walls during/after stent implantation. To date, several FEA studies have been conducted providing scientific evidence for PCI procedures (Morlacchi and Migliavacca 2013). Although the majority of FEA studies have focused on the stent platform, there has been a paucity of research on the design of the delivery system. The modelling of balloon expansion has always been a challenging task due to its complex shape configuration and the complicated contact interaction with the stent. The first analytical balloon model was presented by Laroche et al. (2006) in which the balloon was numerically folded by mapping its nodes in the unfolded configuration to a folded configuration. This methodology was successfully adopted by Mortier et al. (2010) to simulate patient-specific coronary bifurcation stenting. In Gervaso et al. (2008), a three folded balloon was modelled for free stent expansion. The balloon was folded by running a pre-expansion simulation, in which it was deflated by a negative pressure and, after assigning specific boundary condition, the balloon configured by three folds. At the same time, the work by De Beule et al. (2008) was published (see section 2.2.1). However, as the folded models did not have tapered ends boundary conditions were implemented to the balloon ends to the catheter shaft during inflation. More recently, Zahedmanesh et al. (2010) presented a dual step numerical methodology to fold the virtual balloon to the catheter shaft by deflating a balloon to three unfolded wings and then wrapping the wings around the catheter shaft. However, this approach has some limitations. The numerical folding can be carried out easily only for non-curved and planar expansions and it is computationally expensive. Additionally, the idealised models lack realistic characteristics which may affect the final result. As for the material model to describe the inflation behaviour of a balloon, different models have been used in the literature during the last decade. In particular, a two parameter Mooney-Rivlin model was used by Chua et al. (2003). Liang et al. (2005) adopted a hyperelastic model to describe the transient expansion of the balloon. Laroche et al. (2006) implemented an Ogden hyperelastic model. Later, Kiousis et al. (2007) used a cylindrically orthotropic constitutive model to simulate balloon-stent expansions. In De Beule et al. (2008), a method for mimicking the actual compliance of a specific size balloon was introduced. The constitutive model was assumed to be linear isotropic and the Young's modulus was extracted from the actual compliance charts provided by the manufacturers. This method has been implemented broadly during recent years in many state-of-the-art numerical studies (Conway et al. 2012, Foin et al. 2012, Grogan et al. 2011, 2013, Martin and Boyle 2013, Mortier et al. 2008, 2010, 2011a, 2014, Pant et al. 2011). Interestingly, there are also many other studies using isotropic, linear-elastic models to characterise the balloon inflation(Gastaldi et al. 2010, Gervaso et al. 2008, Lim et al. 2008, Morlacchi et al. 2011, 2014, Zahedmanesh et al. 2010). Although the actual inflation of an angioplasty balloon is characterised by anisotropic and hyperelastic behaviour, a linear isotropic model can adequately approximate the response of the balloon especially for nominal pressures. Beyond nominal pressures, and depending on balloon material and geometric characteristics, the balloon stiffening is more rapid and demonstrates a higher non-linear behaviour. Thus, to simulate the full transient response of an angioplasty balloon under a large range of pressures, a linear elastic model cannot be representative.

In this chapter, multi-folded balloon models were developed to mitigate the risk of SM. All virtual balloon models were calibrated and compared to manufacturer compliance charts to mimic actual compliance behaviour (especially at target diameters) as shown in section 5.2.3. The virtual delivery systems were then applied to patient-specific simulations of stent deployment. For the purposes of this work, the second and the third reconstructed patient-specific challenging segments (second RCA and the LMB case) presented in Chapter 3 were simulated. In particular, the major challenge in these cases was to cover disease running from larger diameters into smaller diameters with only a single procedural approach[3] so as to avoid prolonged and technically challenging procedures that may result in further complications. The main objective of the work presented in this chapter was to compare different balloon delivery systems particularly with respect to increasing the minimum lumen area and complete strut apposition on the vessel walls under uniform balloon pressure. The authors believe that the investigated clinical problem of SM is highly correlated with the balloon mechanical performance. Specifically, it is dependent on the diameter and the pressure of the balloon.

---

[3] single procedural approach is the deployment of the stent without post dilation to reshape its malapposed struts

## 7.2 Materials and methods

### 7.2.1 Geometry meshes and constitutive models

#### 7.2.1.1 Multi-folded balloon models

The multi-folded balloon models which were used were constructed as shown in section 4.3. The constitutive material models along with the mesh resolution information of the delivery system FEA models was provided in section 5.2.3.

**Delivery models for patient-specific simulations** In the simulations that were conducted, the uniform balloons along with the tapered model were generated with six folds. As shown by Mortier et al. (2008), six folded balloons can demonstrate more uniform and symmetric stent expansions, especially in cases where the deployment diameter is not constant along the length of the stent system (tapered balloon). However, the stepped balloon was designed with 12 folds since the diameter discrepancy between the proximal and the distal initial profile was $\sim 1.3\ mm$. The material of the balloon is significantly increased for a 4.5 mm balloon, therefore, a twelve folded balloon can result in lower delivery system profile than a six fold (as can be noted from Figure 4.10). As a result, especially for computational purposes, the semi-crimped stent can be mounted on the balloon more easily.

#### 7.2.1.2 Patient-specific vessels & stent model

For the purposes of the simulations in this chapter, the second and the third reconstructed patient-specific vessels presented in Chapter 3 were used. Only one stent model was simulated. This was representative of the XIENCE platform (Abbott Lab., IL, USA) generated as shown in section 4.2.2. The constitutive material models along with the mesh resolution information of the reconstructed challenging vessels and the stent model was provided in section 5.2.1 and 5.2.2, respectively. All the simulations were considered to be quasi-static and their parameters were set as shown in section 5.3.

Figure 7.1a and 7.1b illustrate the virtual space for the reconstructed RCA and the LMB, respectively. The mesh resolution for the RCA and the LMB assembly is depicted in Figure 7.1c and 7.1d, respectively.

#### 7.2.1.3 Indicators of stenting

To quantify the performance of stenting in the patient-specific cases, different measurements are defined. Some of the metrics are based on the geometric properties of the vessels and others on the structural response of the vessel walls. The metrics that are dependent on the geometrical characteristics of the deformed vessels have been calculated by using the vessel centre curve, $CP$, which is defined in section 3.3.2.3.

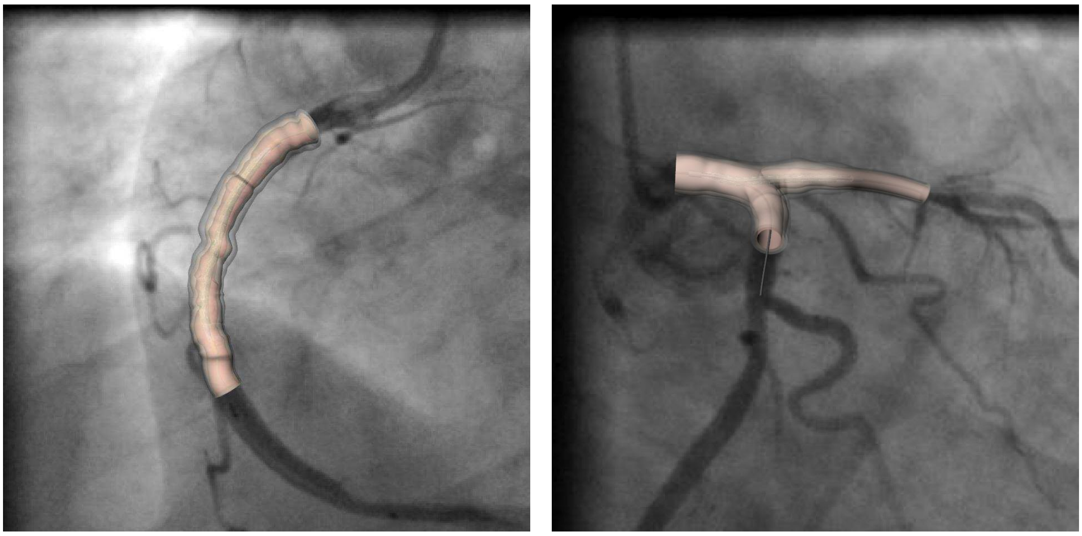

(a) Virtual RCA model

(b) Virtual LMB model

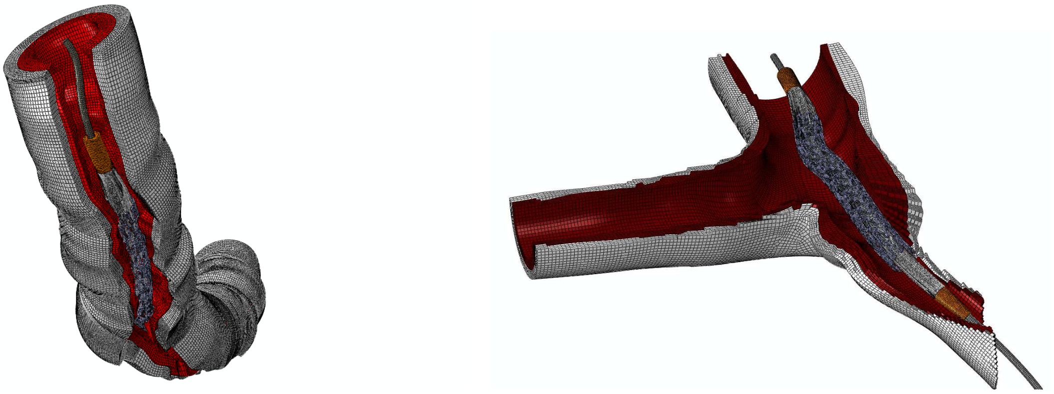

(c) Structured hex mesh for RCA generated in ABAQUS

(d) Structured hex mesh for LMB generated in ABAQUS

Figure 7.1: Virtual reconstructed models back-projected to the CA images and numerical mesh discretisation for the RCA case

**Total Average Curvature (TAC)** A scalar metric is proposed to quantify the global curvature of the central curve, $CP$, pre and post-stenting. This metric, $TAC$, was defined as

$$TAC = \frac{\int_t k(t)_{CP}\|\mathbf{cp}'(t)\|dt}{\int_t \|\mathbf{cp}'(t)\|dt} \tag{7.1}$$

Since the curve has been sampled and parametrised along its length, $TAC$ can be calculated using

$$TAC = \frac{\sum\limits_{i=1}^{i=n_t} k_{cp_i} \delta cp'_i}{\sum\limits_{i=1}^{i=n_t} \delta cp'_i} \tag{7.2}$$

where $n_t$ is the total number of curve sampling points, $k_{cp_i}$ is the local curvature[4] of the central curve at the $i$th sampling point and $\delta cp'_i$ is the magnitude of the $\mathbf{cp}'$ at the $i$th sampling point.

**Total Average Torsion (TAT)** Similarly to $TAC$, $TAT$, is a global metric for the pre and post-stenting central curve torsion and was defined as

$$TAT = \frac{\int\limits_t \tau(t)_{CP} \|\mathbf{cp}'(t)\| dt}{\int\limits_t \|\mathbf{cp}'(t)\| dt} \tag{7.3}$$

Again, since the curve has been sampled over its length, $TAT$ can be calculated from

$$TAT = \frac{\sum\limits_{i=1}^{i=n_t} \tau_{cp_i} \delta cp'_i}{\sum\limits_{i=1}^{i=n_t} \delta cp'_i} \tag{7.4}$$

where $\tau_{cp_i}$ is the local torsion[5] of the central curve at the $i$th sampling point.

**Volume Average Stress (VAS)** $VAS$ represents the average change in the stress environment induced by the stent implantation. It was firstly proposed by Holzapfel et al. (2005b) and later adopted by Pant et al. (2012). The $VAS$ formula was defined as

$$VAS = \frac{\int_V \sigma dV}{\int_V dV} \tag{7.5}$$

where, $\sigma$ represents the circumferential stresses, and the integrals are calculated over the volumes, $V$, of intima and media. Since the volume has been discretised by finite elements, the formula is rearranged as

$$VAS = \frac{\sum\limits_{i=1}^{i=n_v} \sigma_i \delta V_i}{\sum\limits_{i=1}^{i=n_v} \delta V_i} \tag{7.6}$$

---

[4] for the definition of curvature look Eq. 3.5

[5] for the definition of torsion look Eq. 3.6

where $n_v$ is the total number of elements within the intima-media volume, $\sigma_i$ represents the circumferential stress in the $i$th element of the volume, and $\delta V_i$ is the volume of the $i$th element.

**Spatial Quantification of SM** To quantify the spatial variation of SM the outer surface of each stent was extracted and represented by a triangulated mesh. The SM along the outer surface of each stent were calculated as

$$d_i = \|\mathbf{x}_i - \mathbf{y}_i\| \tag{7.7}$$

where the $d_i$ is the Euclidean distance between the $\mathbf{x}_i$ vertex of the triangulated mesh and its projected $\mathbf{y}_i$ point to the lumen surface (c.f. Figure 7.2).

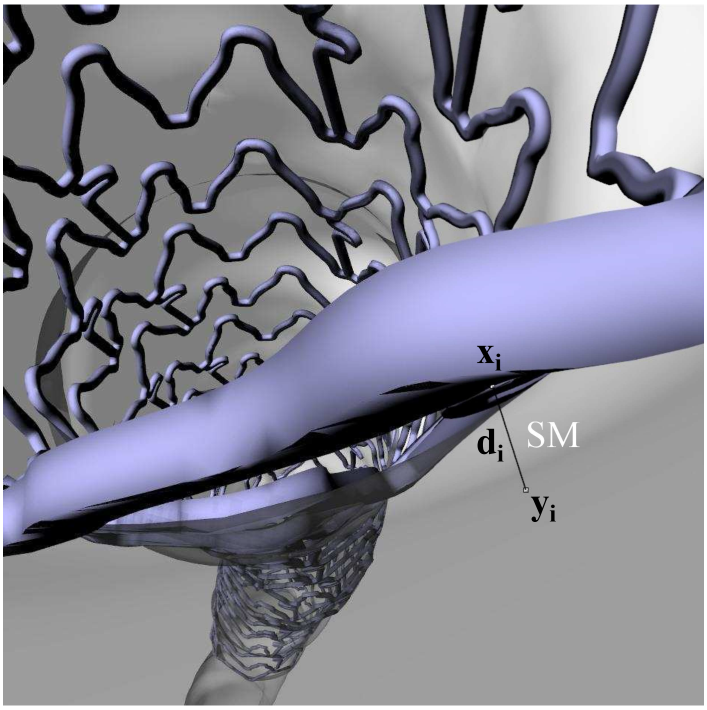

Figure 7.2: Demonstration of the spatial variation of stent malapposition quantification: a vertex point $\mathbf{x}_i$ lying on the outer surface of the stent is projected to the vessel surface ($\mathbf{y}_i$)

**Area Average Stent Malapposition (AASM)** Similarly to $VAS$, a metric for calculating the average malapposition was used post operatively. The $AASM$ can be expressed as

$$AASM = \frac{\int_A SM dA}{\int_A dA} \tag{7.8}$$

with $A$ the area of the upper stent surface, and SM the stent malapposition. Since the surface is meshed by triangulated elements, eq. 7.8 can be rearranged to

$$AASM = \frac{\sum_{i=1}^{i=n_s} SM_i \delta A_i}{\sum_{i=1}^{i=n_s} \delta A_i} \tag{7.9}$$

where $n_s$ is the total number of the triangulated elements, $SM_i$ is the malapposition in the $i$th element given by eq. 7.7 with $\mathbf{x}_i$ the centre point of the $i$th element and $\mathbf{y}_i$ its projection to the lumen surface. $\delta A_i$ is the area of the $i$th element expressed as

$$\delta A_i = \frac{1}{2} \|(\mathbf{v}_3 - \mathbf{v}_1) \times (\mathbf{v}_2 - \mathbf{v}_1)\| \tag{7.10}$$

where $\mathbf{v}_j$ $(j = 1, 3)$ denote the position vectors of the vertices of each element.

**Minimum Lumen Area (MLA) & Volume Gain (VG)** For each cross section, $\mathcal{R}(t)_{CP}$[6] (c.f. Figure 3.7), the area is calculated as

$$A(t) = \iint_{\mathcal{D}(t)} dA(r, p) \tag{7.11}$$

The MLA is identified as the minimum area, $A(t)_{min}$, of a cross section $\mathcal{R}(t)_{CP}$ lying on the normal plane $\mathcal{P}(t)_{CP}$ for all $t$. Moreover, the lumen volume $V(\mathcal{Q})$ was calculated. According to a technical note published by England and Miller (2001), the volume of an object $V(\mathcal{Q})$ (c.f. Figure 3.7) which contains a curve arbitrarily parametrised can be calculated by

$$V(\mathcal{Q}) = \int_t A(t)(1 - k(t)\overline{r}(t))\|\mathbf{c}'(t)\|dt \tag{7.12}$$

where $\overline{r}(t)$ is the $\mathbf{n}(t)$ coordinate of the centroid of the cross section of the solid $\mathcal{Q}$ at $\mathbf{c}(t)$. Since the central point was calculated for each $\mathcal{R}(t)$, and the solid central curve was interpolated through these points, by taking the $CP$ curve, $\overline{r}(t)$ was zero and $V(\mathcal{Q})$ was given by

$$V(\mathcal{Q}) = \int_t A(t)\|\mathbf{c}'(t)\|dt \tag{7.13}$$

and $VG$ was calculated as

$$VG = \frac{V(\mathcal{Q}) - V(\mathcal{Q})_0}{V(\mathcal{Q})_0} \tag{7.14}$$

---

[6] for the definition of a cross section $\mathcal{R}(t)_{CP}$, see Eq. 3.16

with $V(\mathcal{Q})_0$ and $V(\mathcal{Q})$ the volume of the investigated vessel segment before and after stenting, respectively.

## 7.3 Results

### 7.3.1 Multi-folded balloon simulations

#### 7.3.1.1 Tapered balloon free expansion

The transient expansion of the tapered balloon model is depicted in Figure 7.3a. The six-folded balloon is characterised by a uniform stent expansion with its proximal and distal segment expanded to 3.5 $mm$ and 4.25 $mm$, respectively. In Figure 7.4a, the virtual balloon compliance is illustrated. As can be observed, the balloon transient diameter variation has been recorded with or without the mounted stent and there was no significant expansion diameter discrepancy ($< 2\%$). The pressure has been applied uniformly by a smooth curve up to 0.842 $MPa$ along the entire inner surface of the balloon. The balloon was designed with a proximal unpressurised diameter, $D_{b0}$, of 3.33 $mm$ gradually increased to 4.04 $mm$ distally along the length of the balloon.

#### 7.3.1.2 Stepped balloon free expansion

Frames at certain times in the stepped balloon expansion have been captured in Figure 7.3b. On the left panel, the full stepped stent-catheter system is depicted whereas on the right, cross sections centrally to the model are illustrated demonstrating the transient unfolding of a twelve-folded balloon. The virtual stepped balloon was then designed with proximal and distal unpressurised diameters, $D_{b0}$, of 2.80 $mm$ and 4.1 $mm$, respectively, and target diameters 3.02 $mm$ and 4.46 $mm$. Figure 7.4b depicts how these are obtained by applying a uniform pressure of 1.012 $MPa$. Similarly to the tapered model, the virtual compliance was extracted for the stepped balloon with or without stent and discrepancies below 2% were recorded for the expansion diameter.

### 7.3.2 Patient-specific simulations

#### 7.3.2.1 RCA “stenting”

On the left panel of Figure 7.5, the expansion simulations using a uniform balloon of 3.5 $mm$ and the tapered balloon (section 7.3.1.1) are illustrated. Frames have been captured at specific times to demonstrate critical steps of the expansion simulations. The steps demonstrate (i) & (ii) the duration of the dog-boning phase, (iii) the maximum inflation of each balloon up to 0.842 $MPa$ and (iv) the final configuration of

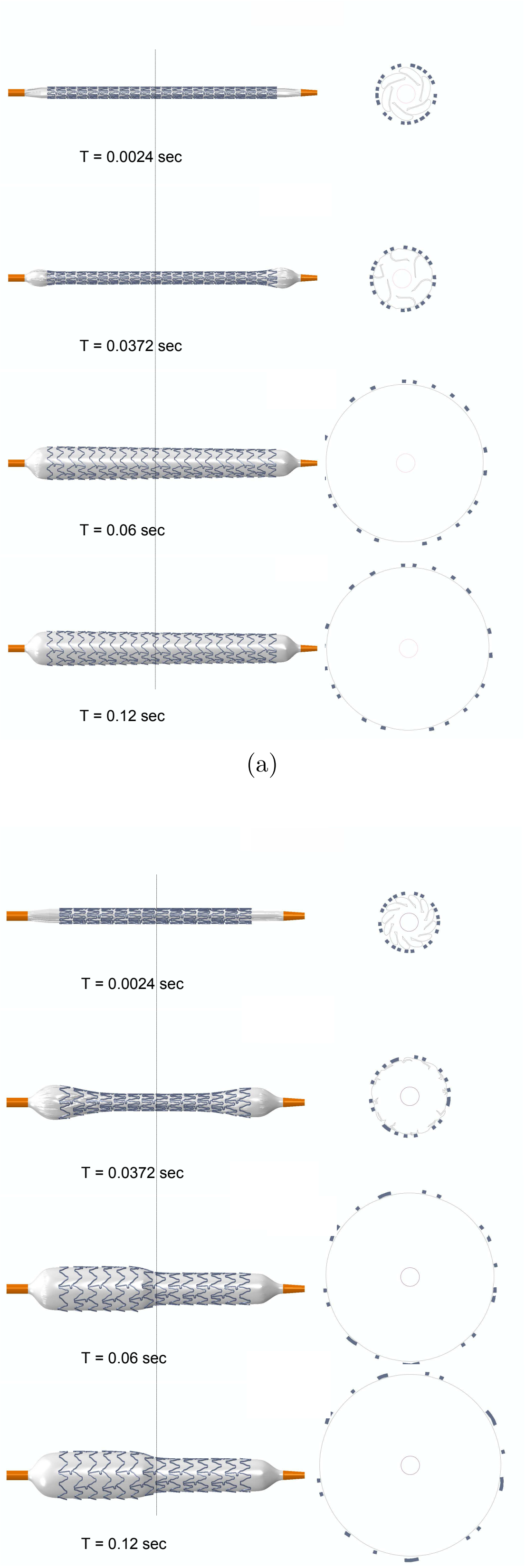

(a)

(b)

Figure 7.3: Transient inflation of varying diameter virtual balloon models. (a) Transient free stent expansion with a tapered balloon. On the right, cross sections centrally to the model (dashed line) are extracted to illustrate the transient unfolding of the six-folded balloon. (b) Transient free stent expansion with a stepped balloon.

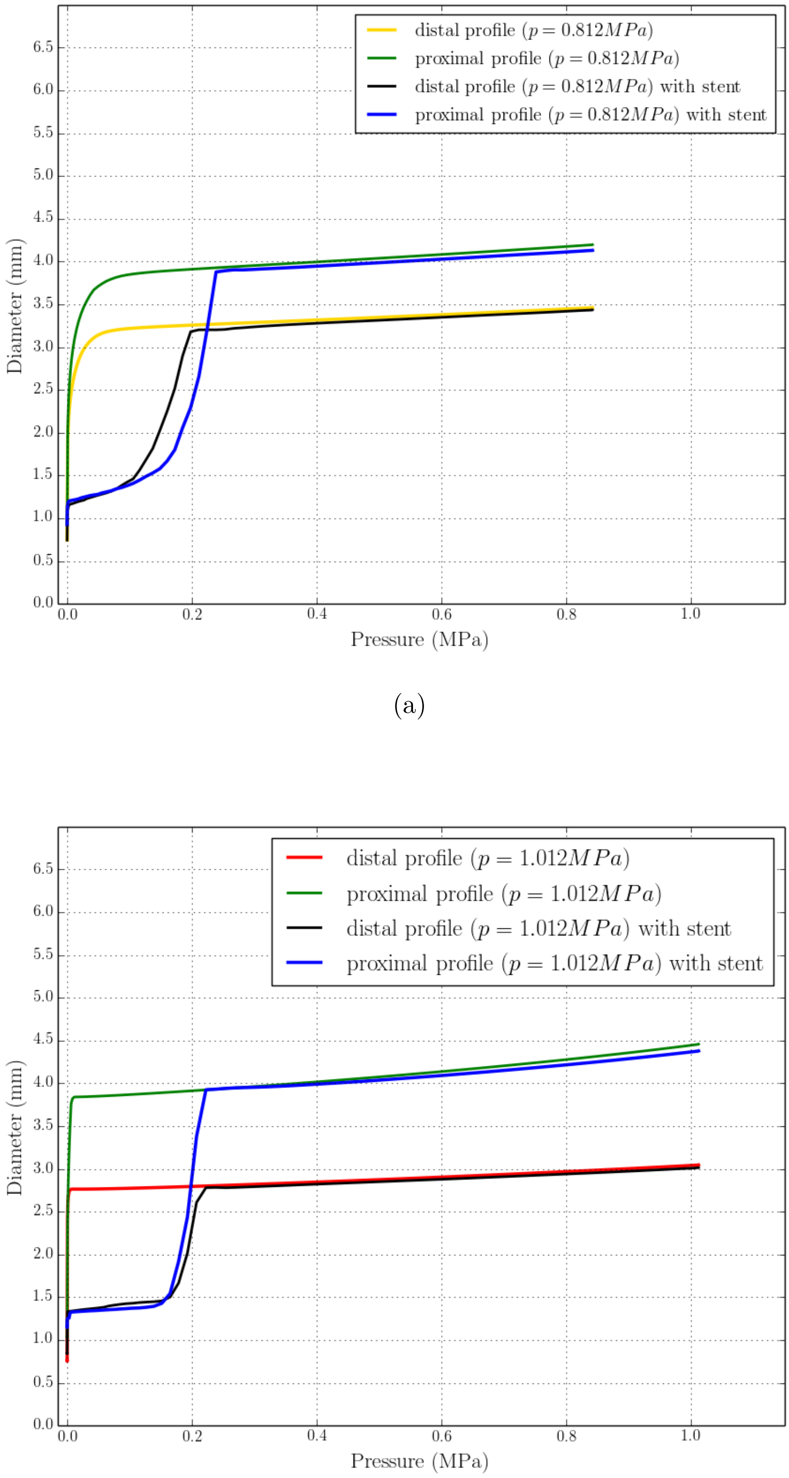

(a)

(b)

Figure 7.4: Virtual compliance charts for varying diameter delivery systems without/with mounted stents. (a) Virtual compliance for a tapered balloon: proximal and distal target diameters of 3.5 $mm$ and 4.25 $mm$, respectively. (b) Virtual compliance for a stepped balloon: proximal and distal target diameters of 3.02 $mm$ and 4.46 $mm$, respectively.

the model after the deflation of the balloon. On the right panel, cross sections in the proximal portion of the vessel are illustrated to show the transient unfolding of the balloon model within the artery. Moreover, in the cross section images, regions with SM can be clearly observed. To quantify the better apposition produced by the tapered balloon evidenced in Figures 7.5 and 7.6a, a more analytical quantification is given by the cumulative distribution function (CDF) as shown in Figure 7.7a. In particular, the CDF plots demonstrate the possibility of a range of SM within the vessel[7] (spatial quantification of SM calculated on the vertices of the upper triangulated stent surface). For instance, strut malapposition within a range of $0.00 - 0.025$ $mm$ is approximately 66% and 74% for the uniform and the tapered balloon, respectively. Moreover, values of SM within a range of $0.00 - 0.05$ $mm$ occur for 75% and 83% of stent outer surface for the uniform and tapered models, respectively. The greatest value of SM occurs in the proximal part of the uniform model and is calculated to be 0.715 $mm$, a gap which is approximately equal to the difference between the balloon and the vessel diameter. Importantly, high values of SM can be observed in both segments close to the middle of the vessel length. However, this is due to some aneurysmatic regions of the diseased reconstructed segment. In Table 7.1, the scalar "stenting" indicators for the RCA case are reported. The values show that the tapered model has significantly decreased the overall SM. At the same time, the MLA and the volume of the lumen have been significantly increased. The MLA relative to the reference model (pre-stenting) has been increased by 130% and 132% for the uniform and the tapered model, respectively. Correspondingly, the volume has increased by 4% and 12.8%. The $TAC$ index indicates that the tapered balloon has been shown not to affect the curvature of the vessel. However, the tapered model does have a considerable impact on the planarity of the segment, as indicated by the $TAT$ index. As far as the average stresses are concerned, the $VAS$ index indicates that the tapered model has resulted in relatively higher stresses. The latter could be explained by the fact that the stent interacts with more volumetric mesh of the arterial walls, especially in the proximal portion of the vessel. As a result more stresses contribute to the calculation of the $VAS$ index (higher $VAS$ numerator).

#### 7.3.2.2 LM bifurcation "stenting"

Figure 7.8 illustrates different frames of the transient stent expansion simulation by an under-sized, an over-sized and a stepped balloon model (from left to right) presented in section 7.3.1.2. As for the RCA case, the frames have been captured at specific

---

[7] In CDF graphs, a higher percentage of malapposed stent struts within a low malapposition range (e.g. $0.00 - 0.05$ $mm$) indicates that the investigated device perform better (with respect to SM) than a stent with smaller percentage of malapposed struts within the same range.

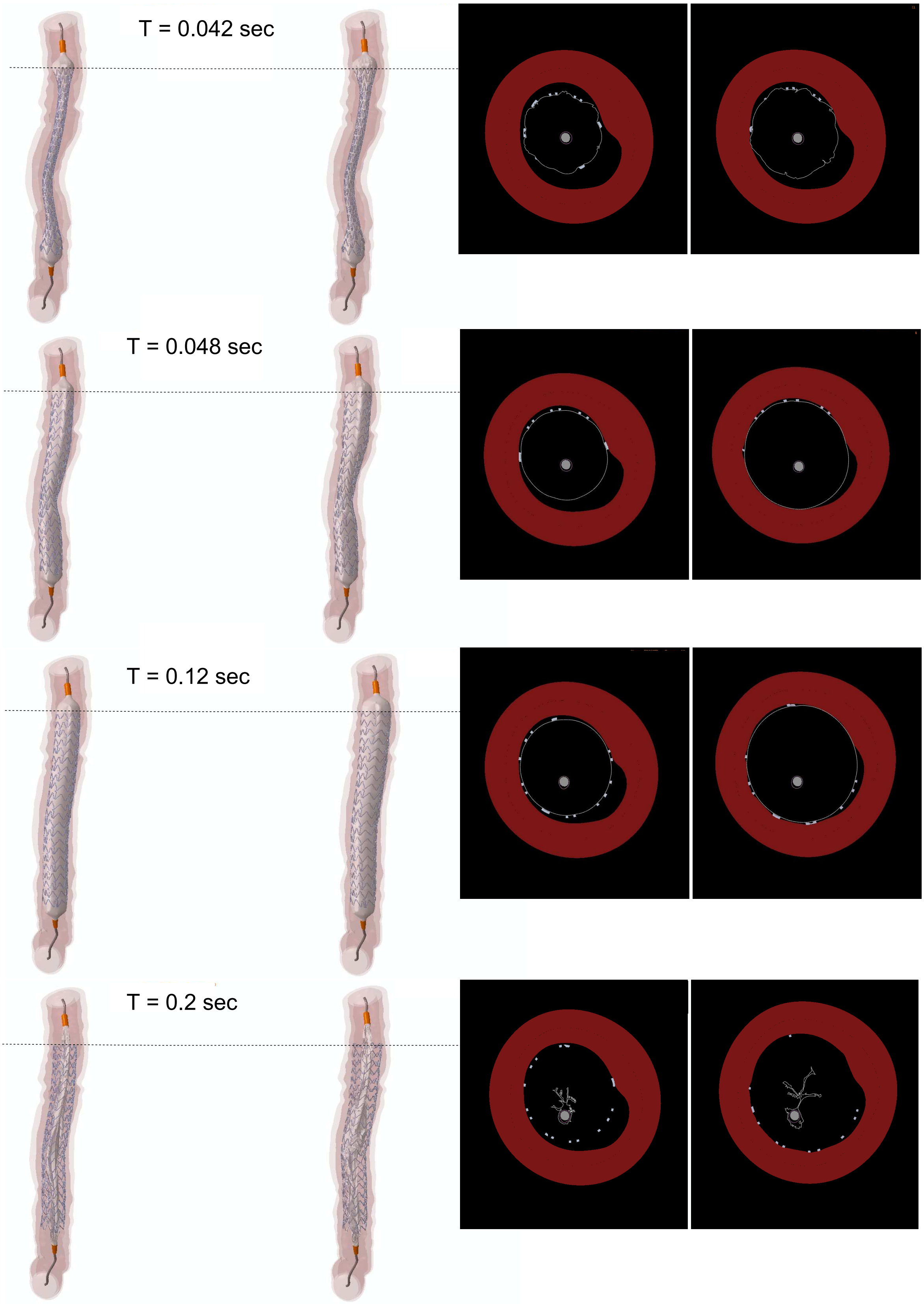

Figure 7.5: Transient patient-specific RCA stent expansion with a non-tapered and a tapered balloon: From top to bottom, the steps demonstrate (i) & (ii) the duration of the dog-boning phase, (iii) the maximum inflation of each balloon up to 0.842 $MPa$ and (iv) the final configuration of the model after the deflation of the balloon. On the right panel, cross sections in the proximal portion of the vessel are illustrated.

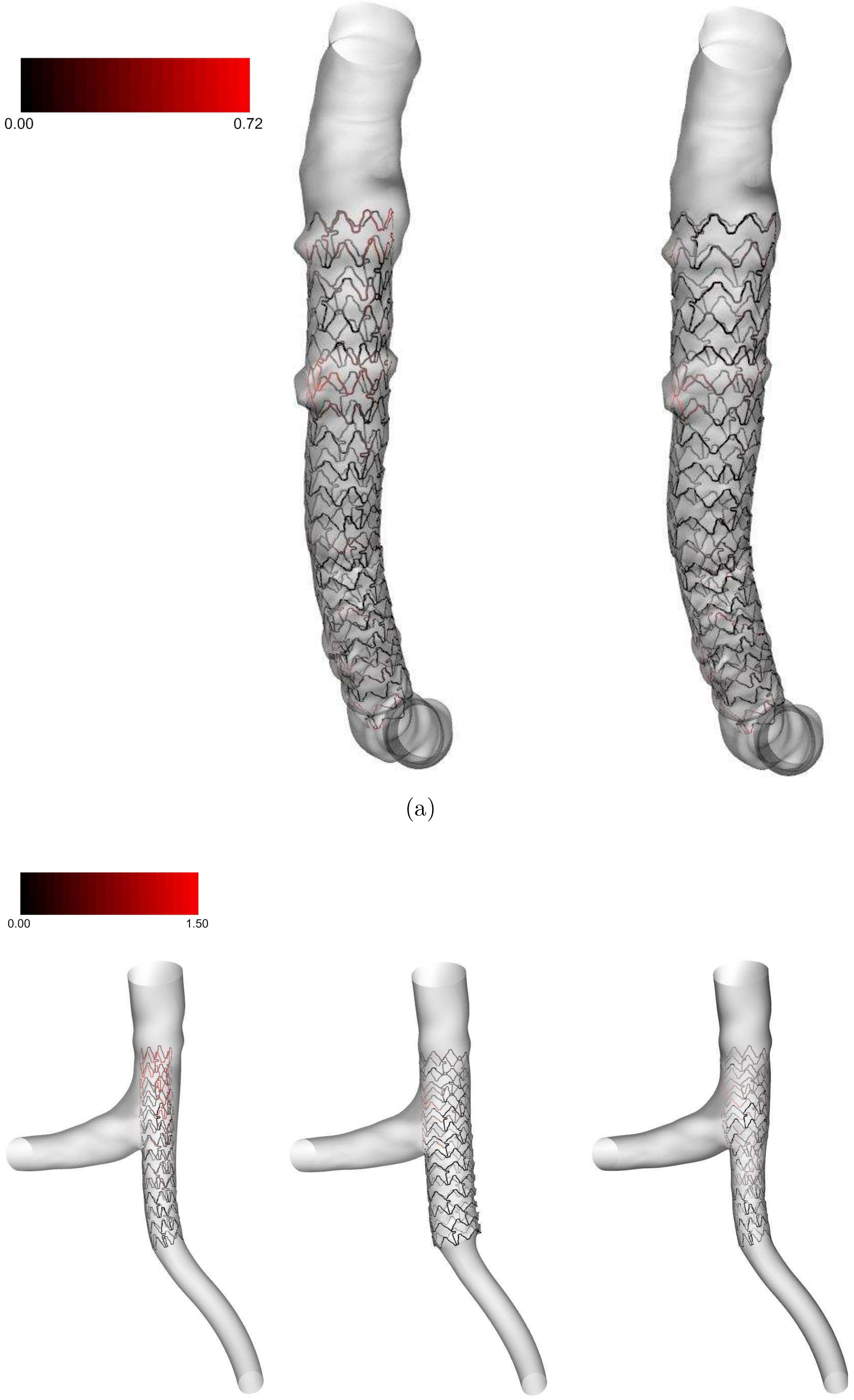

(a)

(b)

Figure 7.6: Patient-specific spatial stent malapposition after stent deployment. (a) Actual stent malapposition after stent deployment in the RCA case. (b) Actual stent malapposition after stent deployment in the LMB case. Areas of stent with the red colour are incomplete apposed to the lumen walls. The higher the intensity of red, the higher the amount of malapposition.

Table 7.1: "Stenting indicators" for the RCA segment

| Model | VAS | TAC | TAT | AASM | MLA ($mm^2$) | VG |
|---|---|---|---|---|---|---|
| RCA reference | - | 0.139 | 0.224 | - | 3.714 | - |
| RCA stented by uniform model | 0.019 | 0.110 | 0.224 | 0.053 | 8.557 | 0.040 |
| RCA stented by tapered model | 0.025 | 0.110 | 0.144 | 0.031 | 8.601 | 0.128 |

times of the deployment simulations demonstrating clearly transient model deformations throughout the entire period of the expansion simulations. In particular, the steps demonstrate (i) & (ii) the duration of the dog-boning phase, (iii) the maximum inflation of each balloon up to 1.012 $MPa$ and (iv) the final configuration of the model after the balloon deflation. On the right panel of Figure 7.8, cross sections in the middle of the stented region have been extracted. As can be observed, the stepped balloon provides very similar strut apposition with an oversized balloon based on the $AASM$ index (c.f. Table 7.2) whereas the undersized balloon results in significant malapposition. The highest value of malapposition has been identified in the left main of the under-expanded model ($\sim$ 1.5 $mm$). As can be observed, high SM values are identified in the ostium of the Cx for all models due to the fact that the struts facing the Cx ostium are "wall-free" (Figure 7.6b and 7.8). A more analytical description of SM can be given by the CDF shown in Figure 7.7b. The percentage of strut malapposition within a range of $0.00 - 0.025$ $mm$ is approximately 43%, 52% and 57% for the under-sized, stepped-sized and over-sized models, respectively. High values of SM for all the models is due to the Cx ostium. The percentage of exposed struts in a range of $0.00 - 0.1$ $mm$ SM is $\sim$ 63%, $\sim$ 75% and $\sim$ 83% for the under-sized, the stepped-sized and the over-sized model, respectively. The stenting indicators for the LMB case are reported in Table 7.2. The MLA relative to the reference vessel is 1.6%, 3.6% and 2.3% higher for the under, over and stepped-sized approach, respectively. The volume gain relative to to the reference model is 2.1%, 19.8% and 3.5%. However, it can be observed that the stepped model provides a better approach compared to the undersized and the oversized delivery systems. In particular, the average malapposition has been decreased by half relative to the undersized approach and $VAS$ is 65% less than that produced by the oversized balloon. Also, $TAC$ and $TAT$ indicate that the stepped approach is closer to the geometrical properties of the reference vessel especially relative to the over-sized balloon model.

Table 7.2: “Stenting indicators” for the LM bifurcation

| Model | VAS | TAC | TAT | AASM | MLA ($mm^2$) | VG |
|---|---|---|---|---|---|---|
| LM bifurcation reference | - | 0.061 | 0.217 | - | 4.929 | - |
| LM bifurcation stented by under-sized model | 0.004 | 0.059 | 0.175 | 0.445 | 5.010 | 0.021 |
| LM bifurcation stented by over-sized model | 0.020 | 0.050 | 0.059 | 0.228 | 5.108 | 0.198 |
| LM bifurcation stented by stepped-sized model | 0.007 | 0.058 | 0.216 | 0.230 | 5.044 | 0.035 |

## 7.4 Discussion

In the present work, the modelling strategy for the delivery system has been based on the parametric design of virtual balloons following comparison to commercially available compliance charts. As shown by Mortier et al. (2008), changing the balloon parameters (model length, the folding pattern and the relative position of stent on the catheter) can significantly affect the symmetry and uniformity of the transient expansion especially when the expansion target diameter is inconsistent. In particular, for large diameter transitions, the number of the folds has to be increased for ensuring expansion uniformity. The latter has been observed by the expansion of a twelve-folded balloon in the bifurcation case where the proximal and distal diameters differ by approximately 1.5 $mm$ (c.f. Figure 7.3b and 7.8). On the other hand, for a diameter difference of 0.7 $mm$, the deployment of a six-folded balloon resulted in relatively uniform expansion (c.f. Figure 7.3a and 7.5).

Furthermore, this work has introduced several numerical indices quantifying and identifying local and global values of the investigated problem along with geometric characterisation of the vessels pre and post-stenting. These indices can provide a general idea of the procedural outcomes and, hopefully, in the future, could help to inform coronary interventions. The results demonstrate clearly that non-uniform delivery systems can significantly increase the MLA and in parallel decrease the overall SM, especially, proximally to the stented segment, a region which is highly correlated with further unwanted procedural events (Hanratty and Walsh 2011, Williams et al. 2012) and ST. This is illustrated in Figures 7.6a and 7.6b where the proximal stent segments are completely apposed to the vessel walls for the tapered and the stepped balloons. Also, the cross section images, Figures 7.5 and 7.8, indicate clearly the superior outcomes of the proposed deployments which could avoid the need for post-stenting dilation using a non-compliant balloon. Especially for the bifurcation, it is well established that single stent procedures are preferable (Al Suwaidi et al. 2001, Hildick-Smith et al. 2010, Pan et al. 2004). The suboptimal apposition of the stent struts to the proximal part of the main vessel could be solved by a provisional optimisation technique (Lefevre et al. 2010). This would require an additional procedural step. Therefore, the

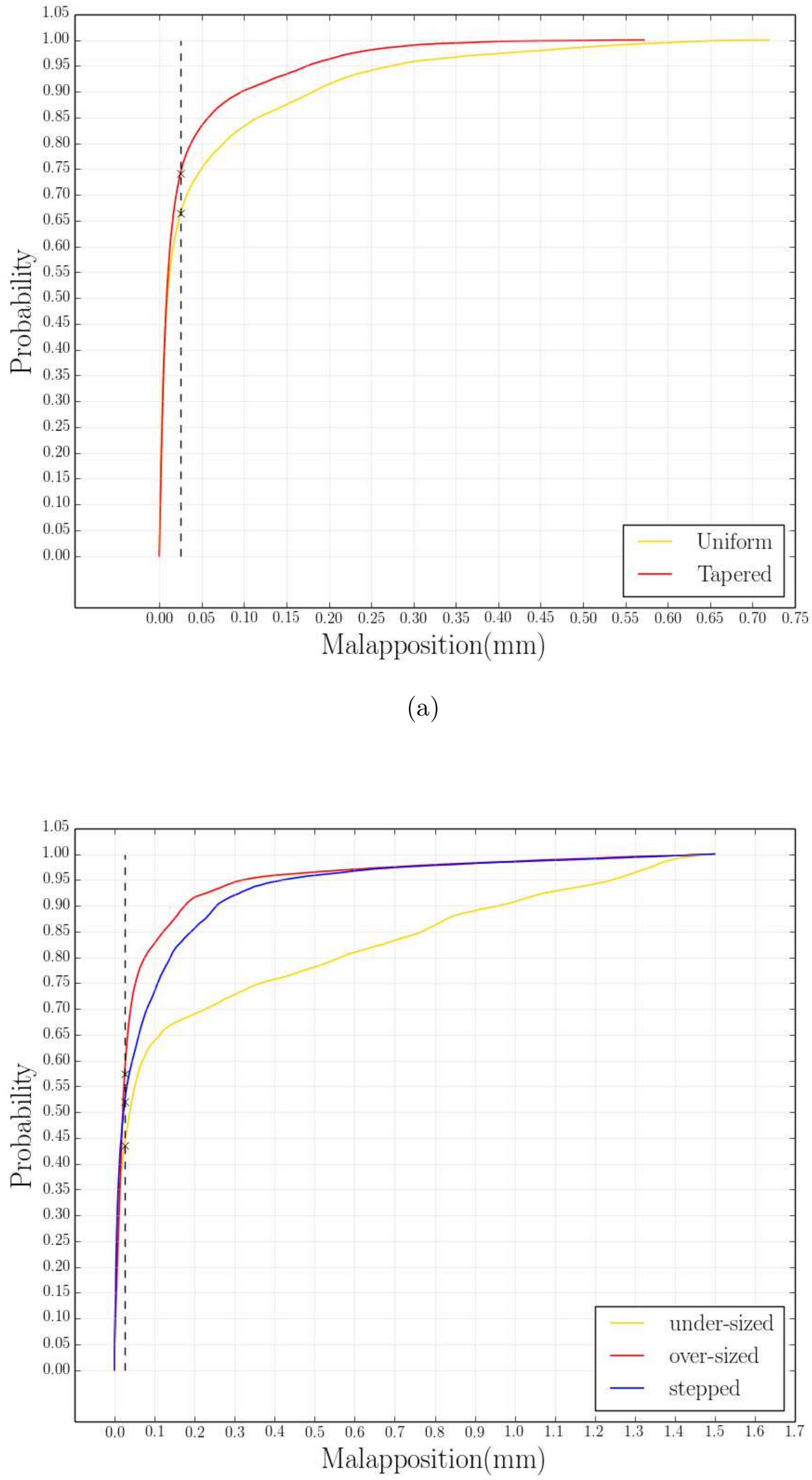

(a)

(b)

Figure 7.7: Cumulative distribution functions for patient-specific spatial SM after each expansion step. (a) CDF graphs of virtual stent malapposition within the RCA segment. (b) CDF graphs of virtual stent malapposition within the LM bifurcation segment.

proposed virtual balloons could potentially limit the procedure to a single step and, under a specific folding configuration, these models can be optimised for vessel stenting. In addition, the wall stresses induced by non uniform balloons are kept within acceptable ranges (c.f. Tables 7.1 and 7.2) in comparison to the standard models. This has also been numerically demonstrated in Morlacchi et al. (2011), in which a tapered balloon resulted in reduced circumferential stresses after kissing balloon dilation in a bifurcated vessel. This is significant since high stress values have been shown to result in cellular proliferation (Wang et al. 1995).

When the PCI operator is aware that the proximal part of the stent is malapposed, the recommended action is to post-dilate the malapposed struts with a non compliant balloon. However, SM is frequently not detected using angiography alone. Given the low overall use of IVUS/OCT imaging in most catheterisation laboratories, it is likely that the incidence of SM in lesions other than those of short length is relatively high. Our results indicate that a dedicated delivery system chosen by patient-specific criteria could help to avoid this procedural limitation by improving stent deployment in a single step. Importantly, it has been shown that under a specific pressure, non-uniform virtual balloon expansions can result in lumen gain by increasing the overall area along the entire length of the vessel. In contrast, by post-dilating only proximally malapposed struts, the MLA and the overall volume of the vessel are not likely to be significantly increased (always relatively to a non-uniform deployment) along the entire length of the stented segment.

The reconstructed vessels represent two real cases that include challenges frequently seen in clinical practice. Both segments are characterised by significant diameter discrepancy ($> 0.5\,mm$) along their lengths. It has been shown that analytical geometrical quantification of the vessels can drive PCI with very good outcomes especially in improving the investigated complications. In particular, after calculating cross sectional areas along the intervened region, multi-folded balloons can be designed according to the desired inflation pressure and the diameter variation. This is very important for adequate stent expansion as has been shown in Tables 7.1 and 7.2. Specifically, the stepped balloon which has been designed for the bifurcated vessel provided superior performance compared to both the under-sized and the over-sized balloons as indicated by the indices. For almost the same average complete stent apposition with the over-sized balloon, it resulted in considerably less average stress, whereas the indices of $TAC$ and $TAT$ indicate that the stepped balloon has not changed the global geometrical properties of the intervened segment. Recently, a dedicated stent platform mounted on a semi-compliant stepped balloon has been developed (Magro and van Geuns 2010) demonstrating impressive clinical outcomes (Fysal et al. 2014, Pleva et al. 2014). As for the tapered expansion, both MLA and VG were increased and at the same time AASM

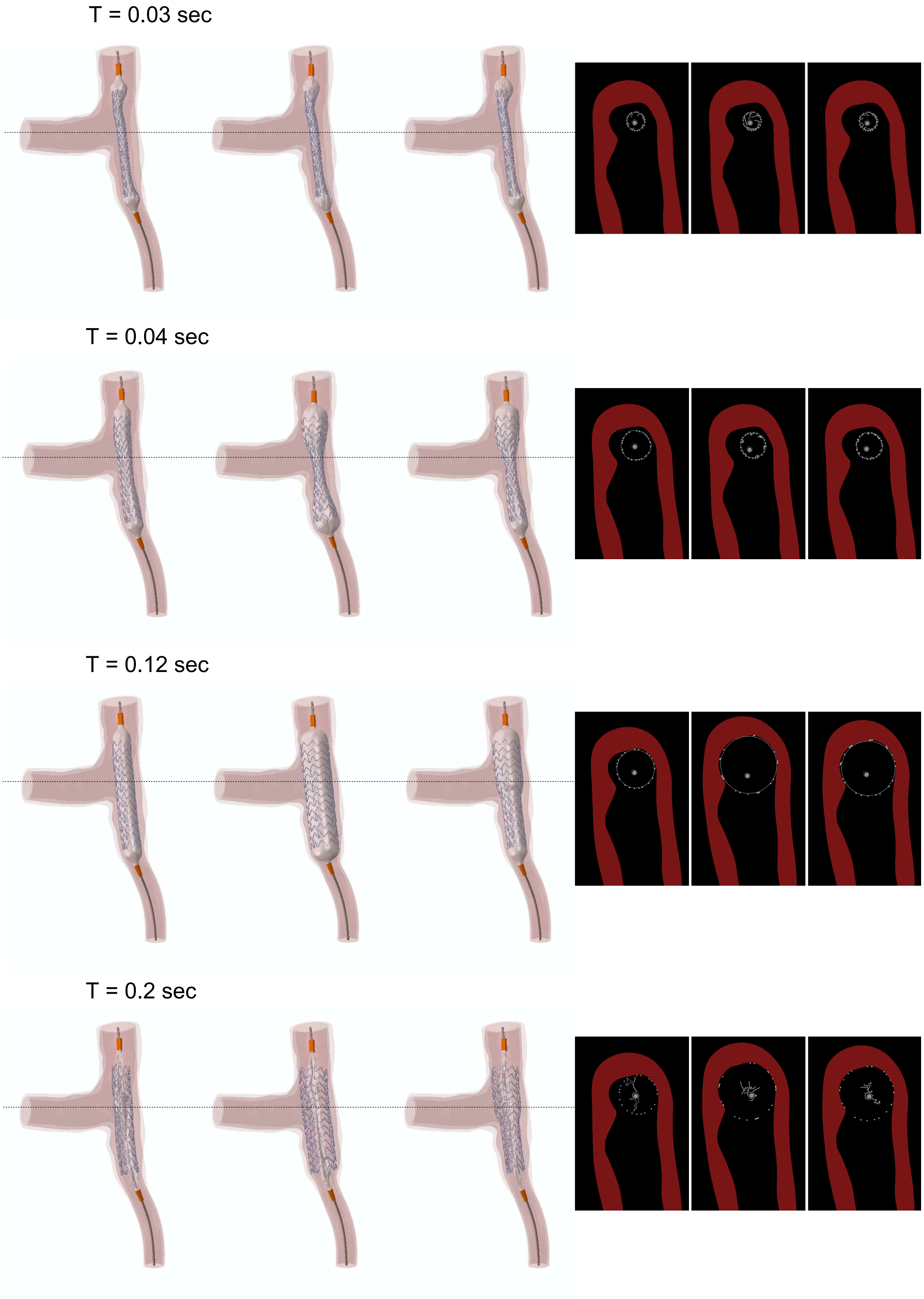

Figure 7.8: Transient patient-specific bifurcation stent expansion with undersized, oversized and a stepped balloon model: From top to bottom, the steps demonstrate (i) & (ii) the duration of the dog-boning phase, (iii) the maximum inflation of each balloon up to 1.012 $MPa$ and (iv) the final configuration of the model after the balloon deflation. On the right panel, cross sections in the middle of the stented region are illustrated.

was decreased. Interestingly, the TAC index indicates clearly that the tapered model does not have any additional influence in the curvature of the vessel when compared with the standard model. However, it does have an impact on the planarity of the vessel. This could be explained by the fact that the tapered model attaches the stent to more volumetric elements (constituting the walls), especially in the proximal region of the vessel. The latter might be the reason for experiencing higher VAS in the RCA vessel expanded by the tapered balloon model.

### 7.4.1 Limitations

The major limitation of the work presented in this chapter is the constitutive laws characterising the material behaviour of the vessel walls and the balloon models. These limitations have been discussed in section 5.4. In particular, the discrete values of the numerical indices used in this study would be different if the constitutive laws describing the vessel walls and the plaque incorporated anisotropy and plasticity, respectively. Moreover, these indices cannot be generalised to other patient-specific cases but the ones investigated in this chapter. However, due to the comparative nature of the current study, the utility of using these indices is still important. Furthermore, these numerical indices which were used to evaluate the performance of each delivery system have not been validated in clinical practice. Therefore, there is no knowledge of any index critical value. Hence, the evaluation of the extracted indices in this chapter was based on assumptions.

## 7.5 Conclusions

Numerical modelling by means of FEA can provide comprehensive and useful results for analytical investigation of stent deployment in PCI that could lead to the avoidance of complications in clinical practice. Although ideal vessels can serve as a general tool for investigating clinical issues, patient-specific simulations provide a more realistic quantification (especially with respect to the vessel's topology) of the investigated clinical issues and allow for subject-specific potential solutions. In this chapter, a framework has been developed in which virtual balloon models have been proposed to mitigate the risk of SM in two patient-specific reconstructed vessels. Where a single step approach is to be followed, such delivery systems could potentially ensure optimal strut apposition to the walls of the vessel. Scalar metrics based on the geometrical properties and the induced mechanical environment have been implemented to demonstrate numerically the pre- and post-stenting vessel state. These metrics can direct more analytic optimisation studies and guide procedural planning (as it is demonstrated in Chapter 8).

As far as is known, this work is the first computational investigation of patient-specific "stenting" purely focused on the delivery system. The outcomes indicate that under constant pressure, non-uniform balloon models can result in better strut apposition and simultaneously increase the MLA and the vessel volume. Also, it has been shown that the geometrical properties of the stented segment do not alter significantly and the vessel is not exposed to higher stresses. Finally, whilst it should be emphasised that the comparisons herein are very specific to the investigated vessels, it may be possible to derive more general delivery system definitions using population based studies and optimisation. Thus, for any given patient-specific vessel, optimum delivery system can be derived according to its its geometrical and morphological properties.

# Chapter 8

# MULTI-OBJECTIVE OPTIMISATION OF STENT DILATION STRATEGY IN A PATIENT-SPECIFIC CORONARY ARTERY VIA COMPUTATIONAL AND SURROGATE MODELLING

OPTIMISATION! Although contemporary stents have been shown to improve short and long term clinical outcomes, the optimum dilation protocol is still uncertain in challenging cases characterised by long, highly calcified and tortuous anatomy. Recent clinical studies have revealed that in these cases, sub-optimal delivery can result in ST and/or neointimal thickening as a result of SM and/or severe vessel trauma. One of the major contributors to vessel trauma is the damage caused by balloon dilation during stent deployment. In the work presented in this chapter, a Kriging based response surface modelling approach was implemented to search for optimum stent deployment strategies in a clinically challenging, patient-specific diseased coronary artery. In particular, the aims of this work were: i) to understand the impact of the balloon pressure and unpressurised diameter on stent malapposition, drug distribution and wall stresses via computer simulations and ii) obtain potentially optimal dilation protocols to simultaneously minimise stent malapposition and tissue wall stresses and maximise drug diffusion in the tissue. The results indicate that SM is inversely proportional to tissue stresses and drug deliverability. After analytical multi-objective optimisation, a set of "non-dominated" dilation scenarios was proposed as a post-optimisation methodology for protocol selection. Using this method, it has been shown that, for a given patient-specific model, optimal stent expansion can be predicted. Such a framework could potentially be used by interventional cardiologists to minimise stent malapposition and tissue stresses whilst maximising drug deliverability in any patient-specific case[1],[2].

## 8.1 Introduction

Clinical studies have revealed that contemporary devices, especially DES, demonstrate better short and long term outcomes than BMS (Stefanini and Holmes 2013) and the second and the third generation DES are critically superior to first generation DES. However, clinical complications have been reported which are associated with the recent advances in stent design, the implantation protocol and the complexity of the treated vessel (Cook et al. 2007, Hanratty and Walsh 2011, van der Hoeven et al. 2008a, Hong et al. 2006, Williams et al. 2012).

As seen in Chapters 6 and 7, one of the adverse outcomes in such challenging cases is SM which is largely dependent on multiple factors including the so-called "reference diameter"[3], plaque morphology, lesion length, stent length and the balloon inflation pressure (Cook et al. 2007, van der Hoeven et al. 2008a). Depending on the vessel length and its anatomy, reference diameter is normally calculated in the distal end of the target lesion. This often results in malapposed struts in the proximal end of the stented segment particularly in a longer lesion, which has a diameter discrepancy between the proximal and distal end. When SM is detected, a non-compliant balloon is inflated in the malapposed region to reshape the stent and increase the stent area. However, such post-stenting procedures may trigger further clinical complications including vessel wall dissection or stent fracture (Hanratty and Walsh 2011). Therefore, in such challenging vessels, it is preferable to limit stenting to a single step approach resulting in i) maximum stent strut apposition, ii) minimum vessel stress and iii) maximum drug diffusion to the vessel walls.

In the current work, the optimal dilation strategy in a patient-specific RCA with challenging disease (second reconstructed RCA case presented in Chapter 3) was investigated by FEA and surrogate modelling. Firstly, twenty different dilation protocols were defined with respect to the balloon unpressurised diameter and the balloon pressure following their simulation. The performance of each protocol was measured by three figures of merit (objective functions) representing i) tissue stresses, ii) SM and

---

[1] A part of the following content has been published in the Annals of Biomedical Engineering Journal: **Design optimisation of coronary artery stent systems**, N. Bressloff, G.Ragkousis, N. Curzen, 2015

[2] The content of this chapter has been published in the Journal of Biomechanics: **Multi-objective optimisation of stent dilation strategy in a patient-specific coronary artery via computational and surrogate modelling**, G. Ragkousis, N. Curzen, N. Bressloff., 2015

[3] Reference diameter is defined as the diameter of a healthy arterial cross section along the length of the intervened segment. Interventional cardiologists size the stent which is to be implanted according to the non-diseased diameter in the distal part of the segment.

iii) drug delivery. Surrogate models were constructed for each objective function to describe the functional relationship between the input parameters and the performance. Then, based on a dedicated population based algorithm, non-dominated designs (optimum dilation protocols) were obtained. Three update points were taken along the Pareto front of the objective function space and further computer simulations were carried out to enhance the surrogates and improve the optimal responses. This process was repeated until a stopping criterion was satisfied.

## 8.2 Materials and methods

The pyKriging package (http://www.pyKriging.com/) (Paulson and Ragkousis 2015) was used to construct the surrogates and guide the multi-objective optimization study. A validation of the algorithms that were used in this chapter is presented in Appendix E. A non-sorting genetic algorithm (NSGA-II) (Deb 2001), as implemented in pyOpt (http://www.pyopt.org/) (Perez et al. 2012) was used to extract the optimal Pareto front after each optimisation phase[4].

### 8.2.1 Geometry & mesh discretisation

#### 8.2.1.1 Vessel, dilation catheter and stent platform

For the purposes of the simulations in this chapter, the second reconstructed patient-specific vessel presented in Chapter 3 was simulated. One representative XIENCE (Abbott Lab., IL, USA) stent model was used (c.f. section 4.2.2). The constitutive material models along with the mesh resolution information of the reconstructed challenging vessel and the stent model was provided in section 5.2.1 and 5.2.2, respectively. Six-folded balloon models were used, constructed as shown in section 4.3. The constitutive material models along with the mesh resolution information of the delivery system FEA models was provided in section 5.2.3. In Figure 8.1, the **CAD** assembly of a baseline model along with its mesh discretisation is depicted.

#### 8.2.1.2 Dilation strategy parametrisation

The balloon profile and the inflation pressure were taken as the design variables of this optimisation problem. Although, all the balloons were six-folded, depending on the parameterised balloon-profile length (unpressurised diameter), the folding configuration was varied to fit in the semi-crimped stent. The design space was defined by: i)

---

[4] In appendix G, the multi-objective optimisation algorithm (developed for the purposes of this work) is presented. In particular, the python class is presented followed by a script to call this class.

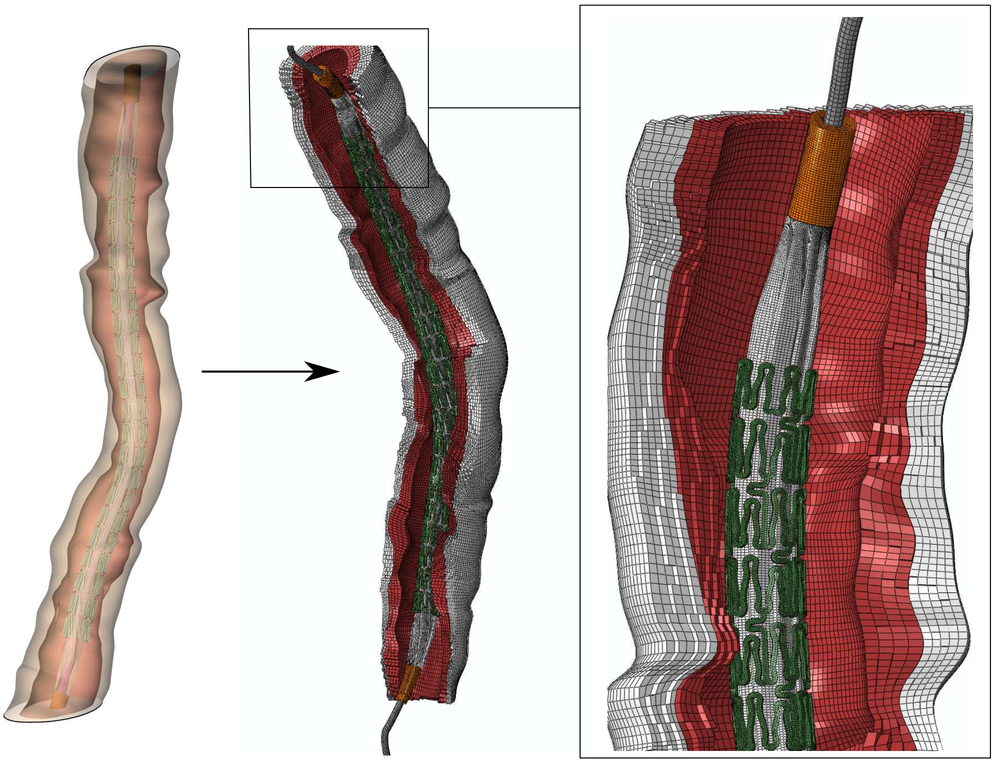

Figure 8.1: Baseline model: virtual model assembly of the reconstructed artery and structured mesh discretisation

the initial diameter sampled around ±20% of the baseline model and ii) the inflation pressure varying between $0.6 - 1.5$ $MPa$, a range widely used in stenting practice.

### 8.2.2 Simulations

#### 8.2.2.1 Stent crimping and expansion

For the baseline model, the design variables were chosen according to the reference diameter measured in the distal part of the reconstructed segment. Then, a virtual balloon was generated and calibrated as shown in section 5.2.3. For each model, the stenting process comprised two steps: i) the stent system was mapped to the catheter line and then, the stent was crimped on the shaft and ii) the expansion of the stent by a six-folded balloon. Both of these steps were conducted in ABAQUS using the explicit solver to overcome convergence issues related to large element deformation and highly non-linear contact between surface pair interactions. All the simulations were considered to be quasi-static and their parameters were set as shown in section 5.3. In Figure 8.2, the transient expansion of the baseline point simulation is depicted.

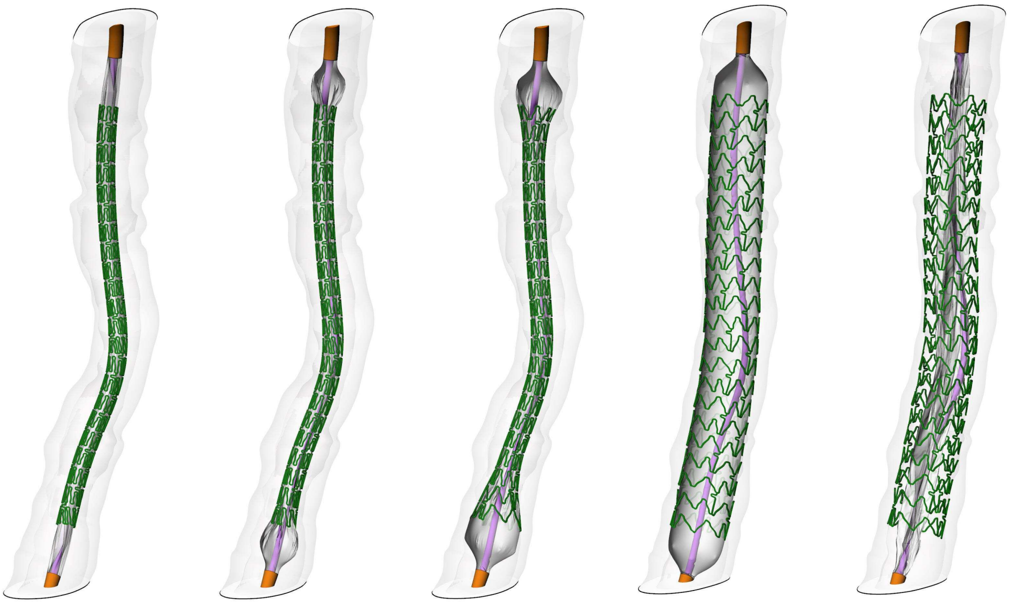

Figure 8.2: Baseline point simulation: from left to right, crimping and positioning of the stent system in the intervened region, dog-boning phase during the expansion, inflation of the balloon to the target diameter and balloon deflation

#### 8.2.2.2 Drug release

After stent deployment, the deformed artery and stent geometry was used to simulate drug release in the walls of the vessel. A heat transfer solution scheme was used as an analogue of the drug delivery process similarly to the work presented by Hose et al. (2004). The release of the drug was simulated as a steady state event by using the forced heat convection analysis capability of ABAQUS/Standard. The boundary conditions for the transport simulation were defined as in other studies (Feenstra and Taylor 2009, Hose et al. 2004, Pant et al. 2012, Zunino 2004). In brief, the boundary conditions were: i) zero flux at the outer part of the vessel, ii) zero flux at the luminal part of the vessel that is not in contact with the stent, iii) zero concentration at both ends of the vessel and iv) a unity concentration on the stent boundaries. By disregarding the porosity field, the diffusivity and the conductivity values were adopted from Feenstra and Taylor (2009).

### 8.2.3 Objective functions

#### 8.2.3.1 VAS

To evaluate numerically the mechanical environment induced by each of the interventional protocols, the $VAS$ index was implemented. For further information on the

$VAS$ metric, see section 7.2.1.3.

#### 8.2.3.2 AASM

To calculate the performance of each dilation strategy regarding SM, the $AASM$ metric was implemented. For further information on the $AASM$ index, see section 7.2.1.3.

#### 8.2.3.3 VAD

Similarly to the $VAS$ index, a volume average index for drug release was proposed by Pant et al. (2012) to measure the amount of drug transported into the tissue. The $VAD$ index is numerically expressed as

$$VAD = \frac{\int_V c dV}{\int_V dV} \tag{8.1}$$

where, $c$ represents the drug concentration in the wall region, and the integrals are calculated over the volumes of intima and media. The volume for which was reconstructed by the IVUS images. Since the volume has been discretised by finite elements, the formula is rearranged as

$$VAD = \frac{\sum_{i=1}^{i=n_v} c_i \delta V_i}{\sum_{i=1}^{i=n_v} \delta V_i} \tag{8.2}$$

where $n_v$ is the total number of elements within the intima-media volume, $c_i$ represents the drug concentration in the $i$th element of the volume, and $\delta V_i$ is the volume of the $i$th element.

### 8.2.4 Optimisation problem & solution methodology

The multi-objective optimisation problem was formulated as follows:

$$Minimise \quad VAS(d,p) \tag{8.3}$$

$$Minimise \quad AASM(d,p) \tag{8.4}$$

$$Minimise \quad -VAD(d,p) \tag{8.5}$$

such that

$$2.672 \leq d \leq 4.008 \tag{8.6}$$

$$0.6 \leq p \leq 1.5 \tag{8.7}$$

where $d$ and $p$ are the diameter and the pressure parameters, respectively. Note that $-VAD$ index should be maximised. However, the negative sign was included so that lower values of $-VAD$ indicate better performance. Therefore, the aim was to minimise $-VAD$.

In Figure 8.3, a flow chart detailing the optimisation process is depicted. The process commenced with the optimal distribution of the initial sampling points in the design space, followed by structural and drug simulations for each design configuration. Discrete values of the performance metrics were extracted to construct Kriging response surface models for each metric. The models were then searched by a population-based algorithm (NSGA-II) to obtain optimum solutions for surrogate model improvement. From the optimum set, three points were selected as infill points to the initial sampling plan or the previous optimisation step. The process stopped when the stopping criterion was satisfied (see section 8.2.4.2).

#### 8.2.4.1 Sampling plan

The initial two-dimensional design space consisted of twenty points optimally distributed as a function of balloon unpressurised diameter and balloon pressure. This represents the sampling plan or DoE. The DoE was constructed by an optimised Latin hyper-cube (LHC) ensuring the maximum space filling (Morris and Mitchell 1995). Optimised LHCs can maximise the minimum distance between each pair of points. In Figure 8.4, the optimised initial DoE is depicted against a non-optimised LHC. Notice the smaller $\Phi$ value which is the scalar-valued criterion function used to rank different sampling plans (Forrester et al. 2008, Morris and Mitchell 1995).

#### 8.2.4.2 Surrogate modelling, NSGA-II & infill strategy

*Surrogate models*

To model the response of each objective function to variations in balloon pressure and unpressurised diameter a GP methodology, known as Kriging, was used. Appendix F contains the basic equations for Kriging model construction. For detailed derivation, consult the work by Jones (2001) and Forrester et al. (2008). Kriging models have been also implemented successfully in previous studies on stent optimisation, such as in Pant et al. (2011) and Gundert et al. (2012). For a detailed overview in recent optimisation and surrogate modelling studies, consult the review paper by Bressloff et al. (2015), including reference to earlier studies such as the one by Timmins et al. (2007).

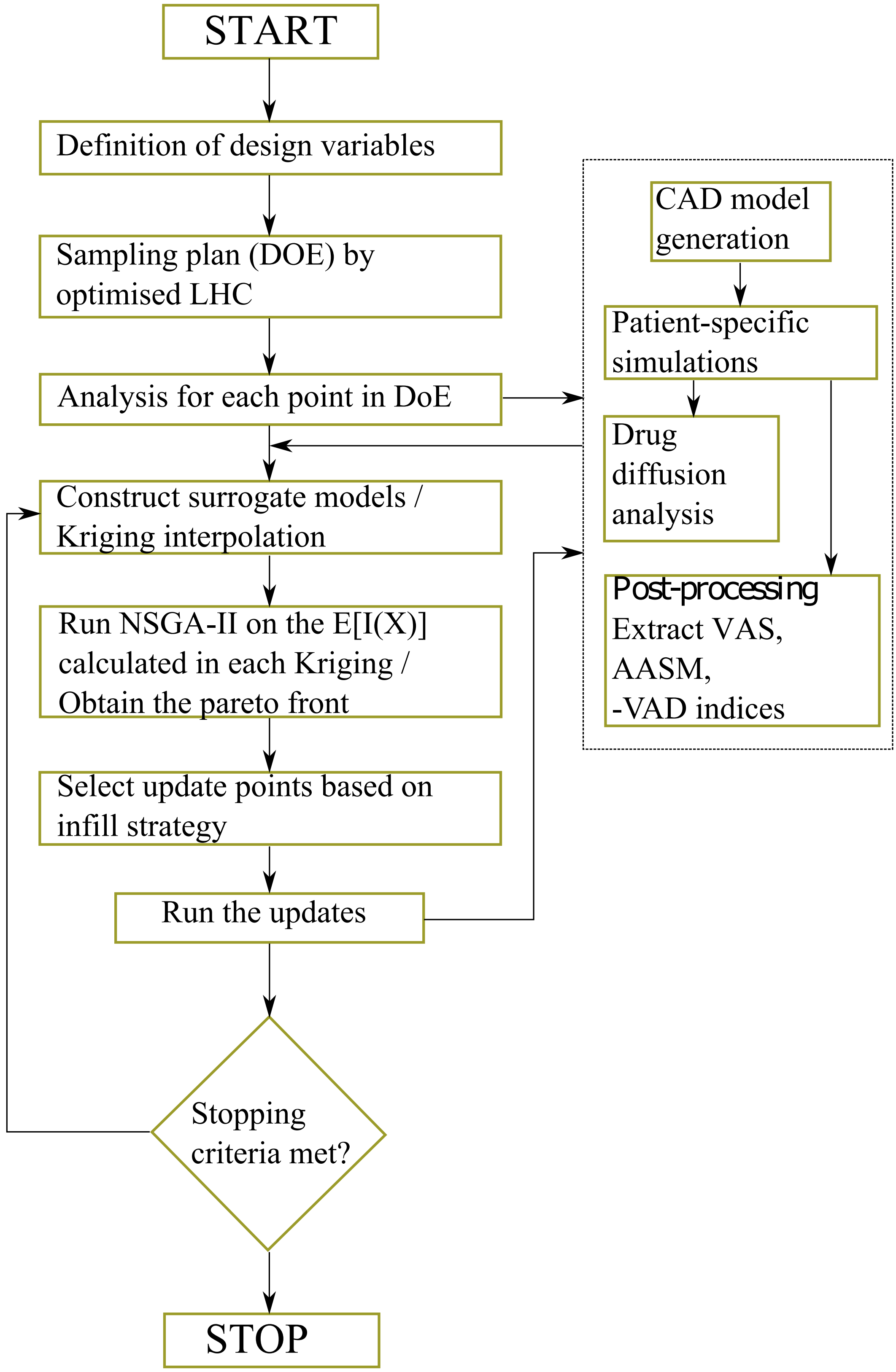

Figure 8.3: Flow chart on the description of the adopted optimisation methodology of this work

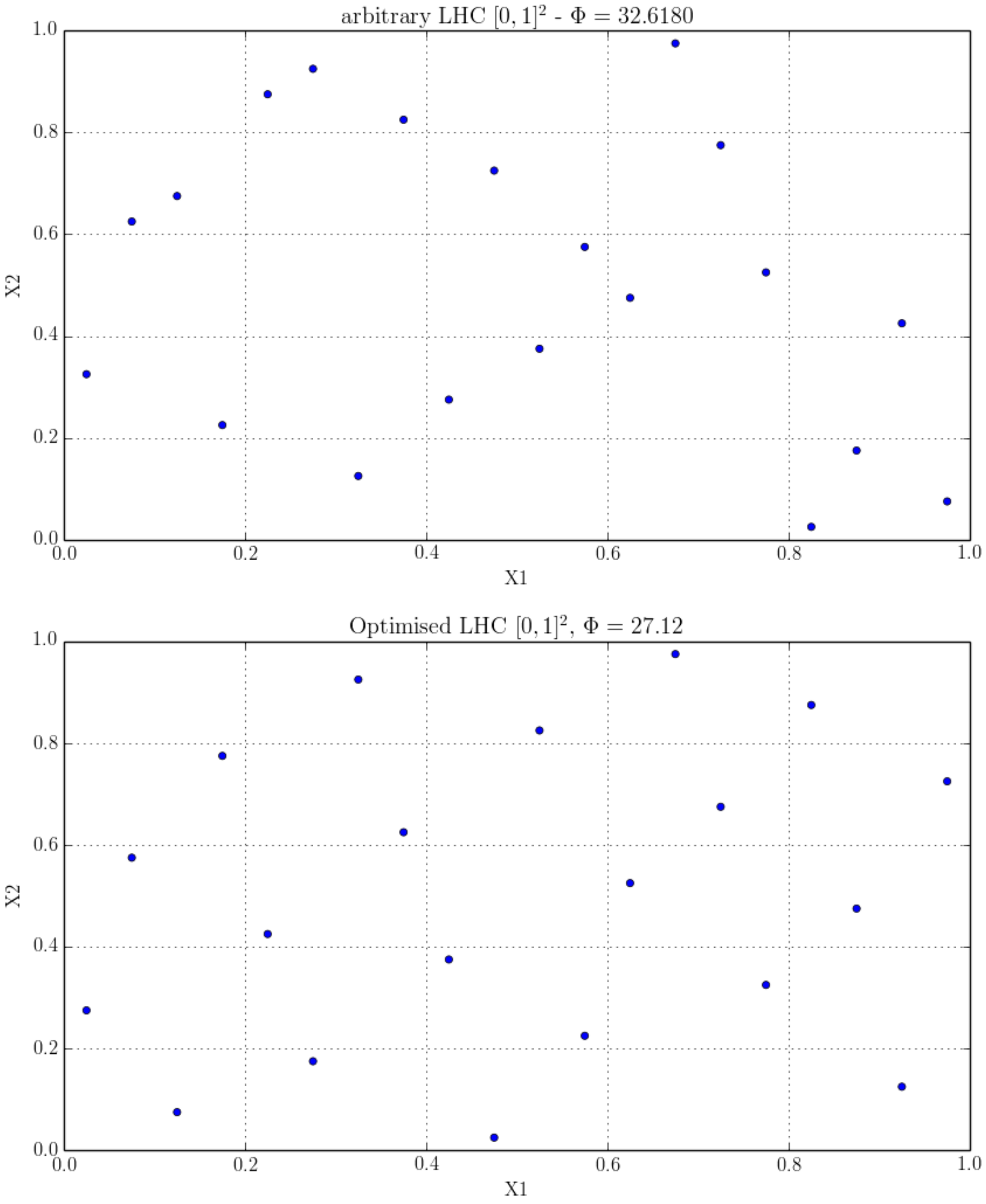

Figure 8.4: DoE obtained from an optimised LHC. An arbitrary LHC (top panel) with $\Phi$ value equal to 32.618 and the optimised LHC used in this work with $\Phi$ value equal to 27.12.

### *Validation of surrogates*

Once the surrogates are built, validation has to be carried out to ensure that the model predicts well the actual function. One obvious solution would be to select and run additional points to check the correlation of the surrogate at these points. However, this would be computationally impractical given the available computational budget. This has led to the development of other methods to validate the surrogate models (Jones et al. 1998, Kolachalama et al. 2007). One of these methods is the $SCVR$, and is defined as

$$SCVR_i = \frac{y(\mathbf{x}^{(i)}) - \hat{y}_{-i}(\mathbf{x}^{(i)})}{\sqrt{C_{-i}(\mathbf{x}^{(i)}, \mathbf{x}^{(i)})}} \tag{8.8}$$

where $y$ is the observed value at the $i^{th}$ point (point that is left out), $\hat{y}_{-i}$ denotes the prediction of the $i^{th}$ left out point and $C_{-i}$ is the posterior variance of the prediction at the left out point. The model is valid when all $SCVR_i$ discrete points lie in $[-3, +3]$. This can be interpreted as that each of the predictions lie between plus or minus three standard errors (99.7% confidence). Further, a "leave-one-out" method was used to test for model reliability (Jones et al. 1998). Again, for each surrogate model, one point of the DoE was left out and a surrogate model with constant parameters constructed for the remaining sampling points. Then, a prediction was made at the point that was left out and compared to the actual value. This process was repeated for all the points that comprise the DoE and a correlation residual was calculated for each model.

### *NSGA-II*

The superiority of GP models is the fact that such surrogates contain the estimation of model uncertainty, expressed by the mean square error (MSE). This allows the calculation of an estimated error in the model. Therefore, it is possible to use $MSE$ to position infill points where the uncertainty in the predictions of the model is the highest. The $MSE$ in a Gaussian process is expressed as

$$\hat{s}^2(\mathbf{x}) = \sigma^2 \left[ \mathbf{1} - \psi \mathbf{\Psi}^{-1} \psi + \frac{(\mathbf{1} - \mathbf{1}^T \mathbf{\Psi}^{-1} \psi)^2}{\mathbf{1}^T \mathbf{\Psi}^{-1} \mathbf{1}} \right] \tag{8.9}$$

where $\sigma^2$ is the process variance, $\mathbf{\Psi}$ is the correlation matrix, and $\psi$ is a vector of correlations between the observed data and the new predictions (see Appendix F).

Additionally, a highly attractive tool in stochastic optimisation is the expected improvement (EI) (Jones et al. 1998), which indicates the magnitude of improvement towards the optimum solution. It is expressed as

$$E\left[I(\mathbf{x})\right] = \begin{cases} (y_{min} - \hat{y}(\mathbf{x}))\mathbf{\Phi}(\frac{y_{min}-\hat{y}(\mathbf{x})}{\hat{s}(\mathbf{x})}) + \hat{s}\phi(\frac{y_{min}-\hat{y}(\mathbf{x})}{\hat{s}(\mathbf{x})}), & \text{if } \hat{s} > 0 \\ 0, & \text{if } \hat{s} = 0 \end{cases} \tag{8.10}$$

where $\mathbf{\Phi}$ and $\phi$ are the probability distribution and probability density functions, respectively; $y_{min}$ is the minimum value evaluated in the sampling plan thus far and $\hat{y}(\mathbf{x})$ is the prediction in a sampling point $\mathbf{x}$. Since the EI can be evaluated for each objective function, NSGA-II was used to search the Pareto front for maximisation of the multi-objective EI. NSGA-II was run for 130 generations, each generation having a population size of 100 resulting in 13100 function evaluations per search.

*Infill strategy and convergence criterion*

In each optimisation phase, two steps were performed to select update points. In the first step, three points were selected with two of the points positioned at the ends and a third point located in the middle of the Pareto front. The second step comprised the mapping of these points to the design space to check their shortest distance with respect to the initial/previous sampled points. Around each update point, a circle with radius equal to 1% of the variable range (0.01 here since the variables were normalised in the range $[0-1]^2$) was constructed and if there was no point already sampled in this circle, the selection was approved. Otherwise, the point was rejected and the next closest non-dominated point was selected. This two-step procedure ensured both exploration and exploitation. The first step ensured exploitation while the second step contributed to the exploration (very essential in a mathematical optimisation routine). Due to the high computational cost for each simulation (average point simulation duration was approximately 160 hours on a 32 *GB* RAM node, split over 32 domains), a convergence criterion was set to avoid a large number of optimisation iterations. In particular, in each step, updated surrogates were constructed containing the infill points from the previous iteration and a second NSGA-II search (this time on the updated response surfaces of the prediction) were carried out. Then, an optimum point was calculated as the Pareto front point with the minimum Euclidean distance from the ideal vector/“utopia” point. More specifically, the obtained Pareto front was normalised with respect to the utopia (ideal vector) and the nadir (maximum objective function vector) point as

$$\bar{f}_i(\mathbf{x}) = \frac{f_i(\mathbf{x}) - z_i^*}{n_i^* - z_i^*} \tag{8.11}$$

where $f_i(\mathbf{x})$, $z_i^*$, and $n_i^*$, the non-normalised objective function value, the minimum objective function value and the maximum objective function value of the $i^{th}$ model, respectively (Miettinen 1998). Then, the minimum Euclidean distance was calculated from the weighted $l_2 - metric$ proposed by Miettinen (1998) as

$$\begin{aligned} minimise \quad d_2(\mathbf{f},\mathbf{z},\mathbf{w}) &= (\sum_{i=1}^{k} w_i |f_i(\mathbf{x}) - z_i^*|^2)^{\frac{1}{2}} \\ subject \quad to \quad & \mathbf{x} \in \mathbb{S} \end{aligned} \tag{8.12}$$

with $\mathbb{S}$ being the entire search space and $\sum_{i=1}^{k} w_i = 1$. When the predicted optimum point (with $w_1, w_2, w_3 = 1/3$) was the same in two subsequent iterations, the optimisation process was terminated.

## 8.3 Results & discussion

### 8.3.1 Baseline and DoE point simulations and Kriging interpolation

The results for the baseline model are reported in the first row of Table 8.1. From the second to the last row of Table 8.1, the discrete objective function evaluations of the initial DoE are reported. Surrogate models were constructed for each objective function. The response surfaces along with the $MSE$ and the EI of the surrogates are depicted in Figure 8.5. The x-axis and the y-axis represent the normalised balloon diameter and pressure, respectively. It can be noted that the diameter parameter has a stronger effect than the pressure for all models. This is expected since larger diameters result in higher surface area interaction (between the balloon and vessel walls) and, subsequently, less SM and higher circumferential stresses imposed to the vessel walls. In the first column of Figure 8.5, the model predictions indicate that stent malapposition is inversely proportional to tissue stress and drug diffusion (note that drug diffusion contours or +VAD, would have the opposite behaviour from $-VAD$). Consequently, $VAS$ is competing against both $AASM$ and $-VAD$. This can be explained by the fact that when SM decreases, more stent struts interact with the vessel walls and higher tissue stresses are imposed by the stent, especially when using higher balloon pressures. Moreover, since more struts interact with the wall, the drug diffusion is increased. In contrast, when malapposition increases, the drug diffusion is decreased ($-VAD$ is increased) as a result of the reduced wall-stent interaction. In the second column of Figure 8.5, $MSE$ error indicates that high uncertainty exists in the corners for all the surrogates. This is expected as, in this optimisation work, LHC was used to generate the initial DoE leaving the corners and the edges of the design space unsampled. Finally, in the third column, the EI indicates where model improvement can be obtained via infilling the design space in regions where EI is maximum. In general, the EI tends to be large in regions where the predicted value is larger than the minimum actual value (extracted by the simulations) and/or there is a high level of uncertainty associated with the prediction. As stated by Sobester et al. (2005), EI is a balance between seeking promising areas of the design space and the uncertainty in the model.

Table 8.1: Baseline, DoE point parameters and objective function evaluations

| **Design** | **Diameter** X1 (0 - 1) | **Pressure** X2 (0 - 1) | **Diameter** X1 (mm) | **Pressure** X2 (MPa) | **VAS** | **AASM** | **-VAD** |
|---|---|---|---|---|---|---|---|
| Baseline | 0.532 | 0.268 | 3.383 | 0.842 | 0.01999 | 0.05313 | -0.0786 |
| DOE_01 | 0.625 | 0.525 | 3.507 | 1.0725 | 0.026465 | 0.040062 | -0.08594 |
| DOE_02 | 0.474 | 0.025 | 3.306 | 0.622 | 0.01727 | 0.084921 | -0.06723 |
| DOE_03 | 0.275 | 0.174 | 3.039 | 0.757 | 0.015359 | 0.088589 | -0.06306 |
| DOE_04 | 0.174 | 0.775 | 2.905 | 1.297 | 0.014705 | 0.096926 | -0.06100 |
| DOE_05 | 0.325 | 0.925 | 3.106 | 1.432 | 0.019671 | 0.063213 | -0.07577 |
| DOE_06 | 0.925 | 0.125 | 3.907 | 0.712 | 0.038519 | 0.024668 | -0.09277 |
| DOE_07 | 0.074 | 0.574 | 2.772 | 1.117 | 0.011525 | 0.141287 | -0.04639 |
| DOE_08 | 0.974 | 0.724 | 3.974 | 1.252 | 0.045297 | 0.023369 | -0.09267 |
| DOE_09 | 0.025 | 0.275 | 2.705 | 0.847 | 0.008847 | 0.203502 | -0.03103 |
| DOE_10 | 0.125 | 0.074 | 2.838 | 0.667 | 0.010284 | 0.16601 | -0.03772 |
| DOE_11 | 0.824 | 0.875 | 3.774 | 1.387 | 0.039838 | 0.026552 | -0.09127 |
| DOE_12 | 0.724 | 0.675 | 3.64 | 1.207 | 0.034793 | 0.026546 | -0.09148 |
| DOE_13 | 0.525 | 0.824 | 3.373 | 1.342 | 0.02745 | 0.039425 | -0.08733 |
| DOE_14 | 0.574 | 0.225 | 3.44 | 0.802 | 0.024807 | 0.044335 | -0.08335 |
| DOE_15 | 0.375 | 0.625 | 3.173 | 1.162 | 0.019721 | 0.064665 | -0.07467 |
| DOE_16 | 0.775 | 0.325 | 3.707 | 0.892 | 0.033875 | 0.029117 | -0.09065 |
| DOE_17 | 0.424 | 0.375 | 3.239 | 0.937 | 0.017456 | 0.074464 | -0.06904 |
| DOE_18 | 0.875 | 0.474 | 3.841 | 1.027 | 0.039197 | 0.023864 | -0.09244 |
| DOE_19 | 0.225 | 0.424 | 2.972 | 0.982 | 0.013872 | 0.11152 | -0.05528 |
| DOE_20 | 0.675 | 0.974 | 3.573 | 1.477 | 0.032538 | 0.030896 | -0.09075 |

### 8.3.2 Validation of the surrogates

On the left column of Figure 8.6, the $SCVR$ for all the Kriging models are shown. It can be observed that all points lie within the interval $[-3, +3]$ for all the surrogate models. Consequently, the interpolated models predict with 99.7% confidence. The leave-one-out plots are depicted in the right column of Figure 8.6. As can be observed, all the surrogate models predict close function values to their corresponding “actual” values (extracted by the computational analyses). This is evident by the fact that all leave-one-out plots have approximately linear behaviour ($R^2$ was 0.97, 0.92 and

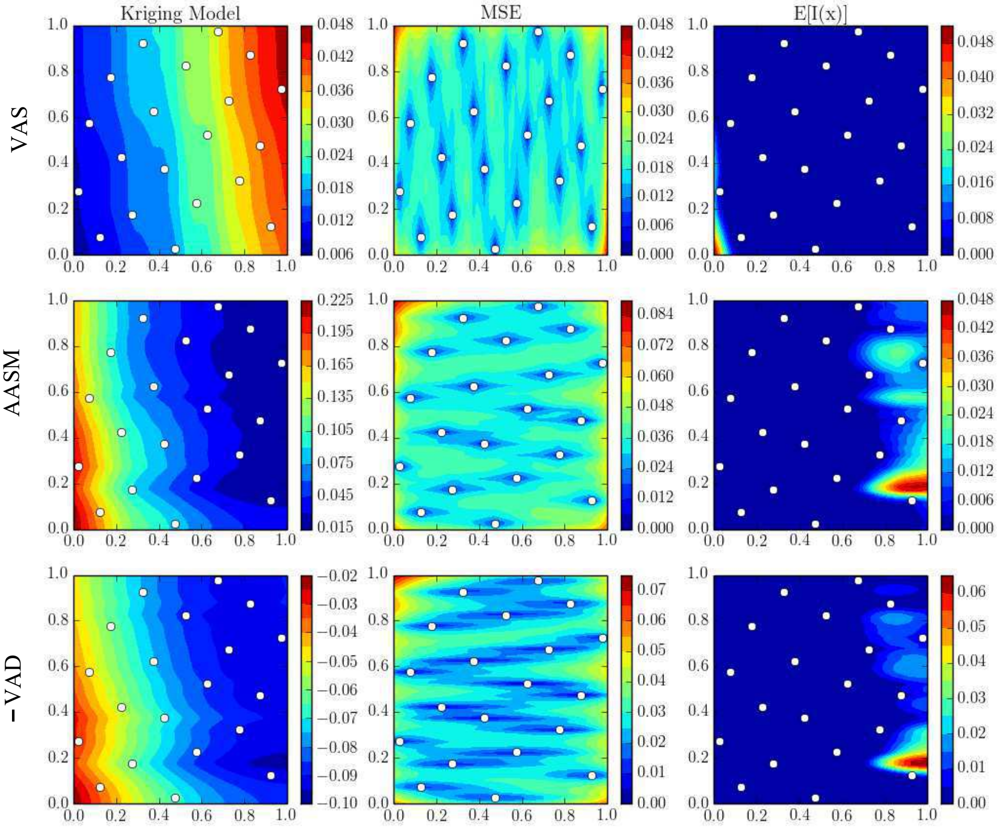

Figure 8.5: Surrogate models interpolated to the objective function evaluations after the initial DoE. From up to bottom, surrogates for VAS, AASM, and -VAD are depicted. The x-axis and y-axis represent the normalised balloon diameter and pressure. From left to right, Kriging interpolation surface of the prediction, MSE and EI for each model

0.95 for $VAS$, $AASM$ and $-VAD$, respectively). Therefore, all the surrogates can be considered to be sufficiently reliable.

### 8.3.3 Infill point simulations, update Kriging construction and selection criteria

Three update cycles were performed before satisfying the convergence criterion. The resulting nine infill point parameter values along with the objective function evaluations at each point are reported in Table 8.2. The corresponding updated surrogates in each optimisation iteration are depicted in Figure 8.7. It can be noted that the maximum and minimum values of all the surrogates appear to be close to convergence from the second optimisation iteration. In Figure 8.8, the EI of each model from the initial step (first row), to the last optimisation step (last row) are depicted. The implemented algorithm selects points on the Pareto front where the EI is the maximum. Since two of the objectives ($AASM$ and $-VAD$) have relatively similar behaviour, the first update is chosen based on both maximum EI values. The second update is selected where the EI for $VAS$ is the maximum and the third update is selected in the middle part of the Pareto front. As can be observed in Figure 8.8, all the update points, meet the filtration criterion of the 0.01 radius. As discussed in section 8.2.4.2, the optimisation process is stopped when the convergence criterion is met. In the last two optimisation steps the Pareto front obtained by NSGA-II run using the prediction surfaces is not significantly changed. Consequently, the same optimum point is predicted.

Table 8.2: Infill point parameters and objective function evaluations

| **Design** | **Diameter** X1 (0 - 1) | **Pressure** X2 (0 - 1) | **Diameter** X1 (mm) | **Pressure** X2 (MPa) | **VAS** | **AASM** | **-VAD** |
|---|---|---|---|---|---|---|---|
| UPD_01 | 0 | 0 | 2.672 | 0.6 | 0.008702 | 0.211611 | -0.02916 |
| UPD_02 | 0.935 | 0.176 | 3.921 | 0.758 | 0.038047 | 0.02439 | -0.09234 |
| UPD_03 | 0.715 | 0 | 3.627 | 0.6 | 0.02765 | 0.039457 | -0.08616 |
| UPD_11 | 0.028 | 0 | 2.71 | 0.6 | 0.008942 | 0.205837 | -0.03044 |
| UPD_12 | 0.897 | 0.767 | 3.87 | 1.291 | 0.046635 | 0.022709 | -0.09294 |
| UPD_13 | 0.262 | 0.761 | 3.022 | 1.285 | 0.017237 | 0.083795 | -0.06794 |
| UPD_21 | 0 | 0.367 | 2.672 | 0.931 | 0.008782 | 0.213357 | -0.02949 |
| UPD_22 | 0.901 | 0.617 | 3.876 | 1.156 | 0.042577 | 0.022664 | -0.09209 |
| UPD_23 | 0.651 | 0.145 | 3.541 | 0.731 | 0.026895 | 0.040592 | -0.08517 |

### 8.3.4 Visualisation of the simulated sampling points

In Figures 8.9 and 8.10, spatial SM and wall circumferential stress contours, respectively, are mapped to the deformed simulated models. It is evident that models with

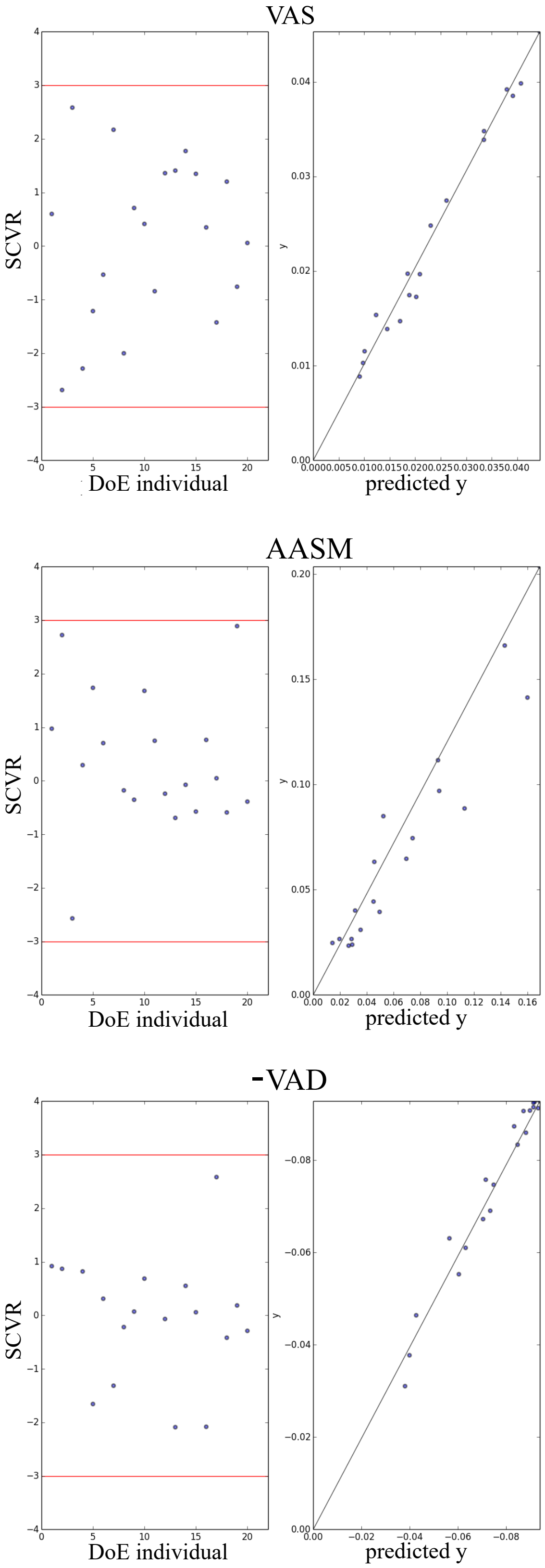

Figure 8.6: Surrogate model validation: On the left panel, SCVR values for all models (rows). On the right panel, leave-one-out plots for all models (rows). Predicted y stands for values extracted from the surrogates while y stands for values extracted from the computational analyses.

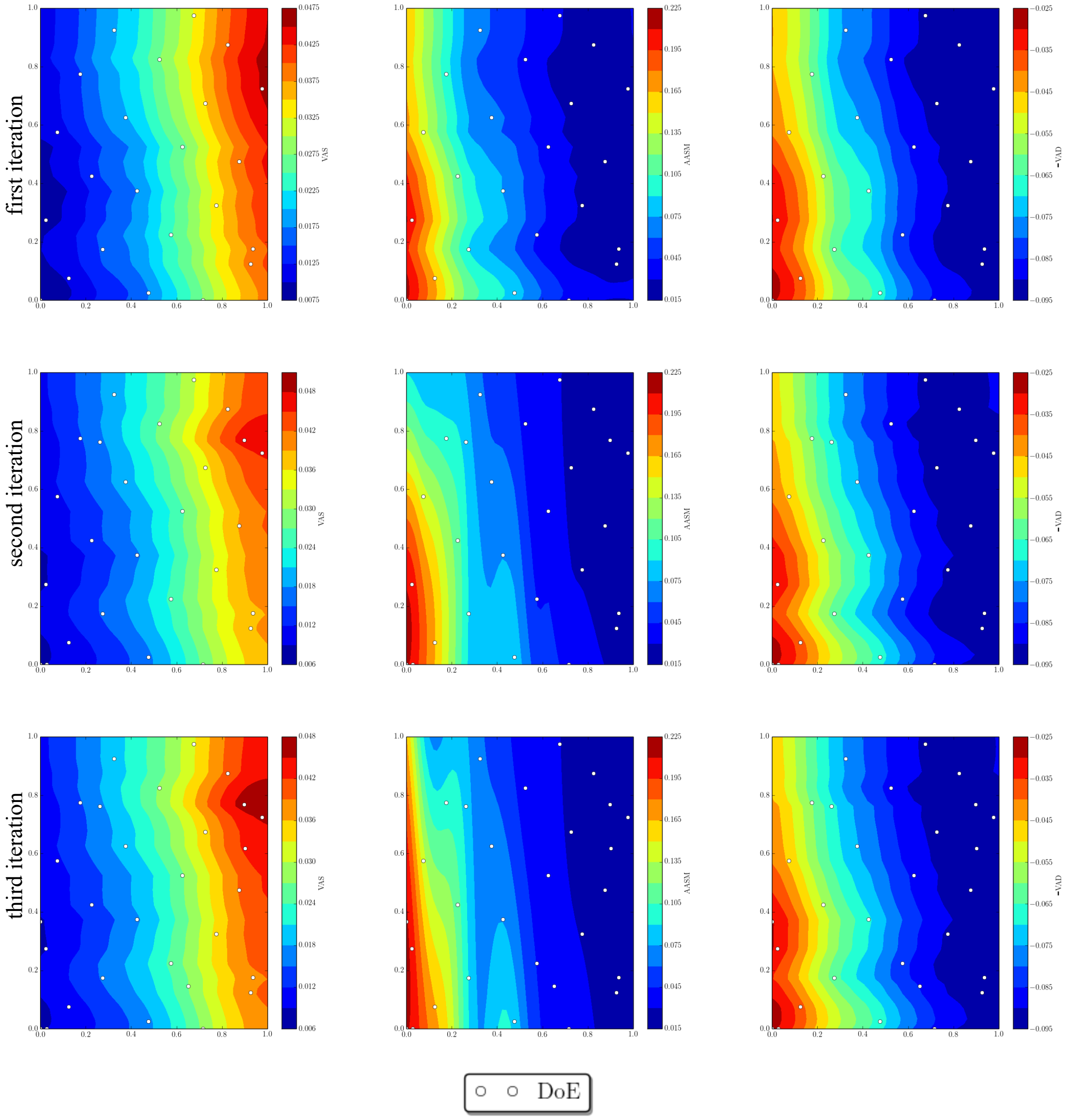

Figure 8.7: GP interpolation surfaces for the three models (columns) after each optimisation iteration (rows).

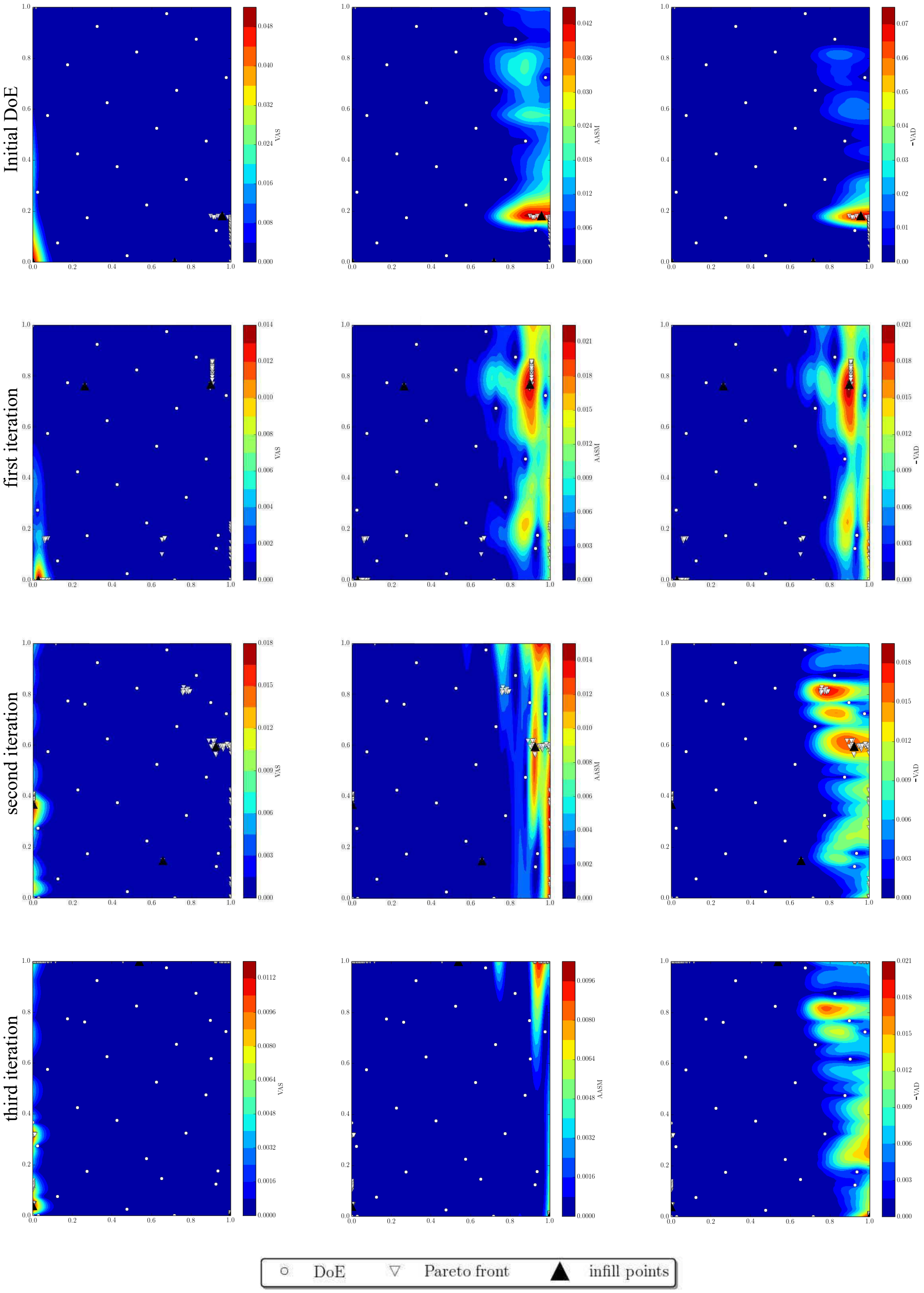

Figure 8.8: NSGA-II search in the EI of the GP models (columns) in the initial DoE and each optimisation iteration (rows). The Pareto non-dominated solutions along with the update points are also mapped onto the design space to ensure exploitation and exploration.

reduced SM result in higher tissue stresses (c.f. Tables 8.1 and 8.2), for instance $DoE\_08$, $DoE\_11$, $DoE\_12$, $DoE\_16$, $DoE\_18$, $UPD\_12$, and $UPD\_22$. This is expected from the fact that luminal gain leads to higher stresses in the arterial wall. Especially in $DoE\_08$, $DoE\_11$, $UPD\_12$ and $UPD\_22$, the increased $VAS$ index is as a result of stent over-expansion. Interestingly, while dilation scenarios, $DoE\_11$ and $DoE\_12$, have similar strut apposition results, the $VAS$ index for the $DoE\_11$ is 12.66% higher. Such stress differences between models may lead to biomechanical responses which in turn may result in different restenosis rates in the dilated segment. This has been shown in recent studies (Keller et al. 2014, Timmins et al. 2011) reporting localised biological response as a result of mechanical forces imposed by the stent system during deployment and, consequently, the radial compression of the arterial wall. On the other hand, models with low induced mechanical environment are as a result of suboptimal stent and wall interaction or stent under-expansion. This is well demonstrated in models $DoE\_02$, $DoE\_09$, $UPD\_11$ and $UPD\_21$ where, especially for the proximal parts, severe stent malapposition is observed which, in clinical practice, would likely necessitate post-operational manoeuvrings to restore the malapposed struts. These findings suggest that a dilation protocol should be used that balances lumen gain and the imposed mechanical stress environment for a given specific case.

### 8.3.5 Post-optimisation point selection

Generally, once a final Pareto front is obtained, the weighted $l_2 - metric$ can be implemented to locate optimum points according to the user's preference. This post-optimisation technique, which is also known as "compromise programming", picks a solution which is minimally located from a given reference point (Deb 2001). Then, according to the user's judgement and the given patient-specific case, corresponding weights to each objective function can be applied and, by minimising the weighted $l_2 - metric$, the optimum point can be located. Using the ideal vector (utopia point), the first point selected was the closest Pareto front point to the ideal vector. To locate this point, equal weights were used in Eq. 8.12.

In Figure 8.11, the final Pareto front obtained by a NSGA-II search of the prediction models is depicted. The Pareto front is normalised according to the nadir and utopia point (see eq. 8.11). The minimum Euclidean distance, or alternatively, the weighted $l_2 - metric$ is the same in the last two iterations. Consequently, the same optimum point is predicted. In Figure 8.11a, the sphere represents equal weighted $l_2 - metric$ (with $w_1, w_2, w_3 = 1/3$), and its radius is tangent to the Pareto front point which in turn is the closest point to the utopia point. In Figure 8.11b, the elliptical sphere represents a non-equal weighted $l_2 - metric$. By way of example, the weights that were

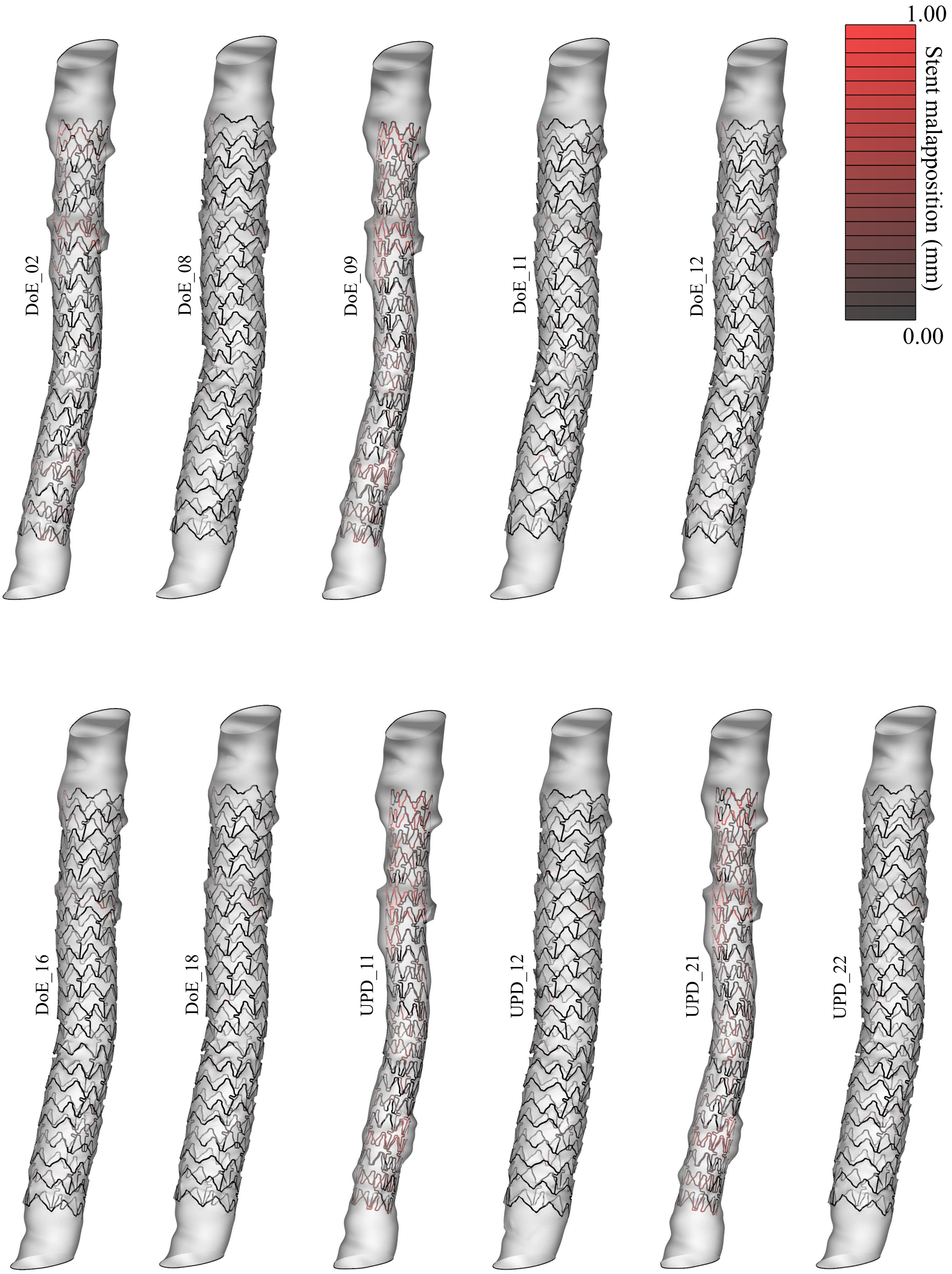

Figure 8.9: Spatial SM superimposed on the deformed stent models after balloon deflation: the spatial SM was calculated as the Euclidean distance between triangulated vertex points on the external surface of the deformed stent and their normal projections to the deformed lumen surface after the virtual expansion.

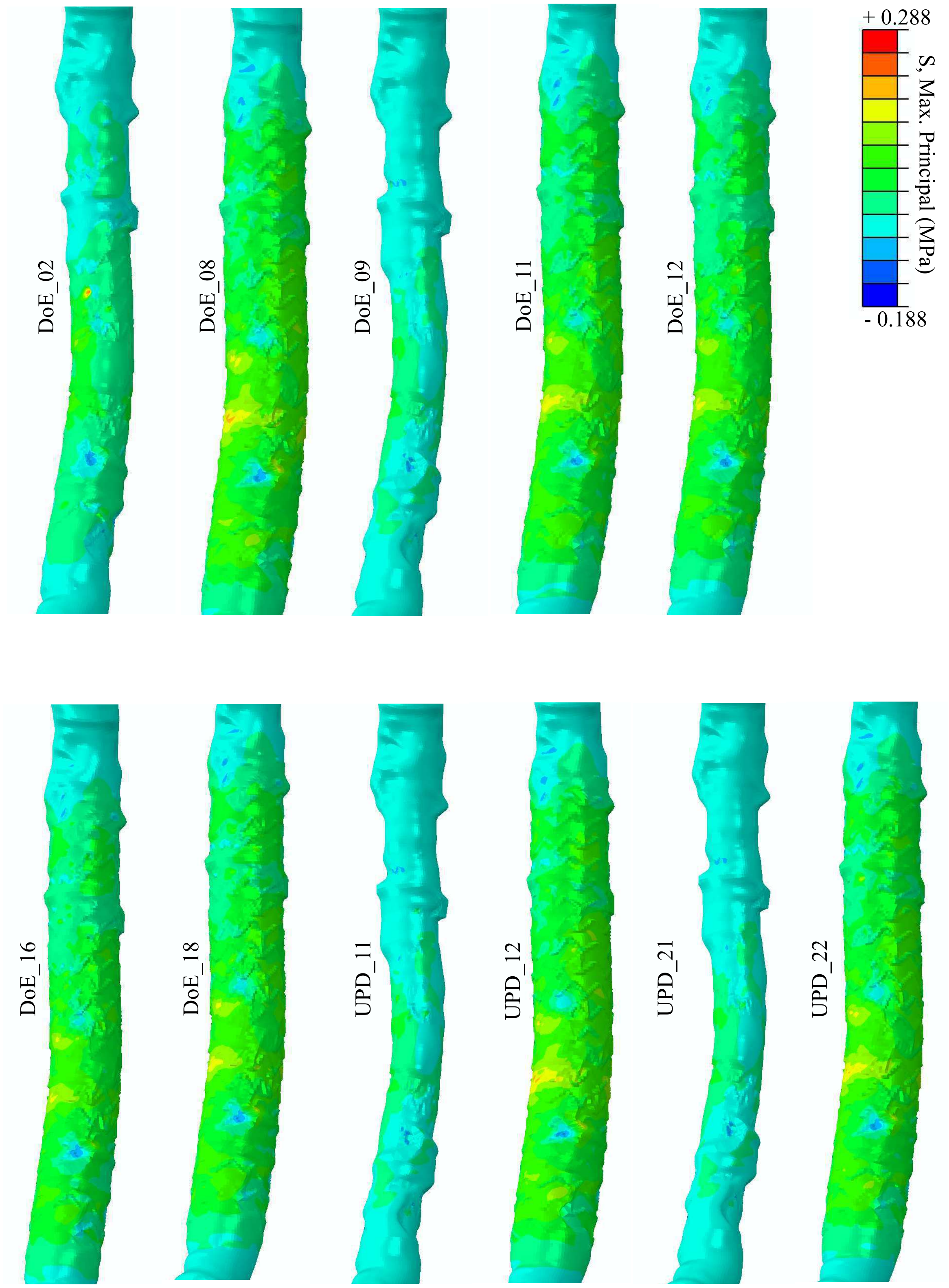

Figure 8.10: Maximum principal stress plots superimposed on the deformed lumen surface after balloon deflation.

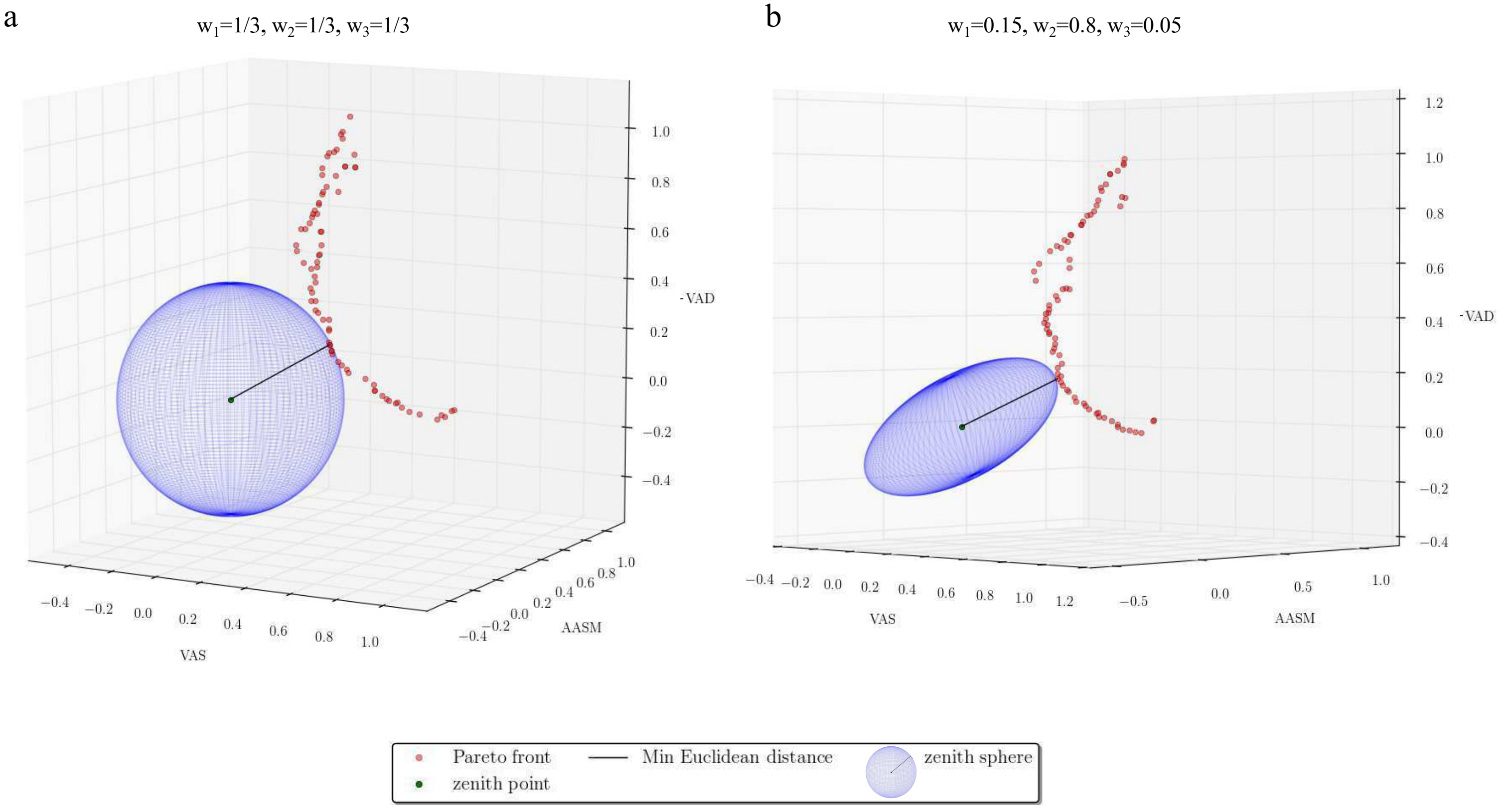

Figure 8.11: Final Pareto front obtained by NSGA-II search in the final surrogate: a) the optimum point is selected according to the minimum distance from utopia criterion, by applying equal $w_i$ to the weighted $l_2 - metric$. b) optimum point selected by setting $w_1 = 0.15, w_2 = 0.8, w_3 = 0.05$

applied to the minimisation problem were $w_1 = 0.15, w_2 = 0.8, w_3 = 0.05$. Its long axis is equal to the Euclidean distance between the ideal vector and the point for which the weighted $l_2 - metric$ is the minimum. Its short axes are equal to the minimum weighted $l_2 - metric$. Therefore, with this method, a Pareto front point can be easily located in which an objective function is made to have higher importance than the others. In Figure 8.11b, $AASM$ has been assigned a greater weight to locate a dilation protocol for which stent malapposition is of greater importance.

### 8.3.6 A set of optimum points

In Figure 8.12, results of SM and circumferential wall stresses are illustrated as extracted from the FEA simulations of the Pareto optimum point $OPT\_01$ (according to the minimisation problem of Eq. 8.12). The discrete values of the objective functions for this model as extracted from the computational analysis are reported in Table 8.3.

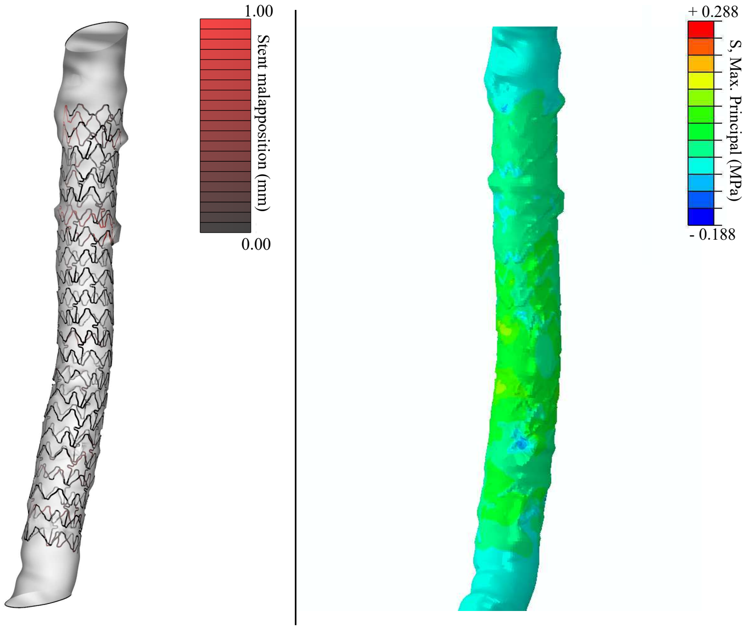

Figure 8.12: Results extracted from the FEA simulations of the $OPT\_01$ point: a) Spatial SM and b) maximum principal stresses superimposed on the deformed lumen surface after balloon deflation.

In Table 8.4, a set of Pareto optimum points are reported (according to the minimisation problem of Eq. 8.12) along with their discrete values of the objective metrics as predicted by the final surrogates. The predicted values for $OPT\_01$ (c.f. Table 8.4) are within an acceptable difference of ±5% with the respective values extracted from the computational analysis (c.f. in Table 8.3). As it can be observed, signif-

Table 8.3: Values for objective metrics extracted from computational analysis for Pareto optimum point, $OPT\_01$.

| **Design** | $w_1$ | $w_2$ | $w_3$ | **Diameter** X1 (mm) | **Pressure** X2 (MPa) | **VAS** | **AASM** | **-VAD** |
|---|---|---|---|---|---|---|---|---|
| OPT_01 | 0.15 | 0.8 | 0.05 | 3.412 | 1.077 | 0.0247300 | 0.0436589 | -0.084500 |

icant improvement in $AASM$ and $-VAD$ (compared to the BASELINE point) can be accomplished when selecting the $OPT\_01$ interventional protocol. The $OPT\_02$ point is the dilation strategy in which all the investigated objectives are of the same importance. Interestingly, compared to the BASELINE point, a general improvement of SM and $-VAD$ index has been made. Contrarily, in $OPT\_03$, the $VAS$ metric has been improved while the $AASM$ and $-VAD$ were compromised. At last, the optimum scenarios of $OPT\_04$ and $OPT\_05$ represent the cases in which the $AASM$ and $VAS$, respectively, has the maximum importance. As expected, $OPT\_04$ and $OPT\_05$, result in the lowest $AASM$ and $VAS$ index, respectively.

Table 8.4: A set of optimum points selected according to the weighted $l_2 - metric$ and their mechanical performance predicted by the final surrogates.

| **Design** | $w_1$ | $w_2$ | $w_3$ | **Diameter** X1 (mm) | **Pressure** X2 (MPa) | **VAS** | **AASM** | **-VAD** |
|---|---|---|---|---|---|---|---|---|
| OPT_01 | 0.15 | 0.8 | 0.05 | 3.412 | 1.077 | 0.0233370 | 0.0420568 | -0.08476108 |
| OPT_02 | 1/3 | 1/3 | 1/3 | 3.338 | 1.075 | 0.0211685 | 0.0500785 | -0.0815423 |
| OPT_03 | 0.4 | 0.4 | 0.2 | 3.153 | 1.090 | 0.0174181 | 0.0661508 | -0.07158087 |
| OPT_04 | 0 | 1.0 | 0 | 3.925 | 1.500 | 0.0429983 | 0.0214624 | -0.09061541 |
| OPT_05 | 1.0 | 0 | 0 | 2.672 | 0.622 | 0.0084910 | 0.2125050 | -0.02778052 |

### 8.3.7 Model limitations

The presented multi-objective optimisation process searched for optimum dilation protocols in the design space created by the two-variable parameterisation used. Moreover, this search was carried out only for one patient-specific case. Therefore, a more “rich” optimisation (involving more parameters), for delivery system (e.g. compliance, length, etc.) and/or for the investigated vessel (e.g. stiffness of the plaque, geometry of the vessel, etc.) could provide better outcomes when searching optimum dilation strategies in patient-specific vessels with challenging disease. An additional limitation of this work is the fact that more sophisticated constitutive models (especially for the vessel) might result in different realisations of objective functions (scalar indices). However, due to the comparative nature of the current work along with the fact that there is no clinical record of the investigated performance indices, the implemented constitutive models can still provide valuable and potentially reliable results (especially in the effort to indicate the non-physiologic stress state in regions interacting with the stent system).

## 8.4 Conclusion

The work presented in this chapter investigated the optimisation of a dilation protocol in a patient-specific RCA using balloon pressure and unpressurised balloon diameter as variables. In particular, the mechanical performance of a modest number of protocol realisations was predicted for metrics that quantify tissue stress, stent strut malapposition and drug delivery. Due to the expense of FEA simulations for each realisation, a Kriging surrogate modelling approach was employed using updates selected from the multi-objective Pareto front derived from the expected improvement of each objective function. Then, a post-optimisation method was used to demonstrate how, interventional protocols can be derived for the selection of a patient-specific device, balancing the competing objectives of minimised tissue stress and strut malapposition. The proposed approach thus provides a tool for dilation system selection (e.g. alternative size balloons and compliance charts could be supplied for a given stent) and design optimization of lesion-specific dilation systems, a process that will become realizable in non-urgent cases with increases in computer power.

# Chapter 9

# FINAL REMARKS

Conclusions! The following content addresses the main findings, and consequently, the major contributions made by this doctoral work. The current chapter closes with recommendations on future work.

## 9.1 Conclusions

### 9.1.1 Knowledge from previous studies

In Chapters 1 and 2, recent contributions in PCI evolution are presented and elaborated. These developments regard information extracted by clinical, experimental and numerical studies that were carried out during the last two decades. It is clear that the majority of these studies focused on the investigation of PCI evolution potentially with respect to ISR and ST. After defining the major factors associated with these complications, numerous studies conducted to refine the stent systems, and consequently, the *in vivo* biomechanical performance. Remarkably, the outcomes of this exhaustive research by both clinicians and engineers demonstrate that contemporary coronary artery stents can now be safer in short and long-term basis, especially as far as ISR is concerned. On the other hand, the refinement of stents seems to be connected with "new generation" clinical complications particularly after DES implantation and/or when the intervened lesion is characterised by tortuous and long geometry with diameter discrepancy along its length ("challenging disease").

Despite consensus on stent design to improve its clinical performance with respect to ISR has been reached, numerous issues associated with SM are still debatable. This is more evident in the so-called "challenging cases" where optimum treatment solutions have not yet been established. In particular, scientific evidence on the optimal stent dilation protocol is still lacking and, as a result, SM and/or vessel trauma have been extensively reported recently in clinical studies. Thus, the motive of this thesis was directed by the need to elucidate or trigger the scientific community with state-of-the-art patient-specific numerical studies investigating how to optimise the delivery system to refine (and ultimately eliminate) the clinical problem of SM, and consequently, LSD. The work in this thesis represents the first numerical investigation of i) patient-specific SM and LSD, ii) the mechanical performance of multi-folded and non-uniform diameter dilation systems and iii) optimum dilation protocols in patient-specific reconstructed arteries.

### 9.1.2 Main conclusions

The literature review of structural studies presented in Chapter 2 reveals the capabilities of the finite element method in the optimisation of the stent design and the procedural techniques in bifurcated vessels. In particular, the latest studies on bifurcation stenting (Foin et al. 2012, Morlacchi et al. 2014, Mortier et al. 2014) along with the optimisation studies carried out by Pant et al. (2011) and Grogan et al. (2013) represented state-of-the-art in the computational interventional cardiology modelling. The authors of these studies constructed very elegant structural models to investigate various bifurcation techniques and optimum designs of certain stents with respect to different performance metrics. However, these studies would not have been feasible without the publication of earlier studies shedding light on the fundamentals of stent mechanics (Auricchio et al. 2001, Holzapfel et al. 2000, Migliavacca et al. 2002) and the recent advances in high performance computing power.

Nowadays, it is accepted by all authors in computational biomechanics that the most essential elements to built credibility and confidence for presented models are i) verification and ii) validation. These two prerequisites, within the range of possibility, are now indispensable to be presented prior to the outcomes. In Henninger et al. (2010), it stated that "...regardless of the use, confidence in computational simulations is only possible if the investigator has verified the mathematical foundation of the model and validated the results against sound experimental data...". Schwer (2006) defines verification as "the process of determining that a computational model accurately represents the underlying mathematical model" and validation as "the process of determining the degree to which a model is an accurate representation of the real world".

Succinctly, verification is the process carried out to ensure that the implemented mathematical equations are solved correctly and that the numerical mesh resolution does not result in a compromised computed solution. The latter has now been considered as a conventional process which is satisfied by numerical mesh convergence tests. The former is usually satisfied by the so-called "code verification", literally, the testing of the computer algorithms used to solve the mathematical equations. In the current doctoral work, the commercial software ABAQUS (Simulia, Dassault Systemes, Waltham, MA, USA) was used for the structural simulations. Therefore, it has been verified by the code developers. Regarding the mesh resolution, mesh convergence tests were presented in section 5.2. In addition to the mesh resolution, since the stent event cannot be modelled in the duration of the actual time period, a sensitivity analysis was conducted to ensure that the selected time period did not affect the numerical solution. This was presented in section 5.3.

On the other hand, validation is the process to ensure that the implemented mathematical assumptions are valid to describe the actual physical system. This process is the most demanding and it can be categorised into two predominant types, direct and indirect validation (Henninger et al. 2010). Direct validation is the process in which the investigator is setting an experiment that closely matches the numerical simulation so that each material behaviour and the applied boundary conditions are incorporated. Indirect validation is when the researcher is implementing experimental results from the literature, therefore, he cannot control them. Amongst the two, indirect validation seems to be unavoidable for numerical models of stenting for which the direct validation is a costly, time consuming process and faces some challenging problems (e.g. high complexity and variability of the biological system). The latter is the main reason why only indirect validation was carried out in this doctoral thesis. In particular, experimental data was used to ensure that the virtual balloon-stent models have a realistic inflation behaviour. The data used compliance charts provided by the manufacturers (Abbot-Vascular 2008, BostonScientific 2011) and were compared against virtual compliance charts extracted by the numerical simulations (see sections 5.2.3, 7.3.1.1 and 7.3.1.2). As for the investigated stents, experimental data published by Ormiston et al. (2011) was used to test whether the virtual compression of the investigated devices matches with that of the actual behaviour reported in that study.

The verification tests demonstrate that the selected mesh resolutions did not have any impact to the final solution. In addition, the validation tests showed that the investigated virtual model behaviour was in good agreement with the actual one. Thus, it can be noted that these two prerequisites were satisfied, consequently, the numerical results presented here can be considered as reliable and accurate especially for the comparative nature of this work.

The main hypothesis in this thesis is that patient-specific vessels can be reconstructed prior to PCI and following the extraction of vessel geometric characteristics, optimum stent delivery can be accomplished to eliminate the incidence of SM and further complications such as LSD. This has the potential to assist PCI planning, accurate sizing of the stent system and, consequently, optimisation of stent deployment. Therefore, virtual spaces were generated and, via the finite element method, computer simulations were carried out to investigate the mechanical performance of i) contemporary stents and ii) dilation systems with respect to SM and LSD in reconstructed vessels with challenging disease.

The reconstruction process was presented in Chapter 3, and the methodology was based on the fusion of CA and IVUS. Despite the fact that only CA has been used in the majority of the PCI procedures, recent scientific clinical studies (Redwood et al. 2010, Takumi et al. 2014, Yoon and Hur 2012) confirm the importance of utilizing IVUS as a supplementary tool especially in challenging cases. One of the major advantages of IVUS is the ability to provide anatomic information, such as exact diameter, lumen area, wall thickness and disease distribution in any cross section along the intervened lesion. Furthermore, IVUS can detect sub-optimal stent delivery such as SM (c.f. Figure 1.7) and LSD (c.f. Figure 1.8). For these reasons, many interventional cardiologists are now using IVUS pre and post-operatively to size the stent and ensure optimum stent delivery, respectively. This is the rationale of the presented reconstruction methodology, from which not only the 3D geometry of the vessel but the volumetric substance of the vessel wall can be extracted.

Chapter 6 proceeded with the first computational work investigating the mechanical performance of three commercial stents along with a modified platform (ultimately adopted by the company) with respect to SM, and subsequently, LSD in a reconstructed challenging RCA case. The proposed model demonstrated i) the spatial SM, ii) the integrity and iii) the validation of contemporary stent designs. Regarding SM, all the devices had almost similar results, with sub-optimal stent apposition in the proximal part of the vessel. This agrees with the hypothesis that proximal malapposition is primarily dependent on the variation in vessel diameter and the associated diameter mismatch that occurs when sizing the stent on the distal diameter. These malapposed regions are prone to further complications such as ST (Cook et al. 2009) if not detected immediately or LSD in the attempt to restore the malapposed struts (Hanratty and Walsh 2011) when malapposed struts are detected immediately after stenting. On the other hand, the compression simulations demonstrated that there is a significant difference in stent integrity between the investigated devices. Interestingly, the results revealed that the deformation response of a stent exposed in a localised load differ to the deformation response of a device which is exposed to a distributed load. In particular, the modified stent which was proposed showed significantly higher longitudinal resistance in a localised load than a distributed load. This suggests that stent *in vitro* performance can differ significantly from that *in vivo*. Unsurprisingly, the tested workhorse stent (Stent D; CYPHER stent) demonstrated drastically higher stiffness. This can be explained by the fact that this platform is characterised by thick struts and many connectors between the stent rings. However, as has been shown in previous studies, such thick devices impose high stresses on the vessel walls (Timmins et al. 2011) and non-physiologic flow patterns (Foin et al. 2014) leading to vessel trauma and ISR. They are also relatively inflexible. The previous studies conclude that although a thinner platform is preferable, attention should be paid to potential flows that can be generated by finer stents. Therefore, it was speculated that by modifying a contemporary stent design just in the very proximal part, its stiffness can be significantly improved, consequently, avoiding the potential of stent strut protrusion in the lumen.

As a result of the observations made in Chapter 6 (especially the outcomes of SM), this work moved forward to investigate how SM can be prevented by novel non-uniform and multi-folded dilation systems. In Chapter 7, the first structural work investigating SM in varying diameter patient-specific vessels was presented. In particular, the aim was to minimise the average SM with a single-step procedural protocol. The hypothesis was that optimum delivery in challenging cases should be accomplished by a single-step approach, thus minimising the potential of further clinical complications as a result of SM. It was demonstrated that the proposed delivery systems can mitigate possible malapposed struts in the proximal part of the intervened vessels whilst maintaining a relatively low induced stress environment. Arithmetic metrics were derived to evaluate the performance of each simulated system with respect to SM, wall circumferential stresses and geometrical vessel changes. The results indicate that there was a 41.5% and 48.31% decrease in average stent strut malapposition for the RCA segment and bifurcated vessel, respectively. Furthermore, these systems can increase both the MLA and the $VG$ when compared with the baseline models (uniform dilation systems). More specifically, in the vessel with 20% diameter variation between the proximal and the distal part (second RCA segment), the increase in MLA and $VG$ was 2% and 8.8%, respectively. For the bifurcated vessel with 50% diameter difference between the proximal and the distal ends, the increase in MLA and $VG$ was 0.7% and 1.4%, respectively. The fact that the MLA is maximised by the proposed systems is very important for the success of the PCI procedure where the general aim is to maximise minimum lumen area. Furthermore, the global geometric characteristics of the intervened vessels did not alter significantly. Therefore, there was no observation of the so-called “vessel strengthening” which results in tissue prolapse and higher stresses in the inner curvature of the vessel, and consequently, in ISR (Wu et al. 2007). So, this clinically motivated work, shed light on the potential for changing direction from the current trend in computational studies in which the major focus is the refinement of the stent platform. Thus, the general prospect was that optimum stent delivery could potentially be achieved by alternative delivery systems that can result in complete stent expansion, optimum stent apposition, complete lesion coverage and low vessel stress environment.

Finally, the first multi-objective optimisation study on dilation system was presented in Chapter 8. It was shown that via structural and surrogate modelling, optimum dilation scenarios in patient-specific challenging vessels can be devised. The optimum performance was derived with respect to average malapposition, tissue stress and drug diffusion in the vessel walls. The work was parametrised in a two-dimensional design space, comprising the balloon unpressurised diameter (initial profile length) and the nominal pressure applied to the inner surface of the balloon. As for the study parameters, the results indicated that the balloon initial diameter made stronger contribution than the applied pressure for all the investigated metrics of performance. The constructed surrogates demonstrated that stent malapposition was inversely proportional to tissue stress and drug diffusion. Aiming to identify multiple optimum design models lying on the so-called “Pareto front” the NSGA-II algorithm was implemented in a novel multi-objective optimisation routine which updates the surrogates by locating regions in the design space where the EI would be maximum. Finally, a post-optimisation strategy demonstrated how different optimum points can be selected according to the importance of each performance metric. The latter could potentially be used as a useful tool in PCI planning and assist interventional cardiologists to select optimum patient-specific dilation strategies.

### 9.1.3 Contributions

The most significant contributions made by this thesis are:

- it was shown that patient-specific stent malapposition in the proximal part of the intervened lesion was dependent on the variation of vessel diameter and not on different stent platforms.

- it was shown that longitudinal stent deformation is significantly different between different stent platforms. In particular, the results indicated that stent longitudinal integrity depends on the number of the connectors between the circumferential rings. The proposed modified stent demonstrated a high longitudinal strength and, as result, its axial resistance prevented any stent protrusion in the vessel lumen.

- the patient-specific simulations revealed that the threshold where contemporary stents lose their longitudinal resistance may differ *in vivo* compared to *in vitro*.

- it was demonstrated that variable diameter dilation systems can result in more than a 40% decrease in average malapposition relative to currently used systems. In parallel, the proposed systems did not alter significantly the stress environment such that the risk of vessel trauma, tissue prolapse and, consequently, restenosis is assumed to be minimised.

- it was shown that i) the initial balloon profile length plays a far more important role than the applied pressure when average malapposition, tissue stress and drug diffusion are considered and ii) stent malapposition is inversely proportional to tissue stress and drug deliverability.
- it was demonstrated that the proposed multi-objective optimisation algorithm can ensure both exploitation and exploration during the update steps. As a result, the surrogates can be improved both globally and locally and the final solution can be achieved in an effective way. Furthermore, the proposed post-optimisation method can locate optimum points by both "deterministic" and "heuristic" means.

## 9.2 Recommendations for future directions

At present, it is well known that numerous computational studies on stenting have been conducted by different research groups both in academia and industry. Therefore, innovations/ideas are still needed for procedural evolution. This evolution concerns i) further stent refinement, ii) development of new dilation systems and iii) insights on the optimisation of the procedural steps.

The methods and the outcomes presented in this doctoral work can be used as a reference point in future computational studies (both structural and optimisation) for coronary artery subject-specific modelling. Below, from the author's perspective, suggestions for future work are given. In addition several recommendations to improve the techniques and methodologies applied in this thesis are also provided.

In general, the most significant improvements that can be achieved in future studies are outlined below, and they can be classified into two main categories:

1. Suggestions for improvement in stent modelling
    - improvements in subject-specific modelling (morphological and constitutive)
    - development of methods for computational virtual space validation
    - development of transient computational models
    - improvements in dilation system modelling
2. Suggestions for improvement in multi-objective optimisation studies
    - introduction of new design variables and objective functions

- refinement of the objective functions for constrained optimisation
- population based studies to optimise stent dilation protocols according to any patient-specific vessel

### 9.2.1 Suggestions for improvement in stent modelling

#### 9.2.1.1 Improvements in subject-specific modelling

In this thesis, the reconstructed vessels were modelled by an isotropic hyperelastic material. In reality, all human coronary arteries are anisotropic. A more sophisticated constitutive model was proposed by Holzapfel et al. (2005a). This model is more realistic since it considers the collagen fiber orientation and dispersion in each layer representing heterogeneous and anisotropic behaviour. Over the last five years, this model has been successfully implemented by Mortier et al. (2011a), Mortier et al. (2010) and Conway et al. (2012). However, Holzapfel et al. (2005a) investigated the passive mechanical properties of different arterial layer strips. The interconnection of the layers was not investigated and the experimental tests concerned only small arterial segments. Moreover, the segments which were investigated were extracted by only thirteen coronary arteries. Therefore, to fill the gap between clinical findings and computational results, future studies could potentially aim to consider subject-specific constitutive parameters derived from the whole length of the investigated segment. Furthermore, an essential development in the upcoming computational models could be the inclusion of i) the plaque composition variation and ii) the residual stresses before stenting.

#### 9.2.1.2 Development of validation methods

Mortier et al. (2011a) built silicon vessel models to validate their numerical models. Although an overall satisfactory agreement was achieved, specific discrepancies between the numerical and the experimental outcomes were reported. These discrepancies would have been higher if the modelled vessels were not idealised but their geometry would have been obtained from patient-specific vessels. Therefore, silicon models might serve as a good experimental tool for conducting studies of a comparative nature. However, more sophisticated materials could provide a more reliable tool when the focus is on the deformation of the vessel walls.

#### 9.2.1.3 Development of transient computational models

All the structural simulations presented in this doctoral work were considered as quasi-static. The quasi-staticity was ensured by eliminating the inertial forces to that of the deformation of structure only. The time period was defined by frequency analysis (see section 5.3). Therefore, in all the patient-specific simulations, approximately the same time period was used. Interestingly, Kawasaki et al. (2009) investigated the impact of DES delivery inflation time in eighty-one coronary lesions. By means of IVUS, it was shown that the prolonged delivery time duration resulted in better stent expansion (see Figure 9.1). Therefore, it would be of real interest to include the parameter of time in future structural simulation particularly when stent optimum expansion is considered. Furthermore, in the optimisation study presented in Chapter 8, the drug diffusion was modelled as time independent. In reality, the problem of drug transport is transient. Future studies investigating drug deliverability could take into account the parameter of time. Ideally, an exponential function could be derived to describe the drug release from the stent to the vessel walls. Finally, the remodelling of the vessel wall as a function of time could be a potential area of investigation in future studies.

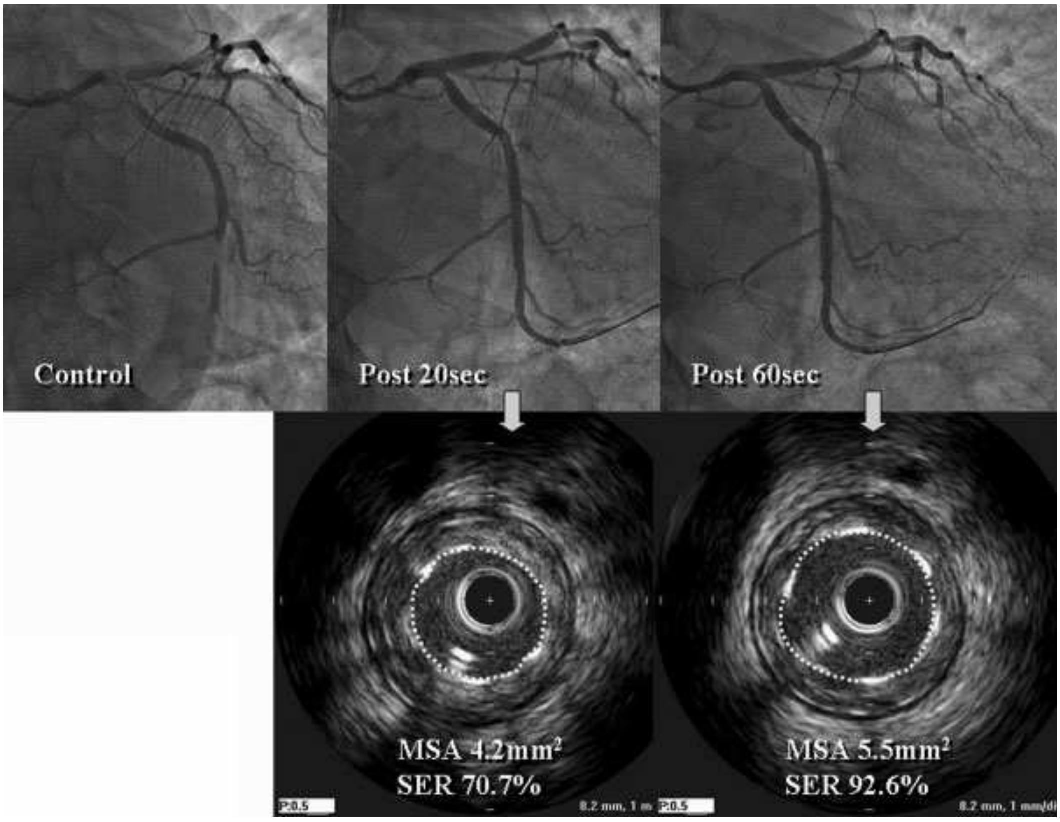

Figure 9.1: Comparison of stent deployment for 20 *sec* duration with that of additional stent inflation for 60 *sec*: A 61-year-old male with 99% stenosis of the distal left circumflex underwent recanalization therapy with a 2.5 *mm* sirolimus-eluting stent. IVUS imaging showed that the stent cross-sectional area at the lesion increased from 4.2 $mm^2$ after inflation for 20 *sec* to 5.5 $mm^2$ after the additional inflation for 60 *sec*. As a result, the stent expansion ratio also clearly increased from 70.7 to 92.6%. Image reused from Kawasaki et al. (2009), with permission from John Wiley and Sons.

#### 9.2.1.4 Improvements in the dilation system modelling

As stated in section 5.4, one of the major limitations in the presented deployment simulations is the constitutive model which was used to describe the balloon models. In reality, instead of isotropic, and linear elastic, the balloons used in interventional cardiology are considered as cylindrically orthotropic as described in Holzapfel (2000) and successfully implemented in Kiousis et al. (2009). Interestingly, from Figure 9.2, it can be observed that the overall numerical compliance behaviour presented in Kiousis et al. (2009) is very similar with those presented in Chapters 5 (c.f. Figure 5.7) and 7 (c.f. Figure 7.4). Therefore, when the focus of the numerical study is the final deformation of the balloon; especially at nominal pressures, the assumptions made in this doctoral work are still acceptable. On the other hand, if numerical studies investigate the transient inflation behaviour of balloon models used in interventional cardiology, more advanced constitutive models should be adopted. Additionally, a very interesting contribution in the effort to optimise dilation models would be to model the manufacturing process that has a direct impact on the final balloon inflation behaviour.

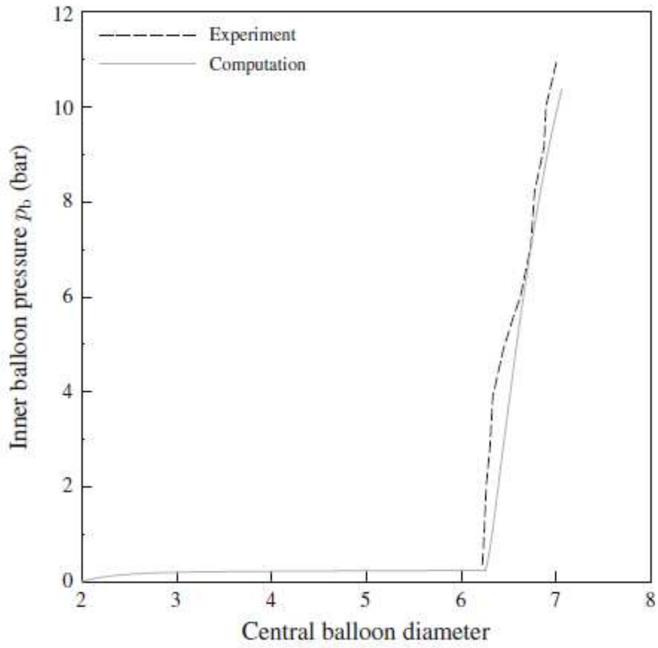

Figure 9.2: Experimental results in comparison with results obtained from a finite element simulation of the dilation pro-ess of the Bridge Assurant balloon analyzed with the material model (6). Inner balloon pressure $p_b$ vs. central balloon diameter. Up to about $p_b = 0.5$ bar the balloon diameter increases considerably and beyond that pressure the balloon stiffens circumferentially. The computational model shows good agreement with the experiments. Image reused from Kiousis et al. (2009), with permission of Springer.

### 9.2.2 Improvements in multi-objective optimisation studies

#### 9.2.2.1 Introduction of new design variables and objective functions

*Design variables*

In the multi-objective optimisation study (Chapter 8) the design space comprised two design variables: the initial balloon diameter and the applied pressure to expand the stent to a certain diameter. In reality, the optimisation of the dilation strategy depends on other parameters as well, such as the compliance of the balloon, the inflation time (Kawasaki et al. 2009) and finally, the vessel resistance to stent deployment. Therefore, future optimisation studies could include one or more of the additional design parameters to optimise the dilation strategy and evaluate the contribution of each design variable to each of the objective functions.

*Objective functions*

Three objective functions were implemented to search for optimum dilation scenarios. These objectives are based on average values derived as a function of wall vessel volume and stent surface area. However, there is not yet any information from clinical studies on such objective functions. Although increased stress values and vessel overstretching are highly associated with ISR (Keller et al. 2014, Timmins et al. 2011), there is no clinical evidence whether these stresses concern average values or peak values. Similarly, even though it has been found that SM is correlated to ST (Cook et al. 2007), it is still questionable whether this regards overall or localised strut malapposition. Also, complications from suboptimal drug deliverability might be associated with specific regions where the drug is not diffused and not with the overall intervened volumetric wall region. Therefore, if future clinical studies can provide quantitative information on stent performance, next computational studies could consider this data as objective functions and/or as threshold values to set constraints in multi-objective optimisation studies.

#### 9.2.2.2 Introduction of population based studies

Although the current doctoral work indicated favourable results compared to standard practice, the outcomes cannot, at this stage, be generalised for all cases. The results are specific to the few patient cases considered in this work. Thus, the main aim of future research could be to perform population based studies in which many tens of patient cases will be processed to generate data for geometry characterisation, classification and uncertainty. This has the potential to assist interventional cardiologists to optimise stent delivery in any patient-specific case based on surrogate models constructed after numerous multi-objective optimisation studies.

# Appendices

# Appendix A

# LUMEN AND WALL SEGMENTATION

The second step of this reconstruction methodology concerns the definition of lumen and media-adventitia border contours. This is performed by an interactive segmentation process which is based on active contour models (snakes). Snakes have been used broadly for edge detection within the medical image processing. A snake is nothing more than an ordered set of points (snaxels), and the aim is to minimise the energy (equation A.1) of a parametric close curve by external forces, which has to be initially defined on the image plane. The general definition of the minimising energy function is

$$E_{snake} = E_{int} + E_{ext} \tag{A.1}$$

where $E_{int}$ is the internal energy formed by the snake configuration itself and $E_{ext}$ is the external energy formed by external forces affecting the snake. In the IVUS Angio-Tool approach, the energy functional A.1 is defined as

$$E_{snake} = E_{cont} + E_{curv} + E_{image} \tag{A.2}$$

where $E_{cont}$ and $E_{curv}$ represents the internal energy, while $E_{image}$ corresponds to the external energy. In more detail a linear combination of the equation A.2 is used, having the following form

$$E_{snake,i} = \alpha_s E_{cont,i} + \beta_s E_{curv,i} + \gamma_s E_{image,i} \tag{A.3}$$

where $\alpha_s$, $\beta_s$, $\gamma_s$ are weighting factors controlling the relative influence between the terms. All the above are more analytically explained in (Giannoglou et al. 2007) and (Papadogiorgaki et al. 2008).

# Appendix B

# SIMULATION DESIGN METHODOLOGIES

*Simulation set up*

In order to reduce the computational time in simulations of stent deployment in the reconstructed vessels, two methodologies were compared in which stenting procedure was simulated in the first RCA case presented in Chapter 3. The first methodology consisted of three steps (crimping, positioning, and expansion), whilst the second consisted of two steps (crimping, expansion). Figure B.1 illustrates the different approaches followed. Specifically, in the first approach (from the top left and anticlockwise), the positioning of the stent into the diseased site was undertaken using FEA, a fact that increases the total computational time. On the other hand, the second approach (from the top left and clockwise) positioned the stent system into the vessel within the **CAD** software with geometrical transformation which maps the central axis of the stent system on the reconstructed IVUS catheter line. The displacement of the stent-catheter shaft into the stenotic section of the RCA (expensive approach) was managed by the application of a longitudinal smooth load displacement on the distal nodes of the catheter shaft. Surface-to-surface contact definition was used for the contact pair of catheter shaft-guide wire, with contact properties defined as tangential and frictionless. To ensure that the stent stays positioned on the catheter shaft, a continuous pressure load ($\approx 0.01\ MPa$) throughout the step was applied on its outer surface, while its contact with the catheter shaft was modified as tangential and rough. To expand the stent, a deformable cylinder was used. A surface-to-surface contact algorithm was used for the stent-vessel pair, and a friction of 0.05 was defined for the tangential contact property (Auricchio et al. 2011, Dunn et al. 2007). All other contacts (including self-contacts) were modelled with 0.2 friction coefficient for the tangential contact behaviour (De Beule et al. 2008, Mortier et al. 2010).

*Results*

The simulation steps for both design methodologies are illustrated in Figure B.2. On the bottom right, it can be observed that the final configuration of the stent is well matched between the two approaches.

In Figure B.3, boxplots of the average nodal von Mises stresses of the stent, for the two simulation methodologies, are illustrated indicating almost identical results at the end of the stent expansion. The discrepancy of maximum, minimum and average von Mises stress yield values within the acceptable range of $0.7 - 3.7\%$ (see Table B.1).

Table B.1: Quantitative comparison of the two simulation design strategies

| Simulation Strategy | Max. Mises Value (MPa) | Min. Mises Value (MPa) | Average Mises Value (MPa) |
|---|---|---|---|
| Approach 1 | 454.934 | 9.9261 | 134.5239 |
| Approach 2 | 451.4660 | 9.7938 | 129.5348 |
| **Relative difference (%)** | **0.7** | **1.3** | **3.7** |

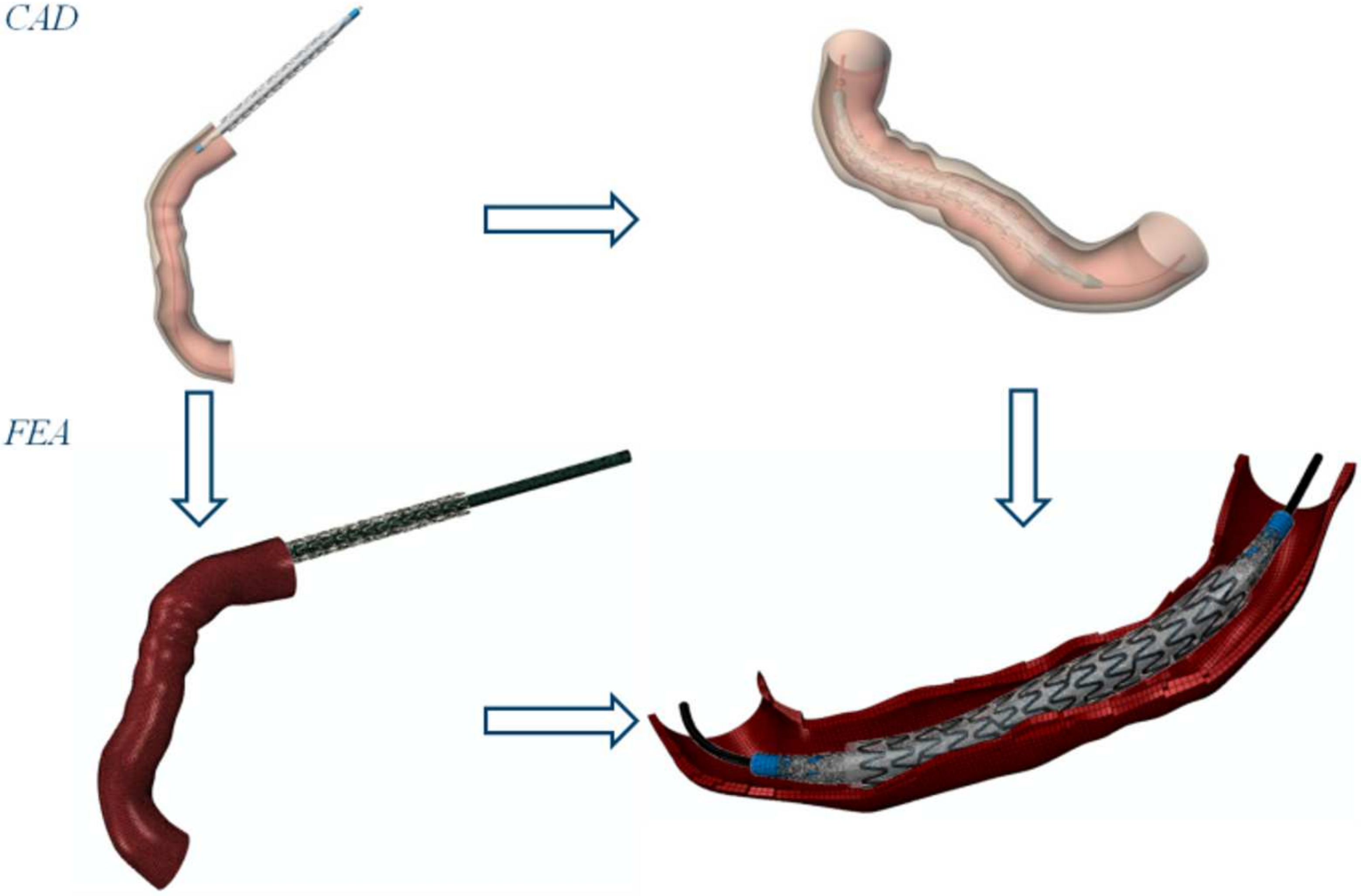

Figure B.1: Illustration of the two simulation design strategies. Approach 1, from the top left and anticlockwise to the bottom right. Approach 2, from the top left and clockwise to the bottom right.

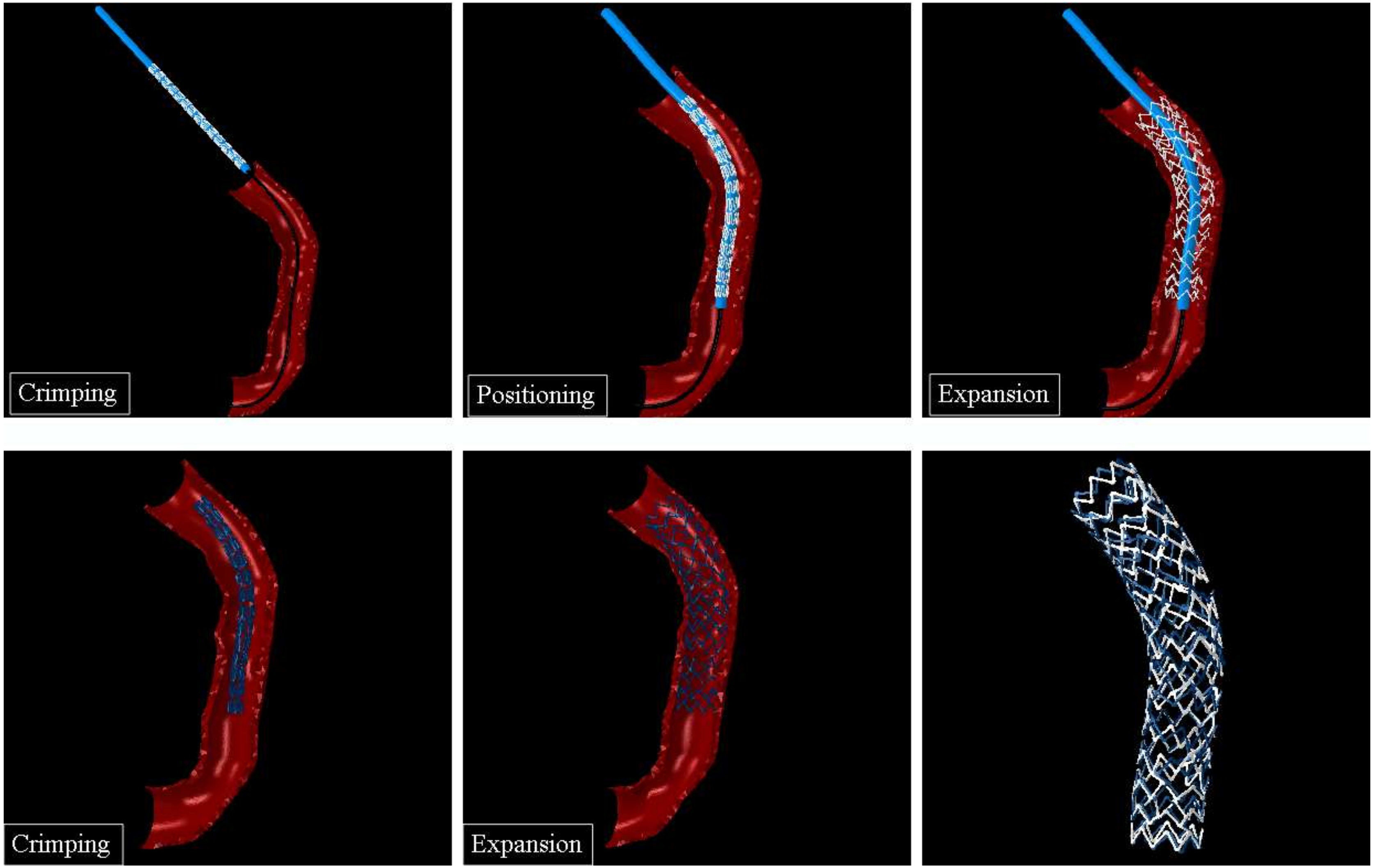

Figure B.2: Qualitative comparison of two design methodologies: Top, the first simulation approach is depicted. The method consisted of three steps. Bottom, the second simulation approach is depicted which consisted of two steps. Bottom right, the deformed stents are superimposed from the two investigated approaches after the deployment steps

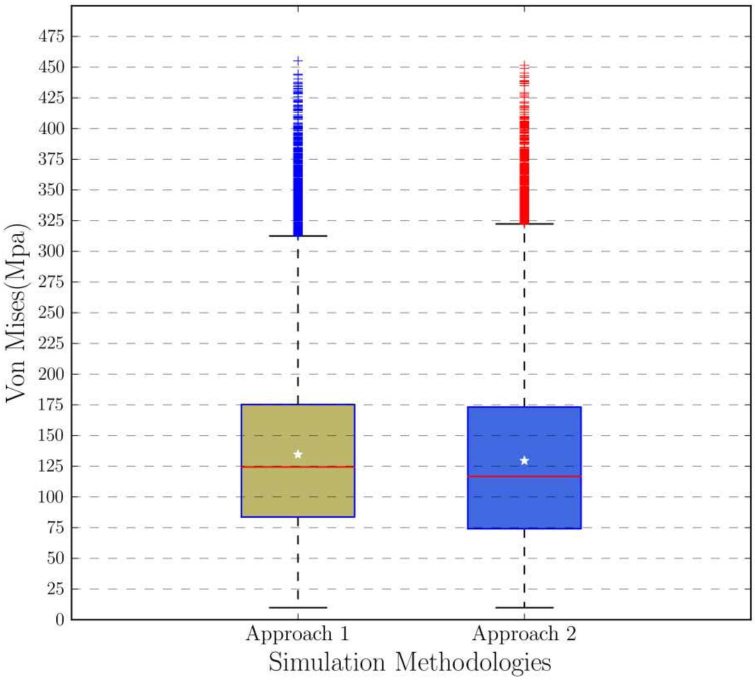

Figure B.3: Boxplots of the average von Mises distribution of the expanded stent between the two simulation approaches

# Appendix C

# SIMPLIFICATION OF THE EXPANSION METHOD

For the purposes of the study presented in Chapter 6, stent deployment was performed with a deformable surface and a realistic five folded balloon. The deformable surface expanded the stent to its nominal diameter with predefined displacement while the balloon deployment was conducted by a gradual applied internal pressure to the inner surface of the balloon. At the end of each expansion, the nodal distances between the upper surface of the stent and the inner surface of the vessel were calculated with a python script developed for post-processing in ABAQUS.

Figure C.1 illustrates stent deployment by a deformable surface (left) and by a realistic five folded balloon (right). The CDF graphs of the resulting malapposition at the end of the expansion steps were plotted, figure C.2) . The CDF graphs indicate that for both expansion methods in this patient specific case, the stent malapposition is identical following device deployment.

As previously discussed, consideration should be taken into the simulation of a virtual stent deployment step. It has been shown (De Beule et al. 2008, Gervaso et al. 2008, Grogan et al. 2012) that when simulating free stent expansion, the balloon model can be replaced by a deformable surface. On the other hand, Gervaso et al. (2008) raised reservations on whether the balloon could be excluded from a stent deployment in a vessel. So, taking into consideration those recent studies, a qualitative and quantitative comparison between two different expansion methods as described in section C was conducted. The objective to be evaluated was the clinical complication of stent malapposition. For this patient specific case, it was found out that the methods yielded almost identical results, Figure C.2. From the CDF graphs, the stent malapposition (nodal euclidean distance after the deployment) values are evenly distributed in both expansion techniques. Therefore, for simulating stent deployment in this patient specific vessel, as an optimal choice, the surface expansion was selected.

Despite the fact that it was managed to minimise the computational cost ($\sim 70\%$ reduction in the time duration of the entire 8-domain parallel simulation) of the stent deployment step, the deformable surface is not recommended without investigating its accuracy. For a more challenging case (e.g case 2 and 3 in Chapter 3), the deformable surface is expected to provide unrealistic results. Balloon expansion causes straightening of the vessel, an effect which has been shown to be a key reason for further clinical complications. On the other hand, the deformable surface does not straighten the artery and the stent seems to take the curvature of the vessel. Thus, before implementing an alternative expansion method from the golden standard (balloon expansion), carefully qualitative and quantitative comparisons should be conducted.

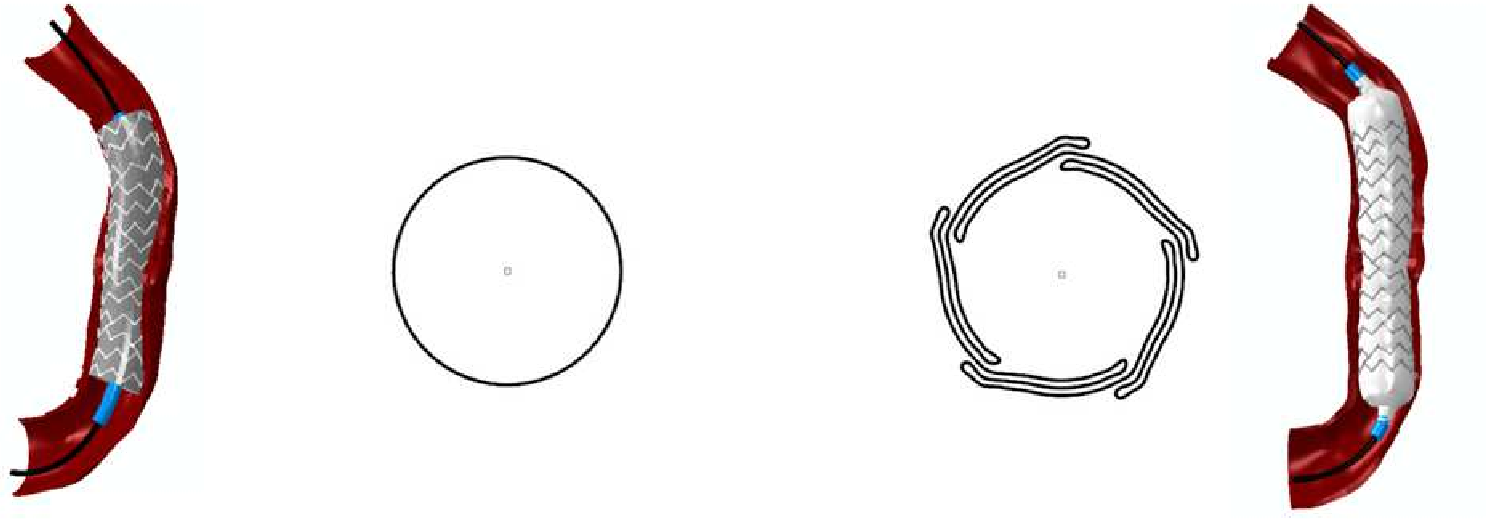

Figure C.1: Illustration of stent expansion with a deformable surface (left) and a realistic five folded balloon (right). Cross sections of the expansion means are depicted next to each model

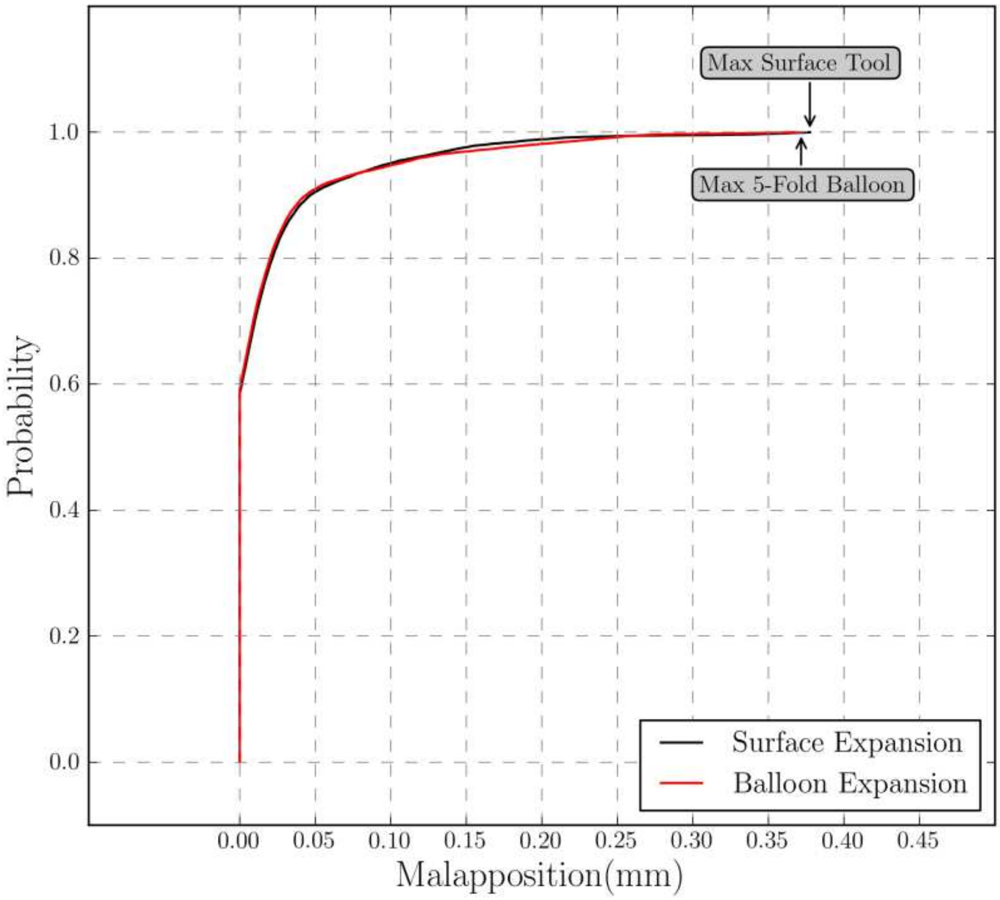

Figure C.2: CDF were plotted after each expansion step measuring the stent malapposition. The CDF graphs are almost identical demonstrating that for this patient specific case, a deformable surface could be used for simplicity

# Appendix D

# MULTI-FOLDED BALLOON GENERATION

## D.1 Main script

Balloon_Model_Fun.py

```
# \Balloon_Model_Fun.py
__author__ = 'GiorgosRagkousis'
import clr
clr.AddReference("mtrand")
import numpy as np
import rhinoscriptsyntax as rs
import subprocess

rs.CurrentView("Right")

# the Catheter_Diameter defines the outer diameter of the catheter/
# maximum tip diameter
Catheter_Diameter = 0.89
# the N_Circles is the number of the concentric circles for the folded balloon
# construction
N_Circles = 5
# L_straight_body is the axial balloon length, without the balloon tapered ends
L_straigh_body = 14.0
# L_tappered_ends is the length of each tapered balloon end
L_tappered_ends = 2.
# the following parameter defines the drag seam parameter
N_seam = 7
# catheter_shaft_diameter is the outer diameter of the catheter shaft
catheter_shaft_diameter = 0.45


# the following part defines the MultiFoldProfile function which will generate
# the crossing profiles it takes two arguments, one is the position along the
# longitudinal axis and the other is the sympy file path which calculates the
# profile
def MultiFoldProfile(position, input_filename):
    # pass the variables of the python sympy script to the IronPython Rhino
    result = subprocess.check_output([input_filename])
    x = result.split("\n")
    t = float(x[2])
    D_initial = float(x[3])
    First_angle = float(x[4])
    Second_angle = float(x[5])
    Circumference = float(x[6])
    N_f = int(x[7])
    # create empty lists for importing the curves and the points
    pts_1 = []
    cocentrics = None
```

```
pts_Guid = []
pts_Guid_first_angle_list = []
pts_Guid_second_angle_list = []
parameter = []
parameter_ = []
parameter__ = []
Curves_1 = []
Curves_2 = []
Curves_3 = []
# This loop will split the circumference of each circle to generate the
# desired profile
for i in range(int(N_Circles)):
        cocentrics = rs.AddCircle(rs.WorldYZPlane(),
                                  (0.5*(D_initial+2*i*(t))))
        points_ = rs.DivideCurve(cocentrics, N_f, create_points=False,
                                 return_points=True)
        pts_1.append(points_)
        for j in points_:
            parameter.append(rs.CurveClosestPoint(cocentrics, str(j)))
        Curves_1.append(rs.SplitCurve(cocentrics, parameter))
        pts_Guid = rs.AddPoints(points_)
        pts_Guid_first_angle = rs.RotateObjects(pts_Guid, (0, 0, 0),
                                                First_angle, copy=True)
        pts_Guid_first_angle_list.append(pts_Guid_first_angle)

        if i >= 3 and Second_angle != 0:
            pts_Guid_second_angle = rs.RotateObjects(pts_Guid, (0, 0, 0),
                                                     Second_angle,
                                                     copy=True)
            pts_Guid_second_angle_list.append(pts_Guid_second_angle)
        elif i >= 3 and Second_angle == 0:
            pts_Guid_second_angle = None
        parameter = []

arrpts_Guid_first_angle = np.array(pts_Guid_first_angle_list)
arrpts_Guid_second_angle = np.array(pts_Guid_second_angle_list)
arrpts_1 = np.array(pts_1)
# first angle point segmentation
# insert the pts into a list and take their coordinates
pts = []
for row in arrpts_Guid_first_angle:
    for k in row:
        pts.append(rs.PointCoordinates(k))
# convert the curves_1 list into a numpy array
Curves_1arr = np.array(Curves_1)
Curves_1arr = np.reshape(Curves_1arr, (5*N_f,))
# convert the pts list to a numpy array
arrpts = np.array(pts)
# import both arrays into a (25,2) array
M_1 = np.array([Curves_1arr, arrpts]).T
# split the circles along with the rotated points (first angle)
for ii in range(len(M_1)):
    parameter_.append(rs.CurveClosestPoint(M_1[ii, 0], str(M_1[ii, 1])))
    Curves_2.append(rs.SplitCurve(M_1[ii, 0], parameter_[ii]))
# second angle point segmentation
# create an empty list for points_ (points of the second angle)
pts_ = []
for row in arrpts_Guid_second_angle:
    for k in row:
        pts_.append(rs.PointCoordinates(k))
# convert the Curves_2 list to an numpy array
Curves_2arr = np.array(Curves_2)
# Curves_1arr = np.reshape(Curves_1arr, (25,))
# convert the pts_ list to a numpy array
arrpts_ = np.array(pts_)
# extract only the two outer arcs of the circles to be segmented
listwing_ends = []
for v in range(len(Curves_2arr)):
    if v >= 3*N_f:
        listwing_ends.append(np.array(Curves_2arr[v, 1]))
# delete the arcs for the first angle
    if v >= 0:
        rs.DeleteObject(Curves_2arr[v, 0])

# convert the list with the curve segment to a numpy array (10,)
arrwing_ends = np.array(listwing_ends)
# create a (10,2) array with the curves guids and the point coordinates
M_2 = np.array([arrwing_ends, arrpts_]).T
```

```
    # iterate through the numpy array and split the curve segments with the
    # points
    # put the segmented curves into a list Curves_3
    for i in range(len(M_2)):
        parameter__.append(rs.CurveClosestPoint(str(M_2[i, 0]),
                                                str(M_2[i, 1])))
        Curves_3.append(rs.SplitCurve(str(M_2[i, 0]), parameter__[i]))
    arrCurves_3 = np.array(Curves_3)
    # Delete the arcs for the second angle
    for i in range(len(arrCurves_3)):
        rs.DeleteObject(arrCurves_3[i, 0])
    # Create arrays for each set of points, arrpts_1, arrpts_2, and arrpts_3
    # arrpts_1.shape = (25,25)  arrpts_2 = (25,25)  arrpts_3 = (2,5)
    arrpts_2 = np.reshape(arrpts, (5, N_f))
    arrpts_3 = np.reshape(arrpts_, (2, N_f))
    # This loop creates the straight line segment to connect the arcs
    for a in range(N_f):
        # small segments connecting the coecentric arcs
        rs.AddLine(arrpts_1[0, a], arrpts_1[1, a])
        rs.AddLine(arrpts_3[0, a], arrpts_3[1, a])

        for i in range(len(arrpts_2)):
            for j in range(len(arrpts_1)):
                if i == 0:
                    if j == 2:
                        rs.AddLine(arrpts_2[i, a], arrpts_1[j, a])
                elif i == 1:
                    if j == 3:
                        rs.AddLine(arrpts_2[i, a], arrpts_1[j, a])
                elif i == 2:
                    if j == 4:
                        rs.AddLine(arrpts_2[i, a], arrpts_1[j, a])

    # select all the curves and join them in a single object Profile_Proximal
    rs.Command('_SelAll', echo=True)
    # join all the selected curves
    rs.Command('_Join', echo=True)
    Profile_Proximal = rs.LastCreatedObjects()
    rs.UnselectObject(Profile_Proximal)
    # smooth the curves
    rs.RebuildCurve(rs.coerceguid(Profile_Proximal), degree=5, point_count=150)
    # scale the smoothed curve profiles
    length_proximal = rs.CurveLength(Profile_Proximal)
    scale_f_pro = Circumference/length_proximal
    Profile_Proximal = rs.ScaleObject(Profile_Proximal, (0, 0, 0),
                                      (scale_f_pro, scale_f_pro, scale_f_pro),
                                      copy=False)
    arrStart = (0, 0, 0)
    arrEnd = (position, 0, 0)
    arrVector = rs.VectorCreate(arrEnd, arrStart)
    Profile_Proximal = rs.MoveObject(Profile_Proximal, arrVector)
    return Profile_Proximal


# ##------------function for the catheter system----------###
def catheter_system():

    circle_cap_proximal = rs.AddCircle(rs.WorldYZPlane(),
                                       0.5*Catheter_Diameter)
    circle_cap_proximal = rs.MoveObject(circle_cap_proximal,
                                        (-(L_tappered_ends+1.0), 0, 0))
    circle_cap_proximal_ = rs.AddCircle(rs.WorldYZPlane(),
                                        0.5*catheter_shaft_diameter)
    circle_cap_proximal_ = rs.MoveObject(circle_cap_proximal_,
                                         (-(L_tappered_ends+1.0), 0, 0))
    circle_cap_proximal_1 = rs.CopyObject(circle_cap_proximal_, (-2, 0, 0))
    circle_cap_proximal_1_ = rs.OffsetCurve(circle_cap_proximal_1, (0, 0, 1),
                                            0.08)

    circle_cap_distal = rs.AddCircle(rs.WorldYZPlane(), 0.5*Catheter_Diameter)
    circle_cap_distal = rs.MoveObject(circle_cap_distal,
                                      ((L_straigh_body+(L_tappered_ends-1.0)),
                                       0, 0))
    circle_cap_distal_ = rs.AddCircle(rs.WorldYZPlane(),
                                      0.5*catheter_shaft_diameter)
    circle_cap_distal_ = rs.MoveObject(circle_cap_distal_,
                                       ((L_straigh_body+(L_tappered_ends-1.0)),
                                        0, 0))
```

```
    circle_cap_distal_1 = rs.CopyObject(circle_cap_distal, (2, 0, 0))
    circle_cap_distal_1_ = rs.CopyObject(circle_cap_distal_, (2, 0, 0))

    outer_prox = rs.AddLoftSrf([circle_cap_proximal_1_, circle_cap_proximal])
    inner_prox = rs.AddLoftSrf([circle_cap_proximal_1, circle_cap_proximal_])

    cap_inner_prox = rs.CapPlanarHoles(inner_prox)
    cap_outer_prox = rs.CapPlanarHoles(outer_prox)

    tip_proximal = rs.BooleanDifference(outer_prox, inner_prox,
                                        delete_input=True)

    outer_dist = rs.AddLoftSrf([circle_cap_distal_1_, circle_cap_distal_])
    inner_dist = rs.AddLoftSrf([circle_cap_distal_1, circle_cap_distal])

    cap_inner_dist = rs.CapPlanarHoles(inner_dist)
    cap_outer_dist = rs.CapPlanarHoles(outer_dist)

    tip_distal = rs.BooleanDifference(inner_dist, outer_dist,
                                      delete_input=True)

    circle_shaft = rs.AddCircle(rs.WorldYZPlane(), 0.5*catheter_shaft_diameter)
    circle_shaft = rs.MoveObject(circle_shaft,
                                 (-(L_tappered_ends+1.0), 0, 0))

    path_id = rs.AddLine((-(L_tappered_ends+1.0), 0, 0),
                         ((L_straigh_body+(L_tappered_ends-1.0)), 0, 0))
    Catheter_shaft = rs.ExtrudeCurve(circle_shaft, path_id)
    return [Catheter_shaft, tip_distal, tip_proximal]

if __name__ == '__main__':

    # generate the balloon crossing profiles proximally and distally for the
    # (non) tapered balloon
    Profile_Proximal = MultiFoldProfile(0, r"..\sympyp_proximal.cmd")
    Profile_Distal = MultiFoldProfile(L_straigh_body, r"..\sympyp_distal.cmd")

    # Create two circles, one for the proximal end, and the other for the
    # distal end
    # define points for vector creation
    Start_vector_prox = (0, 0, 0)
    End_vector_prox = (0 - L_tappered_ends, 0, 0)
    End_vector_distal = (L_straigh_body+L_tappered_ends, 0, 0)
    # create translation vectors
    vector_prox = rs.VectorCreate(End_vector_prox, Start_vector_prox)
    vector_distal = rs.VectorCreate(End_vector_distal, Start_vector_prox)
    # create the circles for closing the balloon ends
    End_circles = rs.AddCircle(rs.WorldYZPlane(), Catheter_Diameter/2.0)
    Proximal_circle = rs.CopyObject(End_circles, vector_prox)
    Distal_circle = rs.CopyObject(End_circles, vector_distal)

    # create a list with all the curve profiles
    Curve_List = [Proximal_circle, Profile_Proximal, Profile_Distal,
                  Distal_circle]

    # change the curve seams of the crossing profiles
    Profile_list = [Profile_Proximal, Profile_Distal]
    i = 0
    for i in Profile_list:
        domain = rs.CurveDomain(i)
        parameter = (domain[0] + domain[1])/(N_seam-1)
        rs.CurveSeam(i, parameter)
    # loft the NURBS profiles
    Balloon_srf = rs.AddLoftSrf(Curve_List, loft_type=2)
    Balloon_srf = rs.MoveObject(Balloon_srf, (-1, 0, 0))

    Balloon_catheter = catheter_system()
```

## D.2 Input script

calculate_balloon_profile.py

```
# \calculate_balloon_profile.py
__author__ = 'GiorgosRagkousis'
import sympy as syp
import math as m
import cmath as cm

# this is the unknown variable that it has to be calculated. C0 is the gap
# between each concentric circle.
C0 = syp.Symbol('C0', real=True)
# initial diameter, circumference of the unloaded balloon
D_s = 2.798
Circ = m.pi*D_s
# number of folds
N_f = 6
# Diameter of the catheter shaft, note this is not the diameter of the
# catheter profile
D0 = 0.6
# angles controlling the folded balloon profile, and outer folded diameter
# (fi is controlling the outer profile)
theta2 = 30.0
fi2 = 59.0
theta1 = (theta2/180.0)*syp.pi
fi1 = (fi2/180.0)*syp.pi
# Definitions of 6 different equations all of them in respect to C0.
C_t = 5.0*syp.pi*(D0+4.0*C0)

St123 = 1.5*theta1*(D0+2.0*C0)

St45 = fi1*(D0+7.0*C0)

l1 = (syp.sqrt((0.5*(D0+4.0*C0)-0.5*D0*cm.cos(theta1))**2 +
      (0.5*D0*cm.sin(theta1))**2))

l2 = (syp.sqrt((0.5*(D0+6*C0)-0.5*(D0+2.0*C0)*cm.cos(theta1))**2 +
      (0.5*(D0+2.0*C0)*cm.sin(theta1))**2))

l3 = (syp.sqrt((0.5*(D0+8.0*C0)-0.5*(D0+4*C0)*cm.cos(theta1))**2 +
      (0.5*(D0+4*C0)*cm.sin(theta1))**2))

# Definition of the general relationship between the above functions.
# Here C0 is unknown and C_b
C_b = C_t + 2*N_f*C0 + N_f*(l1+l2+l3) - N_f*St123 - N_f*St45
# for C_b = 10.4866, find C0
f = syp.nsolve(C_b - Circ, C0, 1)
# print values as output so as to be accessible by the rhino script
print f
print D0
print theta2
print fi2
print Circ
print N_f
print D0+2*f
print D0+4*f
print D0+6*f
print D0+8*f
```

# Appendix E

# SURROGATE MODELLING ALGORITHM VALIDATION

The following section describes the validation of the algorithms used to construct the surrogates and guide the multi-objective optimisation problem. Moreover, the rationale of using twenty points in the initial DoE along with the utility of the EI is outlined.

In particular, a multi-modal two-parameter analytical function, known as the modified version of Branin function (Forrester et al. 2008), was used to ensure that the algorithms implemented in this study can predict with high accuracy the global minimum of a given function by using the EI. The modified Branin function is expressed as

$$f(x) = (x_2 - \frac{5.1}{4\pi^2}x_2 + \frac{5}{\pi}x_1 - 6)^2 + 10\left[(1 - \frac{1}{8\pi})\cos x_1 + 1\right] + 5x_1 \\ with \quad x_1 \in [-5, 10]\,, x_2 \in [0, 15] \tag{E.1}$$

Firstly, different sampling plans (carried out by optimised LHC) were tested to evaluate how many points are needed as a first approximation in a multi-modal two-variable function such as the Branin. Fig. E.1 demonstrates the Kriging models interpolated after evaluating different number of points in each sampling plan. The contours of the analytical function are superimposed on the Kriging model to highlight the difference between the surrogate and the actual function. It can be noted that from the nineteen-point DoE, the surrogate is well approximating the overall landscape of the real function.

Furthermore, the $\theta$ tuning value was recorded to evaluate its convergence throughout different sampling plans. The plot of the $\theta$ convergence is depicted in Fig. E.2. It is well demonstrated that from the nineteen-point sampling plan, the $\theta$ parameter is converged.

Therefore, for a multi-modal two-parameter function, a twenty-point sampling plan

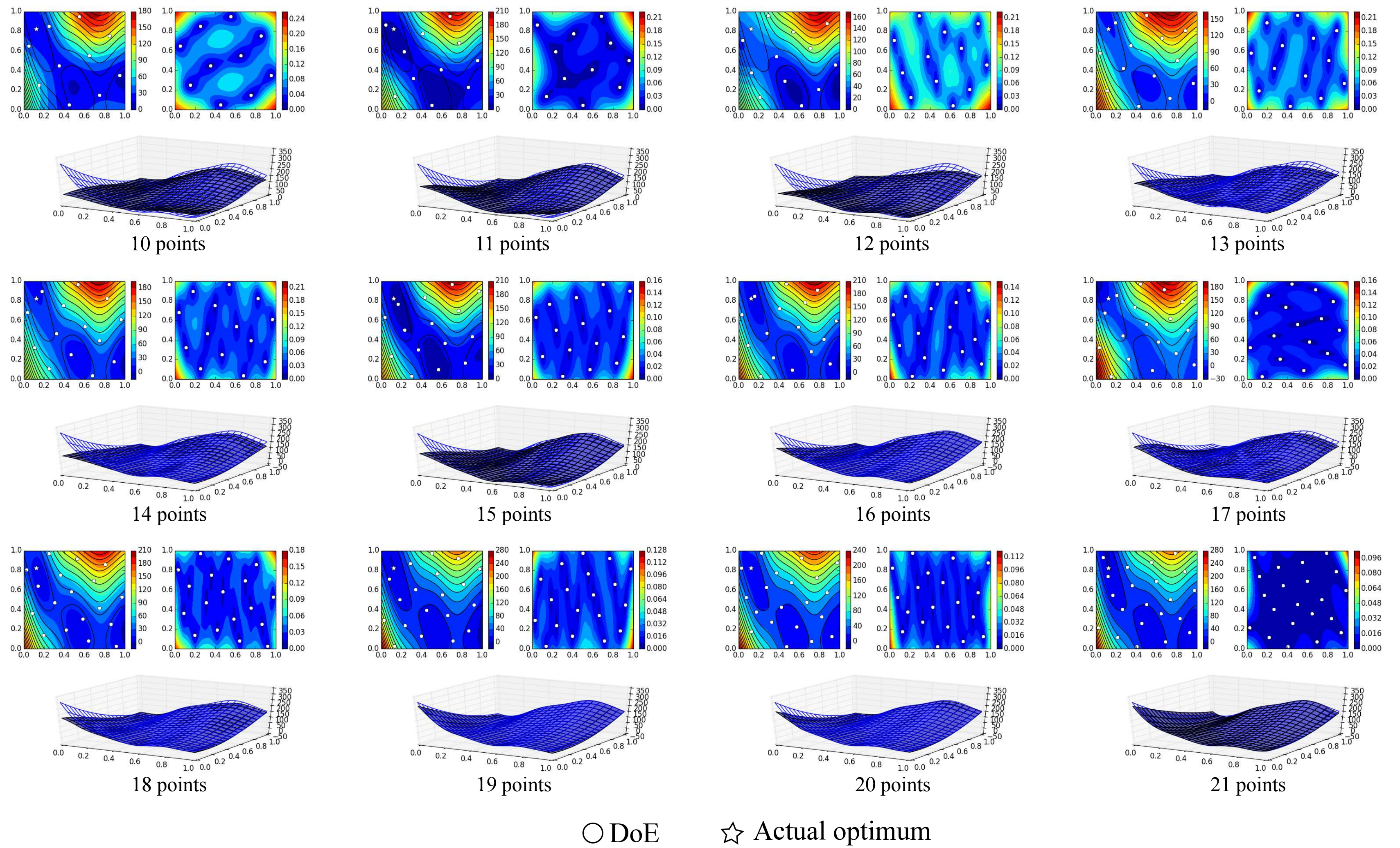

10 points

11 points

12 points

13 points

14 points

15 points

16 points

17 points

18 points

19 points

20 points

21 points

Figure E.1: Construction of Kriging models for different sampling plans of the modified Branin function. The actual contours of the Branin function are superimposed on the surrogate interpolation

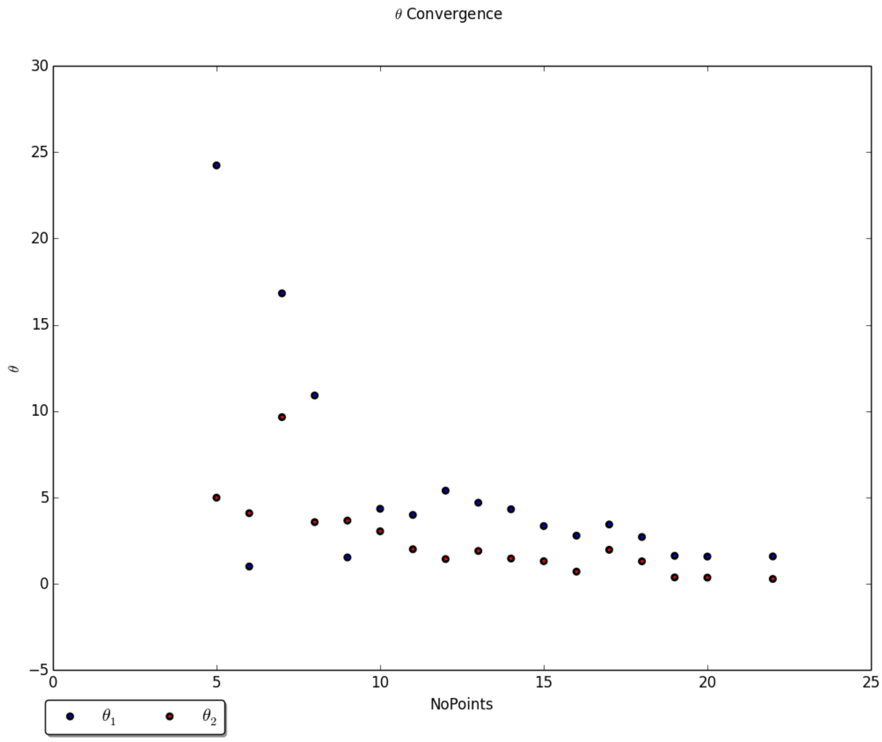

Figure E.2: $\theta$ tuning parameter convergence for different sampling plans

could provide an accurate initial approximation of the overall function landscape and then serve as a solid platform to drive the search of the global minimum. This has been proved in Fig. E.3, where the global minimum is located after five infill iterations. In particular, the optimisation is stopped for a given tolerance between the function evaluation in the nth infill point and the true global optimum calculated by setting

$$[\partial f/\partial x_1, \partial f/\partial x_2]^T = 0 \tag{E.2}$$

The optimisation iterations are guided by the EI of the Kriging model. In each step, an infill point is selected where the EI is the maximum.

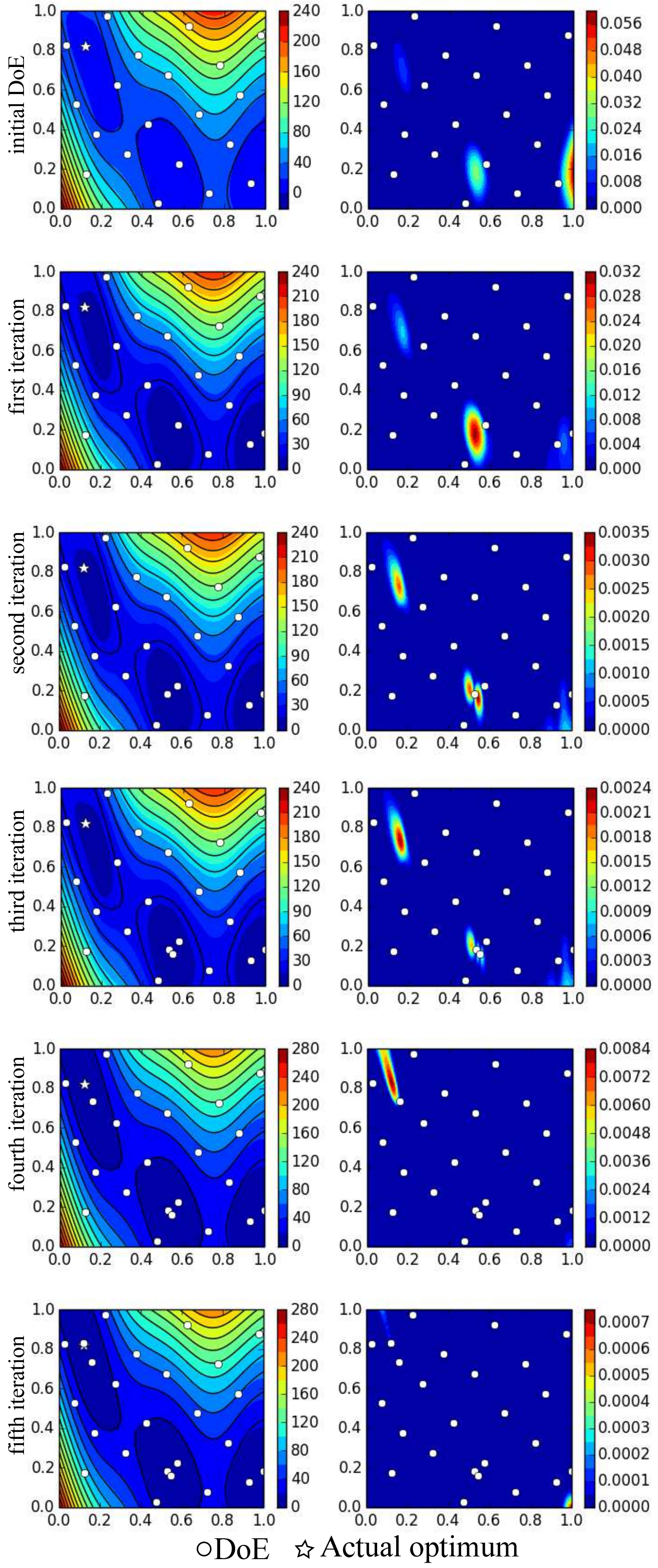

Figure E.3: Search of the global minimum of the modified Branin function guided by the EI. The global minimum is located after five infill iterations.

## Appendix F

# BASIC CONCEPTS FOR KRIGING CONSTRUCTION

In the following, the basic mathematical concepts for constructing a Kriging model are described:

Firstly, let our initial geometry parameterisation be:

$$\mathbf{X} = \left[\mathbf{x}^{(1)}, \mathbf{x}^{(2)}, ...., \mathbf{x}^{(n)}\right]^T \tag{F.1}$$

and the objective function evaluations be

$$\mathbf{y} = \left[y^{(1)}, y^{(2)}, ...., y^{(n)}\right]^T \tag{F.2}$$

Kriging modelling assumes that any number of objective function values $y^{(1)}, y^{(2)}, ...., y^{(n)}$ evaluated at $n$ points $\mathbf{x}^{(1)}, \mathbf{x}^{(2)}, ...., \mathbf{x}^{(n)}$ are random variables which are realisation of the Gaussian random field. The general Gaussian Process model can be expressed as

$$Y(\mathbf{x}) = \beta + \mathbf{Z}(\mathbf{x}) \tag{F.3}$$

where $\beta$, the mean of the random field, and $\mathbf{Z}(\mathbf{x})$ is a Gaussian Process with zero mean the following covariance

$$Cov(Y, Y) = \Gamma(Y, Y) = \sigma^2\Psi \tag{F.4}$$

where $\sigma^2$ is the process variance and $\Psi$ is the parameterised correlation matrix, given by

$$\boldsymbol{\Psi} = \begin{bmatrix} R(Y(\mathbf{x}^{(1)}), Y(\mathbf{x}^{(1)})) & R(Y(\mathbf{x}^{(1)}), Y(\mathbf{x}^{(2)})) & \cdots & R(Y(\mathbf{x}^{(1)}), Y(\mathbf{x}^{(n)})) \\ R(Y(\mathbf{x}^{(2)}), Y(\mathbf{x}^{(1)})) & R(Y(\mathbf{x}^{(2)}), Y(\mathbf{x}^{(2)})) & \cdots & R(Y(\mathbf{x}^{(2)}), Y(\mathbf{x}^{(n)})) \\ \vdots & \vdots & \ddots & \vdots \\ R(Y(\mathbf{x}^{(n)}), Y(\mathbf{x}^{(1)})) & R(Y(\mathbf{x}^{(n)}), Y(\mathbf{x}^{(2)})) & \cdots & R(Y(\mathbf{x}^{(n)}), Y(\mathbf{x}^{(n)})) \end{bmatrix} \tag{F.5}$$

and correlation function

$$R(Y(\mathbf{x}^{(i)}), Y(\mathbf{x}^{(l)})) = \exp^{-\sum_{j=1}^{k} \theta_j |x_j^{(i)} - x_j^{(l)}|^{p_j}} \tag{F.6}$$

with $\theta_j \geq 0$ and $0 < p_j \leq 2$. The $\theta_j$ and $p_j$ are known as the hyper-parameters and determine the rate of correlation decrease and the degree of smoothness in the $j^{th}$ direction, respectively. These hyper-parameters are optimised to maximise the *concentrated ln-likelihood* function

$$\ln(L) = -\frac{n}{2}\ln(\sigma^2) - 0.5\ln|\boldsymbol{\Psi}| - \frac{(\mathbf{y} - \mathbf{1}\beta)^T \boldsymbol{\Psi}^{-1} (\mathbf{y} - \mathbf{1}\beta)}{2\sigma^2} \tag{F.7}$$

Optimal values of $\beta$ and $\sigma^2$ can be derived by taking the partial derivatives of the equation F.7 with respect to $\beta$ and $\sigma^2$ and setting to zero. This yields to a mean

$$\hat{\beta} = \frac{\mathbf{1}^T \boldsymbol{\Psi}^{-1} \mathbf{y}}{\mathbf{1}^T \boldsymbol{\Psi}^{-1} \mathbf{1}} \tag{F.8}$$

and variance

$$\hat{\sigma}^2 = \frac{1}{n}(\mathbf{y} - \mathbf{1}\hat{\beta})^T \boldsymbol{\Psi}^{-1} (\mathbf{y} - \mathbf{1}\hat{\beta}) \tag{F.9}$$

where $\mathbf{1}$ is a $n \times 1$ vector of ones. Thus, the *concentrated likelihood* function will then be

$$\ln(L) \approx -\frac{n}{2}\ln(\hat{\sigma}^2) - 0.5\ln|\boldsymbol{\Psi}| \tag{F.10}$$

which depends on the symmetric matrix, $\boldsymbol{\Psi}$, therefore, on the hyper-parameters which are in turn optimised to maximise the equation. At last, for each set of input data, the hyper-parameters are optimised tuned to build a surrogate model which predicts the response landscape of the objective function and guides the search towards the global minimum (optimum). Given a new input geometry sample $x^{(n+1)} = [x_1, x_2, ...., x_k]$, the posterior mean and covariance can be computed as

$$\hat{y}(\mathbf{x}) = \hat{\beta} + \psi(\mathbf{x})^T \boldsymbol{\Psi}^{-1} (\mathbf{y} - \mathbf{1}\hat{\beta}) \tag{F.11}$$

and

$$Cov(\mathbf{x}, \mathbf{x}^{n+1}) = \sigma^2(\mathbf{\Psi}(\mathbf{x}, \mathbf{x}^{n+1}) - \psi(\mathbf{x})^T \mathbf{\Psi}^{-1} \psi(\mathbf{x})) \tag{F.12}$$

# Appendix G

# MULTI-OBJECTIVE OPTIMISATION ALGORITHM

## G.1 Class for MOO

MooNSGAII.py

```
# \MooNSGAII.py
__author__ = 'GiorgosRagkousis'
import numpy as np
from pylab import rc
from pyOpt import Optimization
from pyOpt import NSGA2
import matplotlib.pyplot as plt
from mpl_toolkits.mplot3d import Axes3D, proj3d

rc('text', usetex=True)
rc('font', **{'family': 'serif', 'serif': ['Computer Modern']})


class MOO():

    def __init__(self, Model_X, Model_y, trained, name):
        self.Model_X = Model_X
        self.Model_y = Model_y
        self.trained = trained
        self.name = name
        self.n, self.k = np.shape(self.Model_X)
        self.l = len(Model_y)
        self.KrigingModels = []
        self.Models = []
        self.Ranges = None
        self.max_weights = None
        self.utopia = None
        self.zenith = None
        self.nadir = None
        self.zenith_n = None
        self.nadir_n = None
        self.GC = None
        self.sphere_radi = None
        self.PF_norm = None
        self.curvature_sphere = None
        self.R = None
        self.index = None
        self.weights = None
        self.infill_errweights = None
        self.infill_wei = None
        self.sortarr = None
        self.mofWeights = []
```

```
    def pyOpt_Read_Output (self , datafile , columns ):
        """
        this function is for reading the data output from the NSGA-II
        algorithm . In particular , it return the best pop from the NSGA-II. It
        can be used for plotting the pareto front . It returns the desired
        columns in floats
        Input :
            datafile - the datafile with the data
            columns - a list with integers , indicating the columns with the
            obj fun
        Output :
            the objfun eval
        """
        best_final_pop = open (datafile , "r")
        lines = best_final_pop . readlines () [2: -1]
        best_final_pop . close ()
        list_columns = []
        for i, j in enumerate ( columns ):
            list_columns . append ([])
            for ind in lines :
                x = ind . split ()
                list_columns [i]. append ( float (x[j]))
        return list_columns

    def normalise (self , x):
        '''Normalise an array of data from 0-1'''
        x_normalised = (x - np. min (x)) / (np. max (x) - np. min (x))
        return x_normalised

    def normaliseX (self , x, X):
        '''Normalise an array of data from 0-1'''
        if type (X) == list :
            X = np. array (X)
            x_normalised = (x - X [0]) / (X [1] - X [0])
        else :
            x_normalised = (x - X [0]) / (X [1] - X [0])
        return x_normalised

    def normalise_PF (self , PF , zenith , nadir ):
        '''Normalise the pareto front according to the zenith & nadir point'''
        return (PF - zenith ) / ( nadir - zenith )

    def euclidean_dis (self , x, y):
                """Function to calculate the Euclidean distance between two points"""
        n = len (x)
        dist = []
        for i in range (n):
            dist . append ((x[i] - y[i]) **2.)
        return np. sqrt (sum ( dist ))

    def gradient3D (self , pointA , pointB ):
                """Function to calculate the 3D spatial gradient between two points"""
        return ((( pointA [2] - pointB [2]) ) / (np. sqrt (( pointA [0] -
                pointB [0]) **2. + ( pointA [1] - pointB [1]) **2.) ))

    def gradient2D (self , pointA , pointB ):
                """Function to calculate the 2D spatial gradient between two points"""
        return (( pointA [1] - pointB [1]) / ( pointA [0] - pointB [0]) )

    def training ( self ):
                """Train the input models (hyper-parameter optimisation)"""
        for i in range (len( self . Model_y )):
            # the following is applied when we want to train the models
#            self . Models . append ( kriging ( self . Model_X , self . Model_y [i],
#                                           name ='Model_%d' % i))
            # we append the trained models
            self . Models . append ( self . trained [i])

    def plot_KrigeModels ( self ):
                """Plot the trained Kriges"""
        for i in range (len( self . Models )):
            self . Models [i]. plot ()

    def SEI ( self ):
                """Calculate the Expected Improvement of the Surrogates"""
        self . Ranges = self . Models [0]. __range__ ()
        sei = np. ones (( self .n, self .l))
        Model_X_norm = np. ones ( self . Model_X . shape )
```

```
        for k in range(self.k):
            Model_X_norm[:, k] = self.normaliseX(self.Model_X[:, k],
                                                 self.Ranges[k])
        for i in range(self.n):
            for j in range(self.l):
                sei[i, j] = self.Models[j].expimp(Model_X_norm[i, :])
        return sei

    def SEI_NSGA_II(self, model, individual):
                """Calculate the Expected Improvement of a discrete point"""
#        self.Ranges = self.Models[0].__range__()
        l = len(individual)
        individual_Norm = []
        for k in range(l):
            individual_Norm.append(self.normaliseX(individual[k],
                                   self.Ranges[k]))
        sei = model.expimp(individual_Norm)
        return sei

    def insert_weights(self, weights):
                """Insert weights for each Objective"""
        l = len(weights)
        for i in range(l):
            self.mofWeights.append(weights[i])

    def mof(self, individual):
        """
        In case of multi-objective optimisation with numerical objective
        function evaluation, mof function is returning the RSMs after
        kriging interpolation
        Input:
            individual- the generation values of the GA (NSGA-II)
            Models- A list consisting of two models after kriging.train
                    (e.g. [VASModel, AASMModel])
        Output:
            the objective function evaluation for f1, f2 based on the
            kriging interpolation
        """
        f = [0.0]*len(self.Models)
        for i in range(len(self.Models)):
            f[i] = self.Models[i].predict(individual)
        g = [0]
        fail = 0
        print f
        return f, g, fail

    def mofEI(self, individual):
        """
        In case of multi-objective optimisation with numerical objective
        function evaluation, mofEI function is returning the RSMs of EI after
        kriging interpolation
        Input:
            individual- the generation values of the GA (NSGA-II)
            Models- A list consisting of two models after kriging.train
                    (e.g. [VASModel, AASMModel])
        Output:
            EI objective function evaluation for f1, f2 based on the
            kriging interpolation
        """
        f = [0.0]*len(self.Models)
        for i in range(len(self.Models)):
            expIMP = self.SEI_NSGA_II(self.Models[i], individual)
            f[i] = (-1.) * expIMP
        g = [0]
        fail = 0
        print f
        return f, g, fail

    def Weightedmof(self, individual):
        """
        In case of multi-objective optimisation with numerical objective
        function evaluation, Weightedmof function is returning the RSMs of
                Weighted Objective functions after kriging interpolation.
        Input:
            individual- the generation values of the GA (NSGA-II)
            Models- A list consisting of two models after kriging.train
                    (e.g. [VASModel, AASMModel])
        Output:
```

```
            the weighted objective function evaluation for f1, f2 based on the
            kriging interpolation
        """
        f = [0.0]*1
        summ = 0
        for i in range(len(self.Models)):
            f[0] = sum([self.mofWeights[i]*self.Models[i].predict(individual),
                       summ])
            summ = f[0]
        g = [0]
        fail = 0
        print f
        return f, g, fail

    def NSGA_II_search(self, X_variables, Y_objectives, minimum, maximum,
                       _fun_='mof'):
                """Set the NSGA-II method for searching the surrogates"""
        if _fun_ == 'mof':
            opt_prob = Optimization('Pareto', self.mof)
            for i, j in enumerate(X_variables):
                opt_prob.addVar(j, 'c', lower=minimum[i],
                                upper=maximum[i])
            for j in Y_objectives:
                opt_prob.addObj(j)
            opt_prob.addCon('g', 'i')
            print opt_prob
            #                 Global Optimization
            # _________________________________________________ #
            # ---------------- Compute Solution ----------------#
            nsga2 = NSGA2()
            nsga2.setOption('PopSize', 80)
            nsga2.setOption('PrintOut', 1)
            # here we define the max Generations
            # nsga2.setOption('maxGen', 135)
            nsga2(opt_prob, store_hst=True)
            print opt_prob.solution(0)
        elif _fun_ == 'mofEI':
            opt_prob = Optimization('Pareto', self.mofEI)
            for i, j in enumerate(X_variables):
                opt_prob.addVar(j, 'c', lower=minimum[i],
                                upper=maximum[i])
            for j in Y_objectives:
                opt_prob.addObj(j)
            opt_prob.addCon('g', 'i')
            print opt_prob
            #                 Global Optimization
            # _________________________________________________ #
            # ---------------- Compute Solution ----------------#
            nsga2 = NSGA2()
            nsga2.setOption('PopSize', 100)
            nsga2.setOption('PrintOut', 1)
            # nsga2.setOption('maxGen', 135)
            nsga2(opt_prob, store_hst=True)
            print opt_prob.solution(0)
        elif _fun_ == 'Weightedmof':
            opt_prob = Optimization('Pareto', self.Weightedmof)
            for i, j in enumerate(X_variables):
                opt_prob.addVar(j, 'c', lower=minimum[i],
                                upper=maximum[i])
            opt_prob.addObj('f1')
            opt_prob.addCon('g', 'i')
            print opt_prob
            # Global Optimization
            # _________________________________________________ #
            # ---------------- Compute Solution ----------------#
            nsga2 = NSGA2()
            nsga2.setOption('PopSize', 100)
            nsga2.setOption('PrintOut', 1)
            # nsga2.setOption('maxGen', 135)
            nsga2(opt_prob, store_hst=True)
            print opt_prob.solution(0)

    def global_criterion(self):
                """Returns the point defined according to the global criterion
                set in the multi-Objective optimisation routine"""
        data_output = "nsga2_final_pop.out"
        ParetoFront = self.pyOpt_Read_Output(data_output, [i for i in
                                             range(len(self.Model_y))])
```

```
        PF = np.array(ParetoFront).T
        if len(self.Model_y) == 3:
            x, y, z = PF[:, 0], PF[:, 1], PF[:, 2]
            self.zenith = np.array([np.min(x), np.min(y), np.min(z)]).T
            self.nadir = np.array([np.max(x), np.max(y), np.max(z)]).T
            self.PF_norm = self.normalise_PF(PF, self.zenith, self.nadir)
            xx = self.PF_norm[:, 0]
            yy = self.PF_norm[:, 1]
            zz = self.PF_norm[:, 2]
            self.zenith_n = np.array([np.min(xx), np.min(yy),
                                      np.min(zz)]).T
            self.nadir_n = np.array([np.max(xx), np.max(yy), np.max(zz)]).T
        elif len(self.Model_y) == 2:
            x, y = PF[:, 0], PF[:, 1]
            self.zenith = np.array([np.min(x), np.min(y)]).T
            self.nadir = np.array([np.max(x), np.max(y)]).T
            self.PF_norm = self.normalise_PF(PF, self.zenith, self.nadir)
            xx = self.PF_norm[:, 0]
            yy = self.PF_norm[:, 1]
            self.zenith_n = np.array([np.min(xx), np.min(yy)]).T
            self.nadir_n = np.array([np.max(xx), np.max(yy)]).T
        self.GC = np.ones((len(self.PF_norm[:, 0])))
        for i in range(len(self.PF_norm[:, 0])):
            if len(self.Model_y) == 3:
                self.GC[i] = np.sqrt((self.PF_norm[i, 0] -
                                     self.zenith_n[0])**2. +
                                     (self.PF_norm[i, 1] -
                                     self.zenith_n[1])**2. +
                                     (self.PF_norm[i, 2] -
                                     self.zenith_n[2])**2.)
            elif len(self.Model_y) == 2:
                self.GC[i] = np.sqrt((self.PF_norm[i, 0] -
                                     self.zenith_n[0])**2.
                                     + (self.PF_norm[i, 1] -
                                     self.zenith_n[1])**2.)
        self.sphere_radi = np.min(self.GC)
        return np.min(self.GC), self.GC, self.GC.argmin(), self.PF_norm

    def global_criterion_weighted(self, weights):
                """Returns the weighted point defined according to the global criterion
                set in the multi-Objective optimisation routine (weighted L-2 metric)"""
        data_output = "nsga2_final_pop.out"
        ParetoFront = self.pyOpt_Read_Output(data_output, [i for i in
                                             range(len(self.Model_y))])
        PF = np.array(ParetoFront).T
        if len(self.Model_y) == 3:
            x, y, z = PF[:, 0], PF[:, 1], PF[:, 2]
            self.zenith = np.array([np.min(x), np.min(y), np.min(z)]).T
            self.nadir = np.array([np.max(x), np.max(y), np.max(z)]).T
            self.PF_norm = self.normalise_PF(PF, self.zenith, self.nadir)
            xx = self.PF_norm[:, 0]
            yy = self.PF_norm[:, 1]
            zz = self.PF_norm[:, 2]
            self.zenith_n = np.array([np.min(xx), np.min(yy),
                                      np.min(zz)]).T
            self.nadir_n = np.array([np.max(xx), np.max(yy), np.max(zz)]).T
        elif len(self.Model_y) == 2:
            x, y = PF[:, 0], PF[:, 1]
            self.zenith = np.array([np.min(x), np.min(y)]).T
            self.nadir = np.array([np.max(x), np.max(y)]).T
            self.PF_norm = self.normalise_PF(PF, self.zenith, self.nadir)
            xx = self.PF_norm[:, 0]
            yy = self.PF_norm[:, 1]
            self.zenith_n = np.array([np.min(xx), np.min(yy)]).T
            self.nadir_n = np.array([np.max(xx), np.max(yy)]).T
        self.GC = np.ones((len(self.PF_norm[:, 0])))
        for i in range(len(self.PF_norm[:, 0])):
            if len(self.Model_y) == 3:
                self.GC[i] = np.sqrt(weights[0]*abs(self.PF_norm[i, 0] -
                                     self.zenith_n[0])**2. +
                                     weights[1]*abs(self.PF_norm[i, 1] -
                                     self.zenith_n[1])**2. +
                                     weights[2]*abs(self.PF_norm[i, 2] -
                                     self.zenith_n[2])**2.)
            elif len(self.Model_y) == 2:
                self.GC[i] = np.sqrt(weights[0]*(self.PF_norm[i, 0] -
                                     self.zenith_n[0])**2.
                                     + weights[1]*(self.PF_norm[i, 1] -
```

```
                                     self.zenith_n[1])**2.)
        self.sphere_radi = np.sqrt(sum([self.PF_norm[self.GC.argmin(), i]**2.
                                        for i in range(self.l)]))
        return np.min(self.GC), self.GC, self.GC.argmin(), self.PF_norm

    def pareto_sort(self):
                """Sort the Pareto front points (Descending order)"""
        if len(self.Model_y) >= 2:
            self.sortarr = self.PF_norm[np.lexsort(
                                        np.transpose(self.PF_norm)[::-1])]

    def pareto_gradients(self):
                """For continuous Pareto front, calculate the gradients of Pareto points"""
        if len(self.Model_y) == 3:
            x = self.sortarr[:, 0]
            y = self.sortarr[:, 1]
            z = self.sortarr[:, 2]
            # first gradients of the curve points
            dx = np.gradient(x)
            dy = np.gradient(y)
            dz = np.gradient(z)
            # c'(t)
            dr = np.array([dx, dy, dz], np.float).T
            # second gradients of the curve points
            ddx = np.gradient(dx)
            ddy = np.gradient(dy)
            ddz = np.gradient(dz)
            # c''(t)
            ddr = np.array([ddx, ddy, ddz], np.float).T
            # ||c'(t)||
            dr_n = np.sum(np.abs(dr)**2., axis=1)**(1./2.)
            dr_n = np.reshape(dr_n, (len(dr_n), 1))
            # ||c''(t)||
            ddr_n = np.sum(np.abs(ddr)**2., axis=1)**(1./2.)
            ddr_n = np.reshape(ddr_n, (len(ddr_n), 1))
            # Tangent (T) (unit)
            T = dr/dr_n
            # Curvature k of the curve
            # c'(t) x c''(t)
            k_cross = np.cross(dr, ddr, axisa=1, axisb=1)
            # ||c'(t) x c''(t)||
            k_cross_num = np.sum(np.abs(k_cross)**2., axis=1)**(1./2.)
            k_cross_num = np.reshape(k_cross_num, (len(k_cross_num), 1))
            # ||c'(t)||^3.
            k_cross_den = dr_n**3.
            # k = ||c'(t) x c''(t)|| / ||c'(t)||^3.
            k = k_cross_num / k_cross_den
            # n = ( ( c'(t) x c''(t) ) x c'(t) ) /
            #                           ||( c'(t) x c''(t) )||.||c'(t)||
            n_num = np.cross(k_cross, dr, axisa=1, axisb=1)
            n_den = k_cross_num * dr_n
            N = n_num / n_den
            # radius of curvature (R = 1/k)
            self.R = 1/k
            for i in range(len(self.sortarr[:, 0])):
                if np.array_equal(self.sortarr[i, :],
                                  self.PF_norm[self.GC.argmin(), :]) is True:
                    self.index = i
                else:
                    pass
            self.curvature_sphere = ((self.sortarr[self.index, :]) +
                                     (self.R[self.index, :] *
                                     N[self.index, :]))
        elif len(self.Model_y) == 2:
            x = self.sortarr[:, 0]
            y = self.sortarr[:, 1]
            # first gradients of the curve points
            dx = np.gradient(x)
            dy = np.gradient(y)
            # c'(t)
            dr = np.array([dx, dy], np.float).T
            # second gradients of the curve points
            ddx = np.gradient(dx)
            ddy = np.gradient(dy)
            # c''(t)
            ddr = np.array([ddx, ddy], np.float).T
            k = (dx*ddy - dy*ddx) / (dx**2 + dy**2)**(3/2.)
            nx = - dy / np.sqrt(dx**2 + dy**2)
```

```
            ny = dx / np.sqrt(dx**2 + dy**2)
            N = np.array([nx, ny], np.float).T
            # radius of curvature (R = 1/k)
            self.R = 1/k
            for i in range(len(self.sortarr[:, 0])):
                if np.array_equal(self.sortarr[i, :],
                                  self.PF_norm[self.GC.argmin(), :]) is True:
                    self.index = i
                else:
                    pass
            self.curvature_sphere = ((self.sortarr[self.index, :]) +
                                     (self.R[self.index] * N[self.index, :]))

    def pareto_infill_Voutchkov(self, sequence):
                """Function for extraction infill points according to the multi-Objective
                optimisation of EI (Dr. Ivan Voutchkon, Rolls Royce, UTC, University of Southampton)"""
        data_output = "nsga2_final_pop.out"
        l = len(sequence)
        if self.l == 3:
            ParetoFront_x = self.pyOpt_Read_Output(data_output, [(i + 4) for i
                                                   in range(self.k)])
        elif self.l == 2:
            ParetoFront_x = self.pyOpt_Read_Output(data_output, [(i + 3) for i
                                                   in range(self.k)])
        n = len(self.PF_norm[:, 0])
        ParetoFront_x = np.array(ParetoFront_x).T
        indices = []
        Voutchkov = np.ones((l + 1, self.k))
        for ind in sequence:
            for i in range(n):
                if np.array_equal(self.PF_norm[i, :],
                                  self.sortarr[ind, :]) is True:
                    index = i
                    indices.append(index)
                else:
                    pass
        Voutchkov[0, :] = ParetoFront_x[self.GC.argmin(), :]
        for i in range(l):
            Voutchkov[i + 1, :] = ParetoFront_x[indices[i], :]
        return Voutchkov

    def check_colinearity(self):
                """This method checks whether nadir, zenith and pareto optimum point
                are colinear"""
        if self.l == 3:
            if self.gradient3D(self.zenith_n,
               self.PF_norm[self.GC.argmin(), :]) == \
                    self.gradient3D(self.PF_norm[self.GC.argmin(), :],
                                    self.curvature_sphere):
                print 'The lines are co-linear'
            else:
                print 'The lines are not co-linear'
            print [self.gradient3D(self.zenith_n,
                   self.PF_norm[self.GC.argmin(), :]),
                   self.gradient3D(self.PF_norm[self.GC.argmin(), :],
                   self.curvature_sphere)]
        elif self.l == 2:
            if self.gradient2D(self.zenith_n,
               self.PF_norm[self.GC.argmin(), :]) == \
                    self.gradient2D(self.PF_norm[self.GC.argmin(), :],
                                    self.curvature_sphere):
                print 'The lines are co-linear'
            else:
                print 'The lines are not co-linear'
            print [self.gradient2D(self.zenith_n,
                   self.PF_norm[self.GC.argmin(), :]),
                   self.gradient2D(self.PF_norm[self.GC.argmin(), :],
                   self.curvature_sphere)]

    def calculate_angles(self, output='Rxz'):
                """Method for calculating transformations matrices"""
        r = self.sphere_radi
        x = self.PF_norm[self.GC.argmin(), 0]
        y = self.PF_norm[self.GC.argmin(), 1]
        z = self.PF_norm[self.GC.argmin(), 2]
        alpha = np.arccos(x/r)
        beta = np.arccos(y/r)
        gamma = np.arccos(z/r)
```

```
        fi = np.arctan(x/y)
        zz = np.sqrt(x**2. + y**2.)
        theta = np.arccos(zz/r)
        Rxz = np.array([[np.cos(fi), -np.sin(fi), 0., 0.], [np.cos(theta) *
                        np.sin(fi), np.cos(theta)*np.cos(fi),
                        -np.sin(theta), 0.], [np.sin(theta)*np.sin(fi),
                        np.sin(theta)*np.cos(fi), np.cos(theta), 0.],
                       [0., 0., 0., 1.]])
        Ryx = np.array([[np.cos(beta), np.sin(beta)*np.sin(alpha),
                         np.sin(beta)*np.cos(alpha), 0.], [0, np.cos(alpha),
                        -np.sin(alpha), 0.], [-np.sin(beta), np.cos(beta) *
                        np.sin(alpha), np.cos(beta)*np.cos(alpha), 0.],
                        [0., 0., 0., 1.]])
        Ryz = np.array([[np.cos(theta)*np.cos(fi), -np.cos(theta)*np.sin(fi),
                         np.sin(theta), 0.], [np.sin(fi), np.cos(fi), 0.,
                        0.], [-np.sin(theta)*np.cos(fi), np.sin(theta) *
                        np.sin(fi), np.cos(theta), 0.],
                        [0., 0., 0., 1.]])
        Rzyx = np.array([[np.cos(beta)*np.cos(gamma), np.cos(gamma) *
                          np.sin(alpha)*np.sin(beta)-np.cos(alpha) *
                          np.sin(gamma), np.cos(alpha)*np.cos(gamma) *
                          np.sin(beta)+np.sin(alpha)*np.sin(gamma), 0.],
                        [np.cos(beta)*np.sin(gamma), np.cos(alpha) *
                         np.cos(gamma)+np.sin(alpha)*np.sin(beta) *
                         np.sin(gamma), -np.cos(gamma)*np.sin(alpha) +
                         np.cos(alpha)*np.sin(beta)*np.sin(gamma), 0.],
                        [-np.sin(beta), np.cos(beta)*np.sin(alpha),
                         np.cos(alpha)*np.cos(beta), 0.], [0., 0., 0., 1.]])
        Rxyz = np.array([[np.cos(beta)*np.cos(gamma), -np.cos(beta) *
                          np.sin(gamma), np.sin(beta), 0.],
                        [np.cos(alpha)*np.sin(gamma)+np.sin(alpha) *
                         np.sin(beta)*np.cos(gamma), np.cos(alpha) *
                         np.cos(gamma)-np.sin(alpha)*np.sin(beta) *
                         np.sin(gamma), -np.sin(alpha)*np.cos(beta), 0.],
                        [np.sin(alpha)*np.sin(gamma)-np.cos(alpha) *
                         np.sin(beta)*np.cos(gamma), np.sin(alpha) *
                         np.cos(gamma)+np.cos(alpha)*np.sin(beta) *
                         np.sin(gamma),
                         np.cos(alpha)*np.cos(beta), 0.], [0., 0., 0., 1.]])
        Rx = np.array([[1., 0., 0., 0.], [0., np.cos(alpha), -np.sin(alpha),
                       0.], [0, np.sin(alpha), np.cos(alpha), 0.], [0., 0., 0.,
                       1.]])
        # return the transformation matrix defined in the output
        if output == 'Rxz':
            return Rxz
        elif output == 'Ryx':
            return Ryx
        elif output == 'Ryz':
            return Ryz
        elif output == 'Rzyx':
            return Rzyx
        elif output == 'Rxyz':
            return Rxyz
        elif output == 'Rx':
            return Rx

    def point_weights(self):
                """Method for calculating the weights of Pareto points with respect to
                objective functions"""
        f_max, f_min = [], []
        for i in range(self.l):
            f_max.append(np.max(self.PF_norm[:, i]))
            f_min.append(np.min(self.PF_norm[:, i]))
        self.weights = np.ones((len(self.PF_norm[:, 0]), self.l))
        for i in range(len(self.PF_norm[:, 0])):
            for j in range(self.l):
                if self.l == 2:
                    self.weights[i, j] = (((f_max[j] - self.PF_norm[i, j]) /
                                          (f_max[j] - f_min[j])) /
                                          (sum([(f_max[0] - self.PF_norm[i, 0])
                                           / (f_max[0] - f_min[0]),
                                           (f_max[1] - self.PF_norm[i, 1]) /
                                           (f_max[1] - f_min[1])])))
                elif self.l == 3:
                    self.weights[i, j] = (((f_max[j] - self.PF_norm[i, j]) /
                                          (f_max[j] - f_min[j])) /
                                          (sum([(f_max[0] - self.PF_norm[i, 0])
                                           / (f_max[0] - f_min[0]),
```

```
                                           (f_max[1] - self.PF_norm[i, 1]) /
                                           (f_max[1] - f_min[1]),
                                           (f_max[2] - self.PF_norm[i, 2]) /
                                           (f_max[2] - f_min[2])])))
        return self.weights

    def updatepoints_weights(self):
                """Method to return the points with the maximum weights"""
        self.max_weights = np.ones((self.l + 1))
        for i in range(self.l):
            self.max_weights[i] = self.weights[:, i].argmax()
        self.max_weights[self.l] = self.GC.argmin()
        return self.max_weights

    def infillerrweights(self):
                """Infill DoE according to point weights"""
        data_output = "nsga2_final_pop.out"
        if self.l == 3:
            ParetoFront_x = self.pyOpt_Read_Output(data_output, [(i + 4) for i
                                                   in range(self.k)])
        elif self.l == 2:
            ParetoFront_x = self.pyOpt_Read_Output(data_output, [(i + 3) for i
                                                   in range(self.k)])
        if self.k == 2:
            samplePoints = []
            Update_samplePoints = []
            for i in range(self.k):
                samplePoints.append(self.normaliseX(self.Model_X[:, i],
                                                    self.Ranges[i]))
                Update_samplePoints.append(self.normaliseX(ParetoFront_x[i],
                                                           self.Ranges[i]))
            # pick the update points
            arrUpdate_samplePoints = np.array(Update_samplePoints).T
            pred_err = np.ones((len(arrUpdate_samplePoints[:, 0]), self.l))
            self.infill_errweights = np.ones((len(arrUpdate_samplePoints[:, 0])
                                              ))
            for i in range(len(arrUpdate_samplePoints[:, 0])):
                for j in range(self.l):
                    pred_err[i, j] = (self.Models[j].predicterr_normalized(
                                      [arrUpdate_samplePoints[i, :]]))
                self.infill_errweights[i] = (np.sum(pred_err[i, :] *
                                             self.weights[i, :]))
            return self.infill_errweights

    def WEI(self):
                """Calculate the weighted EI"""
        data_output = "nsga2_final_pop.out"
        if self.l == 3:
            ParetoFront_x = self.pyOpt_Read_Output(data_output, [(i + 4) for i
                                                   in range(self.k)])
        elif self.l == 2:
            ParetoFront_x = self.pyOpt_Read_Output(data_output, [(i + 3) for i
                                                   in range(self.k)])
        samplePoints = []
        Update_samplePoints = []
        for i in range(self.k):
            samplePoints.append(self.normaliseX(self.Model_X[:, i],
                                                self.Ranges[i]))
            Update_samplePoints.append(self.normaliseX(ParetoFront_x[i],
                                                       self.Ranges[i]))
        arrUpdate_samplePoints = np.array(Update_samplePoints).T
        pred_ei = np.ones((len(arrUpdate_samplePoints[:, 0]), self.l))
        self.infill_wei = np.ones((len(arrUpdate_samplePoints[:, 0])))
        for i in range(len(arrUpdate_samplePoints[:, 0])):
            for j in range(self.l):
                pred_ei[i, j] = (self.Models[j].weightedexpimp(
                                 [arrUpdate_samplePoints[i, :]],
                                 self.weights[i, j]))
            self.infill_wei[i] = (np.sum(pred_ei[i, :]))
        return self.infill_wei
# =============================================================================== #
#                      PLOTTING METHODS                                           #
# =============================================================================== #
    def plot_ParetoFront_Weighted(self):
        if self.l == 3:

            u = np.linspace(0, 2 * np.pi, 100)
            v = np.linspace(0, np.pi, 100)
```

```
            x_s = self.zenith_n[0] + self.sphere_radi * np.outer(np.cos(u),
                                                                 np.sin(v))
            y_s = self.zenith_n[1] + np.min(self.GC) * np.outer(np.sin(u),
                                                                np.sin(v))
            z_s = self.zenith_n[2] + np.min(self.GC) * np.outer(np.ones(
                                                                np.size(u)),
                                                                np.cos(v))
            Ryz = self.calculate_angles()
            h_s = np.ones(x_s.shape)
            n, k = np.shape(x_s)
            xyz = np.array([x_s, y_s, z_s, h_s])
            for i in range(n):
                for j in range(k):
                    xyz[:, i, j] = np.dot(Ryz, xyz[:, i, j])

            x_ss = xyz[0, :, :]
            y_ss = xyz[1, :, :]
            z_ss = xyz[2, :, :]
            figg = plt.figure(figsize=(12, 12), facecolor=’w’,
                              edgecolor=’k’, linewidth= 2.0, frameon=True)
            figg.suptitle(’3d normalised pareto front’)
            axx = figg.add_subplot(1, 1, 1, projection=’3d’)
            axx.plot(self.PF_norm[:, 0], self.PF_norm[:, 1],
                     self.PF_norm[:, 2], linestyle=’’,
                     label="Pareto front",
                     alpha=0.5, markerfacecolor=’r’, markeredgecolor=’k’,
                     marker=’o’, markersize=5)
            axx.plot([self.zenith_n[0]], [self.zenith_n[1]],
                     [self.zenith_n[2]],
                     linestyle=’’, markerfacecolor=’g’,
                     markeredgecolor=’k’,
                     marker=’o’, markersize=5, alpha=1.,
                     label="zenith point")
            axx.plot_wireframe(x_ss, y_ss, z_ss,  rstride=1, cstride=1,
                               color=’b’, alpha=0.1, label="zenith sphere")
            axx.plot([self.PF_norm[self.GC.argmin(), 0], self.zenith_n[0]],
                     [self.PF_norm[self.GC.argmin(), 1],
                     self.zenith_n[1]], [self.PF_norm[self.GC.argmin(), 2],
                     self.zenith_n[2]], ’k’,
                     label=’Min Euclidean distance’)

            axx.set_xlabel(self.name[0])
            axx.set_ylabel(self.name[1])
            axx.set_zlabel(self.name[2])
            axx.legend(loc=’upper center’, numpoints=1, ncol=3,
                       bbox_to_anchor=(0.5, -0.03),
                       fancybox=True, shadow=True)
            figg = plt.show()

    def plot_ParetoFront(self, nsgaII=’Objective’):
        data_output = "nsga2_final_pop.out"
        ParetoFront = self.pyOpt_Read_Output(data_output, [i for i in
                                             range(self.l)])
        if self.l == 3:
            u = np.linspace(0, 2 * np.pi, 100)
            v = np.linspace(0, np.pi, 100)
            x_s = self.zenith_n[0] + self.sphere_radi * np.outer(np.cos(u),
                                                                 np.sin(v))
            y_s = self.zenith_n[1] + self.sphere_radi * np.outer(np.sin(u),
                                                                 np.sin(v))
            z_s = self.zenith_n[2] + self.sphere_radi * np.outer(np.ones(
                                                                 np.size(u)),
                                                                 np.cos(v))
            xc_s = (self.curvature_sphere[0] + self.R[self.index] *
                    np.outer(np.cos(u), np.sin(v)))
            yc_s = (self.curvature_sphere[1] + self.R[self.index] *
                    np.outer(np.sin(u), np.sin(v)))
            zc_s = (self.curvature_sphere[2] + self.R[self.index] *
                    np.outer(np.ones(np.size(u)), np.cos(v)))
            if nsgaII == ’Objective’:
                # ## _____________________________________________  #
                # ##                                                #
                # ## ------------ plot pareto -------------------- #
                fig = plt.figure(figsize=(16, 16), facecolor=’w’,
                                 edgecolor=’k’, linewidth= 2.0, frameon=True)
                fig.suptitle(’3d pareto front’)
                ax = fig.add_subplot(2, 1, 1, projection=’3d’)
                ax.scatter(self.Model_y[0], self.Model_y[1], self.Model_y[2],
```

```
                   label="Evaluation points", alpha=1.,
                   edgecolor='black', facecolor='b', linewidth=2.)
        ax.scatter(ParetoFront[0], ParetoFront[1], ParetoFront[2],
                   label="Pareto front", alpha=1., edgecolor='black',
                   facecolor='r', linewidth=2.)
        ax.scatter(self.zenith[0], self.zenith[1], self.zenith[2],
                   label="zenith point", alpha=1., edgecolor='black',
                   facecolor='g', linewidth=2.)
        ax.scatter(self.nadir[0], self.nadir[1], self.nadir[2],
                   label="nadir point", alpha=1., edgecolor='black',
                   facecolor='k', linewidth=2.)
        ax.set_xlabel(self.name[0])
        ax.set_ylabel(self.name[1])
        ax.set_zlabel(self.name[2])

        ax1 = fig.add_subplot(2, 3, 4)
        ax1.scatter(self.Model_y[0], self.Model_y[2],
                    label="Evaluation points", alpha=0.5,
                    edgecolor='black', facecolor='b', linewidth=2.)
        ax1.scatter(ParetoFront[0], ParetoFront[2],
                    label="Pareto front",
                    alpha=0.5, edgecolor='black', facecolor='r',
                    linewidth=2.)
        ax1.scatter(self.zenith[0], self.zenith[2],
                    label="zenith point",
                    alpha=1., edgecolor='black', facecolor='g',
                    linewidth=2.)
        ax1.scatter(self.nadir[0], self.nadir[2], label="nadir point",
                    alpha=1., edgecolor='black', facecolor='k',
                    linewidth=2.)
        ax1.set_xlabel(self.name[0])
        ax1.set_ylabel(self.name[2])
        ax1.legend(loc='upper center', scatterpoints=1, ncol=4,
                   bbox_to_anchor=(1.75, -0.09),
                   fancybox=True, shadow=True)

        ax2 = fig.add_subplot(2, 3, 5)
        ax2.scatter(self.Model_y[1], self.Model_y[2], alpha=0.5,
                    edgecolor='black', facecolor='b', linewidth=2.)
        ax2.scatter(ParetoFront[1], ParetoFront[2], alpha=0.5,
                    edgecolor='black', facecolor='r', linewidth=2.)
        ax2.scatter(self.zenith[1], self.zenith[2],
                    label="zenith point",
                    alpha=1., edgecolor='black', facecolor='g',
                    linewidth=2.)
        ax2.scatter(self.nadir[1], self.nadir[2], label="nadir point",
                    alpha=1., edgecolor='black', facecolor='k',
                    linewidth=2.)
        ax2.set_xlabel(self.name[1])
        ax2.set_ylabel(self.name[2])

        ax3 = fig.add_subplot(2, 3, 6)
        ax3.scatter(self.Model_y[1], self.Model_y[0], alpha=0.5,
                    edgecolor='black', facecolor='b', linewidth=2.)
        ax3.scatter(ParetoFront[1], ParetoFront[0], alpha=0.5,
                    edgecolor='black', facecolor='r', linewidth=2.)
        ax3.scatter(self.zenith[1], self.zenith[0],
                    label="zenith point",
                    alpha=1., edgecolor='black', facecolor='g',
                    linewidth=2.)
        ax3.scatter(self.nadir[1], self.nadir[0], label="nadir point",
                    alpha=1., edgecolor='black', facecolor='k',
                    linewidth=2.)
        ax3.set_xlabel(self.name[1])
        ax3.set_ylabel(self.name[0])

        plt.show()
        figg = plt.figure(figsize=(12, 12), facecolor='w',
                          edgecolor='k', linewidth= 2.0, frameon=True)
        figg.suptitle('3d normalised pareto front')
        axx = figg.add_subplot(1, 1, 1, projection='3d')
        axx.plot(self.PF_norm[:, 0], self.PF_norm[:, 1],
                 self.PF_norm[:, 2], linestyle='',
                 label="Pareto front",
                 alpha=0.5, markerfacecolor='r', markeredgecolor='k',
                 marker='o', markersize=5)
        axx.plot([self.zenith_n[0]], [self.zenith_n[1]],
                 [self.zenith_n[2]],
```

```
                     linestyle='', markerfacecolor='g',
                     markeredgecolor='k',
                     marker='o', markersize=5, alpha=1.,
                     label="zenith point")
            axx.plot_wireframe(x_s, y_s, z_s,  rstride=1, cstride=1,
                               color='b', alpha=0.1, label="zenith sphere")
            axx.plot([self.PF_norm[self.GC.argmin(), 0], self.zenith_n[0]],
                     [self.PF_norm[self.GC.argmin(), 1],
                     self.zenith_n[1]], [self.PF_norm[self.GC.argmin(), 2],
                     self.zenith_n[2]], 'k',
                     label='Min Euclidean distance')
            axx.set_xlabel(self.name[0])
            axx.set_ylabel(self.name[1])
            axx.set_zlabel(self.name[2])
            axx.legend(loc='upper center', numpoints=1, ncol=3,
                       bbox_to_anchor=(0.5, -0.03),
                       fancybox=True, shadow=True)
            figg = plt.show()

        elif nsgaII == 'Expected Improvement':
            EXPIMP = self.SEI()
            EXPIMP = (-1.)*EXPIMP
            # ## -------------------------------------------------- #
            # ##                                                    #
            # ## -------------- plot pareto ----------------------- #
            fig = plt.figure(figsize=(16, 16), facecolor='w',
                             edgecolor='k', linewidth= 2.0, frameon=True)
            fig.suptitle('3d pareto front')
            ax = fig.add_subplot(2, 1, 1, projection='3d')
            ax.scatter(EXPIMP[:, 0], EXPIMP[:, 1], EXPIMP[:, 2],
                       label="Evaluation points", alpha=1.,
                       edgecolor='black', facecolor='b', linewidth=2.)
            ax.scatter(ParetoFront[0], ParetoFront[1], ParetoFront[2],
                       label="Pareto front", alpha=1., edgecolor='black',
                       facecolor='r', linewidth=2.)
            ax.scatter(self.zenith[0], self.zenith[1], self.zenith[2],
                       label="zenith point", alpha=1., edgecolor='black',
                       facecolor='g', linewidth=2.)
            ax.scatter(self.nadir[0], self.nadir[1], self.nadir[2],
                       label="nadir point", alpha=1., edgecolor='black',
                       facecolor='k', linewidth=2.)
            ax.set_xlabel(self.name[0])
            ax.set_ylabel(self.name[1])
            ax.set_zlabel(self.name[2])

            ax1 = fig.add_subplot(2, 3, 4)
            ax1.scatter(EXPIMP[:, 0], EXPIMP[:, 2],
                        label="Evaluation points", alpha=0.5,
                        edgecolor='black', facecolor='b', linewidth=2.)
            ax1.scatter(ParetoFront[0], ParetoFront[2],
                        label="Pareto front",
                        alpha=0.5, edgecolor='black', facecolor='r',
                        linewidth=2.)
            ax1.scatter(self.zenith[0], self.zenith[2],
                        label="zenith point",
                        alpha=1., edgecolor='black', facecolor='g',
                        linewidth=2.)
            ax1.scatter(self.nadir[0], self.nadir[2], label="nadir point",
                        alpha=1., edgecolor='black', facecolor='k',
                        linewidth=2.)
            ax1.set_xlabel(self.name[0])
            ax1.set_ylabel(self.name[2])
            ax1.legend(loc='upper center', scatterpoints=1, ncol=4,
                       bbox_to_anchor=(1.75, -0.09),
                       fancybox=True, shadow=True)

            ax2 = fig.add_subplot(2, 3, 5)
            ax2.scatter(EXPIMP[:, 1], EXPIMP[:, 2], alpha=0.5,
                        edgecolor='black', facecolor='b', linewidth=2.)
            ax2.scatter(ParetoFront[1], ParetoFront[2], alpha=0.5,
                        edgecolor='black', facecolor='r', linewidth=2.)
            ax2.scatter(self.zenith[1], self.zenith[2],
                        label="zenith point",
                        alpha=1., edgecolor='black', facecolor='g',
                        linewidth=2.)
            ax2.scatter(self.nadir[1], self.nadir[2], label="nadir point",
                        alpha=1., edgecolor='black', facecolor='k',
                        linewidth=2.)
```

```
                ax2.set_xlabel(self.name[1])
                ax2.set_ylabel(self.name[2])

                ax3 = fig.add_subplot(2, 3, 6)
                ax3.scatter(EXPIMP[:, 1], EXPIMP[:, 0], alpha=0.5,
                            edgecolor='black', facecolor='b', linewidth=2.)
                ax3.scatter(ParetoFront[1], ParetoFront[0], alpha=0.5,
                            edgecolor='black', facecolor='r', linewidth=2.)
                ax3.scatter(self.zenith[1], self.zenith[0],
                            label="zenith point",
                            alpha=1., edgecolor='black', facecolor='g',
                            linewidth=2.)
                ax3.scatter(self.nadir[1], self.nadir[0], label="nadir point",
                            alpha=1., edgecolor='black', facecolor='k',
                            linewidth=2.)
                ax3.set_xlabel(self.name[1])
                ax3.set_ylabel(self.name[0])

                plt.show()

                figg = plt.figure(figsize=(12, 12), facecolor='w',
                                  edgecolor='k', linewidth= 2.0, frameon=True)
                figg.suptitle('3d normalised pareto front')
                axx = figg.add_subplot(1, 1, 1, projection='3d')
                axx.plot(self.PF_norm[:, 0], self.PF_norm[:, 1],
                         self.PF_norm[:, 2], linestyle='',
                         label="Pareto front",
                         alpha=0.5, markerfacecolor='r', markeredgecolor='k',
                         marker='o', markersize=5)
                axx.plot([self.zenith_n[0]], [self.zenith_n[1]],
                         [self.zenith_n[2]],
                         linestyle='', markerfacecolor='g',
                         markeredgecolor='k',
                         marker='o', markersize=5, alpha=1.,
                         label="zenith point")
                axx.plot_wireframe(x_s, y_s, z_s,  rstride=1, cstride=1,
                                   color='b', alpha=0.1, label="zenith sphere")
                axx.plot([self.PF_norm[self.GC.argmin(), 0], self.zenith_n[0]],
                         [self.PF_norm[self.GC.argmin(), 1],
                         self.zenith_n[1]], [self.PF_norm[self.GC.argmin(), 2],
                         self.zenith_n[2]], 'k',
                         label='Min Euclidean distance')
                axx.set_xlabel(self.name[0])
                axx.set_ylabel(self.name[1])
                axx.set_zlabel(self.name[2])
                axx.legend(loc='upper center', numpoints=1, ncol=3,
                           bbox_to_anchor=(0.5, -0.03),
                           fancybox=True, shadow=True)
                figg = plt.show()

        elif self.l == 2:
            if nsgaII == 'Objective':
                u = np.linspace(0, 2 * np.pi, 100)
                x_s = self.zenith_n[0] + self.sphere_radi * np.cos(u)
                y_s = self.zenith_n[1] + self.sphere_radi * np.sin(u)
                # ## ------------------------------------------------- #
                # ##                                                   #
                # ## -------------- plot pareto ----------------------- #
                fig = plt.figure(figsize=(8, 8), facecolor='w',
                                 edgecolor='k', linewidth= 2.0, frameon=True)
                fig.suptitle('pareto front')
                ax = fig.add_subplot(1, 1, 1)
                ax.scatter(self.Model_y[0], self.Model_y[1],
                           label="Evaluation points", alpha=1.,
                           edgecolor='black', facecolor='b', linewidth=2.)
                ax.scatter(ParetoFront[0], ParetoFront[1],
                           label="Pareto front", alpha=1., edgecolor='black',
                           facecolor='r', linewidth=2.)
                ax.scatter(self.zenith[0], self.zenith[1],
                           label="zenith point", alpha=1., edgecolor='black',
                           facecolor='g', linewidth=2.)
                ax.scatter(self.nadir[0], self.nadir[1],
                           label="nadir point", alpha=1., edgecolor='black',
                           facecolor='k', linewidth=2.)
                ax.set_xlabel(self.name[0])
                ax.set_ylabel(self.name[1])
                ax.legend(loc='upper center', numpoints=1, ncol=3,
                          bbox_to_anchor=(0.5, -0.03), fancybox=True,
```

```
                      shadow=True)
            plt.show()

            figg = plt.figure(figsize=(8, 8), facecolor='w',
                              edgecolor='k', linewidth= 2.0, frameon=True)
            figg.suptitle('normalised pareto front')
            axx = figg.add_subplot(1, 1, 1)
            axx.plot(self.PF_norm[:, 0], self.PF_norm[:, 1],
                     linestyle='', label="Pareto front", alpha=0.5,
                     markerfacecolor='r', markeredgecolor='k',
                     marker='o', markersize=5)
            axx.plot([self.zenith_n[0]], [self.zenith_n[1]], linestyle='',
                     markerfacecolor='g', markeredgecolor='k',
                     marker='o', markersize=5, alpha=1.,
                     label="zenith point")
            axx.plot(x_s, y_s, color='b', label="zenith circle")
            axx.plot([self.curvature_sphere[0]],
                     [self.curvature_sphere[1]], linestyle='',
                     markerfacecolor='b', markeredgecolor='k', marker='o',
                     markersize=5, alpha=1., label="center of curvature")
            axx.plot([self.curvature_sphere[0], self.PF_norm[
                      self.GC.argmin(), 0], self.zenith_n[0]], [
                     self.curvature_sphere[1],
                     self.PF_norm[self.GC.argmin(), 1],
                     self.zenith_n[1]], 'k',
                     label='Co-linear curve')
            axx.set_xlabel(self.name[0])
            axx.set_ylabel(self.name[1])
            axx.legend(loc='upper center', numpoints=1, ncol=3,
                       bbox_to_anchor=(0.5, -0.03),
                       fancybox=True, shadow=True)
            figg = plt.show()

    def visualise_updates(self, plot='Kriges', _print_=True):
        data_output = "nsga2_final_pop.out"
        ParetoFront_x = self.pyOpt_Read_Output(data_output, [(i + 4) for i in
                                               range(self.k)])
        if self.k == 2:
            samplePoints = []
            Update_samplePoints = []
            Point_dist = np.ones((len(self.PF_norm[:, 0]), self.n))
            Max_dist = np.ones((len(self.PF_norm[:, 0])))
            Max_dist_ind = np.ones((len(self.PF_norm[:, 0])))
            for i in range(self.k):
                samplePoints.append(self.normaliseX(self.Model_X[:, i],
                                                    self.Ranges[i]))
                Update_samplePoints.append(self.normaliseX(ParetoFront_x[i],
                                                           self.Ranges[i]))
            # pick the update points
            arrsamplePoints = np.array(samplePoints).T
            arrUpdate_samplePoints = np.array(Update_samplePoints).T
            for i in range(len(self.PF_norm[:, 0])):
                for j in range(self.n):
                    Point_dist[i, j] = (self.euclidean_dis(
                                        arrUpdate_samplePoints[i, :],
                                        arrsamplePoints[j, :]))
                Max_dist[i] = np.max(Point_dist[i, :])
                Max_dist_ind[i] = Point_dist[i, :].argmax()
            # this needs improvement
            indices_max = np.ones((5), int)
            Max_dist_copy = np.copy(Max_dist)
            for i in range(5):
                idx = Max_dist_copy.argmax()
                indices_max[i] = idx
                Max_dist_copy[idx] = 0.
            # Create a set of data to plot
            plotgrid = 100
            x = np.linspace(0, 1, num=plotgrid)
            y = np.linspace(0, 1, num=plotgrid)
            X, Y = np.meshgrid(x, y)
            contour_levels = 15
            # Predict based on the optimized results
            for i in range(self.l):
                zs = np.array([self.Models[i].predict_normalized([x, y])
                              for x, y in zip(np.ravel(X), np.ravel(Y))])
                Z = zs.reshape(X.shape)
                Z = ((Z*(np.max(self.Model_y[i]) -
                      np.min(self.Model_y[i]))) +
```

```
             np.min(self.Model_y[i]))

        if plot == ’Kriges’:
            plt.figure(figsize=(8, 8), facecolor=’w’, edgecolor=’k’,
                       linewidth= 2.0, frameon=True)
            plt.title(’Pareto points’)
            plt.contourf(X, Y, Z, contour_levels)
            cb = plt.colorbar()
            cb.set_label(self.name[i])
            plt.plot(samplePoints[0], samplePoints[1], ’ow’,
                     label=’DoE’)
            plt.plot(Update_samplePoints[0], Update_samplePoints[1],
                     linestyle=’’, color=’w’, marker=’v’,
                     markerfacecolor=’white’, markersize=8, alpha=.8,
                     label=’Pareto front’)
            plt.legend(loc=’upper center’, numpoints=1, ncol=3,
                       bbox_to_anchor=(0.5, -0.03), fancybox=True,
                       shadow=True)
            plt.show()

        elif plot == ’Weights’:
            plt.figure(figsize=(8, 8), facecolor=’w’, edgecolor=’k’,
                       linewidth= 2.0, frameon=True)
            plt.title(’Pareto Weights’)
            plt.contourf(X, Y, Z, contour_levels)
            co = plt.colorbar()
            co.set_label(self.name[i])
            plt.plot(samplePoints[0], samplePoints[1], ’ow’,
                     label=’DoE’)
            plt.scatter(Update_samplePoints[0][self.max_weights[0]],
                        Update_samplePoints[1][self.max_weights[0]],
                        alpha=1., c=’g’, marker=’o’, s=40,
                        label=’Max weight f1’)
            plt.scatter(Update_samplePoints[0][self.max_weights[1]],
                        Update_samplePoints[1][self.max_weights[1]],
                        alpha=1., c=’b’, marker=’o’, s=40,
                        label=’Max weight f2’)
            plt.scatter(Update_samplePoints[0][self.max_weights[2]],
                        Update_samplePoints[1][self.max_weights[2]],
                        alpha=1., c=’k’, marker=’o’, s=40,
                        label=’Max weight f3’)
            plt.scatter(Update_samplePoints[0][self.max_weights[3]],
                        Update_samplePoints[1][self.max_weights[3]],
                        alpha=1., c=’r’, marker=’o’, s=60,
                        label=’Max weight’)
            plt.legend(loc=’upper center’, scatterpoints=1, ncol=3,
                       bbox_to_anchor=(0.5, -0.03), fancybox=True,
                       shadow=True)
            plt.show()

        elif plot == ’Euclidean distance’:
            plt.figure(figsize=(8, 8), facecolor=’w’, edgecolor=’k’,
                       linewidth= 2.0, frameon=True)
            plt.title(’Pareto maximum Euclidean distance’)
            plt.contourf(X, Y, Z, contour_levels)
            cr = plt.colorbar()
            cr.set_label(self.name[i])
            plt.plot(samplePoints[0], samplePoints[1], ’ow’,
                     label=’DoE’)
            plt.scatter(Update_samplePoints[0][indices_max[0]],
                        Update_samplePoints[1][indices_max[0]],
                        alpha=1., c=’r’, marker=’H’, s=40,
                        label=’Max distance’)
            plt.scatter(Update_samplePoints[0][indices_max[1]],
                        Update_samplePoints[1][indices_max[1]],
                        alpha=1., c=’b’, marker=’p’, s=40,
                        label=’2nd Max distance’)
            plt.scatter(Update_samplePoints[0][indices_max[2]],
                        Update_samplePoints[1][indices_max[2]],
                        alpha=0.5, c=’g’, marker=’H’, s=40,
                        label=’3rd Max distance’)
            plt.scatter(Update_samplePoints[0][indices_max[3]],
                        Update_samplePoints[1][indices_max[3]],
                        alpha=1., c=’k’, marker=’p’, s=40,
                        label=’4th Max distance’)
            plt.scatter(Update_samplePoints[0][indices_max[4]],
                        Update_samplePoints[1][indices_max[4]],
                        alpha=1., c=’c’, marker=’p’, s=40,
```

```
                                label='5th Max distance')
                    plt.legend(loc='upper center', scatterpoints=1, ncol=3,
                               bbox_to_anchor=(0.5, -0.03), fancybox=True,
                               shadow=True)
                    plt.show()
            if _print_ is True:
                print [[ParetoFront_x[0][int(self.max_weights[i])],
                       ParetoFront_x[1][int(self.max_weights[i])]] for i in
                       range(4)]

    def visualise_updates_err(self, plot='MSE', _print_=True):
        data_output = "nsga2_final_pop.out"
        ParetoFront_x = self.pyOpt_Read_Output(data_output, [(i + 4) for i in
                                               range(self.k)])
        if self.k == 2:
            samplePoints = []
            Update_samplePoints = []
            Point_dist = np.ones((len(self.PF_norm[:, 0]), self.n))
            Max_dist = np.ones((len(self.PF_norm[:, 0])))
            Max_dist_ind = np.ones((len(self.PF_norm[:, 0])))
            for i in range(self.k):
                samplePoints.append(self.normaliseX(self.Model_X[:, i],
                                                    self.Ranges[i]))
                Update_samplePoints.append(self.normaliseX(ParetoFront_x[i],
                                                           self.Ranges[i]))
            # pick the update points
            arrsamplePoints = np.array(samplePoints).T
            arrUpdate_samplePoints = np.array(Update_samplePoints).T
            for i in range(len(self.PF_norm[:, 0])):
                for j in range(self.n):
                    Point_dist[i, j] = (self.euclidean_dis(
                                        arrUpdate_samplePoints[i, :],
                                        arrsamplePoints[j, :]))
                Max_dist[i] = np.max(Point_dist[i, :])
                Max_dist_ind[i] = Point_dist[i, :].argmax()
            indices_max = np.ones((5), int)
            Max_dist_copy = np.copy(Max_dist)
            for i in range(5):
                idx = Max_dist_copy.argmax()
                indices_max[i] = idx
                Max_dist_copy[idx] = 0.
            indices_max_ = np.ones((5), int)
            Max_copy = np.copy(self.infill_errweights)
            for i in range(5):
                idx = Max_copy.argmax()
                indices_max_[i] = idx
                Max_copy[idx] = 0.
            # Create a set of data to plot
            plotgrid = 100
            x = np.linspace(0, 1, num=plotgrid)
            y = np.linspace(0, 1, num=plotgrid)
            X, Y = np.meshgrid(x, y)
            contour_levels = 15
            # Predict based on the optimized results
            for i in range(self.l):
                # Calculate errors
                zse = np.array([self.Models[i].predicterr_normalized([x, y])
                                for x, y in zip(np.ravel(X), np.ravel(Y))])
                Ze = zse.reshape(X.shape)

                if plot == 'MSE':
                    plt.figure(figsize=(8, 8), facecolor='w', edgecolor='k',
                               linewidth= 2.0, frameon=True)
                    plt.title('Pareto points')
                    plt.contourf(X, Y, Ze, contour_levels)
                    co = plt.colorbar()
                    co.set_label(self.name[i])
                    plt.plot(samplePoints[0], samplePoints[1], 'ow')
                    plt.plot(Update_samplePoints[0], Update_samplePoints[1],
                             linestyle='', color='w', marker='v',
                             markerfacecolor='white', markersize=8, alpha=.8)
                    plt.legend(loc='upper center', numpoints=1, ncol=3,
                               bbox_to_anchor=(0.5, -0.03), fancybox=True,
                               shadow=True)
                    plt.show()

                elif plot == 'Weights':
                    plt.figure(figsize=(8, 8), facecolor='w', edgecolor='k',
```

```
                       linewidth= 2.0, frameon=True)
            plt.title('Pareto Weights')
            plt.contourf(X, Y, Ze, contour_levels)
            cb = plt.colorbar()
            cb.set_label(self.name[i])
            plt.plot(samplePoints[0], samplePoints[1], 'ow')
            plt.scatter(Update_samplePoints[0][self.max_weights[0]],
                        Update_samplePoints[1][self.max_weights[0]],
                        alpha=1., c='c', marker='o', s=40,
                        label='max weight f1')
            plt.scatter(Update_samplePoints[0][self.max_weights[1]],
                        Update_samplePoints[1][self.max_weights[1]],
                        alpha=1., c='k', marker='o', s=40,
                        label='max weight f2')
            plt.scatter(Update_samplePoints[0][self.max_weights[2]],
                        Update_samplePoints[1][self.max_weights[2]],
                        alpha=1., c='g', marker='o', s=40,
                        label='max weight f3')
            plt.scatter(Update_samplePoints[0][self.max_weights[3]],
                        Update_samplePoints[1][self.max_weights[3]],
                        alpha=1., c='r', marker='o', s=60,
                        label='max weight F')
            plt.legend(loc='upper center', scatterpoints=1, ncol=3,
                       bbox_to_anchor=(0.5, -0.03), fancybox=True,
                       shadow=True)
            plt.show()

        elif plot == 'Euclidean distance':
            plt.figure(figsize=(8, 8), facecolor='w', edgecolor='k',
                       linewidth= 2.0, frameon=True)
            plt.title('Pareto maximum Euclidean distance')
            plt.contourf(X, Y, Ze, contour_levels)
            cf = plt.colorbar()
            cf.set_label(self.name[i])
            plt.plot(samplePoints[0], samplePoints[1], 'ow')
            plt.scatter(Update_samplePoints[0][indices_max[0]],
                        Update_samplePoints[1][indices_max[0]],
                        alpha=0.5, c='r', marker='H', s=40,
                        label='Max distance')
            plt.scatter(Update_samplePoints[0][indices_max[1]],
                        Update_samplePoints[1][indices_max[1]],
                        alpha=1., c='r', marker='p', s=40,
                        label='2nd Max distance')
            plt.scatter(Update_samplePoints[0][indices_max[2]],
                        Update_samplePoints[1][indices_max[2]],
                        alpha=0.5, c='r', marker='H', s=40,
                        label='3rd Max distance')
            plt.scatter(Update_samplePoints[0][indices_max[3]],
                        Update_samplePoints[1][indices_max[3]],
                        alpha=1., c='r', marker='p', s=40,
                        label='4th Max distance')
            plt.scatter(Update_samplePoints[0][indices_max[4]],
                        Update_samplePoints[1][indices_max[4]],
                        alpha=1., c='r', marker='p', s=40,
                        label='5th Max distance')
            plt.legend(loc='upper center', scatterpoints=1, ncol=3,
                       bbox_to_anchor=(0.5, -0.03), fancybox=True,
                       shadow=True)
            plt.show()

        elif plot == 'WMSE':
            plt.figure(figsize=(8, 8), facecolor='w', edgecolor='k',
                       linewidth= 2.0, frameon=True)
            plt.title('Pareto maximum WMSE')
            plt.contourf(X, Y, Ze, contour_levels)
            cv = plt.colorbar()
            cv.set_label(self.name[i])
            plt.plot(samplePoints[0], samplePoints[1], 'ow')
            plt.scatter(Update_samplePoints[0][indices_max_[0]],
                        Update_samplePoints[1][indices_max_[0]],
                        alpha=1., c='w', marker='D', s=40,
                        label='1st Max WMSE')
            plt.scatter(Update_samplePoints[0][indices_max_[1]],
                        Update_samplePoints[1][indices_max_[1]],
                        alpha=1., c='w', marker='D', s=40,
                        label='2nd Max WMSE')
            plt.scatter(Update_samplePoints[0][indices_max_[2]],
                        Update_samplePoints[1][indices_max_[2]],
```

```
                                alpha=1., c=’w’, marker=’D’, s=40,
                                label=’3rd Max WMSE’)
                    plt.scatter(Update_samplePoints[0][indices_max_[3]],
                                Update_samplePoints[1][indices_max_[3]],
                                alpha=1., c=’w’, marker=’D’, s=40,
                                label=’4th Max WMSE’)
                    plt.scatter(Update_samplePoints[0][indices_max_[4]],
                                Update_samplePoints[1][indices_max_[4]],
                                alpha=1., c=’w’, marker=’D’, s=40,
                                label=’5th Max WMSE’)
                    plt.legend(loc=’upper center’, scatterpoints=1, ncol=3,
                               bbox_to_anchor=(0.5, -0.03), fancybox=True,
                               shadow=True)
                    plt.show()

            if _print_ is True:
                print [[ParetoFront_x[0][int(indices_max_[i])],
                       ParetoFront_x[1][int(indices_max_[i])]] for i in
                       range(5)]

    def visualise_updates_wei(self, plot=’EI’, _print_=True):
        data_output = "nsga2_final_pop.out"
        ParetoFront_x = self.pyOpt_Read_Output(data_output, [(i + 4) for i in
                                               range(self.k)])
        if self.k == 2:
            samplePoints = []
            Update_samplePoints = []
            for i in range(self.k):
                samplePoints.append(self.normaliseX(self.Model_X[:, i],
                                                    self.Ranges[i]))
                Update_samplePoints.append(self.normaliseX(ParetoFront_x[i],
                                                           self.Ranges[i]))
            indices_max = np.ones((5), int)
            Max_copy = np.copy(self.infill_wei)
            for i in range(5):
                idx = Max_copy.argmax()
                indices_max[i] = idx
                Max_copy[idx] = 0.
            # Create a set of data to plot
            plotgrid = 100
            x = np.linspace(0, 1, num=plotgrid)
            y = np.linspace(0, 1, num=plotgrid)
            X, Y = np.meshgrid(x, y)
            contour_levels = 15
            # Predict based on the optimized results
            for i in range(self.l):
                # Calculate errors
                zei = np.array([self.Models[i].expimp([x, y])
                                for x, y in zip(np.ravel(X), np.ravel(Y))])
                Zei = zei.reshape(X.shape)

                if plot == ’EI’:
                    infill = self.pareto_infill_Voutchkov([0, -1])
#                    infill = np.array(infill)
                    for k in range(len(infill[0, :])):
                        infill[:, k] = self.normaliseX(infill[:, k],
                                                       self.Ranges[k])
                    plt.figure(figsize=(8, 8), facecolor=’w’, edgecolor=’k’,
                               linewidth= 2.0, frameon=True)
                    plt.title(’Pareto points-EI’)
                    plt.contourf(X, Y, Zei, contour_levels)
                    ca = plt.colorbar()
                    ca.set_label(self.name[i])
                    plt.plot(samplePoints[0], samplePoints[1], ’ow’,
                             label=’DoE’)
                    plt.plot(Update_samplePoints[0], Update_samplePoints[1],
                             linestyle=’’, color=’w’, marker=’v’,
                             markerfacecolor=’white’, markersize=8, alpha=.8,
                             label=’Pareto front’)
                    plt.plot(infill[:, 0], infill[:, 1],
                             linestyle=’’, color=’k’, marker=’^’,
                             markerfacecolor=’k’, markersize=16, alpha=1.,
                             label=’infill points’)
                    plt.legend(loc=’upper center’, numpoints=1, ncol=3,
                               bbox_to_anchor=(0.5, -0.03), fancybox=True,
                               shadow=True)
                    plt.show()
                elif plot == ’WEI’:
```

```
                    plt.figure(figsize=(8, 8), facecolor='w', edgecolor='k',
                               linewidth= 2.0, frameon=True)
                    plt.title('Pareto maximum Weighted EI')
                    plt.contourf(X, Y, Zei, contour_levels)
                    ci = plt.colorbar()
                    ci.set_label(self.name[i])
                    plt.plot(samplePoints[0], samplePoints[1], 'ow')
                    plt.scatter(Update_samplePoints[0][indices_max[0]],
                                Update_samplePoints[1][indices_max[0]],
                                alpha=1., c='r', marker='D', s=40,
                                label='Max WEI 1st point')
                    plt.scatter(Update_samplePoints[0][indices_max[1]],
                                Update_samplePoints[1][indices_max[1]],
                                alpha=1., c='g', marker='D', s=40,
                                label='Max WEI 2nd point')
                    plt.scatter(Update_samplePoints[0][indices_max[2]],
                                Update_samplePoints[1][indices_max[2]],
                                alpha=1., c='b', marker='D', s=40,
                                label='Max WEI 3rd point')
                    plt.scatter(Update_samplePoints[0][indices_max[3]],
                                Update_samplePoints[1][indices_max[3]],
                                alpha=1., c='k', marker='D', s=40,
                                label='Max WEI 4th point')
                    plt.scatter(Update_samplePoints[0][indices_max[4]],
                                Update_samplePoints[1][indices_max[4]],
                                alpha=1., c='c', marker='D', s=40,
                                label='Max WEI 5th point')
                    plt.legend(loc='upper center', scatterpoints=1, ncol=3,
                               bbox_to_anchor=(0.5, -0.03), fancybox=True,
                               shadow=True)
                    plt.show()

            if _print_ is True:
                return [[ParetoFront_x[0][indices_max[i]],
                         ParetoFront_x[1][indices_max[i]]] for i in range(5)]
```

## G.2 Call the MOO class

run_MOO_class.py

```
# /run_MOO_class.py
__author__ = 'GiorgosRagkousis'
import pyKrige.utilities as utilities
import numpy as np
from MooNSGAII import MOO

dataFile = 'OpLHC_DOE_Obj_Fun.txt'
data = np.genfromtxt(dataFile, delimiter=' ', invalid_raise=False)
X = data[:, [3, 4]]
VAS = data[:, [5]][:, 0]
AASM = data[:, [6]][:, 0]
VAD = data[:, [7]][:, 0]
DEV = data[:, [8]][:, 0]
# load the surrogate models
VAS_Model = utilities.loadModel('VAS_Model.pkl')
AASM_Model = utilities.loadModel('AASM_Model.pkl')
VAD_Model = utilities.loadModel('VAD_Model.pkl')

# import the tuned surrogates in the class and define the DoE limits
MOO_PF = MOO(X, [VAS, AASM, VAD], [VAS_Model, AASM_Model, VAD_Model],
             ['VAS', 'AASM', 'VAD'])
# load the trained models in the class
train = MOO_PF.training()
# calculate the expected improvement
sei = MOO_PF.SEI()
# plot the surrogates
plotKriging = MOO_PF.plot_KrigeModels()
# search the surrogates with NSGA-II
NSGA = MOO_PF.NSGA_II_search(['diameter', 'pressure'],
                             ['f1', 'f2', 'f3'], [2.672, 0.6], [4.008, 1.5],
```

```
                              'mofEI')
# global criterion, find the closest point to the ideal vector
minGC, GC, indi, PF = MOO_PF.global_criterion()
# sort the Pareto front
PF_s = MOO_PF.pareto_sort()
# calculate the pareto gradients
gradients = MOO_PF.pareto_gradients()
# define infill points according to Voutchkov criterion
Voutchkov = MOO_PF.pareto_infill_Voutchkov()
# check the colinearity of the ideal vector with its closest Pareto point
MOO_PF.check_colinearity()
# calculate the weights of the Pareto front
weights = MOO_PF.point_weights()
# take update points according to weights
updateweights = MOO_PF.updatepoints_weights()
# take update points according to weighted errors
weights_error = MOO_PF.infillerrweights()
# take update points according to weighted EI
mWEI = MOO_PF.WEI()
# plot pareto front of the expected improvement
plotPF = MOO_PF.plot_ParetoFront('Expected Improvement')
# visualisation of the updates superimposed to response surfaces
plotupdates = MOO_PF.visualise_updates('Kriges', True)
# visualisation of the updates superimposed to MSE
# plotupdateserror = MOO_PF.visualise_updates_err('WMSE')
# visualisation of the updates superimposed to EI
plotWEI = MOO_PF.visualise_updates_wei()
```

# REFERENCES

AbbotVascular (2008) The xience everolimus eluting coronary stent system instructions for use, pp. 59. Accessed 11 July 2014

Al Suwaidi J, Yeh W, Cohen HA, Detre KM, Williams DO, Holmes DR (2001) Immediate and one-year outcome in patients with coronary bifurcation lesions in the modern era (nhlbi dynamic registry). American Journal of Cardiology 87(10):1139 – 1144

Askari A, Shishehbor M, Messerli A, Aviles R (2011) Introductory Guide to Cardiac Catheterization, 2nd edn. Lippincott Williams & Wilkins

Auricchio F, Di Loreto M, Sacco E (2001) Finite-element analysis of a stenotic artery revascularization through a stent insertion. Computer Methods in Biomechanics and Biomedical Engineering 4(3):249–263

Auricchio F, Conti M, Beule MD, Santis GD, Verhegghe B (2011) Carotid artery stenting simulation: From patient-specific images to finite element analysis. Medical Engineering & Physics 33(3):281 – 289

Berkeley-Heart-Lab (2015) Atherosclerosis progression. http://larryalmonte.com/wp-content/gallery/, assessed on April 2015

Bernard IL, Alain T (1999) Biology of the arterial wall. Kluwer Academic Publishers, USA

Berry C, L'Allier P, Gregoire J, Lesperance J, Levesque S, Ibrahim R, Tardif J (2007) Comparison of intravascular ultrasound and quantitative coronary angiography for the assessment of coronary artery disease progression. Circulation 115(14):1851–1857

Berry JL, Manoach E, Mekkaoui C, Rolland PH, Jr JM, Rachev A (2002) Hemodynamics and wall mechanics of a compliance matching stent: In vitro and in vivo analysis. Journal of Vascular and Interventional Radiology 13(1):97 – 105

Blockwise-Engineering (2015) Self-expanding stents. http://www.blockwise.com/stentloaders.htm, assessed April 2015

Boston-Scientific (2011) Stent deformation update, in complex pci forum, https://vimeo.com/channels/bscpciforum/31595011, accessed 8 Sept. 2015

BostonScientific (2009) Platinum chromium element stent series. http://www.bscintlpresskit.com, assessed January 2012

BostonScientific (2011) The promus element coronary stent system instructions for use, http://www.accessdata.fda.gov/cdrh_docs/pdf11/P110010c.pdf, pp. 43. Accessed 11 July 2014

Bressloff NW, Ragkousis GE, Curzen N (2015) Design optimisation of coronary artery stent systems. Annals of Biomedical Engineering pp 1–11

Butany J, Carmichael K, Leong SW, Collins MJ (2005) Coronary artery stents: identification and evaluation. Journal of Clinical Pathology 58(8):795–804

Chatzizisis Y, Coskun A, Jonas M, Edelman E, Feldman C, Stone P (2007) Role of endothelial shear stress in the natural history of coronary atherosclerosis and vascular remodeling: Molecular, cellular, and vascular behavior. Journal of the American College of Cardiology 49(25):2379 – 2393

Chatzizisis YS, Giannoglou GD, Matakos A, Basdekidou C, Sianos G, Panagiotou A, Dimakis C, Parcharidis GE, Louridas GE (2006) In-vivo accuracy of geometrically correct three-dimensional reconstruction of human coronary arteries: is it influenced by certain parameters? Coronary Artery Disease 17(6):545–551

Choi HH, Hwang SM, Kang Y, Kim J, Kang B (2002) Comparison of implicit and explicit finite-element methods for the hydroforming process of an automobile lower arm. The International Journal of Advanced Manufacturing Technology 20(6):407–413

Chua SD, Donald BM, Hashmi M (2003) Finite element simulation of stent and balloon interaction. J Mater Process Tech 143-144(0):591 – 597, proceedings of the International Conference on the Advanced Materials Processing Technology, 2001.

Conway C, Sharif F, McGarry J, McHugh P (2012) A computational test-bed to assess coronary stent implantation mechanics using a population-specific approach. Cardiovascular Engineering and Technology 3(4):374–387

Cook S, Wenaweser P, Togni M, Billinger M, Morger C, Seiler C, Vogel R, Hess O, Meier B, Windecker S (2007) Incomplete stent apposition and very late stent thrombosis after drug-eluting stent implantation. Circulation 115(18):2426–2434

Cook S, Ladich E, Nakazawa G, Eshtehardi P, Neidhart M, Vogel R, Togni M, Wenaweser P, Billinger M, Seiler C, Gay S, Meier B, Pichler WJ, Jani P, Virmani R, Windecker S (2009) Correlation of intravascular ultrasound findings with histopathological analysis of thrombus aspirates in patients with very late drug-eluting stent thrombosis 120(5):391–399

De Beule M (2008) Finite element stent design. PhD thesis, Ghent University

De Beule M, Mortier P, Carlier SG, Verhegghe B, Impe RV, Verdonck P (2008) Realistic finite element-based stent design: The impact of balloon folding. Journal of Biomechanics 41(2):383 – 389

Deb K (2001) Multi-Objective Optimization Using Evolutionary Algorithms. John Wiley & Sons, Inc., New York, NY, USA

Doulaverakis C, Tsampoulatidis I, Antoniadis AP, Chatzizisis YS, Giannopoulos A, Kompatsiaris I, Giannoglou GD (2013) Ivusangio tool: A publicly available software for fast and accurate 3d reconstruction of coronary arteries. Computers in Biology and Medicine 43(11):1793 – 1803

Dumoulin C, Cochelin B (2000) Mechanical behaviour modelling of balloon-expandable stents. Journal of Biomechanics 33(11):1461 – 1470

Dunn A, Zaveri T, Keselowsky B, Sawyer W (2007) Macroscopic friction coefficient measurements on living endothelial cells. Tribology Letters 27(2):233–238

Edelman ER, Rogers C (1998) Pathobiologic responses to stenting 1. The American Journal of Cardiology 81(7, Supplement 1):4E – 6E

England WT, Miller TL (2001) Volumes and cross-sectional areas. Mathematics Magazine 74(4):288–295

Etave F, Finet G, Boivin M, Boyer JC, Rioufol G, Thollet G (2001) Mechanical properties of coronary stents determined by using finite element analysis. Journal of Biomechanics 34(8):1065 – 1075

Feenstra PH, Taylor CA (2009) Drug transport in artery walls: A sequential porohyperelastic-transport approach. Computer Methods in Biomechanics and Biomedical Engineering 12(3):263–276

Fishbein MC (2014) Heart attack pathology. `http://www.medicinenet.com/`, assessed on July 2014

Foin N, Torii R, Mortier P, De Beule M, Viceconte N, Chan PH, Davies JE, Xu XY, Krams R, Di Mario C (2012) Kissing balloon or sequential dilation of the side branch and main vessel for provisional stenting of bifurcations: Lessons from micro-computed tomography and computational simulations. JACC Cardiovascular Interventions 5(1):47 – 56

Foin N, Lee RD, Torii R, Guitierrez-Chico JL, Mattesini A, Nijjer S, Sen S, Petraco R, Davies JE, Mario CD, Joner M, Virmani R, Wong P (2014) Impact of stent strut design in metallic stents and biodegradable scaffolds. International Journal of Cardiology 177(3):800 – 808

Forrester AIJ, Sobester A, Keane AJ (2008) Engineering Design via Surrogate Modelling. John Wiley & Sons Ltd

Fysal Z, Hyde T, Barnes E, McCrea W, Ramcharitar S (2014) Evaluating stent optimisation technique (stentboost) in a dedicated bifurcation stent (the tryton). Cardiovascular Revascularization Medicine 15(2):92 – 96

Gastaldi D, Morlacchi S, Nichetti R, Capelli C, Dubini G, Petrini L, Migliavacca F (2010) Modelling of the provisional side-branch stenting approach for the treatment of atherosclerotic coronary bifurcations: effects of stent positioning. Biomechanics and Modeling in Mechanobiology 9(5):551–561

Gervaso F, Capelli C, Petrini L, Lattanzio S, Virgilio L, Migliavacca F (2008) On the effects of different strategies in modelling balloon-expandable stenting by means of finite element method. Journal of Biomechanics 41(6):1206 – 1212

Giannoglou G, Chatzizisis Y, Koutkias V, Kompatsiaris I, Papadogiorgaki M, Mezaris V, Parissi E, Diamantopoulos P, Strintzis M, Maglaveras N, Parcharidis G, Louridas G (2007) A novel active contour model for fully automated segmentation of intravascular ultrasound images: In vivo validation in human coronary arteries. Computers in Biology and Medicine 37:1292–1302

Gijsen F, Migliavacca F, Schievano S, Socci L, Petrini L, Thury A, Wentzel J, Van der Steen A, Serruys P, Dubini G (2008) Simulation of stent deployment in a realistic human coronary artery. BioMedical Engineering on Line 7(23):1–11

Grech ED (2003) Percutaneous coronary intervention. ii: The procedure. British Medical Journal 326:1137–1140

Grogan J, O'Brien B, Leen S, McHugh P (2011) A corrosion model for bioabsorbable metallic stents. Acta Biomaterialia 7(9):3523 – 3533

Grogan J, Leen S, McHugh P (2012) Comparing coronary stent material performance on a common geometric platform through simulated bench testing. Journal of the Mechanical Behavior of Biomedical Materials 12(0):129 – 138

Grogan JA, Leen SB, McHugh PE (2013) Optimizing the design of a bioabsorbable metal stent using computer simulation methods. Biomaterials 34(33):8049 – 8060

Gundert T, Marsden A, Yang W, LaDisa J (2012) Optimisation of cardiovascular stent design using computational fluid dynamics. Journal of Biomechanical Engineering 134(1):1–8

Guo N, Maehara A, Mintz GS, He Y, Xu K, Wu X, Lansky AJ, Witzenbichler B, Guagliumi G, Brodie B, Kellett MA, Dressler O, Parise H, Mehran R, Stone GW (2010) Incidence, mechanisms, predictors, and clinical impact of acute and late stent malapposition after primary intervention in patients with acute myocardial infarction. Circulation 122(11):1077–1084

Hamon M, Bauters C, McFadden EP, Wernert N, LaBlanche JM, Dupuis B, Bertrand ME (1995) Restenosis after coronary angioplasty. European Heart Journal 16(suppl I):33–48

Hanratty C, Walsh S (2011) Longitudinal compression: a new complication with modern coronary stent platforms-time to think beyond deliverability. EuroIntervention 7:872–877

Hansson G (2005) Inflammation, atherosclerosis, and coronary artery disease. New England Journal of Medicine 352(16):1685–1695

Harewood F, McHugh P (2007) Comparison of the implicit and explicit finite element methods using crystal plasticity. Computational Materials Science 39(2):481 – 494

Henninger HB, Reese SP, Anderson AE, Weiss JA (2010) Validation of computational models in biomechanics. Proceedings of the Institution of Mechanical Engineers, Part H: Journal of Engineering in Medicine 224(7):801–812

Hildick-Smith D, de Belder AJ, Cooter N, Curzen NP, Clayton TC, Oldroyd KG, Bennett L, Holmberg S, Cotton JM, Glennon PE, Thomas MR, MacCarthy PA, Baumbach A, Mulvihill NT, Henderson RA, Redwood SR, Starkey IR, Stables RH (2010) Randomized trial of simple versus complex drug-eluting stenting for bifurcation lesions: The british bifurcation coronary study: Old, new, and evolving strategies. Circulation 121(10):1235–1243 van der Hoeven BL, Liem S, Dijkstra J, Bergheanu SC, Putter H, Antoni L, Atsma ED, Bootsma M, Zeppenfeld K, Jukema WJ, Schalij MJ (2008a) Stent malapposition after sirolimus-eluting and bare metal stent implantation in patients with st-segment elevation myocardial infarction. Journal of the American College of Cardiology 1(2):192–201

van der Hoeven BL, Liem SS, Dijkstra J, Bergheanu SC, Putter H, Antoni ML, Atsma DE, Bootsma M, Zeppenfeld K, Jukema JW, Schalij MJ (2008b) Stent malapposition after sirolimus-eluting and bare-metal stent implantation in patients with st-segment elevation myocardial infarction: Acute and 9-month intravascular ultrasound results of the mission! intervention study. JACC: Cardiovascular Interventions 1(2):192 – 201

Hoffmann R, Jansen C, König A, Haager PK, Kerckhoff G, Vom Dahl J, Klauss V, Hanrath P, Mudra H (2001) Stent design related neointimal tissue proliferation in human coronary arteries; an intravascular ultrasound study. European Heart Journal 22(21):2007–2014

Hoffmann R, Mintz GS, Haager PK, Bozoglu T, Grube E, Gross M, Beythien C, Mudra H, vom Dahl J, Hanrath P (2002) Relation of stent design and stent surface material to subsequent in-stent intimal hyperplasia in coronary arteries determined by intravascular ultrasound. The American Journal of Cardiology 89(12):1360 – 1364

Holzapfel G (2000) Non linear solid mechanics: a continuum approach for engineering. Wiley

Holzapfel G, Gasser T, Ogden R (2000) A new constitutive framework for arterial wall mechanics and a comparative study of material models. Journal of Elasticity 61:1–48, 10.1023/A:1010835316564

Holzapfel G, Stadler M, Schulze-Bauer A Christian (2002) A layer-specific three-dimensional model for the simulation of balloon angioplasty using magnetic resonance imaging and mechanical testing. Annals of Biomedical Engineering 30(6):753–767

Holzapfel G, Sommer G, Gasser CT, Regitnig P (2005a) Determination of layer-specific mechanical properties of human coronary arteries with nonatherosclerotic intimal thickening and related constitutive modeling. American Journal of Physiology - Heart and Circulatory Physiology 289(5):H2048–H2058

Holzapfel G, Stadler M, Gasser T (2005b) Changes in the mechanical environment of stenotic arteries during interaction with stents: computational assessment of parametric stent designs. Journal of Biomechanical Engineering 127(1):166–180

Hong M, Mintz GS, Lee CW, Park D, Park K, Lee B, Kim Y, Song J, Han K, Kang D, Cheong S, Song J, Kim J, Park S, Park S (2006) Late stent malapposition after drug-eluting stent implantation. Circulation 113(3):414–419

Hose D, Narracott A, Griffiths B, Mahmood S, Gunn J, Sweeney D, Lawford P (2004) A thermal analogy for modelling drug elution from cardiovascular stents. Computer Methods in Biomechanics and Biomedical Engineering 7(5):257–264

Htay T, Liu MW (2005) Drug eluting stent: a review and update. Vascular Health and Risk Management 1(4):263–276

Joner M, Finn AV, Farb A, Mont EK, Kolodgie FD, Ladich E, Kutys R, Skorija K, Gold HK, Virmani R (2006) Pathology of drug-eluting stents in humans: Delayed healing and late thrombotic risk. Journal of the American College of Cardiology 48(1):193 – 202

Jones D (2001) A taxonomy of global optimization methods based on response surfaces. Journal of Global Optimization 21(4):345–383

Jones D, Schonlau M, Welch W (1998) Efficient global optimization of expensive black-box functions. Journal of Global Optimization 13(4):455–492

Kastrati A, Mehilli J, Dirschinger J, Pache J, Ulm K, Schuhlen H, Seyfarth M, Schmitt C, Blasini R, Neumann F, Schomig A (2001) Restenosis after coronary placement of various stent types. The American Journal of Cardiology 87(1):34 – 39

Kawasaki T, Koga H, Serikawa T, Orita Y, Ikeda S, Mito T, Gotou Y, Shintani Y, Tanaka A, Tanaka H, Fukuyama T, Koga N (2009) Impact of a prolonged delivery inflation time for optimal drug-eluting stent expansion. Catheterization and Cardiovascular Interventions 73(2):205–211

Keller B, Amatruda C, Hose D, Gunn J, Lawford P, Dubini G, Migliavacca F, Narracott A (2014) Contribution of mechanical and fluid stresses to the magnitude of in-stent restenosis at the level of individual stent struts. Cardiovascular Engineering and Technology 5(2):164–175

Kiousis D, Wulff A, Holzapfel G (2009) Experimental studies and numerical analysis of the inflation and interaction of vascular balloon catheter-stent systems. Annals of Biomedical Engineering 37(2):315–330

Kiousis DE, Gasser TC, Holzapfel GA (2007) A numerical model to study the interaction of vascular stents with human atherosclerotic lesions. Annals of Biomedical Engineering 35(11):1857–1869

Kolachalama V, Bressloff N, Nair P (2007) Mining data from hemodynamic simulations via bayesian emulation. BioMedical Engineering OnLine 6(1):47

Konig A, Schiele TM, Rieber J, Theisen K, Mudra H, Klauss V (2002) Stent design-related coronary artery remodeling and patterns of neointima formation following self-expanding and balloon-expandable stent implantation. Catheterization and Cardiovascular Interventions 56(4):478–486

Konstantinov IE (2000) Robert h. goetz: the surgeon who performed the first successful clinical coronary artery bypass operation. The Annals of Thoracic Surgery 69(6):1966 – 1972

Lally C, Dolan F, Prendergast P (2005) Cardiovascular stent design and vessel stresses: a finite element analysis. Journal of Biomechanics 38(8):1574 – 1581

Lally C, Kelly DJ, Prendergast PJ (2006) Stents, John Wiley and Sons, Inc.

Laroche D, Delorme S, Anderson T, DiRaddo R (2006) Computer prediction of friction in balloon angioplasty and stent implantation. In: Biomedical Simulation, Lecture Notes in Computer Science, vol 4072, pp 1–8

Lefevre T, Darremont O, Albiero R (2010) Provisional side branch stenting for the treatment of bifurcation lesions. EuroIntervention 6:65–71

Lesiak M (2004) Drug-eluting stent penetration in europe. http://www.cxvascular.com/cn-archives/cardiovascular-news-issue-9/, assessed August 2015

Lewis G (2008) Materials, fluid dynamics, and solid mechanics aspects of coronary artery stents: A state-of-the-art review. Journal of Biomedical Materials Research Part B: Applied Biomaterials 86B(2):569–590

Li L, Couse TL, DeLeon H, Xu CP, Wilcox JN, Chaikof EL (2002) Regulation of syndecan-4 expression with mechanical stress during the development of angioplasty-induced intimal thickening. Journal of Vascular Surgery 36(2):361 – 370

Liang D, Yang D, Qi M, Wang W (2005) Finite element analysis of the implantation of a balloon-expandable stent in a stenosed artery. International Journal of Cardiology 104(3):314 – 318

Lim D, Cho SK, Park WP, Kristensson A, Ko JY, Al-Hassani S, Kim HS (2008) Suggestion of potential stent design parameters to reduce restenosis risk driven by foreshortening or dogboning due to non-uniform balloon-stent expansion. Annals of Biomedical Engineering 36(7):1118–1129

Magro M, van Geuns RJ (2010) The tryton side branch stent. EuroIntervention 6:147–150

Mamas M, Williams DP (2012) Longitudinal stent deformation: insights on mechanisms, treatments and outcomes from the food and drug administration manufacturer and user facility device experience database. EuroIntervention 8(2):196–204

Martin D, Boyle F (2013) Finite element analysis of balloon-expandable coronary stent deployment: Influence of angioplasty balloon configuration. International Journal for Numerical Methods in Biomedical Engineering 29(11):1161–1175

Martin D, Boyle F (2015) Sequential structural and fluid dynamics analysis of balloon-expandable coronary stents: A multivariable statistical analysis. Cardiovascular Engineering and Technology pp 1–15

Mazumdar J (1998) Biofluid Mechanics. World Scientific Publishing Co

McGarry J, O'Donnell B, McHugh P, McGarry J (2004) Analysis of the mechanical performance of a cardiovascular stent design based on micromechanical modelling. Computational Materials Science 31(3-4):421 – 438

Medchrome (2012) Coronary arteries. `http://tube.medchrome.com/`, assessed December 2013

Medtronic-Inc (2014) Integrity stent. `www.medtronicstents.com/`, assessed October 2014

Miettinen K (1998) No-preference methods. In: Nonlinear Multiobjective Optimization, International Series in Operations Research & Management Science, vol 12, Springer US, pp 67–76

Migliavacca F, Petrini L, Colombo M, Auricchio F, Pietrabissa R (2002) Mechanical behavior of coronary stents investigated through the finite element method. Journal of Biomechanics 35(6):803 – 811

Migliavacca F, Petrini L, Montanari V, Quagliana I, Auricchio F, Dubini G (2005) A predictive study of the mechanical behaviour of coronary stents by computer modelling. Medical Engineering & Physics 27(1):13 – 18

Millman RS, Parker GD (1977) Elements of Differential Geometry. Prentice Hall Inc, pp. 46

Moore JE, Berry J (2002) Fluid and solid mechanical implications of vascular stenting. Annals of Biomedical Engineering 30(4):498–508

Morlacchi S, Migliavacca F (2013) Modeling stented coronary arteries: Where we are, where to go. Annals of Biomedical Engineering 41(7):1428–1444

Morlacchi S, Chiastra C, Gastaldi D, Pennati G, Dubini G, Migliavacca F (2011) Sequential structural and fluid dynamic nurical simulations of a stented bifurcated coronary artery. Journal of Biomechanical Engineering 133(2):121,010(1–11)

Morlacchi S, Chiastra C, Cutri E, Zunino P, Burzotta F, Formaggia L, Dubini G, Migliavacca F (2014) Stent deformation, physical stress, and drug elution obtained with provisional stenting, conventional culotte and tryton-based culotte to treat bifurcations: a virtual simulation study. EuroIntervention 9:1441–1453

Morris MD, Mitchell TJ (1995) Exploratory designs for computational experiments. Journal of Statistical Planning and Inference 43(3):381–402

Mortier P, De Beule M (2011) Stent design back in the picture: An engineering perspective of longitudinal stent compression. EuroIntervention 7:773 – 775

Mortier P, Carlier S, Van Impe R, Verhegghe B, Verdonck P (2008) Numerical study of the uniformity of balloon-expandable stent deployment. Journal of Biomechanical Engineering 130(2):021,018(1–7)

Mortier P, Holzapfel G, De Beule M, Loo D, Taeymans Y, Segers P, Verdonck P, Verhegghe B (2010) A novel simulation strategy for stent insertion and deployment in curved coronary bifurcations: Comparison of three drug-eluting stents. Annals of Biomedical Engineering 38(1):88–99

Mortier P, De Beule M, Segers P, Verdonck P, Verhegghe B (2011a) Virtual bench testing of new generation coronary stents. EuroIntervention 7:369–376

Mortier P, Van Beusekom H, De Beule M, Krabbendam-Peters I, Van Der Smissen B, De Santis G, Ligthart J, Verhegghe B, van der Giessen W (2011b) Improved understanding of stent malapposition using virtual bench testing. Interventional Cardiology 6(2):106–109

Mortier P, Hikichi Y, Foin N, De Santis G, Segers P, Verhegghe B, De Beule M (2014) Provisional stenting of coronary bifurcations: Insights into final kissing balloon post-dilation and stent design by computational modeling. JACC Cardiovascular Interventions 7(3):325 – 333

Mudra H, Regar E, Klauss V, Werner F, Henneke K, Sbarouni E, Theisen K (1997) Serial follow-up after optimized ultrasound-guided deployment of palmaz-schatz stents: In-stent neointimal proliferation without significant reference segment response. Circulation 95(2):363–370

Nichols W, O'Rourke M (2005) McDonald's blood flow in arteries: theoretical, experimental and clinical principles, 5th edn. Hodder Arnold

NMA I (2008) Ptca. Nucleus Medical Art, Inc

O'Brien BJ, Stinson JC, Larsen SR, Eppihimer MJ, Carroll WM (2010) A platinumŰchromium steel for cardiovascular stents. Biomaterials 31(14):3755 – 3761

Ormiston JA, Webber B, Webster MW (2011) Stent longitudinal integrity: Bench insights into a clinical problem. JACC: Cardiovascular Interventions 4(12):1310 – 1317

Osterud B, Bjorklid E (2003) Role of monocytes in atherogenesis. Physiological Reviews 83(4):1069–1112

Ozaki Y, Okumura M, Ismail T, Naruse H, Hattori K, Kan S, Ishikawa M, Kawai T, Takagi Y, Ishii J, Prati F, Serruys P (2010) The fate of incomplete stent apposition with drug- eluting stents: an optical coherence tomography-based natural history study. European Heart Journal 31:1470–1476

Pan M, Suarez de Lezo J, Medina A, Romero M, Segura J, Pavlovic D, Delgado A, Ojeda S, Melian F, Herrador J, Urea I, Burgos L (2004) Rapamycin-eluting stents for the treatment of bifurcated coronary lesions: A randomized comparison of a simple versus complex strategy. American Heart Journal 148(5):857 – 864

Pant S, Limbert G, Curzen NP, Bressloff WN (2011) Multiobjective design optimisation of coronary stents. Biomaterials 32(31):7755 – 7773

Pant S, Bressloff N, Limbert G (2012) Geometry parameterization and multidisciplinary constrained optimization of coronary stents. Biomechanics and Modeling in Mechanobiology 11(1-2):61–82

Papadogiorgaki M, Mezaris V, Chatzizisis Y, Giannoglou G, Kompatsiaris I (2008) Image analysis techniques for automated ivus contour detection. Ultrasound in Medicine & Biology 34(9):1482 – 1498

Paulson C, Ragkousis G (2015) pykriging: A python kriging toolkit, http://dx.doi.org/10.5281/zenodo.21389

Perez RE, Jansen PW, Martins JRRA (2012) pyOpt: A Python-based object-oriented framework for nonlinear constrained optimization. Structures and Multidisciplinary Optimization 45(1):101–118

Perry M, Oktay S, Muskivitch J (2002) Finite element analysis and fatigue of stents. Minimally Invasive Therapy & Allied Technologies 11(4):165–171

Pleva L, Jonszta T, Kukla P, Zapletalova J, Berger P, Mrozek J, Porzer M, Obzut B (2014) Dedicated tryton side branch stents used in the treatment of coronary bifurcation lesions. Cor et Vasa 56(6):e478 – e485

Prabhu S, Schikorr T, Mahmoud T, Jacobs J, Potgieter A (2012) Engineering assessment of the longitudinal compression behaviour of contemporary coronary stents. EuroIntervention 8(2):275–81

Rachev A, Manoach E, Berry J, JR JM (2000) A model of stress-induced geometrical remodeling of vessel segments adjacent to stents and artery/graft anastomoses. Journal of Theoretical Biology 206(3):429 – 443

Redwood S, Curzen N, Thomas M (2010) Interventional Cardiology. Oxford University Press

Richard LM, Timothy AS (1995) The history of interventional cardiology: Cardiac catheterization, angioplasty, and related interventions. American Heart Journal 129(1):146 – 172

Robert C (1981) Physiology of the heart and circulation, 2nd edn. Year book medical puplishers, USA

Robinson AD, Schreiber TL, Sobh MA, GRINES CL (2011) Deformation, longitudinal shortening, and accordion of an ion stent. Journal of Interventional Cardiology 24(6):493–495

Rogers C, Edelman E (1995) Endovascular stent design dictates experimental restenosis and thrombosis. Circulation 91(12):2995–3001

Rogers C, Tseng DY, Squire JC, Edelman ER (1999) Balloon-artery interactions during stent placement: A finite element analysis approach to pressure, compliance, and stent design as contributors to vascular injury. Circulation Research 84(4):378–383

Ross R (1999) Atherosclerosis: An inflammatory disease. New England Journal of Medicine 340(2):115–126

Rushmer R (1976) Cardiovascular dynaimics, 4th edn. W.B. Saunders company, USA

Schwartz RS, Murphy JG, Edwards WD, Camrud AR, Vliestra RE, Holmes DR (1990) Restenosis after balloon angioplasty. a practical proliferative model in porcine coronary arteries. Circulation 82(6):2190–200

Schwer LE (2006) Guide for Verification and Validation in Computational Solid Mechanics. New York: American Society of Mechanical Engineers

Serruys PW, Kutryk MJ, Ong AT (2006) Coronary-artery stents. New England Journal of Medicine 354(5):483–495, pMID: 16452560

Shah VM, Mintz GS, Apple S, Weissman NJ (2002) Background incidence of late malapposition after bare-metal stent implantation. Circulation 106(14):1753–1755

Sharecare (2012) `http://www.sharecare.com/`, assessed on July 2015

Sigwart U, Puel J, Mirkovich V, Joffre F, Kappenberger L (1987) Intravascular stents to prevent occlusion and restenosis after transluminal angioplasty. The New England Journal of Medicine (129):146–172

SIMULIA (2013) ABAQUS v.6.12-1 User's Manual. Dassault Systems, USA

Smith J, Kampine P (1990) Circulatory Physiology: The essentials, 3rd edn. Williams and Wilkings, USA

Smithuis R, Willems T (2008) Coronary anatomy and anomalies. `http://www.radiologyassistant.nl/en/48275120e2ed5`, assessed July 2015

Sobester A, Leary SJ, Keane AJ (2005) On the design of optimization strategies based on global response surface approximation models. Journal of Global Optimization 33(1):31–59

Stefanini GG, Holmes DR (2013) Drug-eluting coronary-artery stents. New England Journal of Medicine 368(3):254–265

Sun J, Lee K, Lee H (2000) Comparison of implicit and explicit finite element methods for dynamic problems. Journal of Materials Processing Technology 105(1-2):110 – 118

Takebayashi H, Mintz GS, Carlier SG, Kobayashi Y, Fujii K, Yasuda T, Costa RA, Moussa I, Dangas GD, Mehran R, Lansky AJ, Kreps E, Collins MB, Colombo A, Stone GW, Leon MB, Moses JW (2004) Nonuniform strut distribution correlates with more neointimal hyperplasia after sirolimus-eluting stent implantation. Circulation 110(22):3430–3434

Takumi H, Naoki A, Kenji H, Hiroaki Y, Hirofumi T, Ken O (2014) Stent malapposition, as a potential mechanism of very late stent thrombosis after bare-metal stent implantation: A case report. Cardiovascular Revascularization Medicine 15(3):178 – 181

Theoharis T, Papaioannou G, Platis N, Patrikalakis N (2008) Graphics & Visualization: Principles and Algorithms. A K Peters, Ltd, chapter 3,pp73-114

Timmins HL, Miller WM, Clubb JF, Moore EJ (2011) Increased artery wall stress post-stenting leads to greater intimal thickening. Laboratory Investigation 91:955–967

Timmins LH, Moreno MR, Meyer CA, Criscione JC, Rachev A, Moore JE (2007) Stented artery biomechanics and device design optimization. Medical & Biological Engineering & Computing 45(5):505–513

Timoshenko S (1955) Strength of Materials: Elementary Theory and Problems, vol 1, second edition edn. Van Nostrand Company, p41

Townsend N, Wickramasinghe K, Bhatnagar P, Smolina K, Nichols M, Leal J, Luengo-Fernandez R, Rayner M (2012) Coronary heart disease statistics. British Heart Foundation

Wahle A, Prause GPM, DeJong S, Sonka M (1999) Geometrically correct 3-d reconstruction of intravascular ultrasound images by fusion with biplane angiography-methods and validation. Medical Imaging, IEEE Transactions on 18(8):686–699

Wang DL, Wung BS, Shyy YJ, Lin CF, Chao YJ, Usami S, Chien S (1995) Mechanical strain induces monocyte chemotactic protein-1 gene expression in endothelial cells: Effects of mechanical strain on monocyte adhesion to endothelial cells. Circulation Research 77(2):294–302

Wang WQ, Liang DK, Yang DZ, Qi M (2006) Analysis of the transient expansion behavior and design optimization of coronary stents by finite element method. Journal of Biomechanics 39(1):21 – 32

Williams DP, Mamas M, Morgan K, El-Omar M, Clarke B, Brainbridge A, Fath-Ordoubadi, Fraser DD (2012) Longitudinal stent deformation: a retrospective analysis of frequency and mechanisms. EuroIntervention 8(2):267–74

Wong HC, Cho KN, Tang WC (2009) Bending of a stented atherosclerotic artery. In: Proceedings of the COMSOL Conference, COMSOL, Boston

Wu W, Wang WQ, Yang DZ, Qi M (2007) Stent expansion in curved vessel and their interactions: A finite element analysis. Journal of Biomechanics 40(11):2580 – 2585

Yoon HJ, Hur SH (2012) Optimization of stent deployment by intravascular ultrasound. The Korean Journal of Internal Medicine 27:30–38

Zahedmanesh H, John Kelly D, Lally C (2010) Simulation of a balloon expandable stent in a realistic coronary artery: Determination of the optimum modelling strategy. Journal of Biomechanics 43(11):2126 – 2132

Zunino P (2004) Multidimensional pharmacokinetic models applied to the design of drug-eluting stents. Cardiovascular Engineering: An International Journal 4(2):181–191

Zunino P, Dangelo C, Petrini L, Vergara C, Capelli C, Migliavacca F (2009) Numerical simulation of drug eluting coronary stents: Mechanics, fluid dynamics and drug release. Computer Methods in Applied Mechanics and Engineering 198(46):3633 – 3644